Searches for Excited Leptons in $\sqrt{s} = 8$ and 13 TeV CMS Data

Von der Fakultät für Mathematik, Informatik und Naturwissenschaften der RWTH Aachen University zur Erlangung des akademischen Grades eines Doktors der Naturwissenschaften genehmigte Dissertation

vorgelegt von

Matthias Klaus Endres, M.Sc. RWTH

aus Düsseldorf

Berichter: Univ.-Prof. Dr. rer. nat. Thomas Hebbeker
Priv.-Doz. Dr. rer. nat. Oliver Pooth

Tag der mündlichen Prüfung: 12.05.2017

Abstract

This thesis is about searches for excited leptons, being performed with CMS data from proton-proton collisions. The presented analyses are based on data of an integrated luminosity of $19.7\,\mathrm{fb}^{-1}$ that was taken during 2012 at $\sqrt{s} = 8\,\mathrm{TeV}$ (Run I), and $2.7\,\mathrm{fb}^{-1}$ from the 2015 period at $\sqrt{s} = 13\,\mathrm{TeV}$ (Run II). Excited leptons (ℓ^*) are expected to be sign for a possible lepton compositeness. Both analyses from the two different datasets consider the production of an excited muon (μ^*) in association with another muon via contact interactions. The considered decay mode into another muon and a photon leads to a $\mu\mu\gamma$-final state. The factors f and f', that regulate the coupling between excited and Standard Model leptons, are assumed to be one. The observed data is consistent with the expectation from the Standard Model. Limits are set on the excluded signal cross section, as well as on the excited muon mass and the compositeness scale parameter Λ. Masses from 200 GeV up to $2.5(3)\,\mathrm{TeV} \leq \mathrm{M}_{\mu^*} = \Lambda$ are excluded with the Run I (Run II) analysis. At low excited muon masses, values of Λ up to $17(15)\,\mathrm{TeV}$ are excluded. Combining the results from Run I and Run II extends the exclusion in Λ up to $19\,\mathrm{TeV}$. Results from other Run I analyses that consider neutral current decays of excited electrons and muons are also evaluated. Since these channels are also sensitive to different configurations of f and f', excited electron (muon) masses are excluded up to $2.35(2.4)\,\mathrm{TeV}$ for the case that $\mathrm{M}_{\ell^*} = \Lambda$ and $f = -f' = 1$.

Zusammenfassung

Diese Dissertation handelt von Suchen nach angeregten Leptonen, die mit CMS Daten aus Proton-Proton Kollisionen gemacht werden. Die präsentierten Analysen basieren auf $19{,}7\,\mathrm{fb}^{-1}$ an Daten, die im Jahr 2012 bei $\sqrt{s} = 8\,\mathrm{TeV}$ (Run I) genommen wurden, sowie $2{,}7\,\mathrm{fb}^{-1}$ aus dem Jahr 2015 mit $\sqrt{s} = 13\,\mathrm{TeV}$ (Run II). Angeregte Leptonen (ℓ^*) erwartet man als Hinweis für eine mögliche Lepton-Substruktur. Beide Analysen beschäftigen sich mit der Produktion eines angeregten Myons (μ^*), gemeinsam mit einem weiteren Myon über eine Kontaktwechselwirkung. Der betrachtete Zerfallskanal beinhaltet den Zerfall in ein weiteres Myon und ein Photon, was zu einem $\mu\mu\gamma$-Endzustand führt. Die Faktoren f und f', die die Kopplung zwischen angeregten Leptonen und solchen des Standard Modells regeln, werden auf eins gesetzt. Die gemessenen Daten sind konsistent mit der Erwartung des Standard Modells. Ausschlussgrenzen werden auf den Signal-Wirkungsquerschnitt, sowie auf die Masse des angeregten Myons und den Skalenparameter der Substruktur, Λ, gesetzt. Massen von $200\,\mathrm{GeV}$ bis zu $2,5(3)\,\mathrm{TeV} \leq \mathrm{M}_{\mu^*} = \Lambda$ können mit der Run I (Run II) Analyse ausgeschlossen werden. Bei kleinen Massen der angeregten Myonen, werden Werte für Λ bis zu $17(15)\,\mathrm{TeV}$ ausgeschlossen. Durch Kombination der Run I und Run II Ergebnisse kann der Ausschluss auf Λ auf bis zu $19\,\mathrm{TeV}$ erweitert werden. Ergebnisse von anderen Run I-Analysen, die sich mit dem Zerfall von angeregten Elektronen und Myonen über neutrale Ströme beschäftigen, werden ebenfalls ausgewertet. Da diese Kanäle auch für $f = -f' = 1$ sensitiv sind, können für diesen Fall Massen von angeregten Elektronen (Myonen) von bis zu $2{,}35(2{,}4)\,\mathrm{TeV}$ für $\mathrm{M}_{\ell^*} = \Lambda$ ausgeschlossen werden.

List of Publications

CMS Collaboration, "Search for excited leptons in proton proton collisions at $\sqrt{s} = 8$ TeV", CMS-PAS-EXO-14-015, CERN, Geneva, 2015.

CMS Collaboration, "Search for excited leptons in proton-proton collisions at $\sqrt{s} = 8$ TeV", *JHEP* 03 (2016), 125, arXiv:1511.01407.doi:10.1007/JHEP03(2016)125.

CMS Collaboration, "Search for excited leptons in the $\ell\ell\gamma$ final state at $\sqrt{s} = 13$ TeV", CMS-PAS-EXO-16-009, CERN, Geneva, 2016.

Contents

1 | Introduction

"*Eine jede zusammengesetzte Substanz in der Welt besteht aus einfachen Theilen, und es existirt überall nichts als das Einfache, oder das, was aus diesem zusammengesetzt ist.*",

Aus: I. Kant, "Kritik der reinen Vernunft"
Thesis, Zweiter Widerstreit der transscendentalen Ideen [1]

This sentence, formulated by Kant in the 18th century, summarizes one of the basic ideas of modern (particle) physics: To find the most fundamental structure of everything existing, and to describe the observable laws of nature by these fundamental constituents and their interaction. The Standard Model (SM) of elementary particle physics is very close to this idealized model. Based on no more than twelve types of particles that interact by some few forces, it is able to describe most of our (visible) environment with great accuracy. However, some open questions stay unanswered, and some observations cannot be explained. Those are expected to open the door for possible extensions to the Standard Model and are usually referred to as "Beyond Standard Model" (BSM)-physics.

One of these yet unanswered topics is the one about the fundamental character of the Standard Model. Its distinction of three fermion families and their hierarchical mass structure give rise to the question about an even deeper substructure of the known particles, being based on even less constituents that are bound by a simple attracting force.

This is the point, where the idea of searches for excited fermions comes into play. In case, that the known particles are a system of bound subcomponents, it is expected to be possible to excite this system to higher energetic states. Those would then have similar properties except for a higher mass. Being unstable, their de-excitation would manifest itself by typical radiation that is emitted by those heavy fermions. Similar effects are well known from other bound states like hadrons (e.g. protons that can be excited to Δ-resonances) or atoms or molecules. A famous technical use case of the latter are Lasers. The characteristic signature of such an excited fermion decay is expected to be visible to modern particle detectors.

The history of high-energy physics (hep) is a journey through various levels of structural order to decreasing length scales being accessible to the experiments of their times. With increasing available energy, smaller structures successively could be resolved. Thus, the constituents of the Standard Model were identified and measured one by another. The latest success was the discovery of the long predicted Higgs boson. With the now even increased center of mass energy of the Large Hadron Collider (LHC), the chances to access the next level of compositeness, a postulated fermion substructure, increased and the potential to observe new phenomena is higher than ever before.

This thesis presents two analyses for the search for excited muons in the $\mu\mu\gamma$-final state. They differ in the considered dataset, which is the 2012 data at $\sqrt{s} = 8\,\text{TeV}$ on the one hand, and the 2015 data at $\sqrt{s} = 13\,\text{TeV}$ on the other hand. The whole thesis is set up that both analyses are treated in parallel, i.e. the chapters and section are about special topics whose impact on both analyses is outlined, rather than explaining the analyses consecutively. To distinguish between both, the LHC nomenclature is used, referring to 2012 data as "Run I" and to that from 2015 as "Run II". If similar distributions from both analyses are shown in comparison, the one concerning Run I is always on the left, the one about Run II on the right.

The first chapter of this thesis will give an introduction into the topic of excited fermions, giving emphasis on the leptonic part. It combines general information about the theoretical approach, summarized from given literature, and studies of the signal signature as obtained from a generator. Then, in the second chapter, the basic components and functionalities of the experiment are described. Also, details about the acquisition of the used datasets is given. The third chapter describes the reconstruction and selection of particles that are needed to perform the analysis, namely muons and photons. It also includes a measurement of the CMS muon momentum resolution, being based on cosmic muon data and simulation. Standard Model backgrounds, their simulation or estimation from data, and possibilities for their reduction are discussed in chapter four. In the fifth chapter, all resulting information are collected and interpreted in terms of exclusion limits on the excited muon mass and the compositeness scale, Λ. Also, limits on excited muons and electrons are presented from a variety of other processes. This allows to access regions of the possible parameter space, where the presented analyses are not sensitive.

Several documents were provided during the analysis procedure. Publicly available are [2, 3] about the analyses of the Run I data, and [4] about the analyses of the photon channels with Run II data. The first one includes the Run I analysis presented here, as well as a corresponding search for excited leptons in the eeγ-final state, and six other channels from searches for excited electrons and muons concentrating on signatures from Z-boson radiation. The final optimization and interpretation of all channels was done by the author and is also presented in this thesis. The latter includes the searches for excited electrons and muons, this time restricted to the photon channels. Again, the muon channel, and the final selections and the interpretation was provided by the author. The given publications are based on results of the state at the publication date and small changes to those presented here exist and are outlined.

2 | Theoretical Framework

The Standard Model (SM) of elementary particle physics describes the fundamental particles and their interactions as known until today. Before going into detail about the principles of the idea of fermion substructure, a very brief introduction to the SM is given, concentrating on selected, relevant aspects. After that, details about the theory of fermion substructure are given, followed by descriptions about excited lepton specific signatures and simulation studies of excited muon processes.

2.1 A Condensed Introduction to the Standard Model

The Standard Model was developed over several decades. With increasing available technology and experimental methods, more and more aspects of it could be tested and particles were discovered. Despite several open questions, the Standard Model holds every test and its accurate predictions can be verified with extremely precise measurements. Here, some relevant aspects are summarized. However, only some few chosen topics can be mentioned. A full review is far beyond the scope of this thesis and the interested reader is therefore referred to the relevant literature, e.g. [5].

2.1.1 Particles and Forces

The Standard Model of elementary particle physics knows matter particles that are fermions (f), and, being responsible for the interaction between those, gauge bosons. The group of fermions is divided into leptons (ℓ) and quarks (q). Their best known members are the electron (e) on the one hand, and the up- and down quark on the other hand (u/d). The latter cluster into groups of three to build protons (p) and neutrons, being the constituents of atomic nuclei. Together with the electrons atoms are formed that are the basic structure of every kind of stable matter that is known to mankind. Together with the electrically neutral and extremely light neutrinos (ν_e) that take e.g. part in radioactive decays, and the heavier and unstable members of two other fermion families, the fermion content is complete. Representatives of the other families are the muon (μ) and the tau-lepton (τ) and their corresponding neutrinos (ν_μ, ν_τ). All fermions are summarized in table 2.1 with their respective masses.

The concept of different families is not known from the bosons, until now[1]. Being the gauge boson of the electromagnetic force, the photon (γ) interacts with charged particles like electrons and quarks. The bosons of the weak force, the Z- and the W-boson, are responsible for neutral- and charged current interactions, respectively. The neutral Z-boson thereby allows pair production and annihilation of particles and their respective anti-particle of the same family. The charged W-boson allows for the interaction of leptons with their respective

[1] Still, this idea is theoretically plausible and searches for heavy versions of the known bosons (e.g. Z′, W′) are actively pursued.

Leptons (mass)	$\mathbf{e}$ (511 keV) $\boldsymbol{\nu_e}$	$\boldsymbol{\mu}$ (105.7 MeV) $\boldsymbol{\nu_\mu}$	$\boldsymbol{\tau}$ (1.78 GeV) $\boldsymbol{\nu_\tau}$
Quarks (mass)	up ($\mathbf{u}$) (2.3 MeV) down ($\mathbf{d}$) (4.8 MeV)	charm ($\mathbf{c}$) (1.28 GeV) strange ($\mathbf{s}$) (95 MeV)	top ($\mathbf{t}$) (173.2 GeV) bottom ($\mathbf{b}$) (4.18 GeV)

Table 2.1: The Fermions ($S = \frac{1}{2}$), values taken from [6]. Neutrino masses are not finally determined until today. An upper limit of $M_{\bar{\nu}_e} \lesssim 2$ eV on the anti-electron neutrino mass was set [7]. From oscillation measurements, the other masses are known to be non-zero.

Force	Boson	Mass	Spin	Charge	Range /m
Electromagnetic	Photon (γ)	0	1	0	∞
Weak	Z/W ($\mathbf{Z^0}/\mathbf{W^\pm}$)	91.2/80.4 GeV	1	$0/\pm 1$	10^{-13}
Strong	Gluon ($\mathbf{g}$)	0	1	0	10^{-15}
EW Symm. Br.	Higgs ($\mathbf{H}$)	125.7 GeV	0	0	-
Gravity	Graviton ($\mathbf{G}$)	0	2	0	∞

Table 2.2: The Bosons, values taken from [6]. It was not possible to find evidence for the existence of the graviton, yet. Thus, it remains a theoretical concept.

neutrino, or up-type quarks with down-type ones. The gluon (g), as the carrier of the strong force, is responsible for quark-quark binding and thus also allows that stable nuclei are formed from electromagnetically repelling protons. The Higgs-boson (H) is a phenomenon of the spontaneous symmetry breaking that is needed to allow the Z- and W-boson to obtain mass, and by that not a force carrier like the previous ones. The last fundamental force, gravity, could not be described as a gauge theory until now, and a graviton as the force-carrier could not be found. A summary of the bosons is given in table 2.2.

The Standard Model is formulated as a quantum field theory. To model its interactions by boson exchange, the concept of local gauge invariance is crucial. However, the ansatz is not able to explain the masses of the W- and the Z-boson and thus in contrast to the observation. Therefore, the Higgs mechanism is needed.

2.1.2 First Description of the Weak Force: Fermi's Interaction

The existence of the electron neutrino was presumed from the energy measurement of electrons coming from β-decays. Instead of a sharp, peak-like distribution that was expected similarly to the observation from α- or γ-radiation, a broad energy spectrum was found that indicates the existence of another, neutral particle. Thus, the available energy would be shared with another, undetected particle.

After the successful formulation of the Quantum Electro Dynamics (QED) as a locally invariant gauge symmetry it was tried to find a similar solution for the description of the

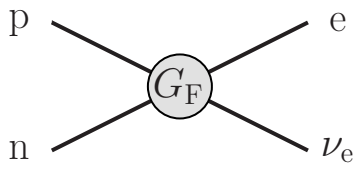

Figure 2.1: Fermi's interaction: Scheme of the β-decay, where all involved particles share one common vertex with the coupling strength G_F.

β-decay. The first formulation was published by Enrico Fermi in 1933 [8]. Therein, the decay was modeled as a directly coupled, four-fermion "Contact Interaction" (CI), where all involved particles interact in one, single vertex (compare figure 2.1). The coupling has a certain strength, called the Fermi constant, G_F.

In his approach, Fermi did not take into account the exchange of a massive gauge boson, in this case the W-boson. As summarized in [5], by doing so, the correct propagator is given by:

$$-i\frac{g_{\mu\nu} - q_\mu q_\nu / M_W^2}{q^2 - M_W^2} \xrightarrow{q^2 \ll M^2} i\frac{g_{\mu\nu}}{M_W^2} \tag{2.1}$$

Therein, $q_{\mu/\nu}$ are the components of the transferred momentum and $g_{\mu\nu}$ denotes the Minkowski metric. However, for a momentum transfer (q^2) being considerably smaller than the square of the propagator's mass (here M_W), it obtains the form of Fermi's four-fermion Contact Interaction. Despite the fact that this approach could not be the correct description, as it is not renormalizable, Fermi was able to predict simple processes like the muon decay with great accuracy. As soon as higher order processes or collisions at an energy scale comparable with the W-mass are considered, the simple approach is no longer applicable. With today's knowledge G_F can be written as

$$G_F = \frac{\sqrt{2}}{8} \cdot \frac{g^2}{M_W^2} = 1.1663787(6) \cdot 10^{-5}\ \mathrm{GeV}^{-2}, \tag{2.2}$$

where g is the weak coupling constant [6].

2.2 Introduction: Compositeness and Excited Fermions

The hierarchical structure of the known fermions is one open question that is not answered by the Standard Model as it is known today. More precisely, there is no explanation for the existence of the three lepton- and quark families and the mass hierarchy within them. An explanation could be a composite nature of the fermions, a deeper substructure, that could not be resolved until now.

If this would be the case, it should be possible to excite these composed bound particles to higher states, just as it is well known from molecules, atoms, or hadrons. Even the lowest excited states of the resulting excited fermions could then have a considerably higher mass than their ground state, and could, by various mechanisms, be produced in high-energy collisions as performed inside CMS [52]. Their de-excitation would lead to characteristic signatures from the decay products that can be used to reconstruct the excited fermion mass. The constituents of this substructure are usually called "Preons" that are bound by a new, unknown interaction that is described by the compositeness scale Λ, "which characterizes the strength of preon-binding interactions and the physical size of composite states" [9].

First concepts for possible heavy electron- and muon states were proposed in the 1960's [10]. Since then, a variety of papers dedicated to the topic of excited quarks and -leptons got published, e.g. [11–21]. Some of them discuss indirect and theoretical constraints [11, 12], others were written under the impression of an unexpected high rate of $Z \to \ell^+\ell^-\gamma$ events that was measured at the UA1 [22] and UA2 [23] detectors of CERN's SPS [13, 14]. Others discuss the production and investigation of excited fermions in e^+e^-- [15–18], ep- [16–18], or pp- and some $p\bar{p}$-collisions [15, 19–21]. The publication that is considered in order to obtain the results of this thesis is "Excited-quark and -lepton production at hadron colliders" by Baur, Spira, and Zerwas [21], which is also the base for the descriptions in the following two sections of this chapter, if no other sources are given.

Given reference [21], the lightest fermions are sorted into isodoublets (exemplary, the first generation is shown), given that excited fermions have a spin and isospin of 1/2:

$$\begin{gathered}\begin{pmatrix}\nu_e\\ e^-\end{pmatrix}_L, e^-_R \quad \begin{pmatrix}\nu_e^*\\ e^{*-}\end{pmatrix}_L, \begin{pmatrix}\nu_e^*\\ e^{*-}\end{pmatrix}_R \\ \begin{pmatrix}u\\ d\end{pmatrix}_L, u_R \quad d_R \quad \begin{pmatrix}u^*\\ d^*\end{pmatrix}_L, \begin{pmatrix}u*\\ d^*\end{pmatrix}_R\end{gathered} \tag{2.3}$$

Following [11, 12, 21], this ansatz allows to avoid strong constraints from g-2 measurements. Without further considerations, a leptonic substructure would lead to contributions to the anomalous magnetic moment of [12]

$$\delta a = \mathcal{O}\left(\frac{m_\ell}{M_{\ell^*}}\right). \tag{2.4}$$

Given the extremely precise measurement of the magnetic moment of electrons (and muons), and its value close to two, this would require excited lepton masses of $M_{\ell^*} > 10^3\,\mathrm{TeV}$ and from that large corrections to the lepton self-energy, $\delta m_\ell = \mathcal{O}(M_{\ell^*})$ [11]. The latter is in contradiction to the actual measured lepton masses. However, it can be shown (section II of [12]) that by introducing chiral symmetry between left- and right-handed excited leptons, the correction of equation 2.4 changes to

$$\delta a = \mathcal{O}\left(\frac{m_\ell^2}{M_{\ell^*}^2}\right). \tag{2.5}$$

This drastically reduces the impact on g-2 and the contributions to the lepton self energy vanish. Thus, much smaller excited lepton masses are allowed.

With this premise, three different couplings between (excited) fermions and bosons can be distinguished. The **gauge interaction** couples either two excited fermions or two fermions (f* or f, respectively) to a boson:

$$\mathscr{L}_{GI} = \bar{f}^*\gamma^\mu\left(g_s\frac{\lambda^a}{2}G^a_\mu + g\frac{\tau}{2}\mathbf{W}_\mu + g'\frac{Y}{2}B_\mu\right)f^* \tag{2.6}$$

In this vector-like coupling that is based on the Dirac matrices γ^μ, the generators of the SU(3), SU(2), and U(1) are λ^a, τ, and Y, respectively. G^a_μ, $\mathbf{W}_\mu$, and B_μ are their respective gauge fields. Y, the weak hypercharge of excited states, is -1 for leptons and 1/3 for quarks. The parameters g_s, $g = e/\sin\theta_W$, and $g' = e/\cos\theta_W$, with the Weinberg-angle θ_W, are the gauge couplings of the strong and electroweak interactions.

Similarly, a gauge-mediated **transition** between left-handed fermions and right-handed excited fermions is possible:

$$\mathscr{L}_t = \frac{1}{2\Lambda}\bar{\mathrm{f}}^*_R\sigma^{\mu\nu}\left(g_s f_s\frac{\lambda^a}{2}G^a_{\mu\nu} + gf\frac{\tau}{2}\mathbf{W}_{\mu\nu} + g'f'\frac{Y}{2}B_{\mu\nu}\right)\mathrm{f}_L + \mathrm{H.c.} \tag{2.7}$$

Here, Λ is the compositeness scale, and the factors f_s, f, and f'[2] weight the scales $\Lambda_i = \Lambda/f_i$ of the different gauge groups [20]. In contrast to equation 2.6, the factors $G^a_{\mu\nu}$, $\mathbf{W}_{\mu\nu}$, and $B_{\mu\nu}$ now describe the field-strength tensors. The transition $\bar{\mathrm{f}}^*_R \to \mathrm{f}_L$ is realized by $\sigma^{\mu\nu} = i/2\cdot[\gamma^\mu,\gamma^\nu]$.

A third production possibility is by a four-fermion **contact interaction** (**CI**), similarly to Fermi's approach of the β-decay. In this case, in contrast to the exchange of Standard Model bosons of the previous possibilities, excited fermions interact with "ordinary" fermions directly by the new, unknown preon interaction. For energies lower than the binding energy Λ, this CI manifests as an effective field theory with the Lagrangian

$$\mathscr{L}_{CI} = \frac{g_*^2}{2\Lambda^2}j^\mu j_\mu \tag{2.8}$$

with the left-handed currents:

$$j_\mu = \bar{\mathrm{f}}_L\gamma_\mu\mathrm{f}_L + \bar{\mathrm{f}}^*_L\gamma_\mu\mathrm{f}^*_L + \bar{\mathrm{f}}^*_L\gamma_\mu\mathrm{f}_L + \mathrm{H.c.} + (L\to R). \tag{2.9}$$

In principle, each of the single currents could have an individual weighting factor. Those are set to one here, and right-handed currents are neglected (compare [21]). The coupling is assumed to be $g_*^2 = 4\pi$ and by that much larger than the electroweak couplings of equations 2.6 and 2.7.

It has to be kept in mind that the ansatz with an effective Lagrangian as in equation 2.8 is able to describe interactions at energies below the compositeness scale Λ. Energies[3] at the scale Λ or above lead to a rise of the cross section (the theory is not renormalizable) and higher-dimensional CI terms become important [21, 24]. In this thesis, effects from the excitation of possible bosons are not taken into account (see [25] for the effect of contributions from excited gluons).

2.3 Production of Excited Fermions

Given the different interactions between excited and ordinary fermions that were introduced in the previous section, a large variety of production mechanisms is possible. Here, the focus is put on those that concern production at hadron colliders and those that are needed to obtain the results in the analyses. Others are summarized for a more complete picture.

Figure 2.2 shows a choice of some important production processes. In figure 2.2(a), an incoming electron is excited by the exchange of a photon or Z-boson with another electron (positron) or a quark. Here, the transition (refer to equation 2.7) allows for single excited electron production at ep or $\mathrm{e^+e^-}$ colliders like HERA [26] or LEP [27, 28], respectively. In case of the quark-gluon fusion (figure 2.2(b)), a single excited quark is resonantly produced,

[2] It has to be distinguished between f and f' representing the coupling factors, and f and f′ for different types of fermions. In the following text, the couplings are given in an *italic* representation, while the fermions (and particles in general) are denoted by upright letters.

[3] Here, energy refers to the momentum transfer in the interaction. For hadron collisions this means that the parton energy $\sqrt{\hat{s}} = x_1\cdot x_2\cdot\sqrt{s}$ has to be used.

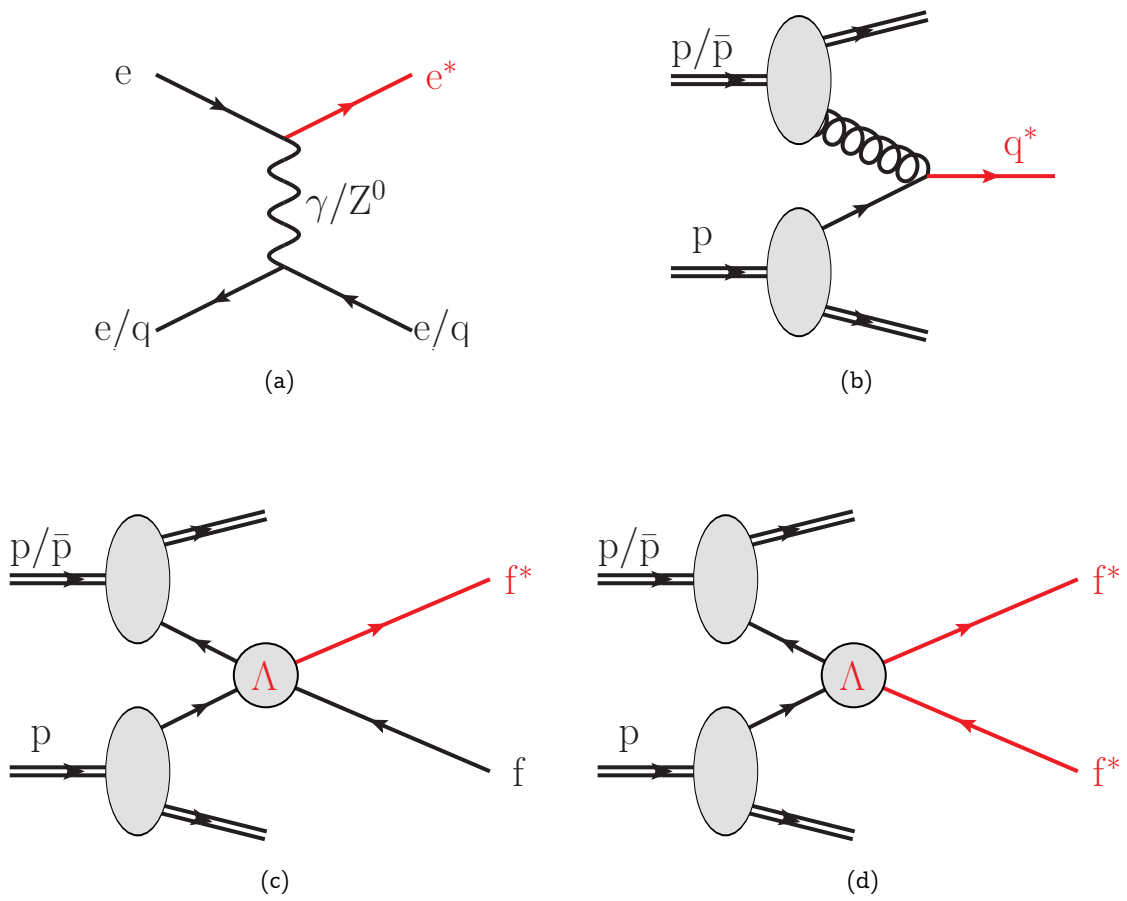

Figure 2.2: Examples for excited fermion (f*) -production: (a) Direct electron excitation by boson exchange in ep and e^+e^- -collisions; (b) Excited quark production by quark-gluon fusion in pp or $p\bar{p}$ collisions; Associated production of an excited and an ordinary fermion (c) and pair-production (d) of excited fermions (ℓ^*/q^*) in pp or $p\bar{p}$ collisions. More production mechanisms exist, e.g. including (excited) neutrinos and W-bosons.

again by the transition of equation 2.7. This is an important production mechanism in $p\bar{p}$ or pp -collisions of hadron colliders like Tevatron [29] or LHC. The two lower diagrams represent the production of a single- (figure 2.2(c)) and a pair of excited fermions (figure 2.2(d)) at hadron colliders via Contact Interactions (equation 2.8). These, and especially the one on the left, are the most important processes to allow for excited lepton -and thus excited muon- production, which is of particular interest for this thesis.

2.3.1 Excited Lepton Production via Contact Interaction

The considerably higher coupling g_* of the CI (eq 2.8) compared to the electroweak couplings of the transition (eq. 2.7) and gauge interaction (eq. 2.6) opens the door for cross sections of the production of excited leptons at the LHC, being sufficiently large to provide a discovery potential. Thus, following the procedure of [21], excited lepton production via CI is here considered as the dominant mechanism.

Given the CI-Lagrangian of equation 2.8, the partonic cross section for the production of a

single excited lepton in association with an ordinary lepton (compare figure 2.2(c)) is:

$$\hat{\sigma}(q\bar{q} \to \ell\bar{\ell}^*/\ell^*\bar{\ell}) = \frac{\pi}{6\hat{s}} \left(\frac{\hat{s}}{\Lambda^2}\right)^2 \left(1 + \frac{\nu}{3}\right) \times \left(1 - \frac{M_{\ell^*}^2}{\hat{s}}\right)^2 \left(1 + \frac{M_{\ell^*}^2}{\hat{s}}\right) \tag{2.10}$$

Similarly, the one for excited lepton pair-production (figure 2.2(d)) is given by

$$\hat{\sigma}(q\bar{q} \to \ell^*\bar{\ell}^*) = \frac{\pi\tilde{\nu}}{12\hat{s}} \left(\frac{\hat{s}}{\Lambda^2}\right)^2 \left(1 + \frac{\tilde{\nu}^2}{3}\right), \tag{2.11}$$

depending on the energy of the partonic interaction $\sqrt{\hat{s}} = x_1 \cdot x_2 \cdot \sqrt{s}$, the excited lepton mass M_{ℓ^*}, and the compositeness scale Λ. The abbreviations ν and $\tilde{\nu}$ are defined as:

$$\begin{aligned} \nu &= \frac{\hat{s} - M_{\ell^*}^2}{\hat{s} + M_{\ell^*}^2} \\ \tilde{\nu} &= \sqrt{1 - 4\frac{M_{\ell^*}^2}{\hat{s}}} \end{aligned} \tag{2.12}$$

The functional behavior of both production mechanisms, depending on M_{ℓ^*}, is illustrated in figure 2.3. It allows to compare the cross sections of pair- (dashed lines) and associated (solid lines) excited lepton production for exemplary values of $\Lambda = 6\,\text{TeV}$, $10\,\text{TeV}$, and M_{ℓ^*}. A partonic center of mass energy of $\sqrt{\hat{s}} = 13\,\text{TeV}$ is used to produce the plot, but other choices result in similar distributions with varying absolute scales of the cross section. Here, only the relative behavior is of interest. That is why no scale is given on the y-axis. As one would expect, the cross sections drop to zero at $M_{\ell^*} \approx \sqrt{\hat{s}}$ in case of the associated production, and at $M_{\ell^*} \approx \sqrt{\hat{s}}/2$ for the pair-production. Throughout the whole range of possible values of the parameters under investigation, the cross sections of the pair-production lie considerably lower than those of the associated one.

In pp-collisions, the real partonic energy is usually much lower than the center of mass energy of the intersecting protons (13 TeV for Run II). Thus, cross sections for the excited lepton pair-production are additionally suppressed when determining the total pp-production cross sections. This explains the large suppression of the total cross section of the pair-production with respect to the one from associated production that are shown in figure 10 of [21], yielding in approximately one order of magnitude for the LHC-model that is assumed there ($\sqrt{s} = 16\,\text{TeV}$). For that reason, searches for excited leptons are usually restricted to the associated production. The same is done for the analyses that are presented in this thesis. In general, the pair-production of excited leptons leads to additional, interesting final states.

2.4 Decay of Excited Leptons

Excited leptons (excited fermions in general) are expected to decay instantaneously into known particles of the Standard Model. This can happen either by the transition interaction (eq. 2.7) via boson radiation, or by the four-fermion contact interaction (eq. 2.8).

Starting with the transition interaction, the partial width for the decay under the emission of a photon is given by:

$$\Gamma(f^* \to f\gamma) = \frac{1}{4}\alpha f_\gamma^2 \frac{M_{\ell^*}^3}{\Lambda^2} \tag{2.13}$$

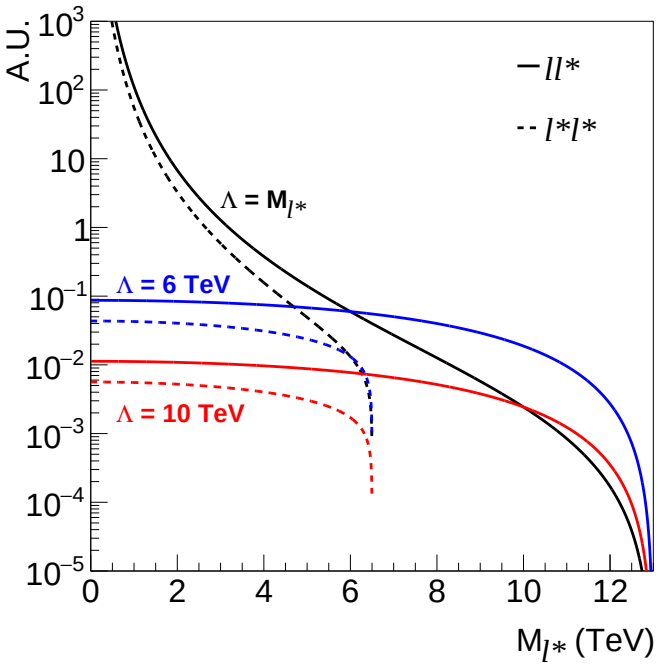

Figure 2.3: Partonic cross sections for the production of an excited lepton in association with an ordinary lepton (solid) and excited lepton pair-production (dashed), as a function of the excited lepton mass. The functional behavior for three different values of Λ is shown, assuming $\sqrt{\hat{s}} = 13\,\mathrm{TeV}$.

Similarly, for completeness, an excited quark could radiate a gluon:

$$\Gamma(q^* \to qg) = \frac{1}{3}\alpha_s f_s^2 \frac{M_{\ell*}^3}{\Lambda^2} \tag{2.14}$$

The partial width of the decay by the radiation of a gauge boson is described by:

$$\Gamma(f^* \to fV) = \frac{1}{8}\frac{g_V^2}{4\pi} f_V^2 \frac{M_{\ell*}^3}{\Lambda^2}\left(1 - \frac{m_V^2}{M_{\ell*}^2}\right)^2\left(2 + \frac{m_V^2}{M_{\ell*}^2}\right) \tag{2.15}$$

Here, m_V is the mass of the gauge (W/Z) boson, and g_V is either $g_W = e/\sin\theta_W$ or $g_Z = g_W/\cos\theta_W$, respectively. The couplings, f_V, are defined as

$$\begin{aligned} f_\gamma &= fT_3 + f'\frac{Y}{2} \\ f_Z &= fT_3\cos^2\theta_W - f'\frac{Y}{2}\sin^2\theta_W \\ f_W &= \frac{f}{\sqrt{2}} \end{aligned} \tag{2.16}$$

with the third component of the weak isospin, $T_3 = -1/2$, and the weak hypercharge $Y = -1$, in the case of excited leptons. The parameters f and f' are already known from the Lagrangian of the transition interaction in equation 2.7. Here, their importance becomes obvious: They directly regulate the coupling of an excited lepton to the gauge bosons ($f_{W/Z}$) and the photon (f_γ). For the latter, the coupling becomes largest in the case $f = f' = 1$, thus maximizing the branching fraction of the decay under photon emission. On the other hand, in the case $f = -f' = 1$, the coupling becomes zero and the photon channel is forbidden.

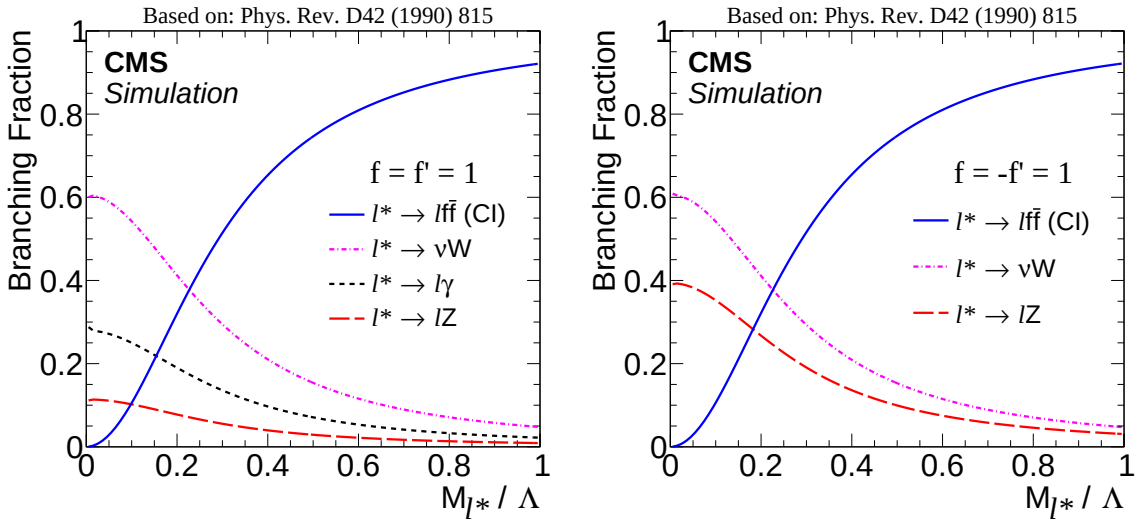

Figure 2.4: Branching ratios of the various ℓ^*-decay modes as a function of M_{ℓ^*}/Λ. Previously published in [3].

The decay via the four-fermion contact interaction has the following decay width:

$$\Gamma(f^* \to ff'\bar{f}') = \frac{M_{\ell^*}}{96\pi}\left(\frac{M_{\ell^*}}{\Lambda}\right)^4 N_C' S' \tag{2.17}$$

with a color factor for the final state fermions f′, being $N_C' = 1$ or 3 for leptons and quarks, respectively. S' is an additional combinatorial factor:

$$\begin{aligned} S' &= 1, && f \neq f' \\ S' &= \frac{4}{3}, && f = f' = q \\ S' &= 2, && f = f' = \ell \end{aligned} \tag{2.18}$$

The resulting branching fractions, as a function of M_{ℓ^*}/Λ are shown in figure 2.4 for the case $f = f' = 1$ (left) and $f = -f' = 1$ (right). It illustrates that in the case $f = f' = 1$, the decay into a neutrino and a W-boson (pink, dashed-dotted) dominates over the photon radiation (black, short dashed) that is subsequently followed by the decay into a lepton and a Z-boson (red, long dashed). For $f = -f' = 1$, the photon contribution vanishes and the decay involving Z-bosons gains drastically. However, in both cases, the decay via contact interaction (blue, solid) strongly dominates for large regions of higher M_{ℓ^*}/Λ values, i.e. high M_{ℓ^*} or small Λ.

The total decay width of an excited lepton, as calculated from the sum of the decay into photons, gauge bosons and by CI (equations 2.13, 2.15, and 2.17), is outlined in figure 2.5, assuming $f = f' = 1$. It shows the total width for different values of Λ as a function of the excited lepton mass, M_{ℓ^*}. The case $\Lambda = M_{\ell^*}$ is thereby represented in a solid black line, and $\Lambda = 10\,\text{TeV}$, which is used for the production of signal MC is given in dashed blue. In the considered mass range, the latter extends over a range from $\Gamma_{\text{tot}} = 0.5\,\text{MeV}$ to $5\,\text{GeV}$. For $\Lambda = 20\,\text{TeV}$, the width goes down to 0.1 MeV at the lowest mass. Given $\Gamma = \tau^{-1}$, the latter corresponds to a lifetime of $\tau \approx 10^{-22}\,\text{s}$ and an instantaneous decay can be assumed. The highest width is reached in the case $\Lambda = M_{\ell^*}$. Being rather flat in comparison to the other distributions, it is in the range of $\mathcal{O}(10 - 100)\,\text{GeV}$.

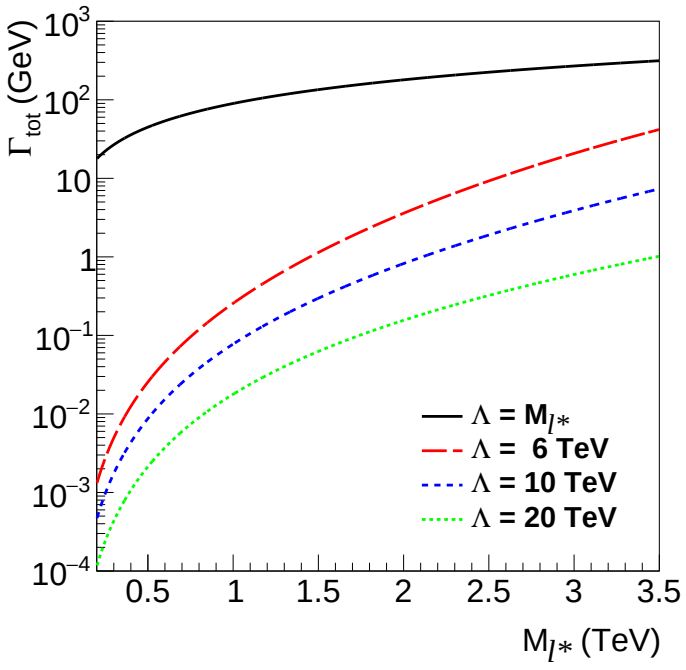

Figure 2.5: Total decay width of an excited lepton as a function of M_{ℓ^*} and different values of Λ. The values are calculated as the sum of the partial widths from the photon, gauge-boson and CI-decays with $f = f' = 1$.

2.4.1 Final States

The various decay channels provide a large variety of final states. Here, in table 2.3, an overview for excited lepton and -quark decays from associated production is given. Pairproduction further extends the accessible final states.

The analyses presented in this thesis focus on the photon decay of excited muons, as given in figure 2.6. The resulting $\mu\mu\gamma$-final state provides a very clean signature. For optimal sensitivity, the results will be interpreted with the assumption that

$$\boxed{f = f' = 1}. \tag{2.19}$$

As this final state is not sensitive to $f = -f' = 1$, and other decay modes are able to provide easy to reconstruct final states and high discovery potentials, more Run I analyses were performed by other CMS members. Their final results were obtained and interpreted by the author and will also be discussed in this thesis.

2.5 Excited Muons: Simulation and Cross Sections

For the Run I analysis, signal samples for the process $q\bar{q} \to \mu\mu^* \to \mu\mu\gamma$ are produced using Pythia8.175 [30, 31] in a M_{μ^*}-range from 200 GeV to 2.6 TeV, in steps of 200 GeV. Respectively, for the Run II analysis, the existing samples are produced with Pythia8.205 in

Decay	Final State (ℓ^*)	Final State (q*)
γ	$\ell\ell\gamma$	qqγ
W	$\ell\nu_\ell\ell'\nu_{\ell'}$ $\ell\nu_\ell$qq$'$	qq$'\ell\nu_\ell$ qq$'$q$''$q$'''$
Z	$\ell\ell$qq $\ell\ell\ell'\ell'$	qqq$'$q$'$ qq$\ell\ell$
CI	$\ell\ell$qq $\ell\ell\ell'\ell'$	qqq$'$q$'$ qq$\ell\ell$
g	–	qqg

Table 2.3: Overview of the possible final states resulting from associated excited lepton and -quark production. Here, leptons can also represent neutrinos ($\ell = \nu$).

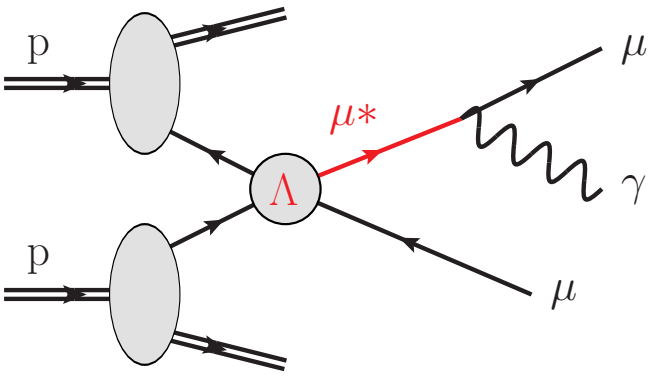

Figure 2.6: The relevant Feynman diagram for the analyses being presented in this thesis: Associated $\mu^*\mu$-production by four-fermion contact interaction with decay via photon radiation, leading to a $\mu\mu\gamma$-final state.

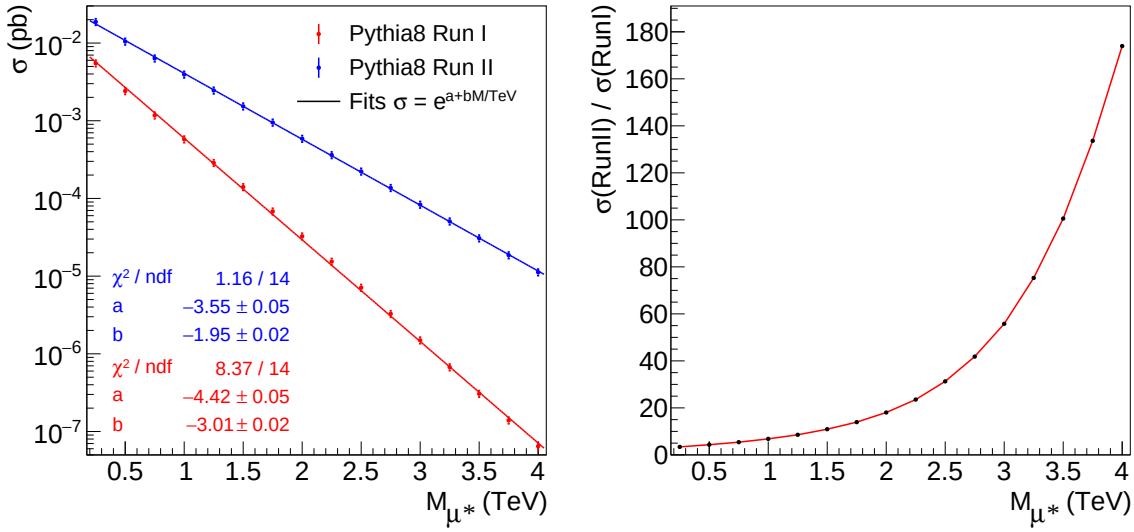

Figure 2.7: Left: Cross sections for the process $q\bar{q} \to \mu\mu^* \to \mu\mu\gamma$ as a function of M_{μ^*} for $\sqrt{s} = 8\,\text{TeV}$ (red) and $\sqrt{s} = 13\,\text{TeV}$ (blue), calculated with Pythia8.205. An exponential function is fitted to both in order to be able to evaluate the cross section at any given mass. An uncertainty of 10% is assigned to the cross sections. Right: Ratio between both. Both plots are for $\Lambda = 10\,\text{TeV}$.

mass steps of 250 GeV, covering a range from 250 GeV to 4 TeV. The detailed sample names can be found in Appendix A.

All available samples are generated with $\Lambda = 10\,\text{TeV}$ by other members of the CMS ℓ^*-group. As the decay via contact interaction is not integrated in the earlier version Pythia8.175, cross sections for $\sqrt{s} = 8\,\text{TeV}$ and $\sqrt{s} = 13\,\text{TeV}$ are calculated with Pythia8.205. Similarly, the total decay width of the Run I samples does not include the CI-contribution. The widths of the Run II samples include all contributions from photon, gauge boson, and CI-decays.

Detailed, mass-dependent k-factors to account for NLO QCD-contributions are provided by the author of [32]. Following this reference, the signal cross sections and k-factors may considerably change under a variation of the factorization- and renormalization scales or the choice of the PDF-set. To account for that, an uncertainty of 10% is assigned to the signal cross section.

The cross sections of both analyses, as a function of M_{μ^*}, are displayed in figure 2.7, left. The dots are the outcome from the calculations with Pythia, with the 10% uncertainty represented by the error bars. As displayed, their evolution with the mass M_{μ^*} can well be described by an exponential function that is fitted to the points. Even though the fit for Run I shows a visible modulation, it is possible to reproduce the cross sections over several orders of magnitude well within the assigned systematic uncertainty. These fits will be used to estimate the cross section at any given M_{μ^*}. The corresponding NLO k-factors for both runs are shown in figure 2.8 and are multiplied to the corresponding cross sections.

Figure 2.7, right, shows the ratio between the Run II and Run I NLO cross sections. It illustrates how the higher center of mass energy results in a gain in the cross section, increasing steadily with higher masses. This promises a high discovery potential for large M_{μ^*}-masses. However, the ratio is considerably higher than one would naively expect from the parton luminosity ratio which is calculated by [33] and shown in figure 2.9 for the ratio 13 TeV/8 TeV.

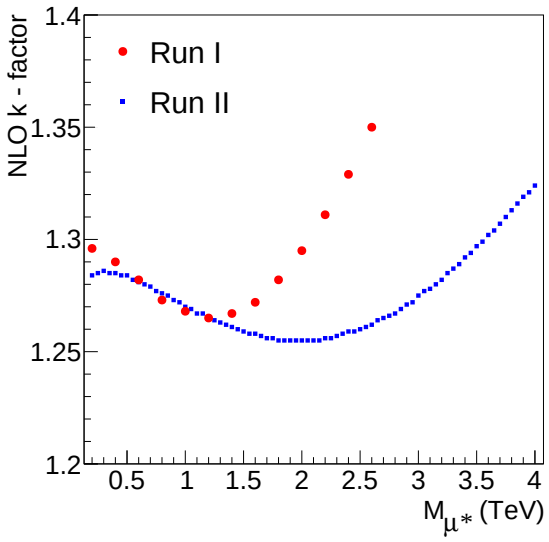

Figure 2.8: NLO k-factors as a function of M_{μ^*} for $\sqrt{s} = 8\,\text{TeV}$ (red points) and $\sqrt{s} = 13\,\text{TeV}$ (blue squares). The exact numbers were provided by the author of [32].

There, the dashed line gives the ratio for $q\bar{q}$-production as a function of the resonant mass. The reason for that discrepancy is the associated production of an excited and an ordinary muon. This will be discussed in more detail in the following section. Table 2.4 summarizes the cross sections and NLO k-factors for all available signal mass samples.

2.6 Signal Properties

In this section, properties of the expected signal of the relevant process $q\bar{q} \to \mu\mu^* \to \mu\mu\gamma$ will be investigated. Based on the simulated $\sqrt{s} = 13\,\text{TeV}$-samples of table 2.4 with $\Lambda = 10\,\text{TeV}$, three signal masses are compared, namely $M_{\mu^*} = 0.25\,\text{TeV}$, $1\,\text{TeV}$, and $2.5\,\text{TeV}$. First, different kinematic properties of the various final state particles are compared. After that, the issue of the reconstruction of the excited muon mass (M_{μ^*}) is discussed. All distributions are based on the bare generator output, i.e. no detector simulation or selections are applied to the simulation.

Before getting started, the used nomenclature has to be introduced. The final state includes two muons. Both can be distinguished by their transverse momentum. The one with the higher p_T, the leading muon, is in the following referred to as μ_1. Respectively, the one with the lower p_T is called μ_2. Both muons can also be distinguished by their origin by relying on information from the generator. The muon that has thereby been identified as the one that is produced in association with the excited muon is called μ_{as}. Similarly, the one coming from the μ^*-decay is named μ_d. The distributions of the following figures are all scaled to unit area. The width of the respective p_T- and invariant mass-bins is given in the label of the y-axis.

	Run I ($\sqrt{s} = 8\,\text{TeV}$)		Run II ($\sqrt{s} = 13\,\text{TeV}$)	
M_{μ^*} (GeV)	σ (pb)	k-factor	σ (pb)	k-factor
200	$6.615 \cdot 10^{-3}$	1.296	–	–
250	–	–	$1.874 \cdot 10^{-2}$	1.285
400	$3.623 \cdot 10^{-3}$	1.290	–	–
500	–	–	$1.048 \cdot 10^{-2}$	1.284
600	$1.984 \cdot 10^{-3}$	1.282	–	–
750	–	–	$6.359 \cdot 10^{-3}$	1.277
800	$1.086 \cdot 10^{-3}$	1.273	–	–
1000	$5.948 \cdot 10^{-4}$	1.268	$3.941 \cdot 10^{-3}$	1.270
1200	$3.257 \cdot 10^{-4}$	1.265	–	–
1250	–	–	$2.459 \cdot 10^{-3}$	1.264
1400	$1.784 \cdot 10^{-4}$	1.267	–	–
1500	–	–	$1.535 \cdot 10^{-3}$	1.259
1600	$9.767 \cdot 10^{-5}$	1.272	–	–
1750	–	–	$9.504 \cdot 10^{-4}$	1.256
1800	$5.348 \cdot 10^{-5}$	1.282	–	–
2000	$2.929 \cdot 10^{-5}$	1.295	$5.878 \cdot 10^{-4}$	1.255
2200	$1.604 \cdot 10^{-5}$	1.311	–	–
2250	–	–	$3.623 \cdot 10^{-4}$	1.256
2400	$8.781 \cdot 10^{-6}$	1.329	–	–
2500	–	–	$2.226 \cdot 10^{-4}$	1.260
2600	$4.809 \cdot 10^{-6}$	1.350	–	–
2750	–	–	$1.369 \cdot 10^{-4}$	1.266
3000	–	–	$8.332 \cdot 10^{-5}$	1.275
3250	–	–	$5.074 \cdot 10^{-5}$	1.285
3500	–	–	$3.079 \cdot 10^{-5}$	1.297
3750	–	–	$1.863 \cdot 10^{-5}$	1.310
4000	–	–	$1.124 \cdot 10^{-5}$	1.324

Table 2.4: Cross sections for $\Lambda = 10\,\text{TeV}$ and NLO k-factors [32] of the signal points that are simulated for the Run I and Run II analyses.

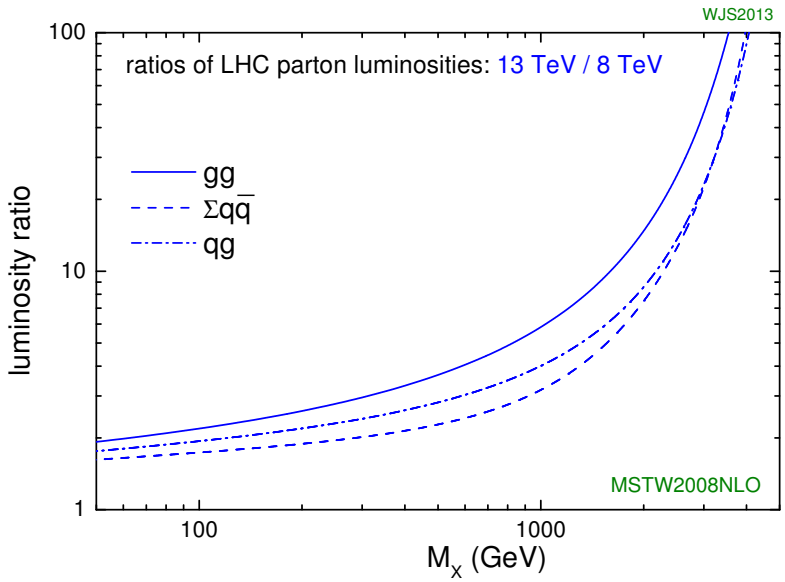

Figure 2.9: Parton luminosity ratio for 13 TeV/8 TeV and different initial states, as a function of the resonantly produced mass. Taken from [33].

2.6.1 Signal Kinematics

Figure 2.10 shows the transverse momenta of the leading and subleading muon on the left and right side, respectively. The momenta of the leading muons peak roughly at half the excited muon mass and are generally distributed over a wide range of several hundred GeV. The momenta of the subleading muons are considerably lower. Especially for low masses, muons tend to have a transverse momentum of only several ten GeV; the two bins of the $M_{\mu^*} = 250\,\text{GeV}$-distribution that have the highest content, cover a range from only 40 to 80 GeV. This has to be taken into account when further selection criteria are defined, in order not to remove too much of a possible signal at lower masses.

Figure 2.11 compares the transverse momenta of the associate muon (μ_{as}, left) and the one from the decay (μ_{d}, right). Comparing both to the distribution of the (sub-) leading muons in figure 2.10, it becomes obvious that both definitions have to be distinguished; i.e. it is not possible to assign the subleading muon to be the one from the decay or the leading muon the one from the associated production, or vice versa, without relying on generator information. Going more into detail, it can be noted that the 250 GeV distribution of μ_{d} can be compared to the corresponding line of μ_2. On the other hand, the shape and normalization of the 2.5 TeV distribution of μ_{d} compares well with the corresponding one from μ_1. As a consequence, the shape evolution of μ_{as} differs strongly from that of the other muons: The average momentum of a distribution rises slower with increasing M_{μ^*}.

Figure 2.12 is about angular distributions of the muons. On the left, the η-distributions of μ_{as} are shown. It can be seen that with rising M_{μ^*}, the distributions of the polar angle become more narrow. The phenomenon is known from many searches for heavy new particles. The reason is that in order to provide enough collision energy for high masses, both interacting partons need to carry a large momentum fraction. In contrast, for low mass productions, it is sufficient if one parton has a low momentum fraction, leading to collisions that are boosted

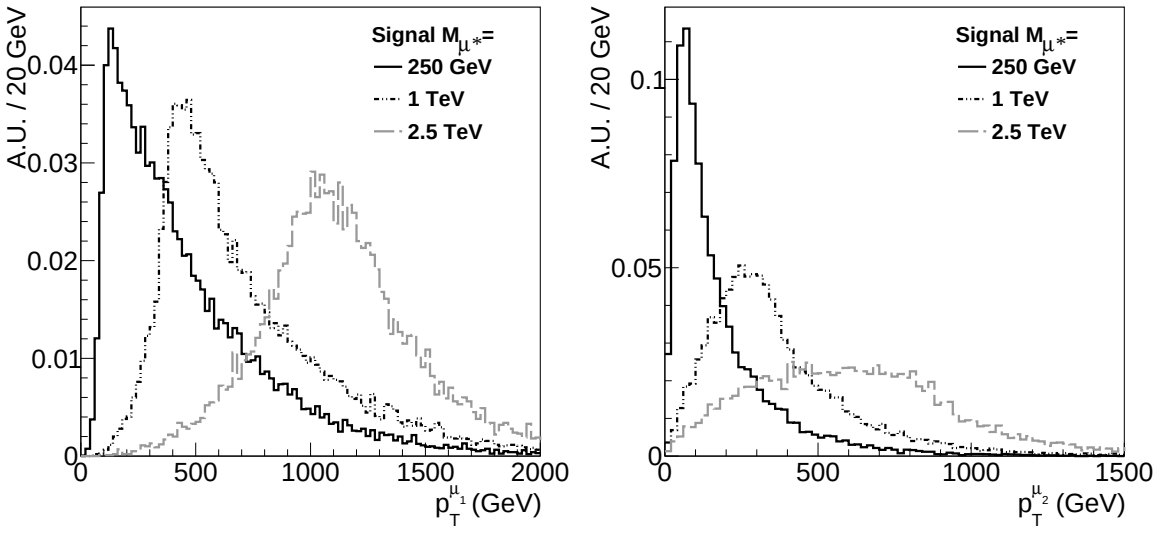

Figure 2.10: Distributions of the transverse momenta of the leading (μ_1, left) and subleading (μ_2, right) muon, as obtained from signal simulation on generator level.

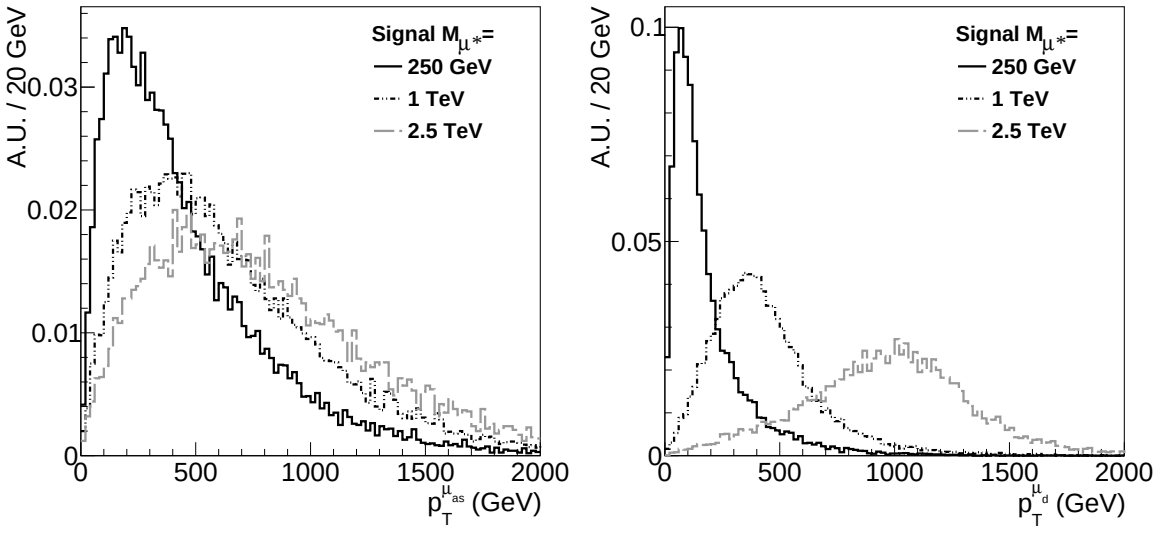

Figure 2.11: Transverse momenta of the muon from the associated production (μ_{as}, left) and the μ^*-decay (μ_d, right), as obtained from signal simulation on generator level.

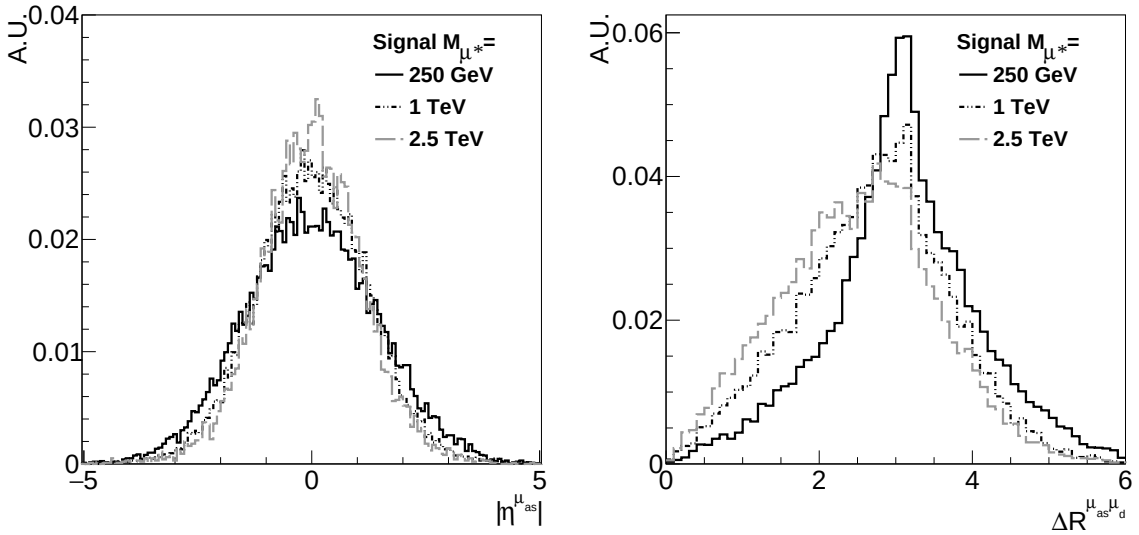

Figure 2.12: Left: η-distributions of the muon from the associated production, μ_{as}. Right: Angle ΔR between both muons. Both are obtained from signal simulation on generator level.

into the forward direction, widening the η-distribution. A similar behavior can be found in the η-distributions of μ_{d}, which are not shown separately.

On the right side, the angle ΔR between both muons is shown. The higher the considered signal mass, the broader the respective distribution becomes. Generally, both muons are well separated and do not risk to influence each other, e.g. when an isolation criterion is applied later on.

Similar p_{T}- and η-distributions for the photons are given in figure 2.13, left and right, respectively. As already observed in the muon-η distributions, those for the photon become more narrow with increasing μ^*-masses.

The distributions of the angles between the photon and the two different muons, μ_{as} and μ_{d}, are shown in figure 2.14, left and right, respectively. As one would expect, photons are well separated from the associated muon, μ_{as}. The corresponding angle between photon and μ_{d} differs. With increasing M_{μ^*}, both become more separated. For lower excited muon masses, contributions from smaller angles become more relevant. However, within the considered masses, contributions at very small angles are negligible.

2.6.2 Invariant Mass Reconstruction

In order to separate signal from background on the on hand, and to identify a possible existing signal and measure its properties on the other hand, it is useful to calculate the invariant mass of the decay products. Thus, a resonant, narrow signal distribution is guaranteed. Figure 2.15, left, shows the invariant mass of μ_{d} and the photon. As expected, sharp peaks at the respective signal mass result. Their absolute widths were discussed in section 2.4, and can be read off from the dashed blue line of figure 2.5. There, Γ_{tot} is below 1 MeV for $\mathrm{M}_{\mu^*} = 250\,\mathrm{GeV}$ and $\mathcal{O}(1\,\mathrm{GeV})$ at $\mathrm{M}_{\mu^*} = 2.5\,\mathrm{TeV}$.

However, in the previous section it has been discussed that it is not possible to distinguish the origin (associated/decay) of the two final state muons from their kinematic properties.

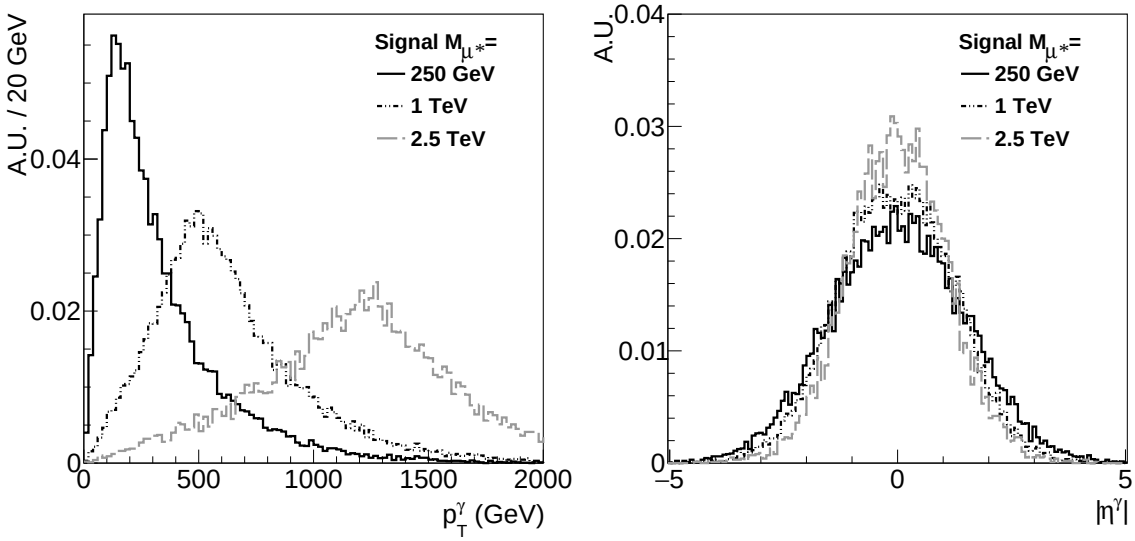

Figure 2.13: Left: Transverse momentum distributions from the photons originating from the μ^*-decay. Right: The corresponding η-distributions. Both are obtained from signal simulation on generator level.

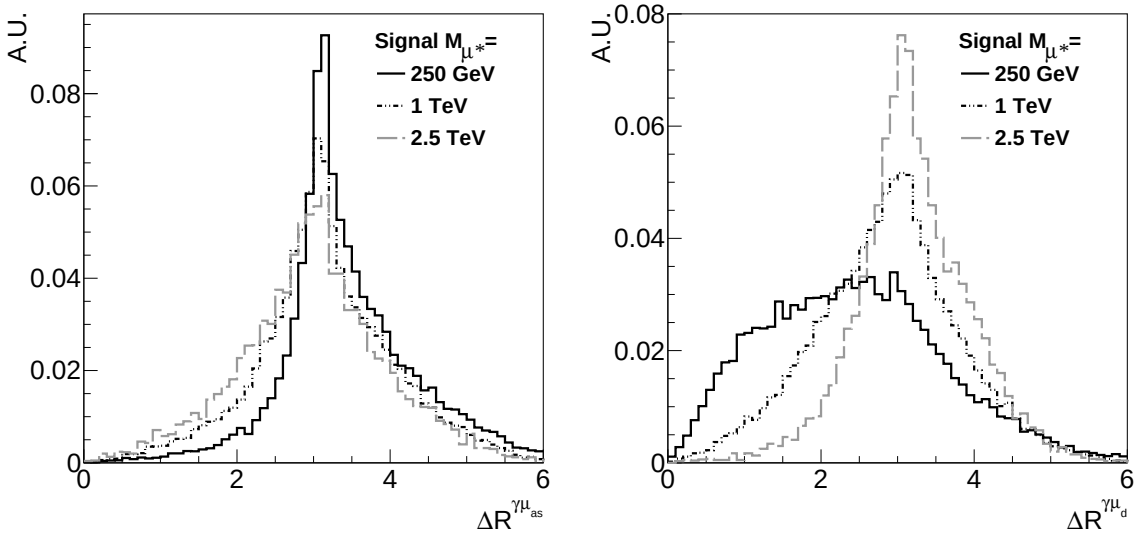

Figure 2.14: Angles ΔR between the photon and μ_d (left) and between the photon and μ_as (right), as obtained from signal simulation on generator level.

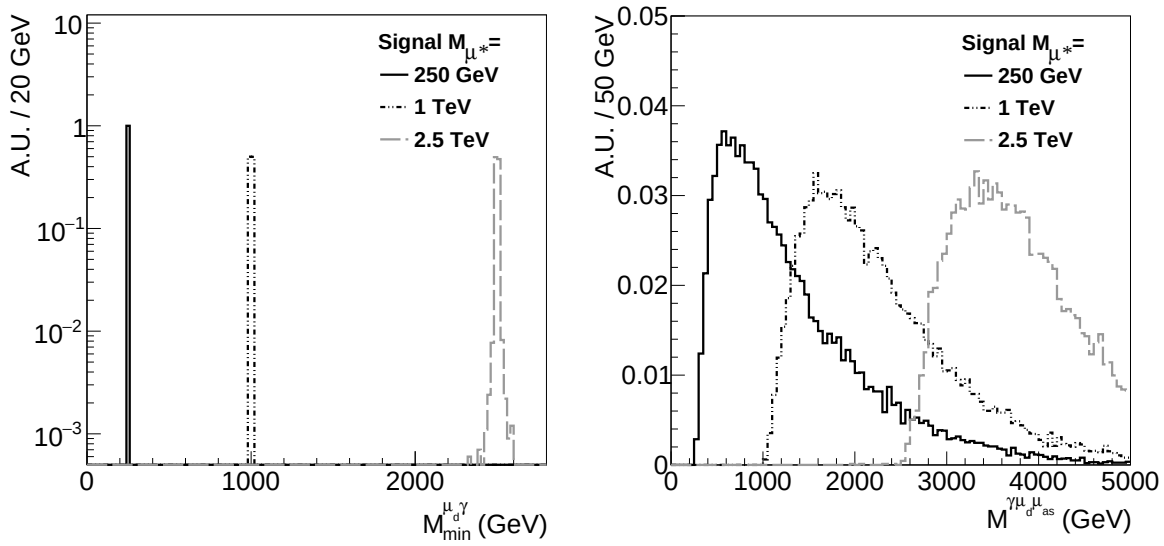

Figure 2.15: Invariant masses of the photon and μ_d (left) and three-body invariant masses (right), as obtained from signal simulation on generator level.

Given that, there is no straightforward solution about which of the two muons has to be used to combine it with the photon in order to calculate the excited muon invariant mass. As can be seen in figure 2.15, right, it is not practicable to rely on the three-body invariant mass, $M^{\mu\mu\gamma}$. It results in a broad distribution, being spread over a width of several TeV, even for low M_{μ^*}.

These three-body invariant mass distributions explain the difference between parton luminosity ratio and the ratio of signal cross sections that was mentioned in the previous section. The mass that has to be used in figure 2.9 is considerably higher than the respective signal mass of interest. As an example, the three-body invariant mass of $\mathrm{M}_{\mu^*} = 2.5\,\mathrm{TeV}$ lies rather at $M^{\mu\mu\gamma} \approx 3.5\,\mathrm{TeV}$, resulting in an expected ratio of approximately 40 (figure 2.9), which is much better comparable to the cross section ratio at $\mathrm{M}_{\mu^*} = 2.5\,\mathrm{TeV}$ (figure 2.7, right).

As the three-body invariant mass is not practicable to be used in analyses, there exist two possible muon-photon combinations to calculate a two-body mass $M^{\mu\gamma}$. The distributions of both are shown in figure 2.16. They are distinguished by their respective mass. The combination with the lower mass is called *minimum invariant mass*, $\mathrm{M}^{\mu\gamma}_{\mathrm{min}}$, and is shown in the left figure. Similarly, the combination of higher mass can be seen in the right figure and is called *maximum invariant mass*, $\mathrm{M}^{\mu\gamma}_{\mathrm{max}}$.

In both cases, a characteristic spike can be found at the respective signal mass. Additionally, a large and rather flat, one-sided tail completes the mass distributions. In case of $\mathrm{M}^{\mu\gamma}_{\mathrm{min}}$ ($\mathrm{M}^{\mu\gamma}_{\mathrm{max}}$), this tail extends to lower (higher) masses. The fraction of signal contribution to the peak can vary significantly depending on the considered signal mass on the one hand, or between $\mathrm{M}^{\mu\gamma}_{\mathrm{min}}$ and $\mathrm{M}^{\mu\gamma}_{\mathrm{max}}$ on the other hand. In an extreme case, where $\mathrm{M}_{\mu^*} = 250\,\mathrm{GeV}$, it ranges from some few percent in $\mathrm{M}^{\mu\gamma}_{\mathrm{max}}$ to almost 100% in $\mathrm{M}^{\mu\gamma}_{\mathrm{min}}$. This behavior makes it difficult to define a strategy that is convenient for all signal masses.

An interesting feature is clarified if both masses, $\mathrm{M}^{\mu\gamma}_{\mathrm{min}}$ and $\mathrm{M}^{\mu\gamma}_{\mathrm{max}}$, are plotted in a two dimensional plane, as shown in figure 2.17. In this case, the signal concentrates at the respective mass in the form of an inverted L. These *L-shapes* would reveal a typical signature, allow to distinguish between signal and background, and will thus play a central role in order

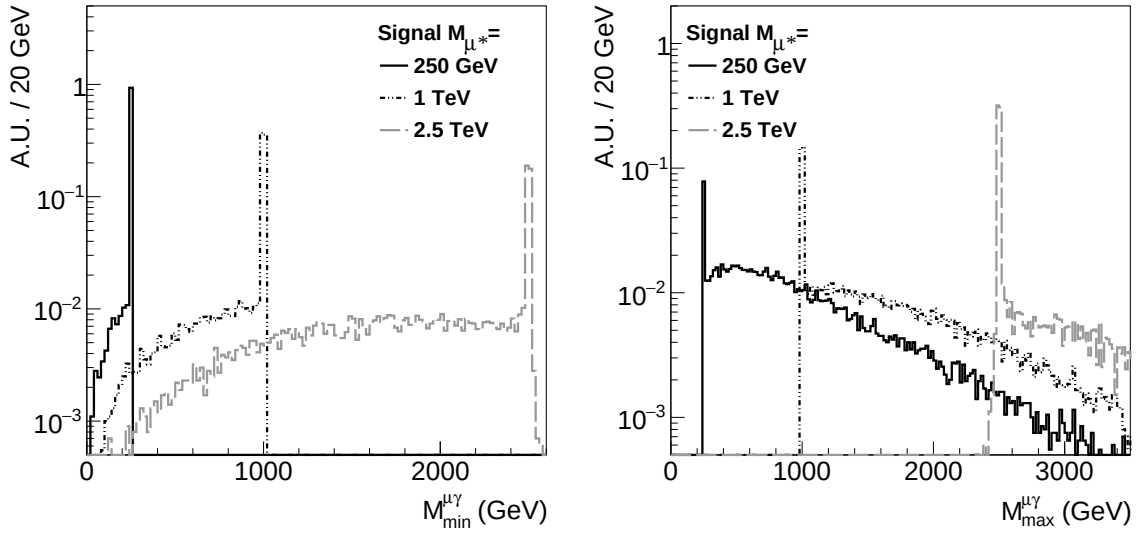

Figure 2.16: Minimum (left) and maximum (right) invariant muon-photon masses, denoted as $M^{\mu\gamma}_{min}$ & $M^{\mu\gamma}_{max}$, as obtained from signal simulation on generator level.

obtaining the final results of the analyses.

2.7 Existing Limits

Searches for excited fermions have a decade-lasting history and have been performed by many hep-experiments. So far, no significant sign for a signal has been observed. That is why repeatedly, exclusion limits were published. With increasing available collision energy, it became possible to constrain the available parameter space more and more. In this section, a brief outline of several different approaches of the past searches and their obtained limits on fermion substructure is given, ordered by the available center-of-mass energy. For detailed information, the interested reader is referred to the given references. Many more results are available but cannot all be discussed here.

When comparing results from different experiments, it has to be distinguished which production- and decay mechanisms were considered. At ep- or e^+e^--colliders, most results do not incorporate effects from CI. In this case (and also for q^* production at hadron colliders), the production cross section depends on

$$\sigma \sim \frac{f_s^2}{\Lambda^2}, \tag{2.20}$$

as expressed for q^* in [21]. At the same time, when assuming that $f = f'$, all dependencies on f and Λ cancel out when calculating the branching fractions. That means, the total product of cross section and branching fraction ($\sigma \times \mathcal{B}$) also depends on f^2/Λ^2, exclusively, and limits on that ratio, depending on the considered signal mass can be quoted. However, if CI contributions are taken into account, which are considered as the dominant excited lepton production mechanism at hadron colliders, the relations described above do not hold (compare dependencies on f and Λ in equations 2.13 to 2.17). In this case, limits on $\sigma \times \mathcal{B}$ are determined that are then recalculated into an exclusion of Λ, depending on M_{ℓ^*}, for a certain choice of f and f'.

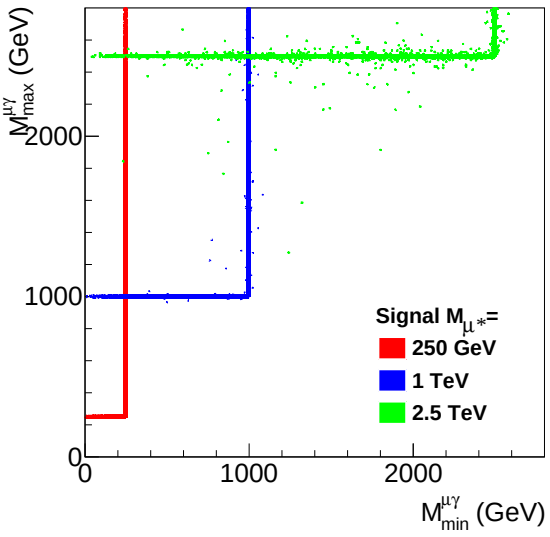

Figure 2.17: Two-dimensional $M^{\mu\gamma}_{min}$-$M^{\mu\gamma}_{max}$-distribution, as obtained from signal simulation on generator level.

At PETRA (=**P**ositron-**E**lektron-**T**andem-**R**ing-**A**nlage), located at DESY, Germany, e^+e^- collisions were performed at $\sqrt{s} = 36.7\,\text{GeV}$. The Mark J collaboration published the results of a search for excited electrons and excited muons [34]. There, a search for excited muon pair production was performed by interpreting the $ee \to \mu\mu$ cross section measurement. A mass of $M_{\mu^*} < 10\,\text{GeV}$ could be excluded. For higher masses, an excluded cross section on $ee \to \mu^*\mu$ as a function of $M_{\mu^*}$is given up to masses of approximately 30 GeV. The corresponding e^*-search concentrates on $\gamma\gamma$-final states, where a virtual e^* is exchanged in the t-channel. By measuring the differential cross section in $\cos\theta$, an excited electron can be excluded up to 58 GeV for a coupling $\lambda' = 1$. The latter is a coupling to the field strength tensor $F^{\mu\nu}$.

LEP (=**L**arge **E**lectron **P**ositron Collider) at CERN was operated in e^+e--mode at up to $\sqrt{s} = 209\,\text{GeV}$. It had four experiments that performed searches for excited fermions (in alphabetical order):

- The ALEPH collaboration published a search for excited electrons, muons, taus and electron neutrinos using data with a center of mass energy of 130-140 GeV [35]. From pair-production ($\ell\ell\gamma\gamma$ final states) excited leptons could be excluded up to masses of approximately 65 GeV. For single ℓ^*-production, limits on $\lambda/M_{\ell^*} = f/\sqrt{2}\Lambda$ are set. They reach $0.0007\,\text{GeV}^{-1}$ ($0.04\,\text{GeV}^{-1}$), assuming an excited electron (muon, tau) mass of 130 GeV.

- DELPHI did a search for all excited lepton types, including neutrinos [36] and various decay channels with photons, W-, and Z-bosons. Limits on the cross section, f/Λ, and different cases for f and f' were set as a function of mass and cannot all be described here. In most cases, the e^*-limits tend to exceed the others significantly due to the accessible production mechanisms.

- The analysis of L3 is very similar to the previous one with respect to considered excited leptons, final states, and results [37]. An example for the limit on $|f|/\Lambda$ as a function on M_{ℓ^*}, for the case $f = f'$, and for the three excited charged leptons is shown in

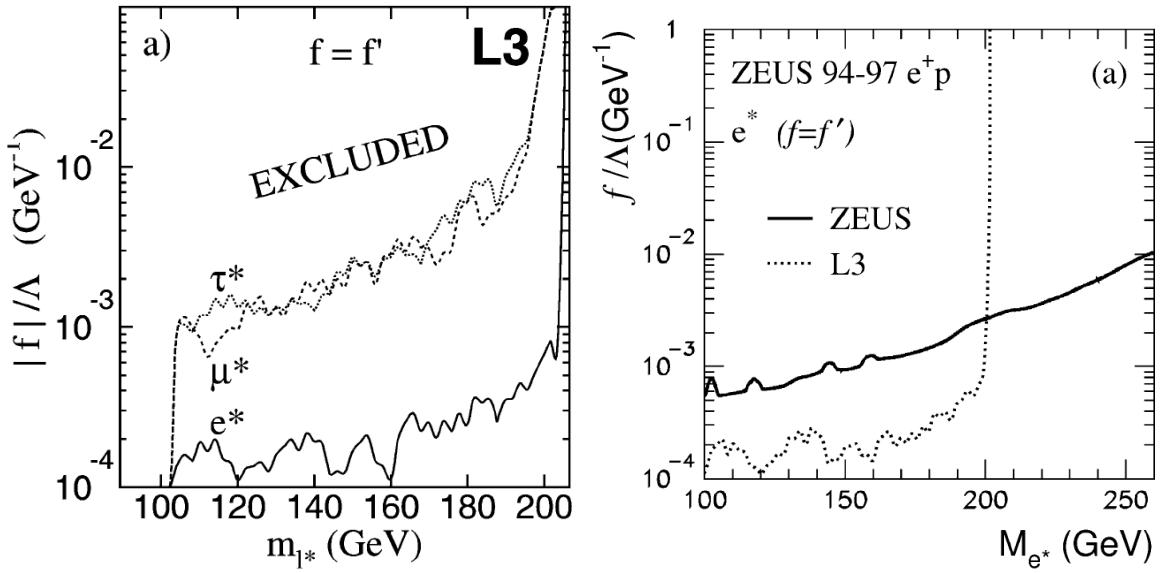

Figure 2.18: Left: Limits on excited charged leptons for the case $f = f'$, as obtained by L3 [37]. Right: Limit on e* as obtained by ZEUS with a comparison to the L3-limit of the left figure [39].

figure 2.18, left. It shows the much better sensitivity for excited electron production, manifested in limits that are about one order of magnitude more stringent than those of the other excited leptons.

- Searches by OPAL were again similar from point of the considered channels and obtained results [38].

Also located at DESY, the HERA accelerator (=**H**adron-**E**lektron-**R**ing-**A**nlage) collided electrons and protons at up to $\sqrt{s} = 318\,\text{GeV}$. There are recent publications from the two collaborations:

- ZEUS published a comprehensive search for excited fermions, including excited electrons, neutrinos, and quarks [39]. Thereby, various mechanisms were taken into account, including the radiation of photons, Z-, and W-bosons, resulting in a large variety of final states. Excited fermions in a range of $100 - 228\,\text{GeV}$ could be excluded, depending on $f/\Lambda = 1/M_{f*}$ for $f = f'$. The corresponding e^*-plot can be seen in figure 2.18, right in comparison with the limit obtained by L3.

- H1 did a similar search focusing on excited electrons [40]. The results are presented in the same way, extending over a mass range of $100 - 272\,\text{GeV}$. Here, also the production and decay via CI was taken into account but found to be small compared to gauge mediated processes.

The TEVATRON is located at Fermilab, USA. Being operated in $p\bar{p}$-mode, it reached center-of-mass energies of $\sqrt{s} = 1.96\,\text{TeV}$. The two main experiments performed searches for excited leptons, here showing those for μ^*:

- The results of CDF consider μ^*-production by gauge mediation and CI [41]. For the decay, the search is restricted to the photon radiation, and by that to $\mu\mu\gamma$-final states.

Here, it becomes obvious how the production via gauge interaction is heavily suppressed at hadron colliders: Masses below 221 GeV (853 GeV) could be excluded for the assumed gauge (CI) production and assuming $\Lambda = M_{\mu^*}$. The latter reduces to 696 GeV, if the branching fractions also take into account the decays via CI.

- The $q\bar{q} \to \mu\mu^* \to \mu\mu\gamma$-search performed by DØ is restricted to CI-production [42]. For $\Lambda = 1\,\text{TeV}$ a mass of up to 618 GeV could be excluded. A limit on Λ is also given, reaching approximately 4 TeV at $M_{\mu^*} = 260\,\text{GeV}$.

From the experiments at CERN's LHC, CMS and ATLAS both have provided results from searches for excited electrons and muons:

- Based on $5\,\text{fb}^{-1}$ of 7 TeV data, CMS searched for decays via photon radiation [43]. For the muon channel, the excluded values of Λ, depending on M_{μ^*}, are shown in figure 2.19(a). Excited lepton masses up to 1.9 TeV could be excluded for the case $M_{\ell^*} = \Lambda$. At low masses, the exclusion of Λ reaches 11-12 TeV. This analysis is the predecessor of the analyses presented here, following a very similar approach.

- A comparable analysis by the ATLAS collaboration, also searching in $\ell\ell\gamma$ final states uses $13\,\text{fb}^{-1}$ of 8 TeV data [44]. The resulting exclusion of cross section time branching ratio for the muon channel can be seen in figure 2.19, lower left. In the same figure, lower right, the corresponding limit on Λ, depending on $M_{\mu^*}$is given. Masses below 2.2 TeV for $M_{\ell^*} = \Lambda$ could be excluded, as well as $\Lambda < 11.5\,\text{TeV}$ at low masses. The CMS limit that was discussed before is also outlined in the same figure. An interesting detail can be seen when comparing both. Despite the higher center of mass energy (and thus signal cross section) and integrated luminosity, the ATLAS result barely exceeds the one from CMS at low masses and is even lower at the lowest mass edge. This is because of a different search strategy. The ATLAS analysis is based on a search in the three-body invariant mass (compare figure 2.15, right), while CMS makes use of the L-shape behavior (figure 2.17), thus being able to discriminate between signal and background more efficiently.

- Another interesting result from the ATLAS collaboration concentrates on μ^*-decays via CI to a $\mu\mu qq$ final state with $20.3\,\text{fb}^{-1}$ of 8 TeV data [45]. From the branching ratios, given in figure 2.4, one would expect that this leads to a gain in sensitivity, especially in the region of $M_{\ell^*} = \Lambda$. This is confirmed by the result, shown in figure 2.20. The exclusion range of Λ at high M_{μ^*}clearly exceeds the $\mu\mu\gamma$ result, excluding excited muons up to masses of 2.8 TeV for the case that $M_{\ell^*} = \Lambda$.

- Despite many searches without any sign of fermion substructure, there are interesting recent results that give hope that this field of new physics is not a dead end. The CMS search for excited quarks, looking at $\sqrt{s} = 13\,\text{TeV}$ data from 2015 [46] found a considerably large excess at an invariant mass of about 2 TeV. The bump that is visible in the $M^{\gamma j}$-spectrum in figure 2.21 reaches a local significance of up to 3.7σ. However, a q^* hypothesis so far could not be verified by the respective ATLAS analysis [47] and is in tension with the corresponding $\sqrt{s} = 8\,\text{TeV}$ results from CMS [48]. If this structure has any physical origin, or is just a statistical fluctuation or other systematic relict, has to be shown by looking at more data and is subject of ongoing analyses.

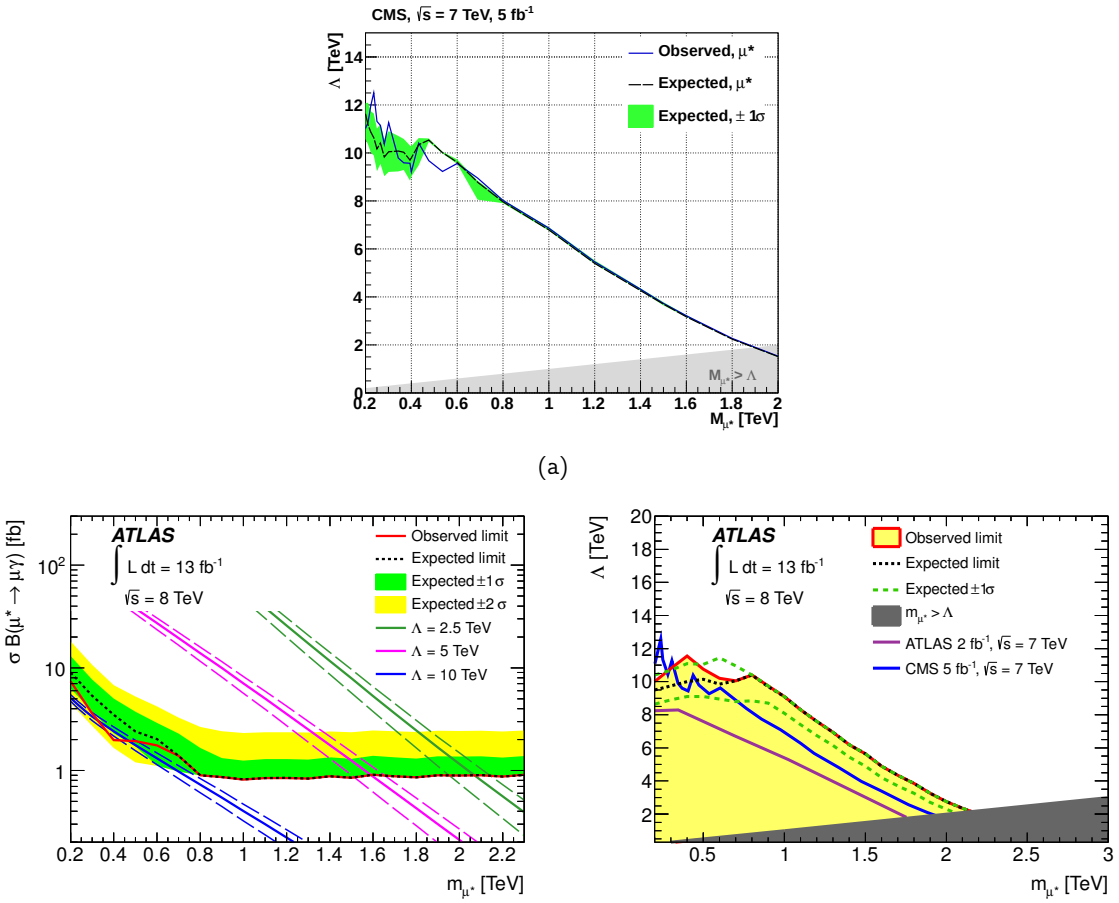

Figure 2.19: Limits on $q\bar{q} \to \mu\mu^* \to \mu\mu\gamma$: Upper figure: Excluded $\Lambda - M_{\mu^*}$ values of the 7 TeV CMS analysis [43]. Lower plots: Cross section (left) and Λ (right) limit of the 8 TeV ATLAS μ^*analysis [44].

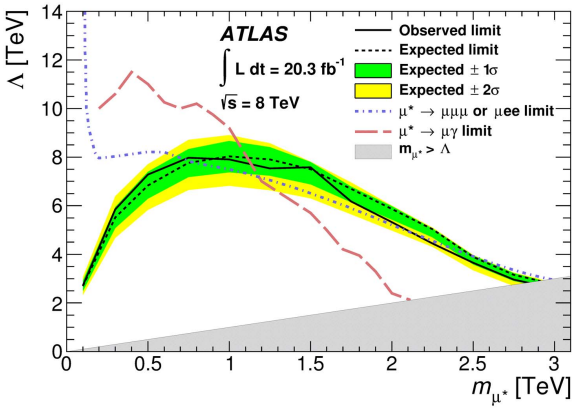

Figure 2.20: Limit of ATLAS' search for excited muons decaying via CI to $\mu\mu qq$ final states [45].

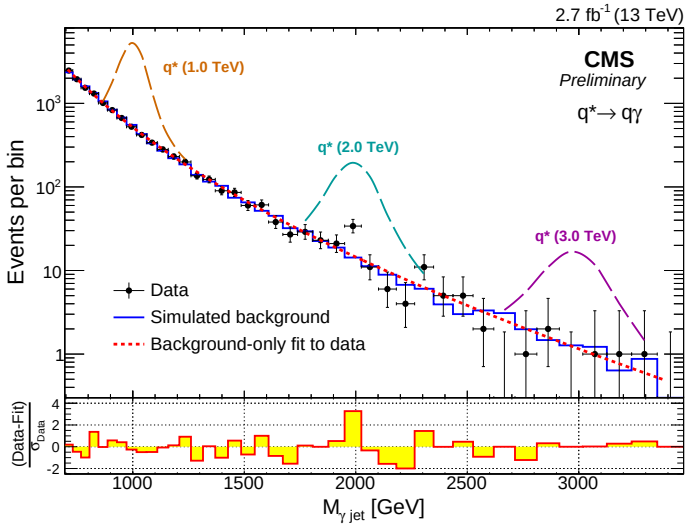

Figure 2.21: Spectrum of the γ-jet invariant mass from the search for excited quarks at $\sqrt{s} = 13\,\text{TeV}$, as published by the CMS Collaboration in [46].

3 | Experiment and Data Taking

The data that is analyzed in this thesis was collected by the *Compact Muon Solenoid* detector that is located at Point 5 of CERN's Large Hadron Collider at the Swiss-French border near Geneva. Both, LHC and CMS will be introduced in this chapter. A summary of the data taking procedure in CMS is given that leads to a detailed description about the datasets that are used in the presented analyses. As the design and operation of the experiment is not in the focus of the thesis, this chapter only provides a summary about these topics, taken from available documentation. More detailed information can be found in the given references.

3.1 The Large Hadron Collider

The Large Hadron Collider (LHC) [49] is a circular particle collider that is used to store, accelerate, and collide beams of protons or heavy ions like lead nuclei. It was designed to reach beam energies of 7 TeV and thus a center of mass energy of 14 TeV. However, after an incident that happened shortly after the start in 2008, data taking started with a reduced center of mass energy of 7 TeV in 2010 that was increased to 8 TeV in 2012. The latter data taking period is usually referred to as Run I. This name will also be used in this thesis to reference this data. Finally, in 2015, Run II started with the highest center of mass energy that was reached so far, 13 TeV.

LHC is a storage ring with a circumference of approximately 27 km located in a tunnel up to 100 m underground. It consists of 1232 dipole magnets that bend the two opposing beams with a magnetic field of 8 T. Quadru-, sextu-, and octupole magnets control and focus the beams. Acceleration is reached by radio-frequency (RF) cavities.

Each dipole is a tube of 15 m length. Innermost, the two beam pipes are enclosed by the superconducting magnets that are cooled with liquid helium to 1.9 K. Cryogenic equipment and heat shielding are installed surrounding the magnets.

The cavities consist of a superconducting niob titanium alloy. They accelerate bunches of particles with a high-frequency electro-magnetic field.

Before being stored and accelerated in the LHC the particles go through various pre-accelerators (see figure 3.1). With each step they gain energy before they are injected into the following machine. In case of the proton operating mode, electrons are stripped from hydrogen atoms to gain protons. These are then accelerated by a linear accelerator, the LINAC 2, to an energy of 50 MeV before being injected into the so-called Proton Synchrotron Booster (PSB, 1.4 GeV). The following steps are the Proton Synchrotron (PS, 25 GeV) and the Super Proton Synchrotron (SPS, 450 GeV). It is not before then that the beam of protons is divided into two separate beams that are finally injected in opposing directions into the LHC [50].

The two beams collide at four interaction points, where the major experiments are located. These are ATLAS [51], CMS [52], ALICE [53], and LHCb [54]. While ATLAS and CMS are multipurpose detectors, designed to measure at high luminosities, the latter two have more specialized layouts. ALICE is optimized for heavy-ion collisions to study e.g. the quark-gluon plasma. LHCb has a one-sided layout in the forward direction, optimized for

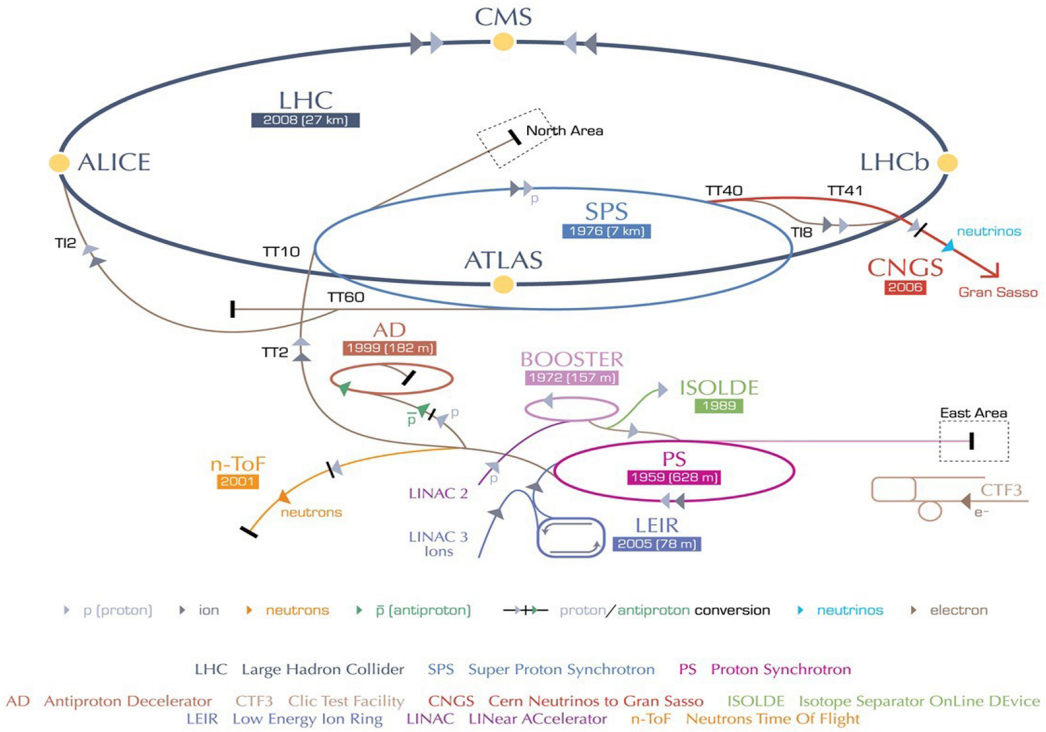

Figure 3.1: The CERN accelerator chain with the LHC and various pre-accelerators. The figure was adapted from [58].

b-physics. Other smaller LHC experiments are TOTEM [55, 56] and LHCf [57], which are both located near the beam pipe, close to one of the other experiments in order to benefit from their collision products that are boosted into the forward direction. TOTEM is located close to CMS and measures the beam luminosity and proton properties like its size. LHCf, in the neighborhood of ATLAS, uses hadronic collisions in order to investigate cosmic showers under laboratory conditions.

3.2 The Compact Muon Solenoid

The Compact Muon Solenoid (CMS) is a multi-purpose particle detector used to identify and measure various types of particles. It consists of several subsystems with different properties. The most important of them will be introduced in this section. The layout of CMS follows an onion-like structure, meaning that the different subcomponents consecutively enclose each other in almost a complete solid angle in order to ensure a good spatial coverage around the collision point.

The structure of the complete detector is divided into two major parts. The central part has the shape of a barrel that is aligned with the beam pipe while the endcaps enclose the apparatus perpendicular to the beams. This geometric principle is applied to all of the major subcomponents, as can be seen in the outline of CMS in figure 3.2.

The nominal collision point (beam spot) defines the origin of a right handed Cartesian coordinate system where the y-axis is oriented upwards, the x-axis points to the center of the LHC ring and thus the z-axis is parallel to the beam. The azimuthal angle ϕ, defined in the x-y-plane, is measured starting from the x-axis. The polar angle, θ, is defined from

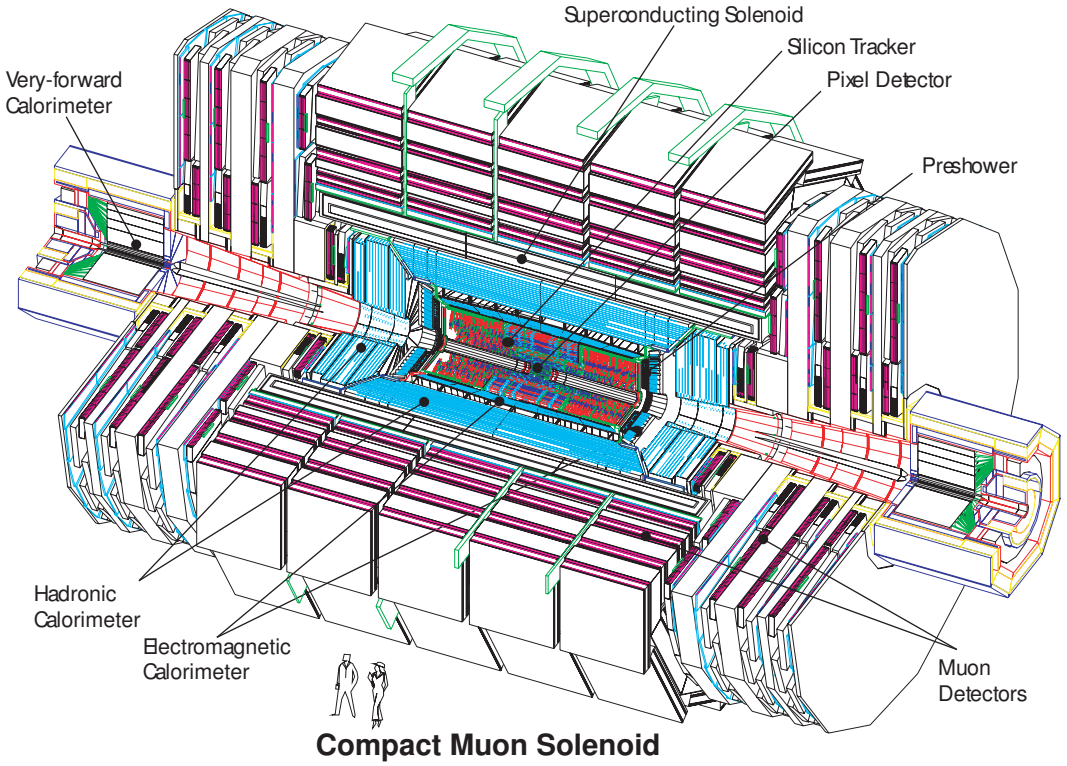

Figure 3.2: Scheme of the CMS detector [59].

the z-axis [52]. Alternatively, the pseudorapidity is widely used to describe the polar angle, defined as

$$\eta = -\ln \tan\left(\frac{\theta}{2}\right) \tag{3.1}$$

With these definitions, a Lorentz invariant spatial angle

$$\Delta R = \sqrt{(\Delta\phi)^2 + (\Delta\eta)^2} \tag{3.2}$$

can be defined.

In the following sections the most important sub-detectors will be introduced starting from the innermost tracker, proceeding to the outer muon system. The summarized information is mostly collected from the respective Technical Design Reports (TDRs) that are referenced in the corresponding sections. The interested reader is referred there for more detailed information.

3.2.1 Tracker

The innermost detector is the tracking system [60]. Its purpose is to measure the tracks of charged particles with great precision. This is needed to measure the momentum of particles on the one hand and to determine the origin of the measured tracks to reconstruct primary vertices and those from subsequent decays (e.g. b-mesons) or additional p-p-collisions (pileup) on the other hand. To achieve the latter the tracker is located as close to the beam spot as possible, radially reaching as close as 4 cm to the nominal point of interaction.

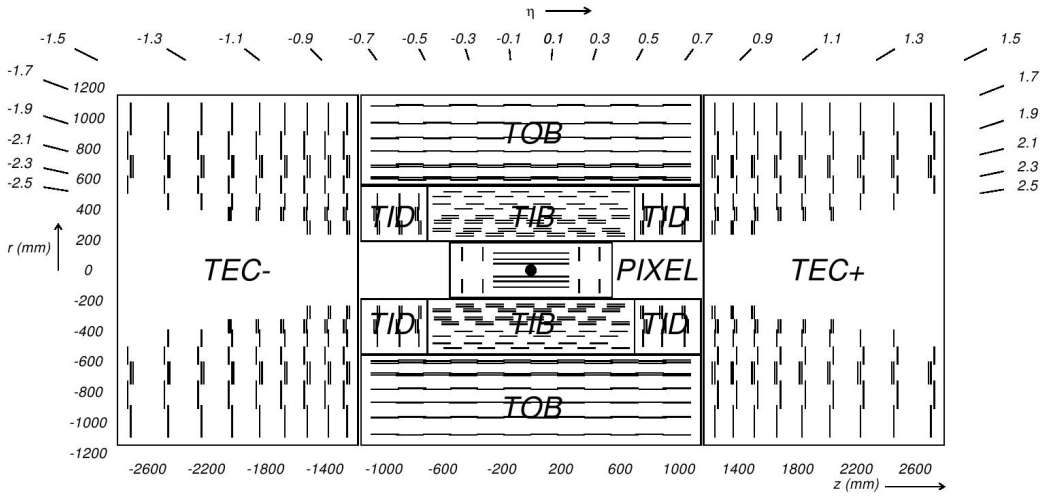

Figure 3.3: The CMS tracking system [52].

The tracker consists of several layers of silicon detectors that measure the location of a traversing charged particle very precisely. Silicon detectors provide a fast response and are thus able to measure with high rates while at the same time being robust enough against radiation damage to have a sufficient lifetime. Both is necessary when operating close to the interaction point. Also, the energy loss of the measured particles is kept at a minimum.

By combining the information from several subsequent layers it is possible to reconstruct the track itself. A scheme of the CMS tracker can be seen in figure 3.3. The tracker is divided into two different parts that have a different approach how to resolve the location of a traversing charged particle. They are the inner pixel detector and the (inner and outer) strip tracker that will be introduced in the following. Overall, the tracker reaches a total relative momentum resolution of $\sigma_{p_T}/p_T \leq 2\%$ and is able to resolve transverse impact parameters with a precision of 10 μm [52].

Pixel Tracker

The pixel tracker uses 66 million rectangular pixels to locate traversing particles. Each of the pixels has a size of $100 \times 150\,\mu\text{m}^2$. It consists of three layers in the barrel part and only two in the disk (endcap) part.

Strip Tracker

Unlike the rectangular pixels of the pixel tracker the detecting parts of the strip tracker have a longitudinal one-dimensional shape, called strips. With a second layer of strips that is mounted in a stereo angle of 100 mrad it is possible to achieve a point-like resolution. Modules with this second layer are marked by a second line in figure 3.3. In total there are 9.3 million strips that extend to a radius of 114 cm. The strip tracker itself is divided into two parts, the Tracker Inner Barrel/Disk (TIB/TID) and the Tracker Outer Barrel/Endcap (TOB/TEC) with detector modules (sensors) having a pitch of 80 μm to 184 μm. Thus, a resolution of 23 μm to 530 μm is achieved.

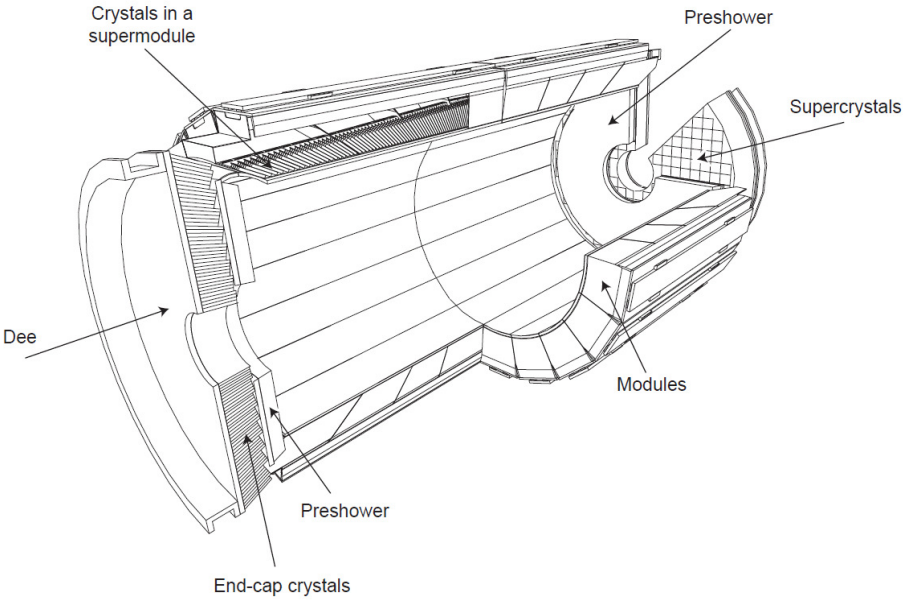

Figure 3.4: The CMS electromagnetic calorimeter [52].

3.2.2 Electromagnetic Calorimeter

The sub-detector enclosing the tracker is the *Electromagnetic Calorimeter* (ECAL) [61]. Its purpose is to stop electromagnetically interacting light particles like electrons and photons, to measure their energy deposit, and to contribute to the energy measurement of hadrons and jets. This is achieved by measuring the amount of scintillation light that is produced in crystals made from lead tungstate ($PbWO_4$) with photo-detectors. These crystals are designed with a length of 22-23 cm, depending on their position, corresponding to 25 electromagnetic radiation lengths and the front side of 22×22 mm, corresponding to one Moliere radius. The width of the rear ends is increased. In that way it is achieved that all crystals are pointing in the direction of the nominal beam spot with an offset of 3° in ϕ and η. Thus, a good spatial resolution can be reached, while at the same time it is avoided that a photon enters the space between two crystals and is hence not detected. Overall, the ECAL fills a volume of 11 m^3 with 61200 (2×7324) crystals in the barrel (endcaps, "Dee" in figure 3.4), weighing over 80 t [52]. An overview can be found in figure 3.4

The energy resolution of the ECAL is

$$\frac{\sigma_E}{E} = \sqrt{a^2 \cdot \frac{\mathrm{GeV}}{E} + \sigma_n^2 \cdot \frac{\mathrm{GeV}^2}{E^2} + c^2} \tag{3.3}$$

with the stochastic term $a = 2.8\%$, the noise term $\sigma_n = 12\%$ and the constant $c = 0.3\%$. However, the numbers of these terms are design values that are expected to worsen with time due to the aging of the ECAL crystals, e.g. by radiation damage. In later references [62], the photon energy resolution is determined to range from 1% for unconverted barrel photons up to 4% for photons in the endcap. With this specification CMS is able to provide a precise energy measurement, especially of highly energetic, electro magnetically interacting light particles.

3.2.3 Hadronic Calorimeter

Energies of heavy particles like hadrons that cannot be stopped in the ECAL, mainly long-lived hadrons like pions and kaons, are measured in the *Hadronic Calorimeter* (HCAL) [63]. It consists of alternating layers of massive absorbers and scintillators. There are 16 layers of absorber made from brass each being some few cm thick, corresponding to less that six hadronic radiation lengths. The scintillating tiles are 3.7 mm thick and are made from plastic. They reach a granularity of $\Delta\eta \times \Delta\phi = 0.087 \times 0.087$ (0.17×0.17) in the barrel (endcap) region. Again, the amount of light is the measure for the deposited energy. It is collected by wavelength shifting fibers.

ECAL and HCAL reach a combined design energy resolution of

$$\frac{\sigma_E}{E} = \sqrt{(100\%)^2 \cdot \frac{\mathrm{GeV}}{E} + 4.5\%} \tag{3.4}$$

The hadronic calorimeter has two additional components that do not follow the basic principle of a combined barrel and an endcap region. They are the Hadron Forward and Hadron Outer Calorimeters.

Hadron Forward Calorimeter

The Hadron Forward Calorimeter (HF) [52] is located outside the main part of CMS and measures particles at high pseudorapidities $|\eta| > 2.7$. This is outside the range that is used for the particle reconstruction of most analyses. Still, it is important, especially for the reconstruction on missing (transverse) energy, and measurements of the luminosity. It consists from solid copper that contains quartz fibers that are oriented parallel to the beam axis and that collect Cherenkov light.

Hadron Outer Calorimeter

Being located outside the coil of the magnet, the hadron outer calorimeter (HO) [52] uses the magnet as absorber. Thus, it consists of two (one) layers of scintillating tiles of 10 mm thickness that are located in wheel 0 (±1, ±2) of the barrel region, exclusively, and is able to extend the HCAL barrel in the central barrel region, where its thickness reaches a minimum of hadronic interaction lengths[1].

3.2.4 Magnet

The magnet [64] is crucial for transverse momentum measurements of charged particles. A high magnetic field is needed to bend the path of high energetic particles. In CMS, a superconducting solenoid is used that is able to produce a magnetic field of up to 4 T parallel to the beam axis. During the data taking periods of Run I and Run II it was usually operated with a magnetic field of 3.8 T. An iron return yoke leads the magnetic flux outside the magnet coil.

[1] 5.4 λ at $|\eta| = 0$, following [52]

3.2.5 Muon System

The muon system [65] builds the outermost part of the whole detector. Muons, as minimal ionizing particles, are able to traverse the whole detector without being absorbed, and leave it long before they decay. Thus, a calorimetric measurement is not feasible and instead the muon system extends the track measurement of the tracker in order to measure the momentum from the track curvature. The muon system consists of different types of gaseous detectors that will be introduced in the following paragraphs. By combining with tracks from the tracking detectors, a transverse momentum resolution of $1.3 - 2.0\%$ can be reached for barrel muons with $20 < p_{\mathrm{T}} < 100\,\mathrm{GeV}$, and better than 10% for such in the endcap region with momenta up to 1 TeV [66]. A measurement of the momentum resolution in the barrel region, using cosmic muons is presented in the following chapter.

Drift Tubes

Drift Tube (DT) chambers are located in the barrel region between the thick layers of the iron return yoke for the magnetic field. They are gas-filled (85% argon and 15% carbon-dioxide) tubes of 2.4 m length. At their center, an anode wire is located while cathode strips are attached to the tubes walls. A muon passing through such a tube ionizes the gas and thus generates a signal on both, cathode and anode. Figure 3.5, left, shows the scheme of one drift tube. By combining many of those tubes to one layer it is possible to locate a traversing muon. Additional layers allow a more precise measurement. The combination of four layers of DTs is called superlayer. There are superlayers measuring the $r-\phi$ component, being oriented in the z-direction, and such that measure the angle η. Each chamber has up to three superlayers. Thereby, the innermost stations have two superlayers that measure the ϕ component and one for the θ-measurement. The fourth, outermost station has two superlayers measuring the ϕ component only.

Resistive Plate Chambers

Resistive Plate Chambers (RPCs) can be found in both, barrel and endcap. They are usually directly attached to DT-chambers and thus add up to a muon station (compare Fig. 3.5). They consist of readout strips that are located between plates with a high electric resistance, being made of phenolic resin. A gas filled gap is located between those plates and additional two outer layers. RPCs are operated in the avalanche mode and achieve a fast response. Thus, they can be used for high detection rates and trigger decisions.

Cathode Strip Chambers

Cathode Strip Chambers (CSCs) are mounted in the endcaps, exclusively. Their purpose is to measure at high rates and to perform well in the surrounding non-uniform magnetic field of this area. They consist of cathode strips that are mounted on seven panels of a trapezoidal shape of 10° or 20° and point in the radial direction towards the beam axis. Perpendicular to those, in gas filled gaps between the panels, layers of anode wires are mounted, thus allowing the measurement of all coordinates of a muon trajectory.

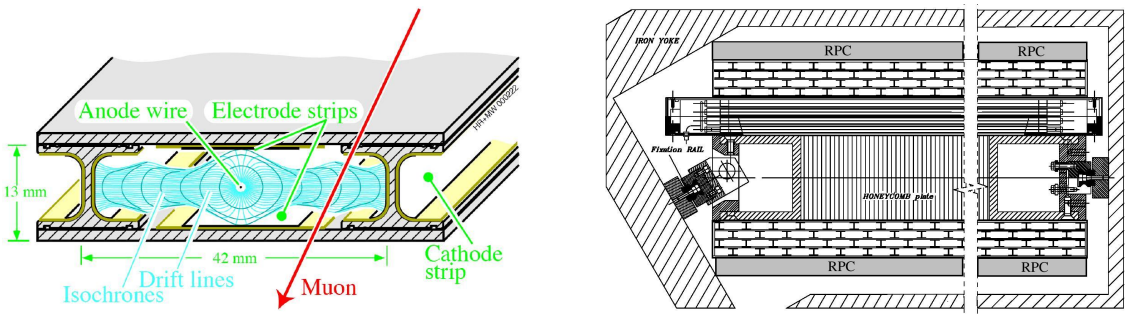

Figure 3.5: Schematic view of a drift tube (left) and a muon station (right) with its superlayers of DTs and RPCs [52]

Run I	HLT_Mu17_TkMu8	
Run II	HLT_Mu17_TrkIsoVVL_Mu8_TrkIsoVVL_DZ HLT_Mu17_TrkIsoVVL_TkMu8_TrkIsoVVL_DZ	OR

Table 3.1: Names of the HLT-requirements of the Run I and Run II analyses that are presented here.

3.2.6 Trigger and Data Acquisition

CMS was designed for collisions occurring every 25 ns. This corresponds to a bunch-crossing rate of 40 MHz. Such rates are much too high to be processed and the amount of data is too large to be stored. That is why CMS has a system to efficiently identify and select events with an important content to reduce the event rates. This so-called triggering system has two consecutive levels, the level-one (L1) trigger and the High-Level Trigger (HLT).

The L1 trigger is a hardware based system that is located on the front-end electronics inside the detector itself or inside the (neighboring service) cavern. The various detector components deliver a rough first information about the measured quantities that are passed to the so-called global triggers (global muon trigger, GMT, and global calorimeter trigger, GCT). Combining their information provides a first estimate if the event is of interest and if it passes L1 (compare figure 3.6). Thus, the rate is reduced to $30 - 100$ kHz. Details about the technical implementation can be found in [52].

The HLT is completely computer based. It has more information available than the L1 and is able to do a more precise event reconstruction. By that, more precise requirements are possible and the measured data can be sorted, reconstructed, and stored corresponding to the event content in so-called data streams. Thus, the rate of recorded events is reduced to some few 100 Hz.

Triggers used in the analyses that are presented in this thesis are listed in table 3.1. All of them have in common that two muons are required with p_{T}-thresholds of 17 GeV and 8 GeV. "TkMu" is a muon track that is reconstructed in the tracker, exclusively. "TrkIsoVVL" refers to a loose isolation requirement in the tracker[2] and "DZ" means that the muon tracks need to have a common origin from the beam spot in z-direction within $\Delta z < 0.2$ mm.

[2] VVL = very, very loose, means that the sum of the transverse momenta of tracks within a cone of $R = 0.3$ around the muon track must not exceed a threshold of 0.4 times the muon transverse momentum.

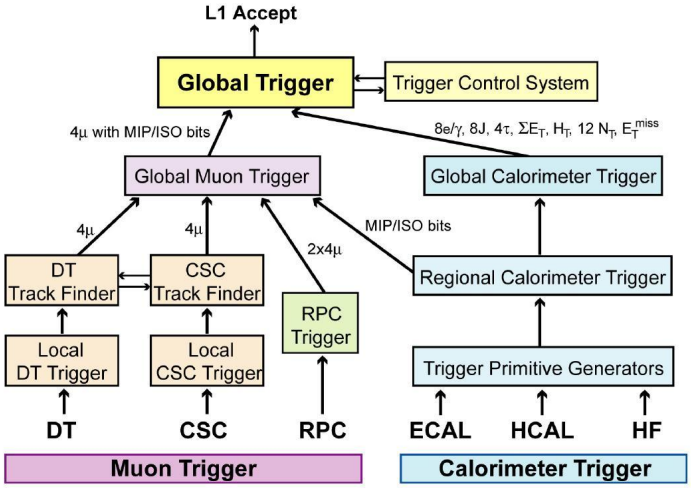

Figure 3.6: Scheme of the CMS L1 trigger (Run I setup) [52].

3.2.7 Data Storage and Distribution

Data is sent to CERN's central computing center for reconstruction and storage. From there it is made available for analysis purposes by the LHC Computing Grid (LCG) [67]. The LCG is a web of computing centers that are distributed over the whole world. It has a hierarchical structure by dividing the different members into so-called "Tiers".

The main site, the "Tier-0", is the mentioned central computing center at CERN. There, the data from the LHC experiments is collected, stored and processed. From there, it is distributed to several Tier-1 that are the main sites for different states or regions (e.g. Tier-1 at KIT, Karlsruhe, Germany). At these sites, large computing tasks on raw data or Monte-Carlo can be be performed.

Processed data is made available to the end-users on the following level, the Tier-2[3]. These local centers provide personal storage and computing resources for the analysts, but are also used for central MC generation and (re-)processing. At some sites, an additional Tier-3 layer is installed.

3.2.8 Luminosity Measurement

Knowledge about the amount of recorded data as exact as possible is mandatory for most analyses. This is why the measurement of the instantaneous luminosity is a crucial part of the experiment. The procedure used at CMS is described in [68] and is shortly outlined here. It is based on the so-called "pixel cluster counting"-method that is calibrated with Van der Meer scans [69].

The Pixel Cluster Counting method [68] is used to estimate the average instantaneous luminosity:

$$L = \frac{\nu \langle n \rangle}{\sigma_{\text{vis}}}, \tag{3.5}$$

with the beam revolution frequency $\nu = 11246$ Hz and the average number of pixel clusters per event, $\langle n \rangle$, happening in zero-bias events that are triggered by two bunches crossing the

[3] In Germany, Tier-2 sites for CMS are located at RWTH Aachen, DESY Hamburg, and KIT in Karlsruhe

interaction point inside CMS. The visible cross section, σ_{vis}, is tuned by so-called Van-der-Meer scans [69]. For these scans, the rate is measured as a function of the beam separation in dedicated LHC runs. Thus, by scanning the beams in the horizontal and vertical plane, the beam profiles can be measured in terms of a rate profile. The visible cross section is then given by

$$\sigma_{\text{vis}} = \frac{2\pi\Sigma_x\Sigma_y \langle n \rangle_{\Delta=0}}{N_1 N_2}, \tag{3.6}$$

where Σ_i is the width of the beams in the $i = x, y$-direction, assuming a Gaussian shape, and $N_1 N_2$ is the product of the proton population in the bunches of the two beams, which is measured by the LHC beam current transformators [70, 71].

With the described technique and additional offline corrections to σ_{vis} that are not discussed here (see e.g. [68]), the total integrated luminosity can be determined with good precision. The systematic uncertainty on the luminosity measurement was determined to be 2.5% in Run I [68] and 2.7% in Run II [72].

3.2.9 Data Taking during Run I and Run II

The Run I data taking happened in the year 2012 at a center of mass energy of $\sqrt{s} = 8\,\text{TeV}$ and a 50 ns bunch spacing. For Run II, only such data is used here that was taken in 2015, at $\sqrt{s} = 13\,\text{TeV}$, with a 25 ns bunch spacing, and the full 3.8 T magnetic field of the CMS magnet[4].

All measured data is monitored and certified by the CMS "data quality monitoring" (DQM) group. There, it is surveyed that all data were taken at proper conditions, e.g. that sub-detectors were working[5].

Table 3.2 summarizes the datasets that are used for the analyses presented in this thesis. It shows the sets of both runs taken from the DoubleMuon-stream, with the most up-to-date reconstruction and their integrated luminosity corresponding to the certification described in the paragraph before. Available data is divided into several periods that distinguish by the respective data taking and run conditions.

3.2.10 Software

The complete offline computing chain, including reconstruction, processing, Monte Carlo generation and provision of data to the users is done within the framework of the CMS Software *CMSSW*, being publicly available at [75]. The presented analyses were performed in context of the versions CMSSW_5_3_X and CMSSW_7_6_X for Run I and Run II, respectively. The analyses themselves are written in C++ and plots are created with the help of ROOT [76]. JaxoDraw [77] is used to produce Feynman diagrams.

[4] In the 2015 data taking period, parts of the data was collected with the magnet being turned off. This data cannot be used here, as no proper muon reconstruction is possible.

[5] Certified data is summarized and provided in
Cert_190456-208686_8TeV_22Jan2013ReReco_Collisions12_JSON.txt and
Cert_13TeV_16Dec2015ReReco_Collisions15_25ns_JSON_Silver_v2.txt
for Run I [73] and Run II [74], respectively.

	Dataset Name	Run Range	$\mathcal{L}(\,\mathrm{fb}^{-1})$
Run I	/DoubleMu/Run2012A-22Jan2013-v1/	190456–193621	0.9
	/DoubleMuParked/Run2012B-22Jan2013-v1/	193833–196531	4.4
	/DoubleMuParked/Run2012C-22Jan2013-v1/	198022–203742	7.1
	/DoubleMuParked/Run2012D-22Jan2013-v1/	203777–208686	7.4
	Sum		19.7
Run II	/DoubleMuon/Run2015C_25ns-16Dec2015-v1/	254227–254914	0.1
	/DoubleMuon/Run2015D-16Dec2015-v1/	256630–260627	2.6
	Sum		2.7

Table 3.2: Datasets used in the analyses with their corresponding run ranges and integrated luminosities. In the Run I analysis so-called "parked" data was used, data that was stored for later reconstruction during the data taking. However, for "Run2012A", due to a misconfiguration in the trigger-setup, parked data cannot be used there.

4 | Object Reconstruction and Selection

To determine properties of individual particles, they have to be reconstructed from bits of information coming from the various detector components. By combining entries from the specific sub detectors, particles can be identified and properties such as direction or (transverse-) momentum are measured. On the analysis level, various selection criteria are applied for the selection of physics objects like particles (e.g. e, μ, τ, γ), jets and missing transverse energy (E_{T}^{miss}). Thus, only properly reconstructed objects are selected and contributions from mis-identified objects are reduced. Both, the reconstruction of objects and the selection criteria of the relevant objects, muons and photons, will be described in this chapter. The performance of the reconstruction of simulated and measured objects is measured by groups within CMS. Differences between simulation and measurement are corrected by applying scale-factors that are provided with corresponding uncertainties. Both, factors and uncertainties, are introduced and listed in Appendix B.

4.1 Particle Flow Algorithm

Many CMS analyses make use of the so-called Particle-Flow (PF)-algorithm [78, 79]. This method uses information from various detector components to identify and reconstruct individual particles, and by that successively build up the complete event. This significantly increases the reconstruction performance of multi-particle objects like jets, $E_{\mathrm{T}}^{miss}$and taus. Also, the reconstruction and identification of other particles benefits, for instance in the calculation of isolation criteria.

The algorithm relies on tracks from charged particles, clusters in the calorimeters, and muon tracks. First, muons are identified and the corresponding tracker track is removed from the collection of all tracks, as well as certain calorimeter deposits. Electron identification follows, again removing the corresponding tracks and calorimeter clusters. Remaining tracks are linked to matching clusters, and neutral hadrons and photons are identified by comparing clusters to the expected calorimeter resolution.

4.2 Muons

4.2.1 Muon Reconstruction

As described in [80], muons are identified as segments that are found by the local reconstruction in the muon system (compare section 3.2.5). Combining those segments to tracks with the help of a Kalman filter algorithm [81] leads to so-called **Standalone muons** that are reconstructed from the muon system, exclusively.

Global Muons

Combining Standalone muons with the best matching tracker track results in global muons. Their momentum is determined by refitting the resulting track, again making use of the Kalman filter technique. The interested reader is referred to [66, 82] for more details.

Tracker Muons

Tracker muons have a different approach. In a first step, all tracker tracks are considered a muon candidate. Then, those tracks are extrapolated to search for matches in the calorimeters and muon system. Again, a more detailed description can be found in [66,82]. This algorithm is especially suitable for low energetic muons as such muons potentially do not traverse the (complete) muon system. As a result, all tracks with $p > 0.5\,\text{GeV}$ and $p_\text{T} > 0.5\,\text{GeV}$ are considered a muon if they have a matched muon detector segment [80].

Other (High-p_T) Muon Reconstructions

For muons with momenta below $p_\text{T} < 200\,\text{GeV}$, the result of the tracker-only fit is used. For higher momenta, where the tracks become more and more straight, additional input from the outer muon system is needed for a reliable track fit. However, due to interactions with the iron of the magnet yoke (multiple scattering and bremsstrahlung), additional hits in the muon system can arise that distort the fit and thus the momentum assignment. To avoid that, other fit algorithms have been developed.

- **Tracker-Plus-First-Muon-Station (TPFMS)**: Only the innermost muon station hit is taken into account for the fit.
- **Picky Muon Reconstruction**: In case of multiple close by-hits in one muon station, such are removed from the fit that deviate too much from the extrapolated muon trajectory. This decision is made by comparing the χ^2-values.

In order not to depend on the (dis)advantages of one certain reconstruction method, the so-called ***TuneP*** algorithm was developed. It chooses the used fit from *tracker-only*, *TPFMS*, and *Picky*, depending on the goodness of the respective fit. The *TuneP* algorithm is used for the reconstruction of this analysis' muons.

For Run II, updates are implemented to avoid small inefficiencies in the muon reconstruction. Additional tracking iterations increase the tracking efficiency by about 2%, especially in conditions with high pileup (see [83, 84] and references therein).

4.2.2 Muon Selection

On analysis level, various additional criteria are applied to muons. Their purpose is to select only such muons for further studies that are properly reconstructed and are not mimicked by particles of a different type. The latter ones are usually referred to as misidentified muons or muon fakes. For example, a high energetic hadron that leaves the hadronic calorimeter can traverse the magnet and mimic a signal in the muon system – a so-called punch-through.

These selection criteria will be introduced and explained in this section. The cuts are similar in the Run I and Run II analyses. They were developed and optimized by groups within the CMS collaboration and are widely used in CMS analyses, e.g. in the searches for dilepton resonances [83,85]. The following list is adapted from the "HighPT Muon" sections of [86,87].

- *Global muon*: The muon is required to be reconstructed as a global muon.
- *Chamber hits* > 0: The global muon track fit needs to include a valid muon chamber hit[1]. This selection is applied against punch-through and secondary muons from decays.
- *Stations* ≥ 2: Segments from at least two muon stations need to contribute. This is analogous to the muon trigger logic.
- $\sigma_{p_\mathrm{T}}/p_\mathrm{T} < 0.3$: The relative p_T-error of the muon fit.
- $\mathrm{d}_{xy} < 0.2$ mm: Transverse impact parameter with respect to the primary vertex[2]. Rejects secondary muons coming from decays and cosmic muons. The value quoted here is smaller than that in the references. The reason for this tighter requirement is that the original value allows muons from b- or c-hadron decays. As this is not needed for analyses with prompt muons, the cut is tightened.
- $\mathrm{d}_z < 5$ mm: Similar to the cut before, using the z-coordinate only.
- *Pixel hits* ≥ 1: Number of hits in the innermost pixel detector. Suppresses non-prompt muons coming from decays in flight.
- *Tracker layers* ≥ 6: Hits in tracker layers. Effect is similar to the cut before. Also, a good track fit is guaranteed.

To further reduce contributions from jets that are reconstructed as muons and non-prompt muons from hadronic decays inside jets, an isolation requirement is applied in addition to the identification requirements of each muon. It is defined as the sum of the transverse momenta of all tracker tracks within a cone of $\Delta R < 0.3$ around the muon, excluding the muon itself, relative to the transverse momentum of the muon:

$$\mathrm{Iso}^{\mu} = \frac{\sum p_\mathrm{T}^{\mathrm{tk}}}{p_\mathrm{T}^{\mathrm{tk}(\mu)}} < 0.1 \tag{4.1}$$

As many of the quoted properties are difficult to model in simulation, Monte Carlo events are weighted in order to account for differences between simulation and measured data. Corresponding scale-factors and their systematic uncertainties are determined and provided by groups within the CMS collaboration [88, 89]. They are provided in bins of p_T and η and are close to unity in the range of a few percent. Plots of these scale-factors with their uncertainties can be found in Appendix B. The scale-factors are calculated using the tag-and-probe method that uses leptonic Z-decays. In general, for this method, one lepton has to fulfill all requirements applied in the analyses (the "tag"-lepton). From all respective other leptons (the "probe"-leptons), the fraction of leptons is calculated that fulfill the requirement under investigation. Thus they can only be determined for transverse muon momenta up to some few hundred GeV with a reasonable statistical accuracy. Muons with higher momentum are weighted corresponding to the highest available p_T-bin.

To illustrate the performance of the muon reconstruction over a wide p_T-range, figure 4.1 shows the p_T-distributions of the two highest energetic muons in both analyses after all ID criteria and scale-factors have been applied. To avoid missing simulation at low masses, a minimum dimuon invariant mass of $\mathrm{M}^{\mu\mu} > 60\,\mathrm{GeV}$ is also required. An excellent agreement

[1] At first glance, this requirement seems obsolete, as the global muon reconstruction already implies a muon hit. The difference is that here, a "valid" hit is selected, that has additional χ^2 requirements.

[2] The primary vertex is defined as the vertex, whose associated charged tracks result in the highest $\sum p_\mathrm{T}^2$.

over the complete range of all distributions can be seen. Only the spectrum of the second energetic muon of the Run I analysis has an excess of data over the background expectation at $p_T > 250$ GeV. The reason for this is the small number of simulated events in the used Drell-Yan background sample. As this background is later replaced by a data-derived background model, the excess is acceptable at this point.

4.2.3 Muon Momentum Resolution and Scale Uncertainties

The p_T-measurement of muons depends on detector properties like tracker alignment, material, and the magnetic field. These things are difficult to model in simulation. This is why their influence on the muon reconstruction is studied with data and compared with the performance of MC [66].

Two effects are investigated and included into the analyses as sources of systematic uncertainties. The muon momentum resolution, defined as $\delta p_T/p_T$, is assumed to have a Gaussian shape. Its effect on the analyses is estimated by applying an additional Gaussian smearing of 0.6% per muon in simulated events. A study of the muon momentum resolution using muons from cosmic rays is presented in the next section.

The muon momentum scale describes a possible bias "κ" in the muon curvature:

$$\frac{q}{p_T} \rightarrow \frac{q}{p_T} + \kappa \tag{4.2}$$

with the muon charge "q". It is estimated using the so-called "endpoint-method", using either data from J/Ψ or Z-boson decays, or cosmic muons. In the latter case, the studies are restricted to a rather narrow reach in $|\eta|$ due to the location of CMS deep underground. J/$\Psi-$ and Z-decays are not able to make a statement on muons with momenta much higher than those from the respective decays. The endpoint method is e.g. explained in [90]. Its idea is to inject a bias of various values and to observe the influence on the p_T-(or energy) spectrum of muons (or any other track). By comparing the normalized q/p_T-distributions of e.g. data with MC, or upper with lower track in case of cosmic muons, a χ^2-distribution as a function of the bias κ can be generated. An example from a study with cosmic muons is shown in figure 4.2. The bias found in such studies is usually well compatible with zero and shows a good agreement between data and simulation [90–92]. The muon POG (=Physics Objects Group) recommends to apply a shift of $\pm 5\%/$ TeV per muon to estimate the influence of systematic uncertainties in the muon momentum scale on an analysis [93]. This is done in the Run I and Run II analyses that are presented here.

4.2.4 Cosmic Muons: Study of the Muon Momentum Resolution

To get an understanding of the muon momentum resolution performance in measured data and compare it to the simulation, it is advantageous to measure it directly from data. Thereby, the basic principle is, to compare the momentum measurement from a certain muon track to that of some reference track. A good opportunity for such a measurement are cosmic muons that reach and traverse CMS which is located deep underground. Such a cosmic muon has a signature that is similar to two muons of opposite charge that are produced in a collision and that leave the interaction point in opposite direction with the same transverse momentum. Exemplary graphical representations of such "cosmic events" are shown in figure 4.3. Such a study, relying on cosmic muon data and -MC is presented in this section.

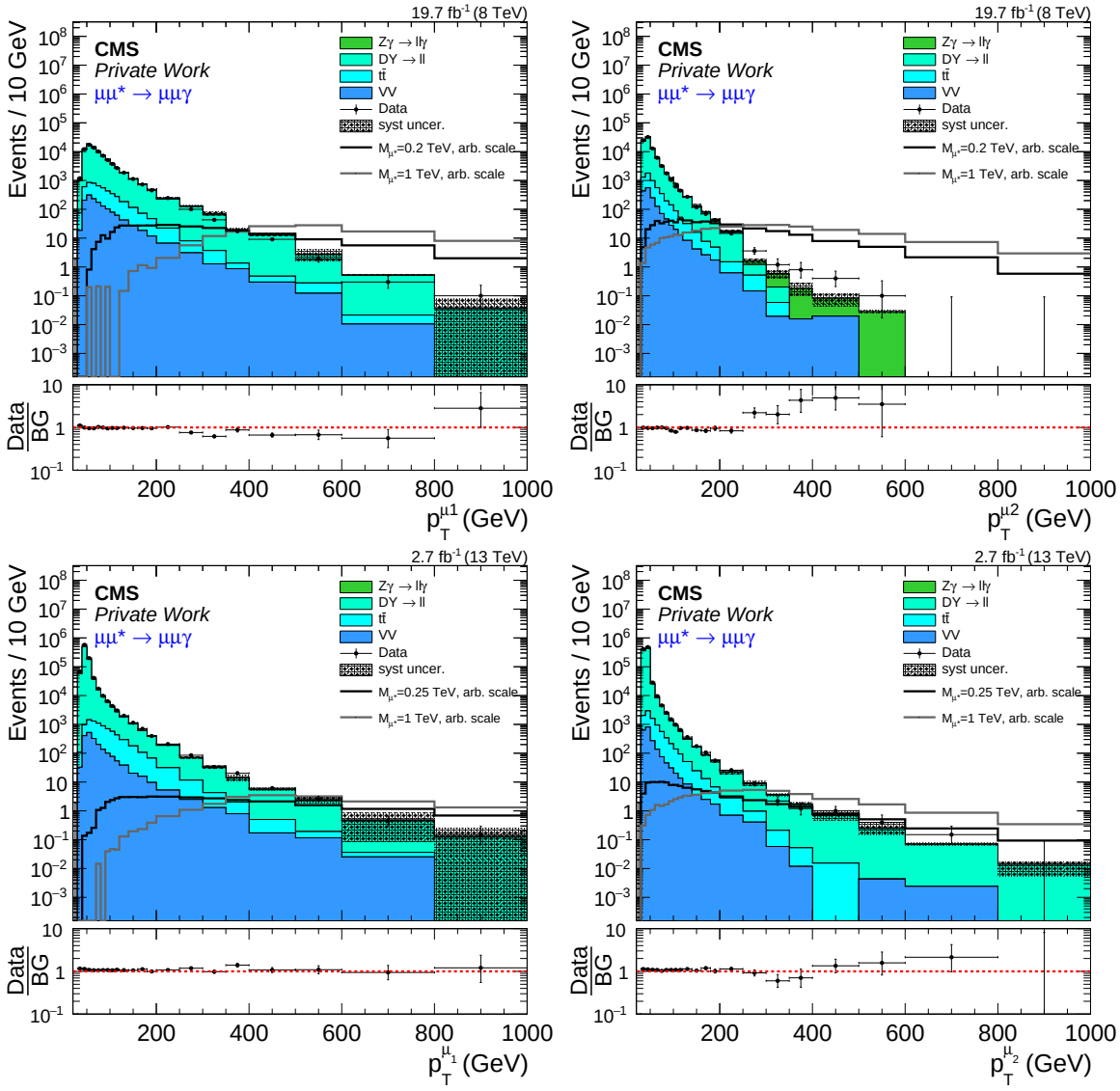

Figure 4.1: p_T-distributions of the leading (left) and subleading (right) muon as obtained in the Run I (top) and Run II (bottom) analyses. Backgrounds in all plots are determined from MC, exclusively. Due to low MC statistics, the backgrounds of the Run I plots stop at certain points in the spectra. As these backgrounds are replaced by a prediction from data later-on, this behavior is not further discussed here. Additionally, the expected signal behavior is given by two exemplary samples, outlined by solid lines. The Run II plots show the results after requiring $M^{\mu\mu} > 60$ GeV.

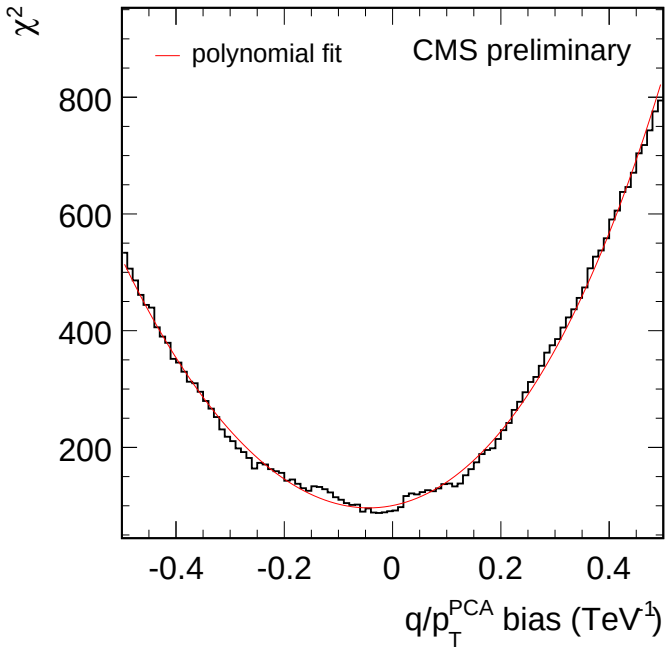

Figure 4.2: Example of a χ^2-distribution obtained from the cosmic endpoint method in [90]. The line is a polynomial function that was fitted to the data.

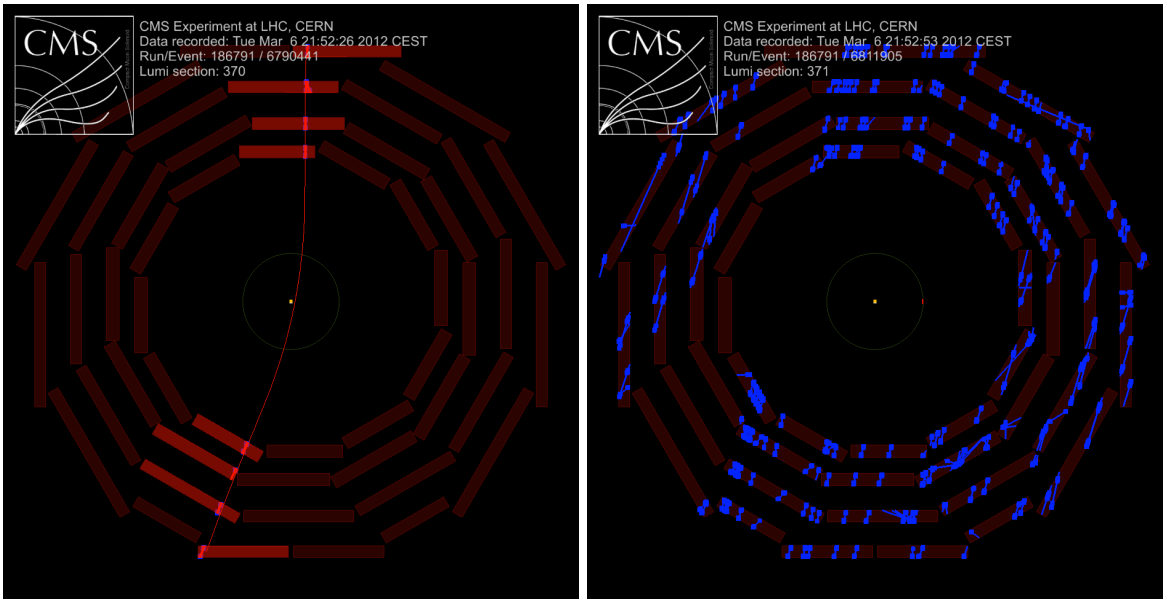

Figure 4.3: Events with cosmic muons in the $r - \phi$ plane of the detector. Left: A single muon traversing the detector with visible bending from the magnetic field that can be used for momentum resolution studies. Right: A shower of cosmic muons. Fascinating, but rather useless for analysis purposes.

Respective studies were performed in the past by CMS groups, e.g. for results published in [94]. The code that is the basis for the study here, originates from these measurements and was further developed in the context of [95]. The present studies were performed in close collaboration with Andreas Güth, and similar results can be found in his thesis [3].

The method uses cosmic muons that pass close to the nominal interaction point, e.g. as in figure 4.3, left. Such a "superpointing" single track is then split into two individual ones and the upper and lower parts are reconstructed as two different muons. In an ideal detector, both would have similar properties despite the fact that they point in opposite directions. However, due to the physical resolution of the detector, differences between both can be used to characterize the detector performance. In this study, the resolution is determined, using the lower track as the reference. It relies on the residual

$$R\left(q/p_{\mathrm{T}}\right) = \frac{\left(q/p_{\mathrm{T}}\right)^{u} - \left(q/p_{\mathrm{T}}\right)^{l}}{\sqrt{2}\left(q/p_{\mathrm{T}}\right)^{l}}, \tag{4.3}$$

with the charge q and p_{T} of the upper (u) and lower (l) muon. The factor $\sqrt{2}$ accounts for two independent track measurements. The spread of R is the measure for the resolution.

Cosmic data is taken with dedicated runs in times, when no collisions happen. During 2012, which is the data-taking period that is considered in this study, over 1.7 million cosmic muon events were recorded. However, this number reduces drastically to $\mathcal{O}(10^4)$ events that end up in the final result, for several reasons. Most events are removed because of unsuitable detector configurations. Depending on the active subsystems, most of the data cannot be certified[4]. Other reasons are e.g. the failing of the track re-fit. Additionally, analysis-like requirements are applied on the cosmic muons that further reduce the number.

To compare the performance of simulation with an actual measurement, a set of simulated cosmic muon events is available. It is divided into three samples, each containing 30 million events, that differ by their range of muon momentum[5], being (10-100, 100-500, >500) GeV. The full name of the samples is listed in the table of Appendix A. The simulation of cosmic muons was done using the CMSCGEN-package [97] with a parametrization of CMS[6] and its surrounding structures of earth and caverns [98]. The response of the detector's triggering system is not included into the simulation. That is why no special requirement on the trigger requirement is applied.

Here, two different muon reconstructions are compared. They are the global muon reconstruction and TuneP. Additional quality criteria are required, where some are based on the "high-p_{T}-ID" to generate analysis-like conditions. They are summarized in table 4.1. Example distributions, comparing cosmic data and -MC, with all selections applied are displayed in figure 4.4 for the global muon reconstruction. It shows the p_{T}- (left) and η-distribution (right) of the reference (=lower) muon track. In both cases, the simulation is scaled to the same total amount of events than found in data. The p_{T}-distribution shows an excellent agreement between measured data and simulation. Its spectrum is steeply falling and ends at approximately 1 TeV in the case of data. The η-distribution shows interesting effects. It has a strong asymmetry towards positive values, in both, data and simulation. The reason

[3] To be published

[4] Certified cosmic data is summarized in [96]
cosmic12_json_MuonPOG_190506_209625_DTGood_PEAK.txt and
commissioning12_json_MuonPOG_185250_190396_DTGood_PEAK.txt.

[5] In fact, the samples reach from the lower value to infinity. By relying on generator information, overlapping tails are removed.

[6] The reconstruction of the simulation is based on the conditions characterized by the global-tag "COSMC_53_PEAC". For cosmic data, the global-tag is "FT53_V21A_AN6".

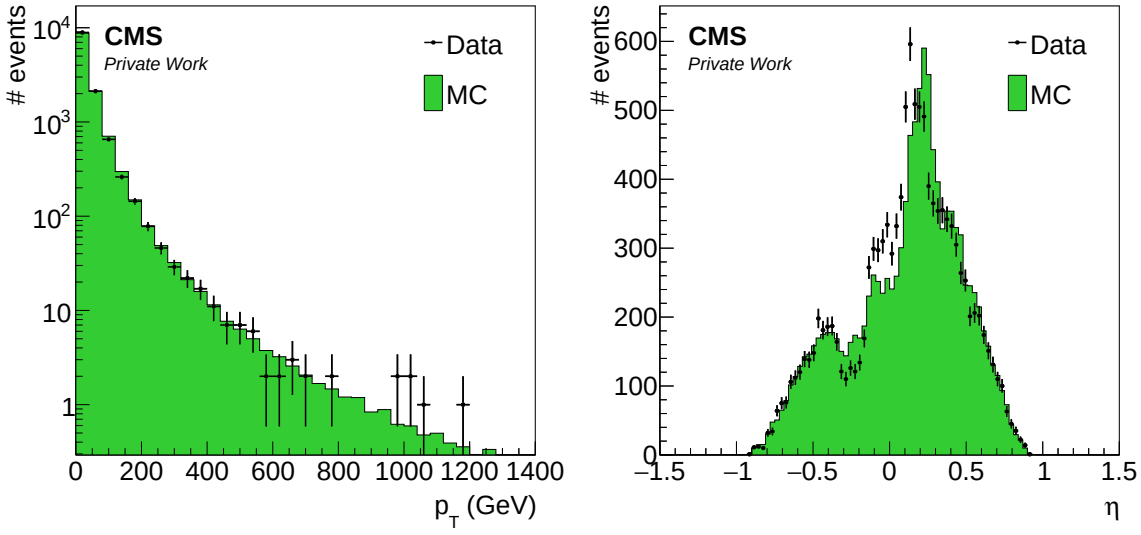

Figure 4.4: Example distributions of the comparison of measured and simulated cosmic muons with the global muon reconstruction. Both have a "high-p_T-ID"-like selection applied.

for this is the shaft leading to the surface that is located asymmetrically above CMS. Muons coming through this shaft are less absorbed than those traversing almost 100 m of rock. Compared to the spectrum of transverse momenta, a worse agreement between data and simulation can be observed. A reason that can be identified as being responsible, are missing RPC hits in a considerable amount of data due to inappropriate run conditions. Requiring at least one RPC-hit considerably increases the agreement in η, but significantly reduces the available data, which is why no additional requirement of RPC-hit is applied. Both distributions also display the limitations of this method. While at low and medium momenta the available statistics is quite high, the spectrum quickly drops and ends at 1 TeV. For a reliable measurement at high momenta (>1 TeV) much more data is needed. Also in η, the sensitivity is strongly limited as the cosmic muons reach CMS from the surface, only.

Two global muons reconstructed
No shared tracker hits
$\Delta\phi < 0.1$ and $\Delta\theta < 0.05$
Veto on CSC-hits
Muon hits ≥ 1
Pixel hits ≥ 1
Tracker layers ≥ 6
$\Delta p_T/p_T < 0.3$

Table 4.1: Summary of all selection criteria used on cosmic muons. The latter ones are adopted from the "high-p_T-ID".

To estimate the muon momentum resolution, distributions of R are calculated in bins of the transverse momentum of the reference track. Three examples are shown in figure 4.5, with

a Gaussian fit in the range of 1.5 × RMS, where the root mean square is calculated from the distribution of the data points. The widths of these distributions are the measure for the resolution. The width can either be defined by the width of the Gaussian fit, or by the RMS of the distribution. Both have (dis-)advantages. The RMS is sensible to wide tails that can be observed in high-p_T bins, especially of the global muon reconstruction (figure 4.5(c)). Unlike the Gaussian width, which suffers from the low statistics in the high-p_T bins in data. Due to low event numbers, a stable fit is not possible there (figure 4.5(b)).

The results here are given in terms of RMS. They can be seen in figure 4.6 for data (left) and simulation (right). Both show the result of the global muon reconstruction and TuneP in a range of up to 2 TeV. The resolution thereby ranges from below 2% at low p_T to $\mathcal{O}(10\%)$ at $p_T = 1\,\text{TeV}$. In both cases, the TuneP results have a better resolution than those from the global muon reconstruction. The highest bin in data suffers from the low statistics and non-Gaussian tails that were mentioned before, which manifests itself considerably in the global muon distribution. A linear function is fitted to the TuneP distributions of both, cosmic data and simulation.

To compare data and MC, both fit results are plotted in figure 4.6, bottom. Both agree fairly well, whereas the slope of the fit to MC is slightly higher. Their relative difference, shown by the red curve in the same plot, is below 2% throughout most of the considered momentum range. The structure is caused by the fact that both fits cross each other.

Overall, this study is able to give an estimate about the muon momentum resolution, and well suitable to compare the performance of of data and simulation. However, the results should not be interpreted as an absolute resolution measurement as the method is not able to account for several possible influences. For example, the influence of energy losses is not taken into account and could bias the residual R. Assuming, that a loss in the upper track would influence both momentum measurements, while one in the lower track would only affect the lower measurement, should result in a shift of the mean of the Gaussian fits to positive values. This could not be observed. Related to that, the p_T-measurements of both tracks are not fully independent. Thus, the combinatorial factor of $\sqrt{2}$ is not an optimal choice, but certainly more justified than assuming fully correlated measurements.

4.3 Photons

4.3.1 Photon Reconstruction

Photons are reconstructed from clusters (energy deposition in multiple adjoining crystals) in the ECAL. As described in [99] 94% (97%) of the original photon energy is deposited in a 3×3 (5×5) cluster. Photons can convert to $e^+ - e^-$-pairs when interacting with the tracker material[7]. Their signature is then smeared in ϕ-direction resulting in a so-called supercluster. Unconverted photons usually only require a cluster of 5×5 crystals [62].

There are several algorithms to reconstruct superclusters. The most important one, the *hybrid algorithm*, that is used in the barrel region, being dedicated to its special geometry, is introduced here, summarizing information from [100]. Interested readers are referred there for more detailed descriptions of this and other clustering algorithms used within the CMS collaboration. Starting from a seed crystal with the highest amount of deposited energy in a neighbor region, consecutively, arrays of crystals are added in both directions of ϕ. These

[7] Up to 60% of the photons convert, depending on the amount of tracker material, according to [62]. Similarly, electrons lose up to 86% of their energy because of photon radiation in the tracker [100].

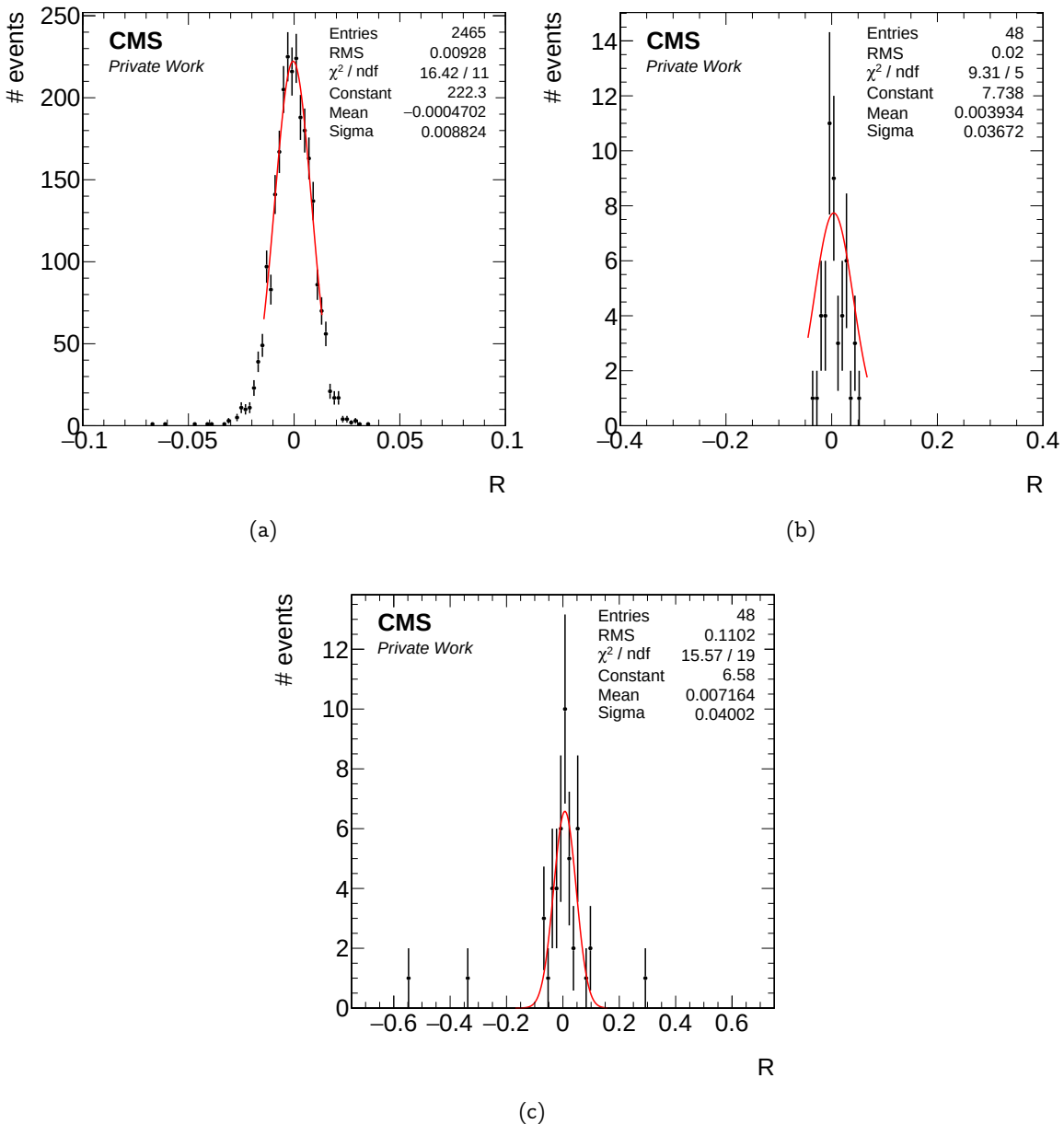

Figure 4.5: Distributions of the residual R (equation 4.3) in different bins of p_{T} with Gaussian fits. (a)&(b): TuneP reconstruction in the bins $(0 < p_{\mathrm{T}} < 10)\,\mathrm{GeV}$ and $(350 < p_{\mathrm{T}} < 500)\,\mathrm{GeV}$. (c): Global muon reconstruction in the bin $(350 < p_{\mathrm{T}} < 500)\,\mathrm{GeV}$.

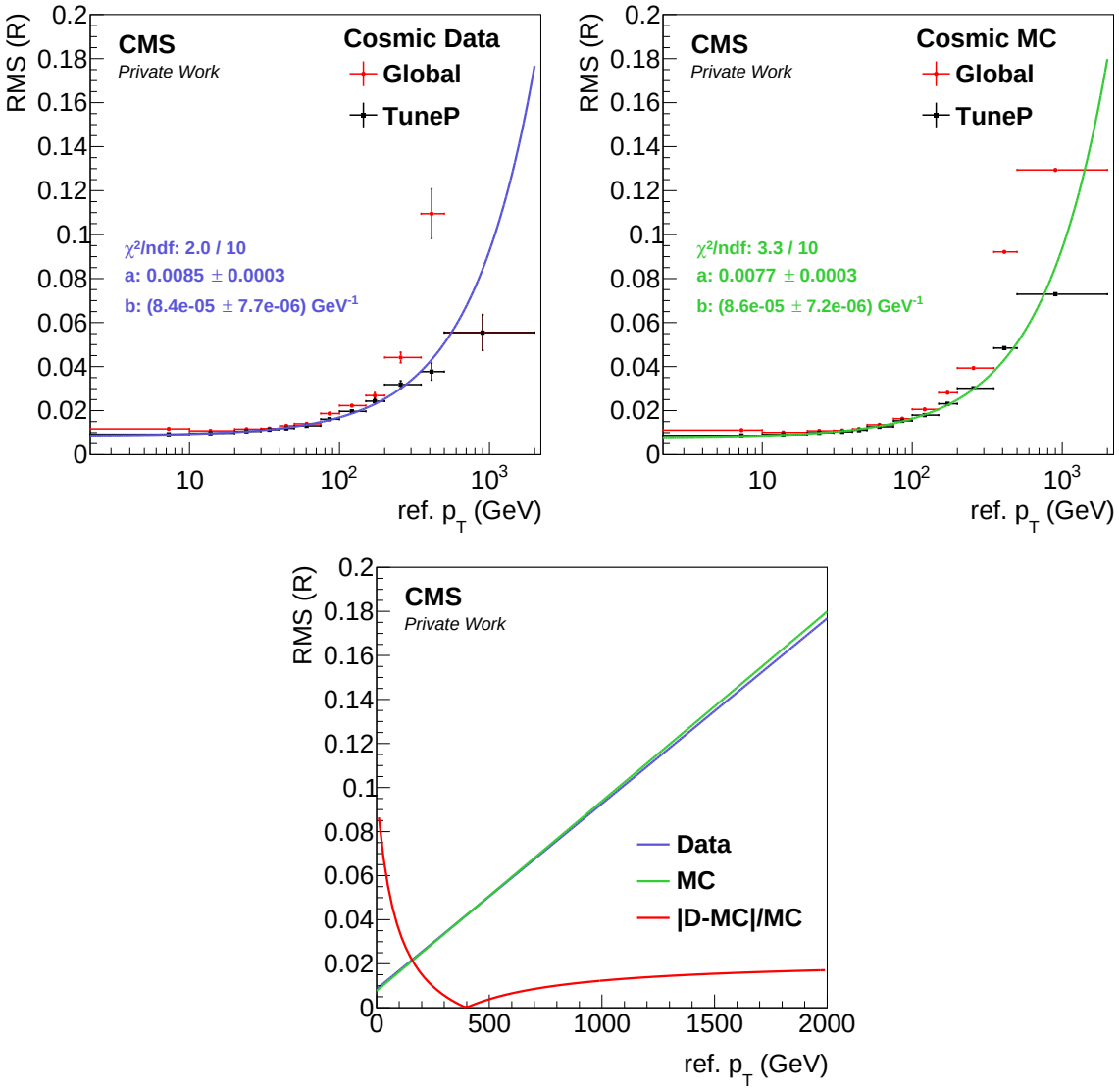

Figure 4.6: Upper two: RMS of the distributions of the residual R, as a function of the reference p_T from cosmic muon data (left) and MC (right) and for the global muon (red) and the TuneP reconstruction (black). Linear functions are fitted to the latter. Below: The results from the fits to Data and MC, as well as their relative difference.

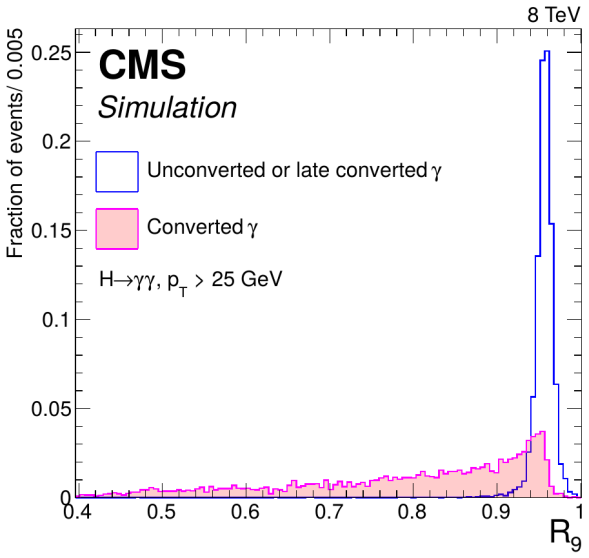

Figure 4.7: R_9-distributions of converted and (almost) unconverted photons. Both are from simulation only. Taken from [62].

arrays consist of 5 crystals that adjoin each other in the direction of η, and need to have more than 0.1 GeV of deposited energy. Only with an array of a seed energy of $E_{\mathrm{ar}} \geq 0.35\,\mathrm{GeV}$, a cluster can be formed that finally adds up to a supercluster.

To distinguish between converted and unconverted photons[8], a variable called R_9 is used. It is calculated for each supercluster by dividing the deposited energy in the 3×3 array around the cell with the highest entry by the energy of the complete supercluster. Unconverted photons result in a narrow peak close to one, while converted photons give a much wider, smeared-out R_9-distribution. An example from simulation can be seen in figure 4.7. Thus, to reconstruct the photon energy, contributions of the whole supercluster are summed up for the case that the photon fulfills $R_9 < 0.94$, and those from a 5×5 array, otherwise [62]. To determine the direction of the photon's momentum it is matched to the reconstructed primary vertex [101].

To only select properly reconstructed photons and reduce contributions from particles that are mis-reconstructed as photons, mainly neutral hadrons like π^0, further quality criteria are applied on analysis level. These selections differ between Run I and Run II. Both will be explained in the following sections.

4.3.2 Photon Selection – Cut Based (Run I)

In Run I, selections were applied to measured properties of the photons. These cuts are usually referred to as *Simple Cut Based ID* in the tight variant within CMS [102]. The requirements, with the definitions as described in [62, 100], are:

- $H/E < 0.05$: The ratio of deposits in the hadronic calorimeter to those in the electromagnetic calorimeter. Reduces the contributions from neutral hadrons that mimic a photon.

[8] Or such, where the conversion happens in one of the last tracker layers. They are called "late converted" in figure 4.7.

- $\sigma_{i\eta i\eta} < 0.011$: Is a measure for the spread of the supercluster in η, given in units of ECAL crystal size (i.e. spread in "i" crystals of given width).
- $I_{\mathrm{ch}} < 0.7\,\mathrm{GeV}$: The "charged hadron isolation", contributions from charged hadrons to the PF-isolation of the photon.
- $I_{\mathrm{n}} < 0.4\,\mathrm{GeV} + 0.04 \cdot E_{\mathrm{T}}^{\gamma}(\,\mathrm{GeV})$: The "neutral hadron isolation", contributions from neutral hadrons to the PF-isolation of the photon.
- $I_{\mathrm{pho}} < 0.5\,\mathrm{GeV} + 0.005 \cdot E_{\mathrm{T}}^{\gamma}(\,\mathrm{GeV})$: The "photon isolation", contributions from photons to the PF-isolation of the photon.
- $CSEV$ applied: The "Conversion Safe Electron Veto" rejects electrons that do not originate from a photon-to-electron conversion.

The photon isolation is used to reduce contributions from particles ($\pi^0, jets$) that are misreconstructed as a photon and such photons that have a non-prompt origin from final state radiation, e.g. from charged leptons. The three isolation variables are calculated making use of the particle flow algorithm (refer to 4.1) by summing up the transverse momenta of the particles being reconstructed within a cone of $\Delta R < 0.3$ around the photon. Energy contributions from the photon itself are thereby excluded. The isolation from neutral hadrons and photons is corrected for contributions by pileup. These corrections, along with a much more detailed description of the isolation procedure, can be found in chapter 6.2 of reference [62] and references therein.

The "Conversion Safe Electron Veto" works by rejecting tracks from charged particles that cannot be identified as electrons coming from a photon conversion. Those rejected tracks must have a hit in the innermost layer of the pixel detector [62]. A conversion is identified by searching for a second charged track that shares a common tangent [100]. In this way, prompt electrons can efficiently be rejected[9] while photons pass the veto as long as they do not convert in the beam pipe.

4.3.3 Photon Selection – Multivariate (Run II)

In Run II, a different approach is chosen for the selection of well reconstructed photons. This multivariate selection is described in [62] and is based on a boosted decision tree (BDT) using the *TMVA* [103] framework. As input, it uses variables similar to those described in section 4.3.2 without the CSEV and additional variables that account for pileup conditions, shower shape, and E_{T} and η of the photon [104]. From the output, each photon obtains one single variable for identification that reaches values in the range from -1 to 1. Thereby, prompt photons reach values close to 1 while those that are different particles reconstructed as photons tend to result in a BDT value of -1.

Finally, on analysis level, only such photons are selected that fulfill a BDT-score of

$$S_{\mathrm{BDT}}^{\gamma} > 0.374 \tag{4.4}$$

in the barrel region and additionally pass the CSEV [104, 105].

Scale-factors to account for differences between measured data and simulation are applied to the Monte-Carlo events. They are determined, including their corresponding uncertainties,

[9] In the barrel region, more than 99% of the photons and approximately 5% of the electrons pass the CSEV, according to [62].

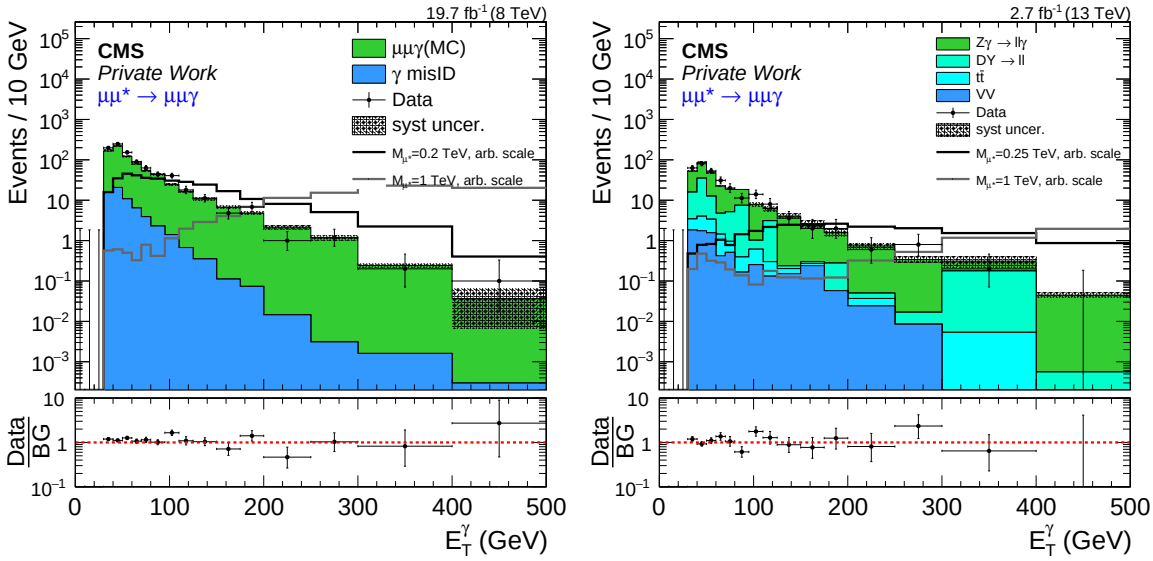

Figure 4.8: Distributions of E_T^γ for Run I (left) with the cut-based photon identification, and Run II (right) using the MVA-identification. Both plots show distributions after the selection of two muons and a photon. The Run I distribution on the left includes a data-derived background contribution, shown in blue.

within the CMS-collaboration for both selection criteria that were described above [102, 106]. To compute them, a tag-and-probe method similar to the one mentioned in section 4.2.2 is used, this time applied to e^-e^+-pairs.

The performance of the cut based and multivariate IDs can be seen in figure 4.8. It shows the E_T^γ-distribution of the respective leading photon of both analyses that fulfills all criteria, with all scale factors applied. In the complete range of measured events ($E_T^\gamma < 500\,\text{GeV}$), data and the Standard Model expectation agree well within the systematic and statistical uncertainties. The main difference between distributions is the composition of the background expectation, which is based on a data-derived ansatz in case of Run I. Details about that will be explained in the following chapter.

4.3.4 Photon Energy Scale and Resolution

Due to the excellent performance of the ECAL, the energy measurement of photons, and thus their resolution and absolute energy scale is very precise, and the corresponding uncertainties are small. Details were studied within the CMS collaboration using electrons from Z-decays in Run I data as described in [62]. There, an energy resolution of $1\% - 2.5\%$ is measured for barrel photons with a very good agreement between data and simulation, and even smaller systematic uncertainties. As this is extremely small compared to other uncertainties, it is not taken into further consideration.

The uncertainties on the photon energy scale are determined to be $0.1\% - 0.15\%$ for barrel photons [62]. Again, these are very small, and hence not further taken into consideration.

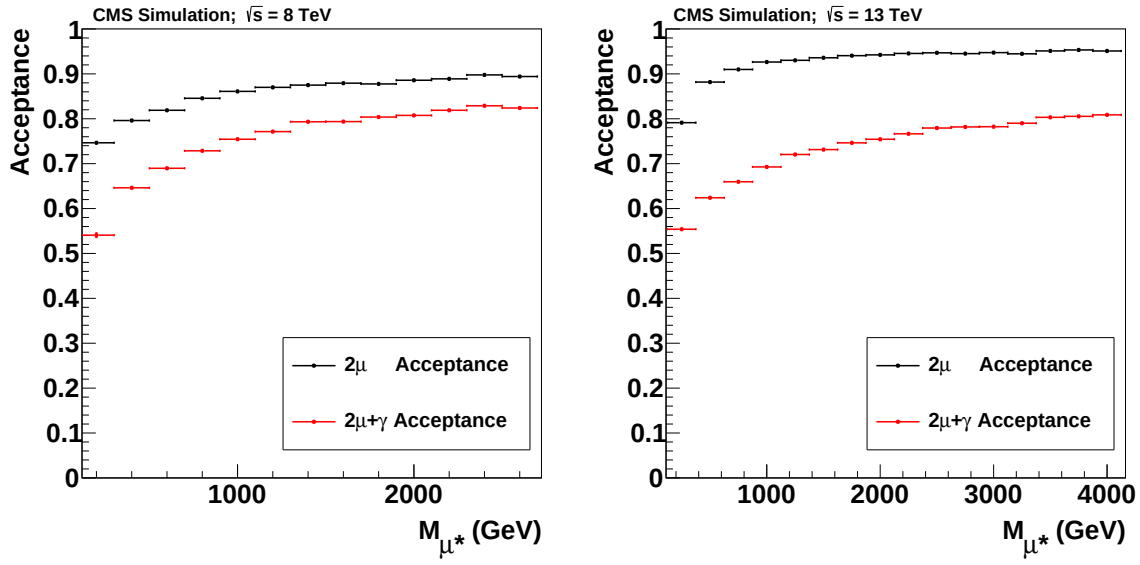

Figure 4.9: Relative amount of signal events, where two muons (black) and a photon (red) fulfill the kinematic requirements ($p_{\mathrm{T}}^{\mu}/et^{\gamma}$ and η) on generator level, depending on M_{μ^*}.

4.4 Kinematic Requirements and Summary

Additional selections are applied to the objects due to geometrical or other experimental restrictions. Here, these selections refer to limitations in the kinematic properties p_{T}^{μ} or E_{T}^{γ}, and η. The choice of thresholds is determined by the trigger selection and the geometric coverage of the detector instrumentation. In this section it will be illustrated, what influence the various object selection criteria have on the signal selection efficiency. Therefore, it is scrutinized how the kinematic requirements restrict the signal selection on generator level. After that, other influences, e.g. from reconstruction and identification are estimated, this time based on the signal on analysis level, i.e, after the full detector simulation and reconstruction chain.

Muons are required to exceed a threshold of $p_{\mathrm{T}}^{\mu} > 35\,\mathrm{GeV}$. This value is well above the trigger threshold of 17 (8) GeV for the (sub-)leading muon (compare section 3.2.6). The reason not to lower the value closer to the trigger threshold is in order to synchronize with the eeγ-channel which is based on a diphoton trigger with thresholds $E_{\mathrm{T}}^{\gamma} > 33\,\mathrm{GeV}$ (see [2]). Additionally, muons are restricted to $|\eta^{\mu}| < 2.1(2.4)$ in the Run I (Run II) analysis.

Similar to the muon selection, photons are required to have $E_{\mathrm{T}}^{\gamma} > 35\,\mathrm{GeV}$. Only barrel photons with $|\eta^{\gamma}| < 1.44$ are used in the analysis. This is in order to avoid strongly enhanced photon misidentification probabilities in the endcaps ($|\eta| > 1.56$).

The influence of these requirements on the signal selection efficiency, called acceptance, is shown in figure 4.9, for the Run I and Run II analyses. It shows the relative amount of signal events that fulfill the kinematic requirements on generator level as a function of the excited muon mass, M_{μ^*}. The black distribution corresponds to the acceptance of two muons, while for the red one, additionally a photon is required.

Comparing the acceptance for two muons between Run I and Run II, it can be seen that the result of Run II is higher. For example, at 1 TeV the acceptance yields about 86% in Run I compared to approximately 92% in Run II. The reason for that is the looser η-requirement

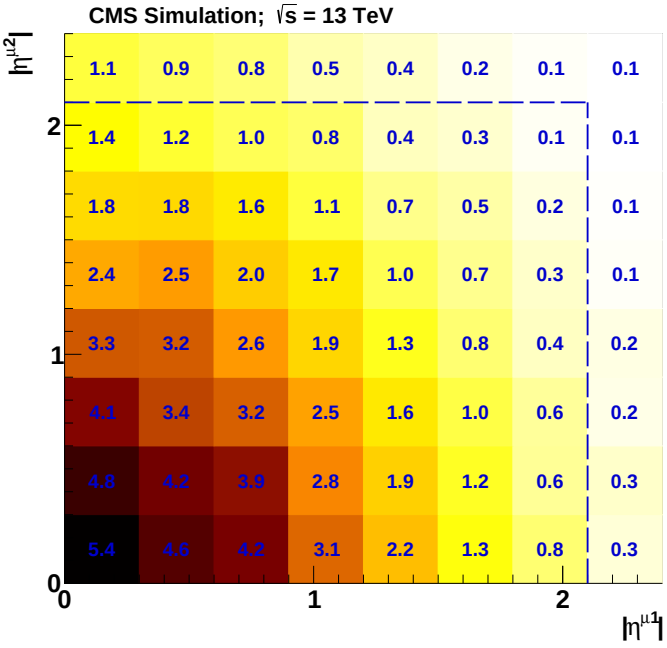

Figure 4.10: Two dimensional distribution of η of two muons at generator level shown for a signal sample with $M_{\mu^*} = 1\,\text{TeV}$ and $\sqrt{s} = 13\,\text{TeV}$. Color coding and numbers refer to the relative number of events in a respective tile, given in percent. The area outside the dashed line yields 5.4%.

in Run II (2.4 compared to 2.1 because of a trigger-misconfiguration in some periods of Run I). To better understand that, exemplary, figure 4.10 shows the relative distribution of the pseudorapidities of both muons on generator level in one plane. The shown distribution is obtained from the 1 TeV signal sample, generated for $\sqrt{s} = 13\,\text{TeV}$. Color and numbers refer to the relative number of events in a tile, given in percent. The dashed blue line refers to the difference between the Run I and Run II η-requirements. Contributions in the area $2.1 < \eta < 2.4$ yield 5.4%.

Comparing the acceptance for the case when an additional photon is required (red distributions), the gain from the wider η-requirement cannot persist. The reason for that is, similar to the discussion about η-distributions in section 2.6, the dependency of the η-distributions on the considered mass and center of mass energy. With rising energy, the probability for an imbalanced momenta of the interacting partons increases, and, as a result, the distribution in the pseudorapidity of the decay products widens. When considering photons with a rather narrow η-acceptance this results in the visible effect.

Table 4.2 summarizes all selection criteria that are applied on analysis level. The corresponding total signal selection efficiencies can be seen in figure 4.11. It shows the cumulative efficiencies of various selection steps determined with signal MC on analysis level after the reconstruction, over wide mass ranges. After a rise that is mainly caused by the p_T-thresholds, the efficiencies stay flat at approximately 48% (left, Run I analysis) and 55% (right, Run 2).

In the first step (black) two reconstructed muons within the kinematic ranges in p_T and η are required. Here, aside from the acceptance being discussed before, the reconstruction

	Run I	Run II
Trigger	HLT_Mu17_TkMu8	HLT_Mu17_TrkIsoVVL_Mu8_TrkIsoVVL_DZ HLT_Mu17_TrkIsoVVL_TkMu8_TrkIsoVVL_DZ
μ	$p_T > 35$ GeV $\|\eta\| < 2.1$ "high-p_T ID" Iso$^\mu < 0.1$	$p_T > 35$ GeV $\|\eta\| < 2.4$ "high-p_T ID" Iso$^\mu < 0.1$
γ	$E_T > 35$ GeV $\|\eta\| < 1.44$ "cut based ID"	$E_T > 35$ GeV $\|\eta\| < 1.44$ "MVA-ID"

Table 4.2: Summary of all object selection criteria for Run I and Run II.

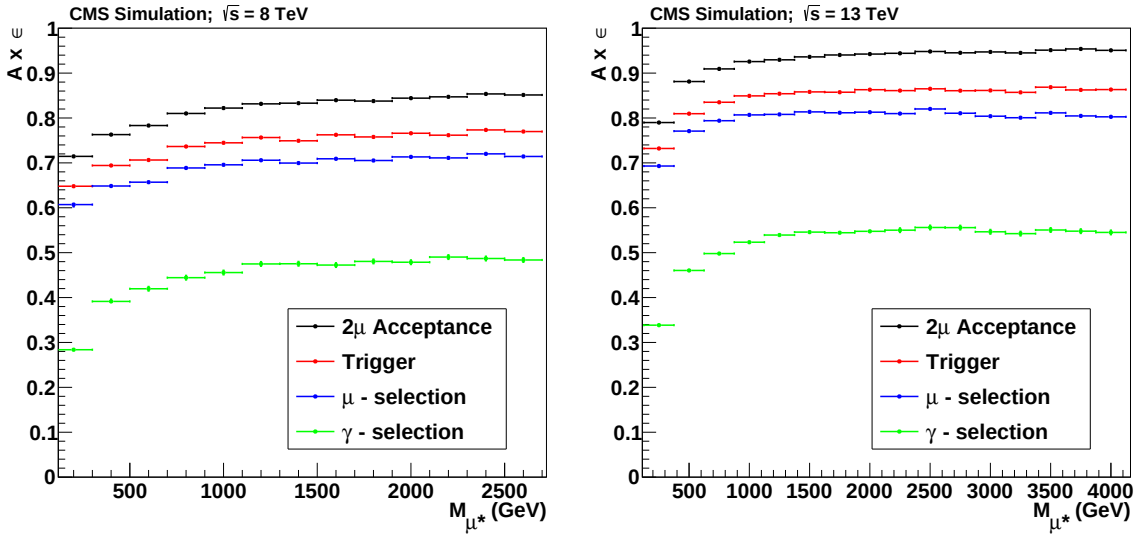

Figure 4.11: Overall selection efficiency as estimated from signal simulation after various requirements for both analyses (analysis level, after reconstruction): After selecting two reconstructed muons within the kinematic range (black), the requirement of the trigger (red), after applying the quality cuts on both muons (blue), and after selecting an additional photon with the respective ID (green).

efficiency is relevant. As mentioned in section 4.2, the Run I reconstruction thereby suffers from a small inefficiency that, together with the effects from the acceptance, adds up to approximately 10% difference when comparing Run I and Run II.

From this step onwards it is possible to estimate the impact of the trigger requirement, as given in red. Run I and Run II thereby perform comparable, similar to the muon selection (blue), that refers to the identification and isolation criteria being introduced in section 4.2.2. The last step shown here requires an additional reconstructed photon within the E_{T} and η ranges described before, and with all identification and isolation requirements (sections 4.3.2 and 4.3.3) applied. Thus, it combines effects from the acceptance, reconstruction, and identification.

5 | Standard Model Background

To make a reliable statement about extensions to the Standard Model it is essential to know the processes from the Standard Model that contribute to the considered final state as background. In most analyses, these contributions are estimated, either by simulation (Monte Carlo or short MC) or by extracting them from the measured data itself. Both approaches find place in the analyses that are described in this thesis.

The probability for an event of a certain process to happen is given by the total integrated luminosity of the considered dataset, multiplied by the cross section of that respective process. Hence, background events from Monte Carlo have to be weighted to the amount of data. The weighting factor that is applied to every single simulated process is calculated by

$$w = f \cdot \frac{\sigma \cdot \mathcal{L}}{N}, \tag{5.1}$$

where σ is the cross section of the process, $\mathcal{L}$ the total integrated luminosity of the data, N the total number of MC events the process sample was originally produced with, and f a weighting factor that accounts for potential additional scales like filter efficiencies. The latter is equal or close to one in most cases.

All processes that are able to provide two muons and a photon in the final state need to be considered. Tables 5.1 and 5.2 list the processes that are considered in the analyses and that are simulated by MC (a list with all samples and their names is given in the table of Appendix A). However, it is obvious that not all those processes provide a prompt photon and two muons. Such backgrounds include a non-prompt photon that is usually a mis-reconstructed jet. In the following sections, various background contributions are discussed in more detail. The simulations of the main background from $Z\gamma$-production will be shown, and the modeling of non-prompt photon contributions from data will be discussed.

5.1 Monte-Carlo Generators and Detector Simulation

Both, signal and background events are generated using various Monte Carlo generators. For the Run I analysis, they are Sherpa1.1 [117], Madgraph5.1 [109] and Pythia6 [30] for the background, and Pythia8 for the signal samples. In Run II, the background samples are generated with Madgraph5_aMC@NLO [113], Powheg [116, 118, 119] and Pythia8.

Matrix element generators like Powheg or Madgraph need an additional generator to simulate the parton shower and hadronization of the events. This is then done by Pythia. Sherpa has its own parton shower and hadronization simulation and thus does not need to rely on any additional framework.

After the generation, the interaction of the decay products with the detector material needs to be simulated, using Geant4 [120, 121]. Also, the full response of the detector, including the electronic signal processing and the selection by the triggering system needs to be simulated. It is not before then, that the reconstruction, that is also used on data, can be applied to the MC events.

Process	Remark	Generator	σ [pb]	$\mathcal{O}(\sigma)$	
$Z\gamma \to \mu\mu\gamma$	$E_T^\gamma > 10$ GeV $M^{\mu\mu} > 50$ GeV $\Delta R^{\mu\gamma} > 0.6$	Sherpa	14.9	NLO	[107]
$t\bar{t}\gamma \to$ incl. $+\gamma$		Madgraph5.1	1.44	LO	[108, 109]
$WW \to$ incl.		Pythia6	56.0	NLO	[107, 110]
$WZ \to$ incl.		Pythia6	23.7	NLO	[107, 110]
$ZZ \to$ incl.		Pythia6	17.0	NLO	[107, 110]
DY $\to \ell\ell$	$M(\ell\ell) > 50$ GeV	Madgraph5.1	3531.9	NNLO	[110, 111]

Table 5.1: Simulated processes involved in the Run I analysis. The last column gives the precision of QCD corrections with the reference to the source where this cross section was calculated and the framework that was used to determine it. The abbreviation "incl." indicates that the decay is not restricted to certain products, e.g. all leptonic and hadronic decays of the t-quark are considered.

Process	Remark	Generator	σ [pb]	$\mathcal{O}(\sigma)$	
$Z\gamma \to \ell\ell\gamma$	$M(\ell\ell) > 30$ GeV	aMC@NLO	117.9	NLO	[112, 113]
$Z\gamma \to \ell\ell\gamma$	$E_T^\gamma > 130$ GeV	aMC@NLO	0.143	LO*	[113, 114]
$t\bar{t}\gamma \to$ incl. $+\gamma$		aMC@NLO	3.70	NLO	[112, 113]
$t\bar{t} \to 2\ell 2\nu$		Powheg	87.3	NNLO	[112, 115]
$WW \to$ incl.		Pythia8	63.2	LO	[31, 114]
$WZ \to$ incl.		Pythia8	47.1	NLO	[107, 112]
$ZZ \to$ incl.		Pythia8	16.5	NLO	[107, 112]
DY $\to \mu\mu$	bins of $M(\mu\mu)$	Powheg	Appendix A	NLO	[114, 116]

Table 5.2: Simulated processes involved in the Run II analysis. The last column gives the precision of QCD corrections with the reference to the source where this cross section was calculated and the framework that was used to determine it. The abbreviation "incl." indicates that the decay is not restricted to certain products, e.g. all leptonic and hadronic decays of the t-quark are considered. [*]: Here, a LO cross section is referenced. However, in the analysis, an E_T-dependent NLO k-factor will be applied. More about that in section 5.3. Here, Madgraph5_aMC@NLO is shortened to aMC@LNO.

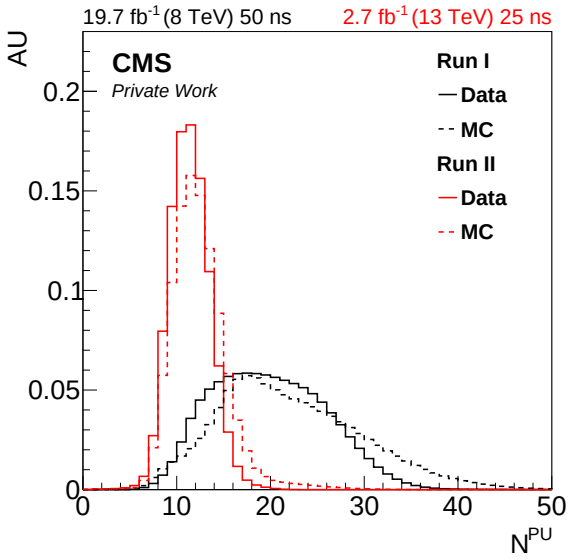

Figure 5.1: Number of pileup interactions as measured in data (solid lines) and as simulated in MC (dashed lines) for Run I (black) and Run II (red). All distributions are scaled to unit area.

5.2 Pileup

As bunches of approximately 10^{11} protons collide, each bunch crossing causes multiple proton-proton collisions. In most cases, only one of these interactions is of interest. Nevertheless, these additional interactions lead to signatures in the detector, called *pileup*, that need to be taken into account in the simulation.

The amount of pileup per bunch-crossing depends on the instantaneous luminosity and is distributed following a Poisson distribution. To determine the pileup contributions in a given dataset, its instantaneous luminosity distribution is convoluted with the corresponding Poisson distribution, multiplied by the minimum-bias cross section[1].

In Monte Carlo, a certain expected amount of pileup is estimated before the central production. For the correct usage, this estimated distribution is reweighted to follow the actual data distribution that is determined by the procedure described in the paragraph above.

Figure 5.1 shows the distributions in data and MC. It can be seen how the estimate of the simulation is approximately fulfilled by the measurement in data. In the 25 ns data of Run II, the mean number of pileup interactions, as well as the width of the distribution, is clearly much lower compared to data of Run II, taken at a bunch spacing of 50 ns. The reason for that is given by the average bunch intensity (= average number of protons per bunch) that decreased by approximately 1/3. As, at the same time the number of bunches was doubled, the influence of pileup could be reduced without losing instantaneous luminosity.

On analysis level, the influence of pileup can be observed when looking at the number of reconstructed vertices. Figure 5.2 shows the vertex multiplicity per event after the correction for pileup for both analyses with the corresponding systematic uncertainty arising from shifting the minimum bias cross section by $\pm 5\%$ [122]. No systematic shift between data

[1]The minimum-bias cross section refers to that amount of the total inelastic cross section that is actually accessible by the experimental setup (coverage, trigger thresholds).

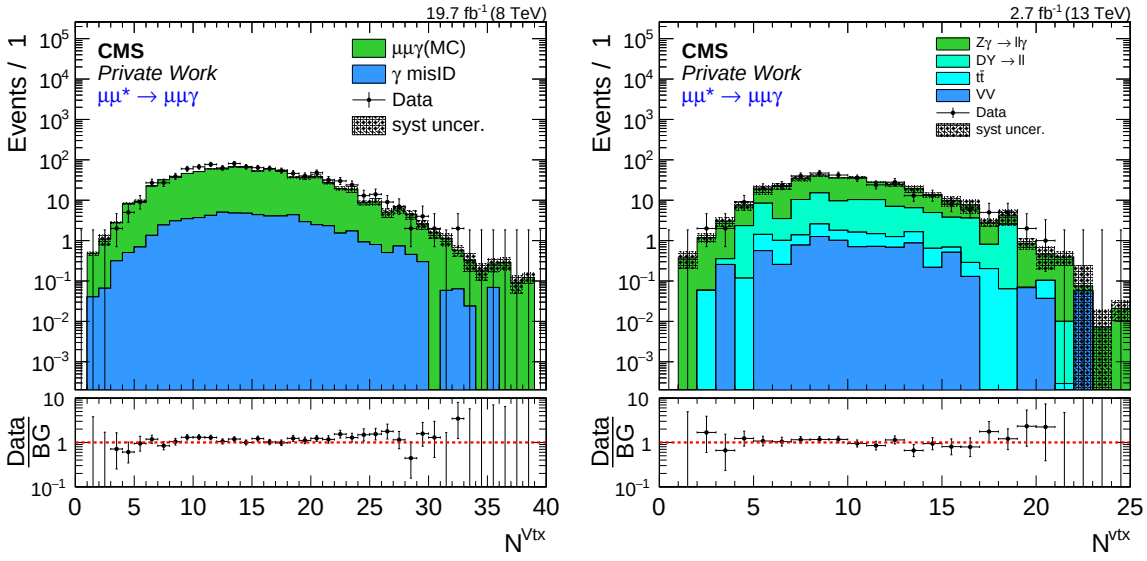

Figure 5.2: Number of reconstructed vertices per event for Run I (left) and Run II (right) with the corresponding systematic uncertainty.

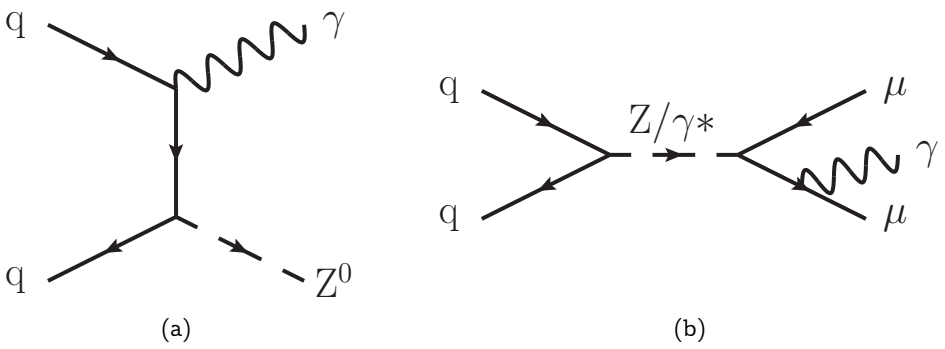

Figure 5.3: Feynman diagram of leading order Zγ production (a) and dimuon production by Drell-Yan with an additional photon from final state radiation (b).

and background can be observed. The systematic uncertainty is rather small in the region around the central value and increases when going to the flanks.

5.3 Zγ-Production

The dominant background is the associated production of a real photon and a Z-boson that then subsequently decays into two muons. This can happen either by initial state radiation (ISR), where a high energetic photon is radiated by an incoming quark (figure 5.3(a)), or by final state radiation (FSR) where the photon is radiated by one of the outgoing muons (figure 5.3(b)). In the latter case, photons are usually rather soft and collinear with the radiating muon.

The collinear FSR photons are hard to simulate which is why a cut on ΔR between the photon and the originating lepton is applied on generator level during the production of the background samples. For the productions of the Run I MCs this cut is $\Delta R > 0.6$. To

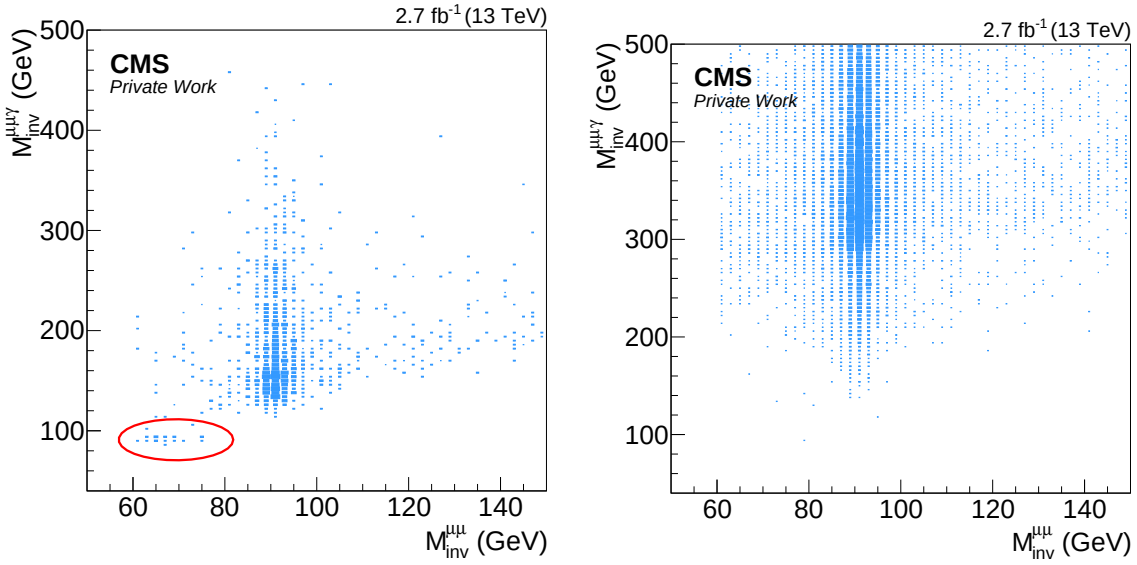

Figure 5.4: Two-dimensional distributions of the dimuon- and dimuon+photon invariant masses. The left plot shows the result from the inclusive sample of table 5.1, while the one on the right is derived from the sample with $E^{\gamma}_{T} > 130\,\text{GeV}$. The red circle indicates the region where events with FSR-photons are expected to cluster. The events in both plots are not weighted to cross section and luminosity, the total scale of the distributions is in arbitrary units.

account for this cut, on analysis level, a requirement of $\Delta R^{\mu\gamma} > 0.7$ is applied to data and background which is also used in Run II where the cut on generator level is $\Delta R > 0.5$. To illustrate the impact of ISR and FSR, figure 5.4 shows the two-dimensional distributions of the invariant masses $M^{\mu\mu\gamma}$ and $M^{\mu\mu}$ of the Run II Zγ-background of table 5.2 that is simulated with Madgraph5_aMC@NLO. The distribution on the left shows the result from the inclusive sample while the one on the right is from the one with $E^{\gamma}_{T} > 130\,\text{GeV}$. Events with photons from ISR are expected to cluster around the Z-mass in $M^{\mu\mu}$ while for those from FSR, $M^{\mu\mu\gamma}$ should result at the approximate Z-mass (red circle). It can be seen that FSR events are strongly suppressed and even further reduced when the photon energy is increased. Thus, they only play a minor role in the analyses.

5.3.1 Higher Orders

Next-to-leading order (NLO) corrections in α_s play an important role to production cross sections and observables of the Zγ-background. Figure 5.5 shows examples of NLO and NNLO corrections to the Zγ-process. It illustrates that not only the final state can be influenced through the emission of additional quarks or gluons, but also additional production processes with gq and even gg initial states are allowed. As an example, figure 5.6 shows mass distributions with (N)NLO contributions at $\sqrt{s} = 7\,\text{TeV}$ that were calculated in [123]. According to those results, at higher masses, contributions from NNLO corrections yield an increase of $8\% - 18\%$ to the NLO cross section. The uncertainty on the cross section yields approximately 10% in the NLO case and is even larger for NNLO at lower masses. For higher masses, they become smaller. However, calculations at high masses are not available. In the analyses presented here, an overall 10% cross section uncertainty was assumed on the Zγ-processes.

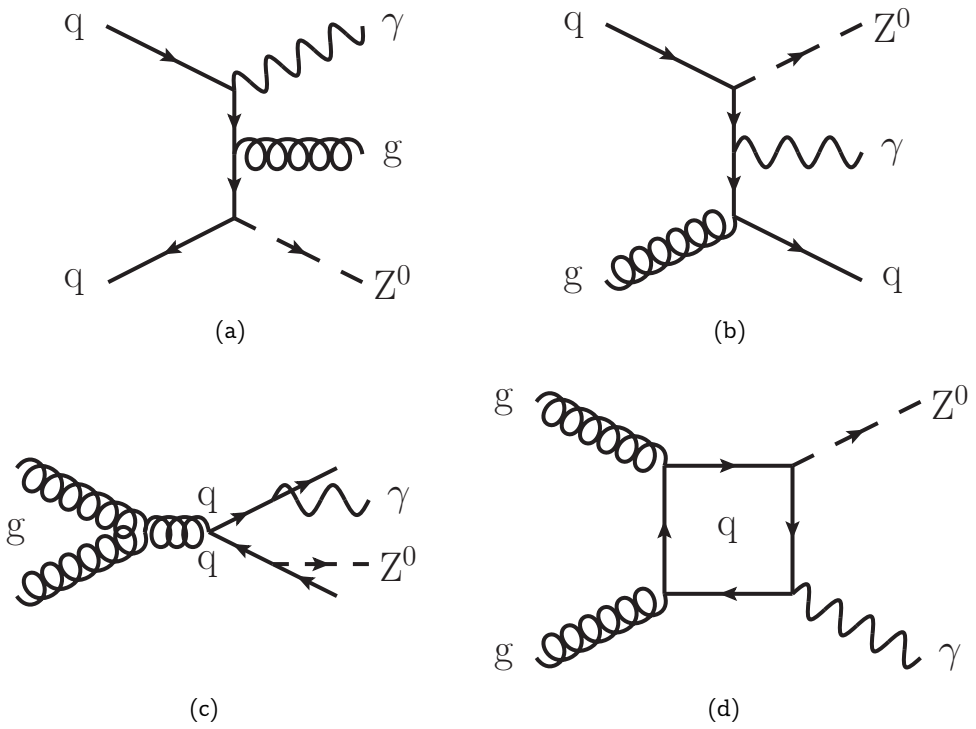

Figure 5.5: NLO (a,b) and NNLO (c,d) corrections to the Zγ-process.

For the Run I analysis, a NLO Zγ-background description simulated with Sherpa is used. Additionally, a cross section with NLO precision, calculated with MCFM [124–126] is applied. Both, sample and cross section, were already used in the Run I Zγ-cross section measurement of CMS [127, 128] and are here adapted from that analysis.

In Run II, the Zγ-background is generated with Madgraph5_aMC@NLO. Two samples are used. An inclusive one, meaning that no special restriction to the phase space is imposed, is here referred to as the "bulk" sample. The second one includes only photons with $E_{\mathrm{T}}^{\gamma} > 130\,\mathrm{GeV}$ to provide large numbers of MC events at high E_{T}^{γ} and will thus be called the "high-E_{T}"-sample. The bulk samples makes use of the MC@NLO formalism [129] to provide a simulation of NLO accuracy. The high-E_{T} sample is generated at LO. To achieve NLO accuracy, the tail sample is fitted to the E_{T}-tail of the bulk sample. Thus, a flat correction factor of 1.37 was determined within the excited lepton group [130]. Figure 5.7 shows the high-E_{T}sample (blue) as well as the bulk sample (black), where events with $E_{\mathrm{T}}^{\gamma} > 130\,\mathrm{GeV}$ are removed on generator level, together with the continuous sum of both (red) that is used for the further analysis.

Characteristic for the Zγ-background is the dimuon-resonance at the Z-mass. Figure 5.8 shows the corresponding $\mathrm{M}^{\mu\mu}$-distributions of the Run I (left) and Run II (right) analysis, after selecting two muons and an additional photon. The Zγ-background is represented by the green area. Over the complete mass range, a reasonable agreement can be observed.

5.4 DY+Jets

Events from the Drell-Yan (DY) process can contribute, if the photon is faked by a jet. That means that the jet itself is either mis-reconstructed as a photon, or the photon has

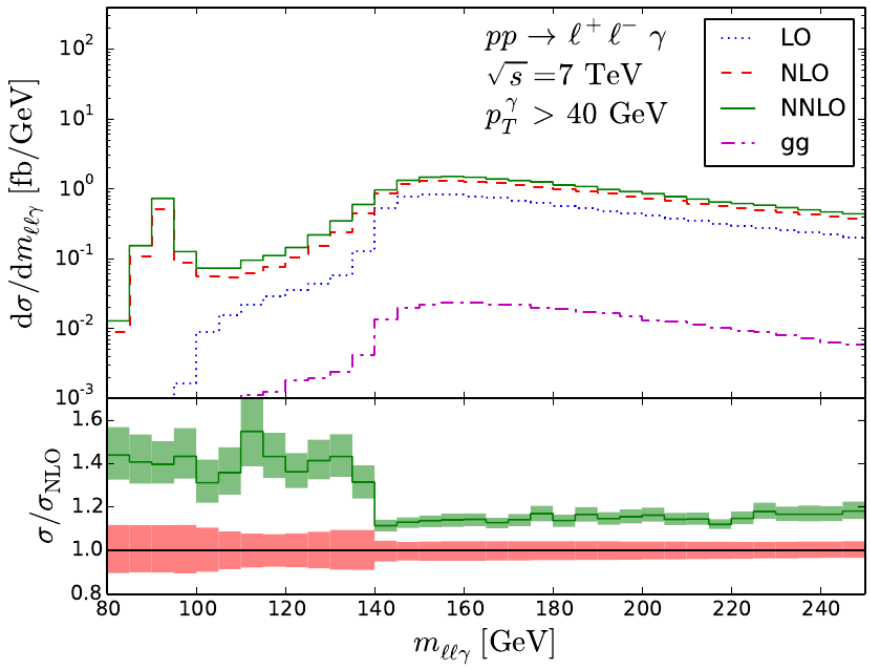

Figure 5.6: Distribution of the $\ell\ell\gamma$ invariant mass with cross sections at LO (dotted blue), NLO (dashed red), NNLO (solid green), and loop processes from gg-fusion (purple) like in figure 5.5(d). The lower plot shows the ratio NNLO/NLO and the uncertainty of the NLO and NNLO predictions as colored bands. Taken from [123]. According to the reference, masses $m_{\ell\ell\gamma} < 97\,\text{GeV}$ are kinematically not accessible at LO. This changes when either the order in QCD is increased or the photon momentum is considerably lowered.

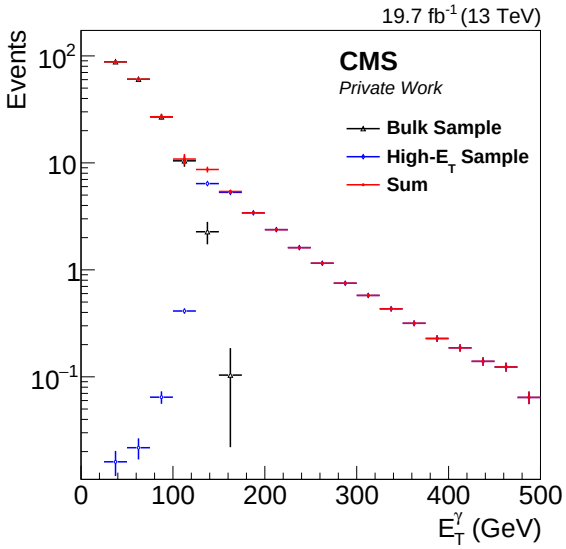

Figure 5.7: Comparison of the bulk sample, where events with $E_\text{T}^\gamma < 130\,\text{GeV}$ are removed (black), the high-$E_\text{T}$sample and the sum of both (red).

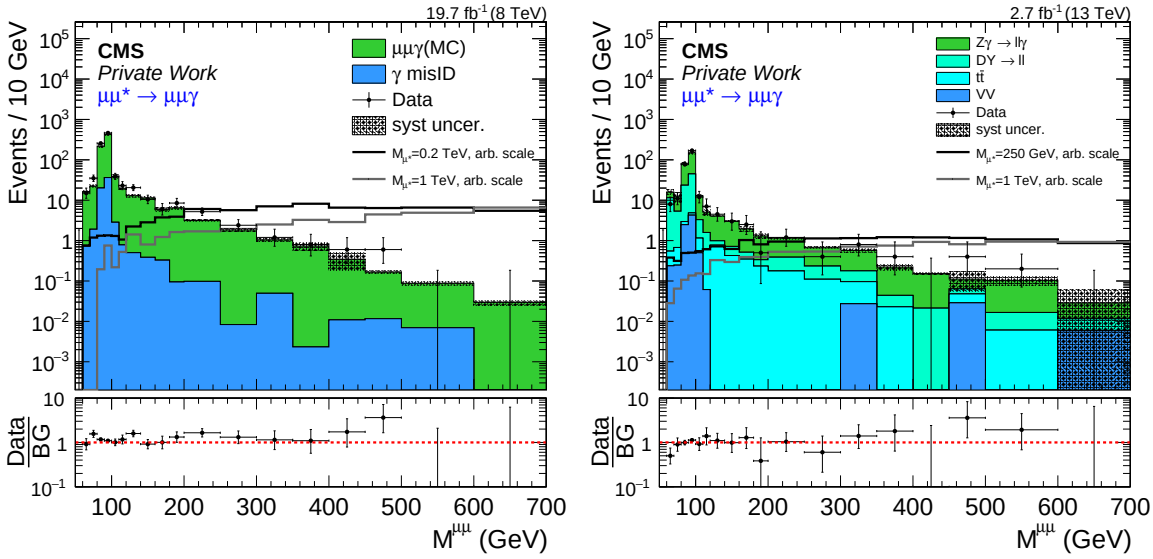

Figure 5.8: Distributions of the dimuon invariant mass $M^{\mu\mu}$ in both analyses.

its origin from hadronic decays inside the jet. An exemplary Feynman diagram is shown in figure 5.9(a). Events that have a prompt photon are removed from the respective samples in tables 5.1 and 5.2 by relying on generator information in order to avoid double counting with the Zγ-samples.

In the Run I analysis, this background takes part of the contributions with misidentified photons that are estimated from data and introduced in the next section. The analysis of Run II relies on an NLO simulation from Powheg that is divided in several samples of consecutive bins of $M^{\mu\mu}$ in order to provide sufficient MC statistics up to high masses. This can be seen in figure 5.9(b) that shows the distribution of the dimuon invariant mass without the requirement of an additional photon. Thus, it is guaranteed that DY+Jets is the dominating background. The complete spectrum, from below the Z-peak up to masses above 2 TeV is well described by the simulation.

5.5 Photon Misidentification

Backgrounds, with a photon of a non-prompt origin, i.e. a photon from secondary decays, or misidentified jets, can be extracted from measured data itself. Thus, the analysis does not depend on these difficult to simulate processes. The analysis of Run I data is based on such a data driven approach that will be outlined here. The misidentification probability is thereby measured in data and then applied to an orthogonal data sample to achieve a prediction of the fake-photon background. This *template method* was developed in the context of 7 TeV CMS analyses [131] and was also published in the corresponding search for excited leptons [43]. The results for the 8 TeV analysis, as they are used in this thesis, were obtained within the ℓ^*-group of CMS. Detailed information can be found in [2, 3, 132, 133].

In the Run II analysis, due to a different photon identification (refer to section 4.3), an alternative method is tested and summarized here. However, the final results are obtained with an MC-based description, exclusively. Here, this thesis differs from the Run II publication [4] that relies on the data driven ansatz. The measurements of both (Run I and Run II) fake photon identification are not the work of the author and only outlines of the methods are

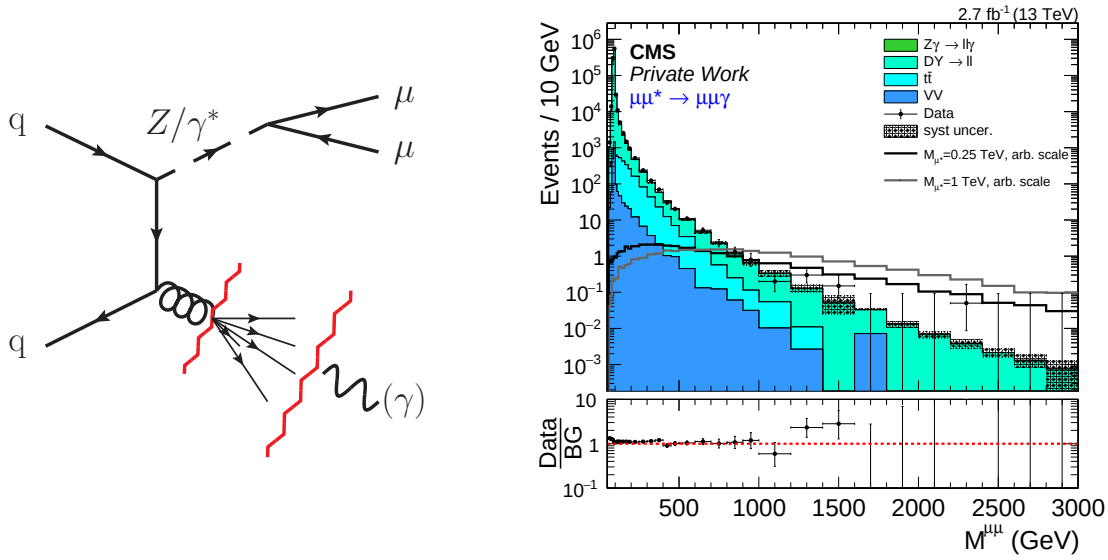

(a) (b)

Figure 5.9: Left: Example Feynman diagram of the DY+Jets process where a jet is misidentified as a photon. Right: Dimuon invariant mass spectrum after selecting two muons. An additional photon is not required.

given, summarized from the references. Only the final application of the probabilities, in order to estimate the faked photon background contribution to the analyses is done by the author himself.

5.5.1 Run I: The Template Method

The template method used in the Run I analysis uses single-photon triggered data that is orthogonal to the data used in the analysis, to measure the jet-to-photon fake probability. By inverting isolation criteria of the photons a "loose ID" is defined. Then, the fake probability is measured, defined as the ratio of faked photons that fulfill the normal tight ID to those passing the loose ID. However, it cannot be guaranteed that the tight sample consists of faked photons, exclusively. Contaminations by prompt, "true" photons need to be subtracted from that sample. Thus, the fake probability is defined by

$$p_{\text{fake}} = \frac{\text{tightID} - \text{contamination}}{\text{loose ID}}. \tag{5.2}$$

This ratio can then be applied to data with photons fulfilling the loose ID to obtain the prediction of non-prompt photons.

For the selection of the loose ID, the identification criteria, as described in section 4.3.2, are modified. The exact definition is shown in table 5.3. Isolation criteria are considerably relaxed and, in addition, it is required that either one of the PF-isolations or the shower shape variable $\sigma_{i\eta i\eta}$ is inverted.

For a proper determination of the fake probability, a sample is needed for the numerator of equation 5.2, that consists of faked photons, exclusively. To achieve that, the contribution

Cut Variable	Value	Logic	
H/E	< 0.05		
I_{ch}	$< Min(5 \cdot 4, 0.2 \cdot E_{\text{T}}^{\gamma}/\,\text{GeV})\,\text{GeV}$		
I_{n}	$< Min(5 \cdot (4.5 + 0.006 \cdot E_{\text{T}}^{\gamma}/\,\text{GeV}), 0.2 \cdot E_{\text{T}}^{\gamma}/\,\text{GeV})\,\text{GeV}$	**AND**	
I_{pho}	$< Min(5 \cdot (4.5 + 0.0025 \cdot E_{\text{T}}^{\gamma}/\,\text{GeV}), 0.2 \cdot E_{\text{T}}^{\gamma}/\,\text{GeV})\,\text{GeV}$		
$CSEV$	✓		**AND**
I_{ch}	$> 4\,\text{GeV}$		
I_{n}	$> (4.5 + 0.006 \cdot E_{\text{T}}^{\gamma}/\,\text{GeV})\,\text{GeV}$	**OR**	
I_{pho}	$> (4.5 + 0.0025 \cdot E_{\text{T}}^{\gamma}/\,\text{GeV})\,\text{GeV}$		
$\sigma_{i\eta i\eta}$	> 0.012		

Table 5.3: Criteria for the loose photon ID.

of the prompt photon contamination is hence estimated by a template fit. The fit is done in terms of the $\sigma_{i\eta i\eta}$-distribution (see figure 5.10). It shows the bin $35\,\text{GeV} < E_{\text{T}}^{\gamma} < 50\,\text{GeV}$ with the distribution from data (black dots), the "Signal" from true photons that need to be removed (green), and the background template that represents the faked photons. The signal template is estimated relying on simulation. Here, the Zγ-sample generated with Madgraph is used and the photons are verified using generator information. The blue background is estimated in a sideband of the charged hadron isolation, i.e. $2\,\text{GeV} < I_{\text{ch}} < 6\,\text{GeV}$.

This procedure is applied to various bins of E_{T}^{γ} and a function is fitted. The result can be seen in figure 5.11. The parametrization of the fit-function is

$$p_{\text{fake}} = a + \frac{b}{(E_{\text{T}}^{\gamma}/\,\text{GeV})^{c}} \tag{5.3}$$

with $a = -1.3 \cdot 10^{-2}$, $b = 1.04$ and $c = 0.77$. The plot also shows a systematic uncertainty of 54% that is applied to the fake-rate prediction. There are two main contributions to this systematic uncertainty. An uncertainty of 45% is observed when varying the definition of the sideband borders. Additional 30% come from differences between quark- and gluon jets that do not have a common probability to fake a photon [132, 133]. Adding both uncertainties in quadrature leads to the referenced value of 54%.

Several cross checks are performed to verify the procedure and its prediction. First of all, the fake-rate is applied to a MC-sample and the prediction of faked photons is compared to the true amount of fakes that can be determined relying on generator information. Additionally, the fake-rate itself is determined from a multijet MC-sample and compared to the measurement from data. All cross checks show a good agreement [132]. In plots and tables of the Run I analysis, contributions from the faked photon estimation are summarized as "γ misID".

5.5.2 Run II: Fake-Identification by MVA

For the Run II analysis, a different approach is needed, as, by using the MVA-based photon identification, the sideband regions that were described in the section before, cannot be defined. The method that is used in Run II was developed within CMS. It is here summarized from [130], and its implications on the presented $\mu\mu\gamma$-analysis are shown. It is also used in the differential γ + Jet cross section measurement of CMS [134]. However it will be shown

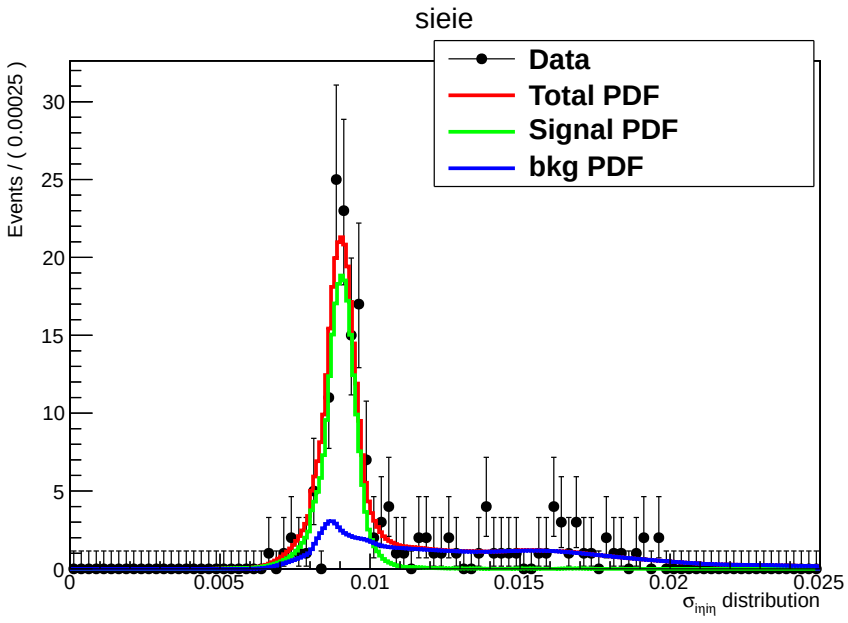

Figure 5.10: Template fit in the bin 35 GeV $< E_{\mathrm{T}}^{\gamma} <$ 50 GeV. Data are the black points, the signal of prompt photons (green) is estimated from MC. The background (blue) is from non-prompt photons estimated from a sideband of the charged hadron isolation. Taken from [132].

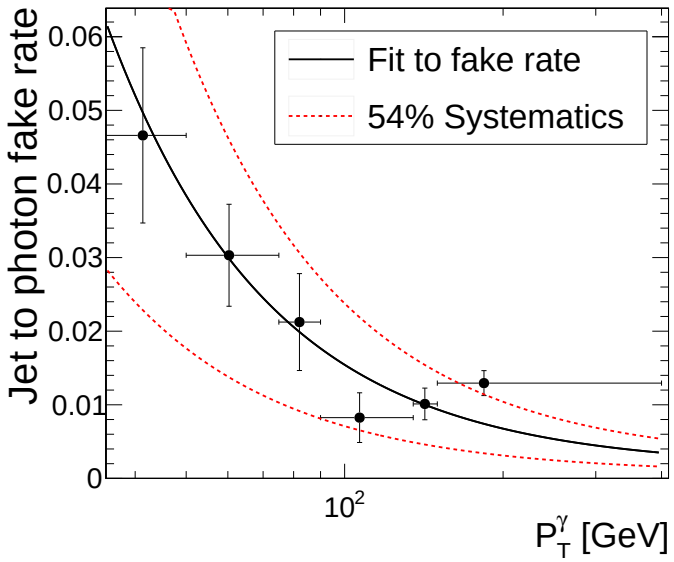

Figure 5.11: Result of the photon misidentification rate in terms of E_{T}^{γ}. Also, a fit to the points and the 54% systematic uncertainty is shown. Taken from [132].

Cut Variable	value
H/E	< 0.08
$\sigma_{i\eta i\eta}$	< 0.012
I_{pho}	< 15 GeV
Worst charged PF Iso	< 15 GeV

Table 5.4: Criteria of the very loose photon preselection (ECAL barrel only). The "worst charged PF Iso" is the worst charged hadron isolation computed with respect to all reconstructed vertices. "Standard" PF-isolations refer only to the primary vertex.

that in case of an analysis of 2015 Run II data, the full-MC approach delivers more reliable results.

Differently to Run I, a fake ratio is defined and measured in data. This time, the discriminating variable that distinguishes between "loose" and "tight" photons is the BDT score $S^{\gamma}_{\text{BDT}} = 0.4$ (compare equation 4.4). With that, the fake ratio is defined as

$$r_{\text{fake}} = \frac{\text{Fakes}(S^{\gamma}_{\text{BDT}} > 0.4)}{S^{\gamma}_{\text{BDT}} < 0.4}. \tag{5.4}$$

A corresponding example distribution from the bin $40\,\text{GeV} < E^{\gamma}_{\text{T}} < 60\,\text{GeV}$ with various contribution is represented in figure 5.12. It shows the S^{γ}_{BDT}-distribution of photons fulfilling a very loose preselection, as described in table 5.4.

Various contributions can be seen. The BDT-distribution of measured data is represented by black dots. A signal sample to study the behavior of prompt photons is shown as a blue line. This contribution is estimated from MC. The red background shows the contribution from faked photons and is estimated from W+Jets events from data. To do so, muons and E^{miss}_{T} from leptonic W-decays are used as tag. Contributions from Wγ-events are subtracted from that sample, relying on MC. Both, the background and the signal sample, are fitted to the data using a binned maximum likelihood technique. The result is shown as a black line. The fake ratio is calculated in bins of E^{γ}_{T} by dividing the number of fakes with $S^{\gamma}_{\text{BDT}} > 0.4$ by the total number in the region $S^{\gamma}_{\text{BDT}} < 0.4$, i.e., with the color-coding matching to figure 5.12

$$p_{\text{fake}} = \frac{\text{Background}(S^{\gamma}_{\text{BDT}} > 0.4)}{(\text{Signal} + \text{Background})(S^{\gamma}_{\text{BDT}} < 0.4)}. \tag{5.5}$$

The result of the measurement of p_{fake}, including statistical uncertainties from the fit and systematic uncertainties, is summarized in table 5.5. In contrast to the falling distribution obtained in the template approach from Run I, the values are flat around 10% with large systematic uncertainties reaching relative values from 30% up to more than 200%.

The systematic uncertainties are estimated by replacing the data driven background sample by simulated W+Jets and γ+Jets samples on the one hand, and varying the cross section of the Wγ by $\pm 15\%$ on the other hand. All single contributions are added in quadrature.

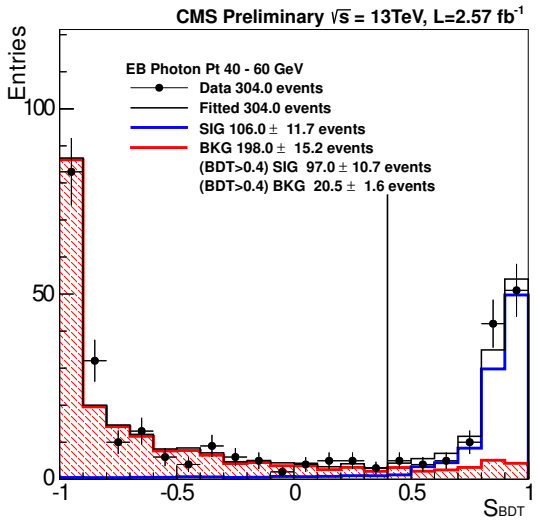

Figure 5.12: Output of the BDT score of preselected photons $S^{\gamma}_{\mathrm{BDT}}$ in the bin $40\,\mathrm{GeV} < E^{\gamma}_{\mathrm{T}} < 60\,\mathrm{GeV}$. Various contributions are shown. Black dots: Outcome from the data. Blue "Signal": True photons estimated from a Wγ-sample simulated with Pythia. Red "Background": Contribution from faked photons, estimated from a W+Jets sample from data, where the lepton is used to tag the events. Black line: Fit of "SIG"+"BKG" to data. Adapted from [130].

E^{γ}_{T}-range (GeV)	$r_{\mathrm{fake}} \pm \mathrm{stat.} \pm \mathrm{syst.}$ (%)
$35 - 40$	$10.1 \pm 1.5 \pm 4.0$
$40 - 60$	$11.0 \pm 1.2 \pm 3.2$
$60 - 90$	$8.7 \pm 1.5 \pm 5.0$
$90 - 120$	$10.8 \pm 3.5 \pm 4.9$
$120 - 500$	$3.6 \pm 1.2 \pm 8.5$

Table 5.5: Photon fake ratio in bins of E^{γ}_{T}. Adapted from [130].

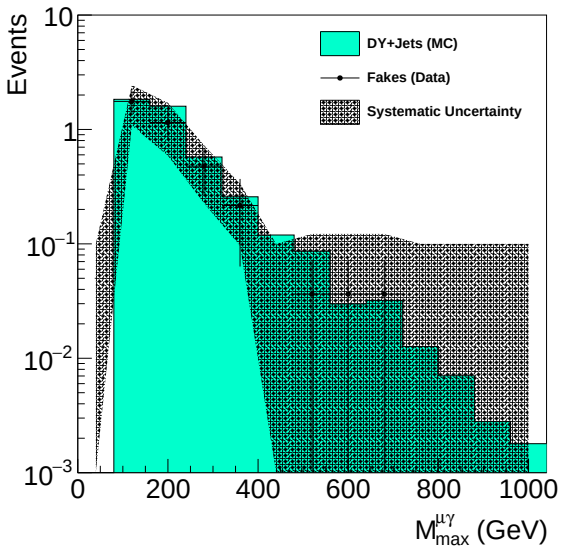

Figure 5.13: Comparison of the data driven description of backgrounds with a faked photon (black dots) with the simulated Drell-Yan background (colored area). The hatched area represents the systematic uncertainty on the fake prediction from data. Empty bins have an assigned systematic uncertainty of 0.1 events.

Figure 5.13 shows the comparison of the resulting fake prediction with the one from Drell-Yan plus jets that is estimated from MC. The data driven background is shown by black points with statistical uncertainties given by the vertical black line. The hatched uncertainty band represents the systematic uncertainty on p_{fake} as given in table 5.5. Empty bins with no entry from data have an additional systematic uncertainty of 0.1 events assigned, which approximately corresponds to the prediction of one single event. The plot illustrates why the approach that is based on simulation is a more appropriate choice for the Run II analysis. The prediction that is estimated from data is based on 39 events that cover an invariant mass range below 700 GeV. The DY+Jets simulation, on the other hand, reaches into the multi-TeV range with thousands of simulated events. Thus, the MC approach is used for further analysis, applying an additional cross section uncertainty of 50% on contributions from misidentified photons, based on the experiences from this study.

5.6 Top-Quark Pair Production $(t\bar{t})$

Another potential source of background contribution comes from the pair-production of top quarks. Similarly to the Drell-Yan process, there are two different sources of reconstructed photons possible. Either the photon is a prompt one, coming directly from the hard interaction, or it is a misidentified or non-prompt photon being related to a jet.

For the first case, both analyses rely on dedicated $t\bar{t}\gamma$-samples that are generated with Madgraph. Those are inclusive samples, meaning all possible top-quark decays are considered, i.e. hadronic and leptonic ones. From those, only such that decay fully leptonically into two muons will end up in the final selection.

Events from $t\bar{t}$-processes with a non-prompt photon are treated differently in the two analyses. In Run I, those events are part of the contribution determined by the template method

(section 5.5.1). The analysis of Run II relies on a sample generated with Powheg that contains only fully leptonic decays of the top-quark pairs. Possible events with a prompt photon are removed from the sample in order to avoid a double counting with the $t\bar{t}\gamma$-sample.

5.7 Others

Other backgrounds have a much smaller contribution. Diboson samples (WW, WZ, ZZ), simulated with Pythia are added to both analyses. More backgrounds have been tested for possible contributions (e.g. $W\gamma$ or processes with Higgs-decays like $H \rightarrow Z\gamma$) but no impact was found. Thus, the latter ones are not considered.

The $W\gamma$-process also opens the question for contributions with non-prompt or misidentified muons being faked by jets. Such contributions are not taken into account here as they are expected to be of a negligible level. This assumption is justified by two considerations. On the one hand, as mentioned before, the simulations of respective backgrounds like $W\gamma$+jets do not contribute to the selection. On the other hand, the probability to select a misidentified muon is known to be much lower than the one to select a misidentified photon because of the clear signature in the muon system. It is even lower than the corresponding probability for a misidentified electron. Respective numbers can e.g. be found by comparing tables 2 and 3 of reference [85], where the contributions from misidentified electrons are about one order of magnitude larger than those from muons. Backgrounds from mis-reconstructed electrons are estimated in the $ee\gamma$-channel of the searches for excited leptons. Their contributions are a bit lower than those of the mis-reconstructed photons, which are already minor (3-5% of the total background yield) [3, 4]. Given that, it can be assumed that events from misidentified muons only contribute at the sub-percent level to the total background.

5.8 Summary: Background Composition and Z-Veto

In this chapter it was described how the single background contributions were obtained. Before going into detail about the statistical interpretation of the results in the next chapter, this section will summarize and compare the single contributions that are used for the results.

For Run I, a mixed background prediction is used. Contributions from faked photons are estimated from data, as described in section 5.5.1 and are labeled as "γ misID" in the corresponding plots. All other backgrounds with prompt photons are estimated from MC, exclusively. Table 5.6 summarizes the single event yields, including the corresponding systematic uncertainties.

In Run II, the final composition is estimated from MC, exclusively. For comparison, the simulation of backgrounds with misidentified photons was compared to a data driven approach, as described in section 5.5.2. The single background contributions of the Run II analysis are summarized in table 5.7. The distributions of the maximum- and minimum invariant masses ($M^{\mu\gamma}_{min}$ & $M^{\mu\gamma}_{max}$) are shown in figure 5.14 for both analyses.

	Events	±stat.	±syst.
$Z\gamma$	762.6	±14.9	±89.2
$t\bar{t}\gamma$	12.7	±2.2	±1.4
γ misID	66.3	±1.5	±35.8
WW	0.14	±0.13	±0.02
WZ	3.7	±0.4	±0.5
ZZ	6.3	±0.5	±0.7
Total BG	**851.7**	**±15.2**	**±98.5**
Data	**976**		

Table 5.6: Summary **Run I**: Event yields of single background contributions with systematic and statistical uncertainties, after the selection of two muons and one photon.

	Events	±stat.	±syst.
$Z\gamma$	188.3	±4.5	±20.2
$Z\gamma(E_{\mathrm{T}}^{\gamma} > 130\,\mathrm{GeV})$	23.9	±0.2	±2.8
$t\bar{t}\gamma$	2.6	±0.1	±0.1
$t\bar{t}$	8.3	±0.6	±4.1
DY+Jets	78.2	±11.3	±39.3
WZ	5.2	±0.8	±0.3
ZZ	2.7	±0.3	±0.1
Total BG	**309.4**	**±12.3**	**±49.9**
Data	**325**		

Table 5.7: Summary **Run II**: Event yields of single background contributions with systematic and statistical uncertainties, after the selection of two muons and one photon.

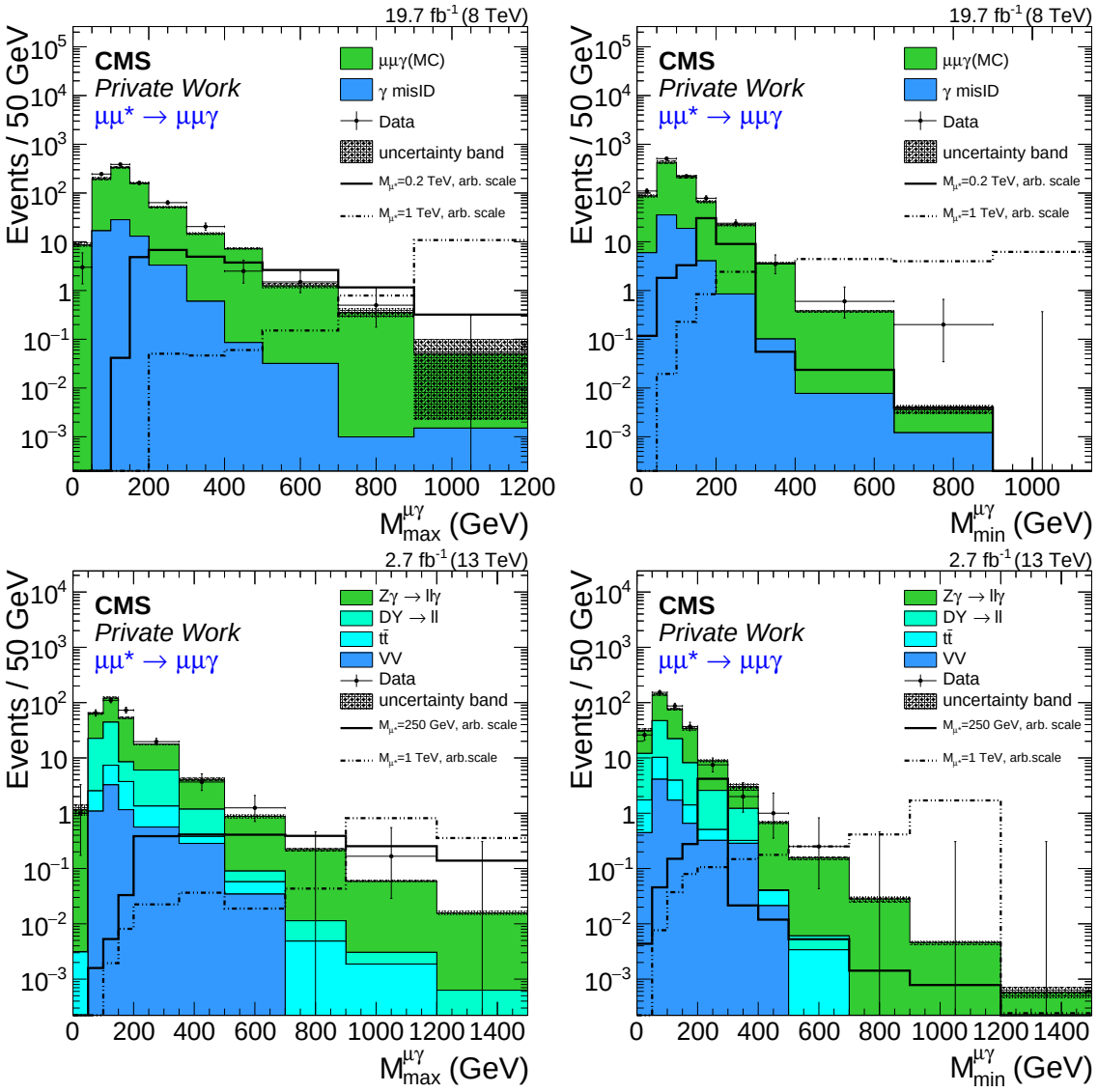

Figure 5.14: Distributions of the masses $M^{\mu\gamma}_{max}$ (left) and $M^{\mu\gamma}_{min}$ (right) of the Run I (top) and Run II (bottom) analyses after the selection of two muons and one photon.

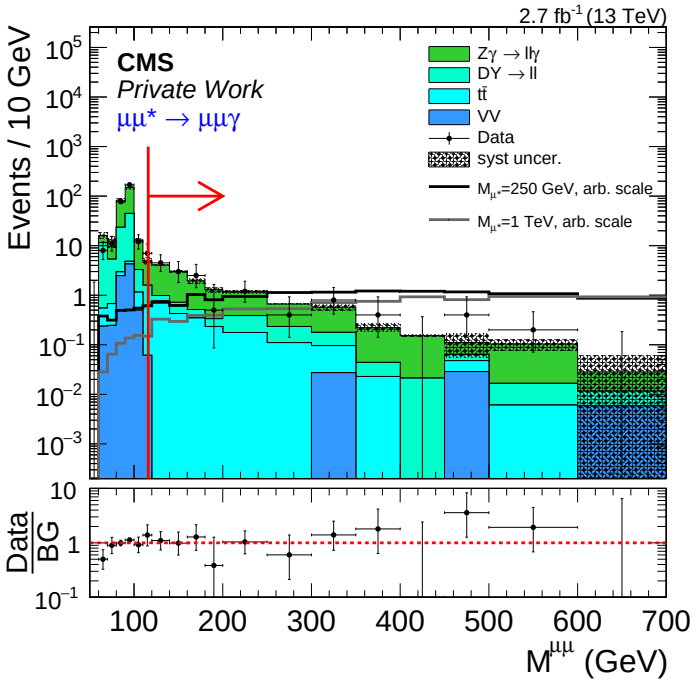

Figure 5.15: Invariant dimuon mass distribution of the Run II analysis showing the Z-veto, which is the requirement of $M^{\mu\mu} > M^{Z} + 25\,\text{GeV}$. Only events in the region marked by the red arrow are considered for further analysis.

The presence of a resonant Z-boson in the main Zγ-background provides a discriminating variable to distinguish between background and the excited muon signal. By requiring that the dimuon invariant mass $M^{\mu\mu}$ exceeds the nominal Z-mass by 25 GeV, the dominating background is effectively removed, while the signal is almost unaffected. This is exemplary shown in figure 5.15. The impact on the event yields is given in tables 5.8 & 5.9. The corresponding distributions of $M^{\mu\gamma}_{\text{min}}$ and $M^{\mu\gamma}_{\text{max}}$ are shown in figure 5.16.

The impact of this cut on the total signal selection efficiency is shown in figure 5.17. Therein, the impact of the Z-veto on top of the selections that are also presented in figure 4.11, is plotted. It can be seen that aside from a very small, acceptable loss at very low μ^*-masses, the signal efficiency is not affected.

Overall, before the Z-veto and after it, a good agreement between the measurement and the Standard Model expectation is observed. A slight over-fluctuation in the Run I analysis is still well compatible within the uncertainties. More detailed studies about the statistical interpretation of the results follow in the next chapter.

	Events	±stat.	±syst.
$Z\gamma$	106.0	±5.6	±12.5
$t\bar{t}\gamma$	8.2	±1.8	±0.9
γ misID	3.9	±0.3	±2.1
WW	0.14	±0.13	±0.02
WZ	0.14	±0.08	±0.02
ZZ	0.55	±0.16	±0.06
Total BG	**118.9**	**±5.9**	**±13.5**
Data	**150**		

Table 5.8: Summary **Run I**: Event yields of single background contributions with systematic and statistical uncertainties, after the selection of two muons and one photon, as well as the additional Z-veto.

	Events	±stat.	±syst
$Z\gamma$	25.1	±1.7	±2.7
$Z\gamma(E_{\mathrm{T}}^{\gamma} > 130\,\mathrm{GeV})$	3.0	±0.6	±0.4
$t\bar{t}\gamma$	2.0	±0.1	±0.1
$t\bar{t}$	5.5	±0.5	±2.8
DY+Jets	4.6	±1.8	±2.4
WZ	0.28	±0.18	±0.02
ZZ	0.053	±0.045	±0.006
Total BG	**40.5**	**±2.6**	**±6.0**
Data	**41**		

Table 5.9: Summary **Run II**: Event yields of single background contributions with systematic and statistical uncertainties, after the selection of two muons and one photon, as well as the additional Z-veto.

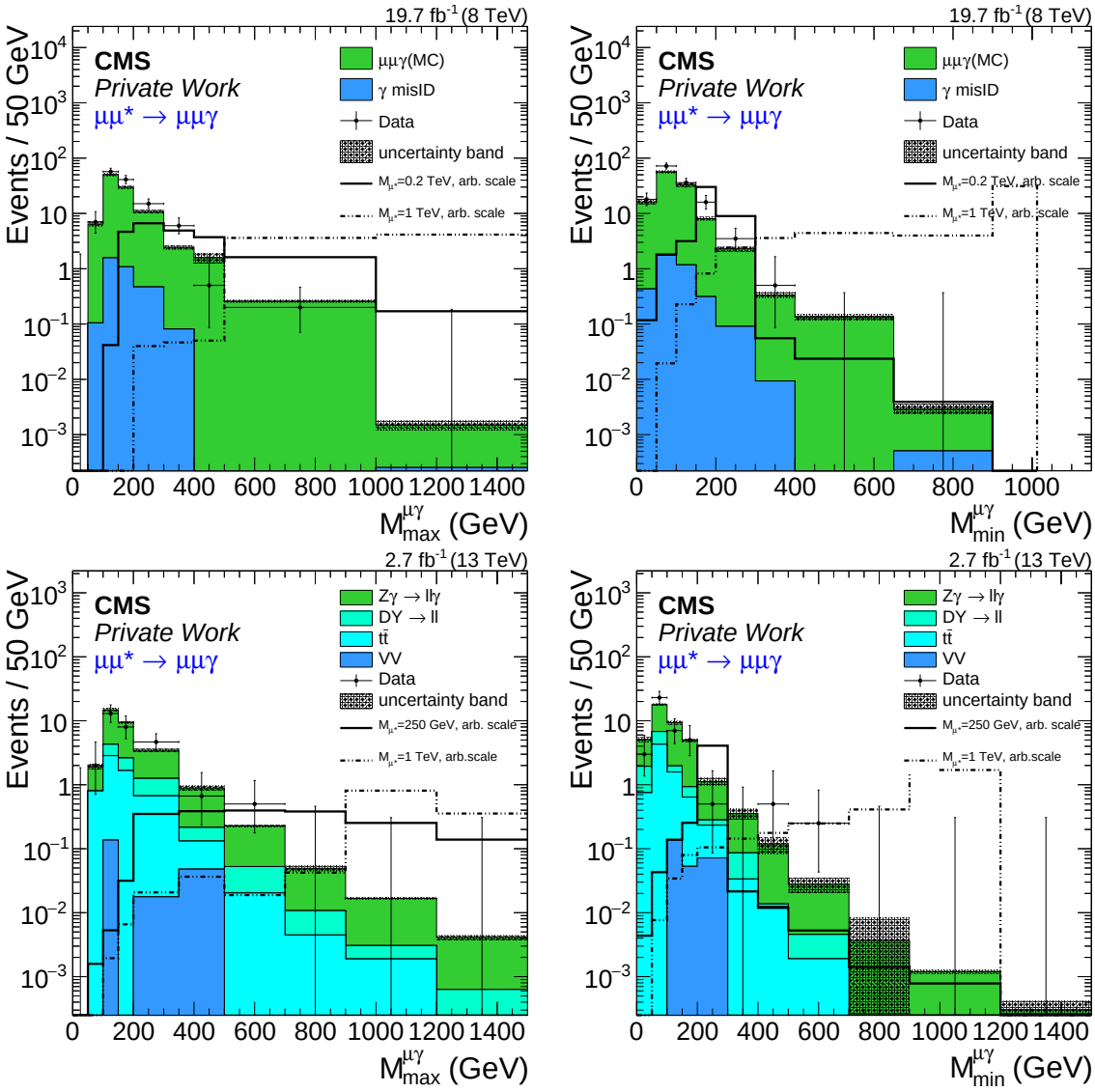

Figure 5.16: Distributions of the masses $M^{\mu\gamma}_{max}$ (left) and $M^{\mu\gamma}_{min}$ (right) of the Run I (top) and Run II (bottom) analyses after the selection of two muons and one photon, as well as the additional Z-veto.

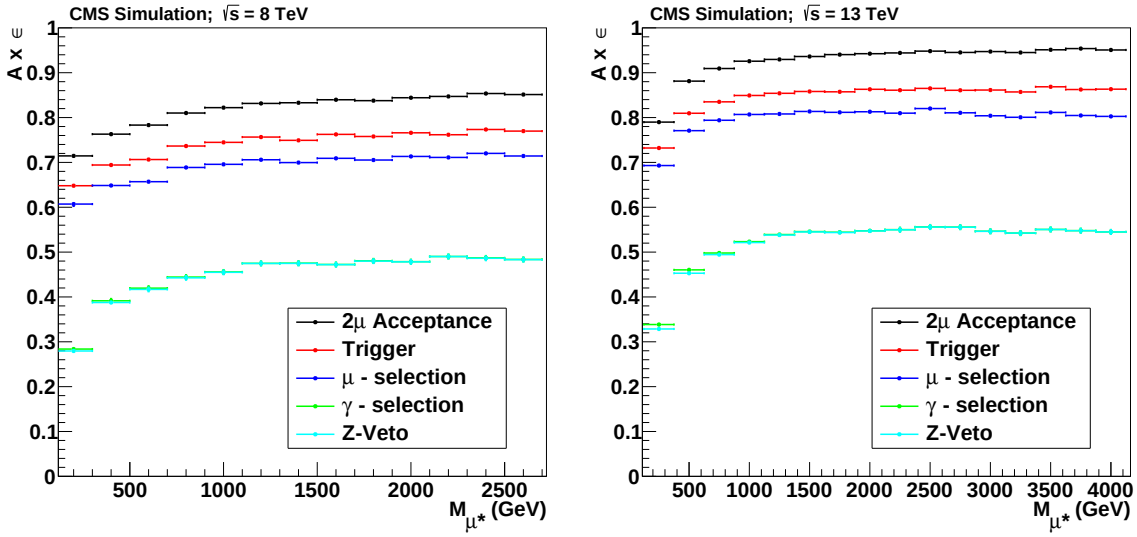

Figure 5.17: Total signal selection efficiency after various requirements on analysis level (after reconstruction) for both analyses: After selecting two reconstructed muons within the kinematic range, the requirement of the trigger, after applying the quality cuts on both muons, after selecting an additional photon with the respective ID, and the negligible impact of the Z-veto.

6 | Results

Properties of the excited muon signal are examined in chapter 2. The modeling of the Standard Model background is described in chapter 5. There, by comparing with the measured data, no significant excess of data could be observed. In order to further examine the results for a possible hidden excited muon signal, a final set of selections is applied making use of the "L-shape" behavior of the signal (compare section 2.6.2). Details about the measured and expected event contents after this final selection are given, including a discussion about systematic uncertainties.

In order to quantify the agreement of expectation and measurement within these regions, and to exclude part of the parameter space of the theoretical setup ($\Lambda - M_{\mu^*}$), exclusion limits are calculated with dedicated statistical methods that are introduced in the following section.

How the final selection is chosen is explained in this chapter, and the results that are obtained in the form of limits are presented for both analyses. To exclude even broader regions of the possible parameter space, the limits of both analyses are combined.

As, in context of corresponding publications [2, 3], limits in various channels, including such from e^*-searches were obtained by the author, these are also presented in this chapter. However, as only the input by other analysts from the CMS ℓ^*-group was used, details of the other analyses themselves will not be given in this thesis. Interested readers are referred to the given documentation.

6.1 Limit Calculation Procedures

A limit can be calculated to compare a so-called "null-hypothesis", $\mathcal{H}^0$, i.e. the Standard Model background expectation, with a signal hypothesis $\mathcal{H}^1$. The aim is to exclude a certain model-parameter of interest, θ. This is often a signal cross section, but can also be in terms of coupling strengths, energy scales, or any other parameter of interest.

In high energy physics, two methods are broadly used in order to determine exclusion limits, the *Bayesian* and the *frequentist* approach. For both, a large variety of publications can be found. Aside from the wrap-up in [6], a comprehensive summary, also mentioning the philosophical dispute between supporters of both approaches, can be found in reference [135]. A comprehensive introduction into statistical data analysis is given in [136].

The results of both approaches are usually very comparable, no matter which method is chosen. However, the meaning of the results, and thus their interpretation, is different. In Bayesian statistics, results are interpreted as probability of the true, unknown value of interest, θ, to lie inside a certain interval. On the other hand, in the frequentist method, a confidence interval is defined that should include θ. As in this case, the confidence interval itself is a probability, and a defined fraction of repeatedly performed experiments, x, is supposed to contain θ in their confidence intervals. Both approaches, including an approximation for the frequentist CL_s-method, are introduced in the following sections.

Results in this thesis are obtained using the Bayesian approach. However, as this is very computing intensive, the optimization of specific search regions is done using the simple and

fast asymptotic CL_s-method. With respect to the number of channels that were considered in the Run I analysis, and the huge amount of mass points that need to be optimized, using the full Bayesian (or frequentist) approach is not practical.

6.1.1 The Bayesian Approach

The Bayesian approach

$$p(\mathcal{H}|x) = \frac{\mathcal{L}(x|\mathcal{H}) \times \pi(\mathcal{H})}{\int \mathcal{L}(x|\mathcal{H}')\pi(\mathcal{H}')d\mathcal{H}'}, \tag{6.1}$$

based on Bayes' theorem [137], transfers the likelihood $\mathcal{L}$, of a certain observation x, given hypothesis $\mathcal{H}$, into the posterior probability density $p(\mathcal{H}|x)$ that the hypothesis is true under the observation. Thereby, $\pi(\mathcal{H})$ is the prior probability density function of $\mathcal{H}$. The denominator is needed to normalize the probability to unity using all possible hypotheses $\mathcal{H}'$ [6]. Thus the Bayesian method takes into account the prior modeling of the hypothesis under consideration.

Following the review in [6], applied to the model parameter θ, and with additional so-called nuisance parameters, ν, that usually represent systematic uncertainties, equation 6.1 becomes

$$p(\theta, \nu|x) = \frac{\mathcal{L}(x|\theta) \times \pi(\theta) \times \pi(\nu)}{\int \mathcal{L}(x|\theta')\pi(\theta') \times \pi(\nu')d\theta'}. \tag{6.2}$$

In order to obtain a posterior probability that is independent of the nuisance parameter(s), they are integrated:

$$p(\theta|x) = \frac{\int \mathcal{L}(x|\theta) \times \pi(\theta) \times \pi(\nu)d\nu}{\int\int \mathcal{L}(x|\theta')\pi(\theta') \times \pi(\nu')d\theta' d\nu'}. \tag{6.3}$$

This can e.g. be achieved by using the Markov Chain Monte Carlo Method.

To determine regions of a certain posterior probability, the density $p(\theta|x)$ is integrated:

$$1 - \alpha = \int_{\theta_{\mathrm{down}}}^{\theta_{\mathrm{up}}} p(\theta|x)d\theta \tag{6.4}$$

For non-negative parameters (e.g. a signal cross section), this integration is performed from $\theta_{\mathrm{down}} = 0$. The probability that is usually assigned to define an exclusion is 95%. That means, equation 6.4 has to be solved for that value of θ_{up}, where $\alpha = 0.05$.

The difficult, and usually not well motivated issue of the Bayesian method is the choice of the proper functional form of the prior(s). It is a common procedure to rely on a flat prior for the parameter of interest, θ. This choice is based on the "principle of insufficient reason", as described in [138]. This is also done to obtain the results in this thesis (for $\theta > 0$).

The priors of nuisance parameters have different functional forms, depending on the systematic uncertainty they represent. Usual choices are normal, log-normal, and gamma functions. The exact choice is explained later. In general, functions that do not have negative contributions are preferred over e.g. a Gaussian that is artificially truncated at zero.

6.1.2 The Frequentist CL_s Method

Another approach for statistical interpretation of hypotheses is the modified frequentist CL_s-method [139–141]. Thereby, CL_s, defined as

$$CL_s = \frac{CL_{s+b}}{CL_b}, \tag{6.5}$$

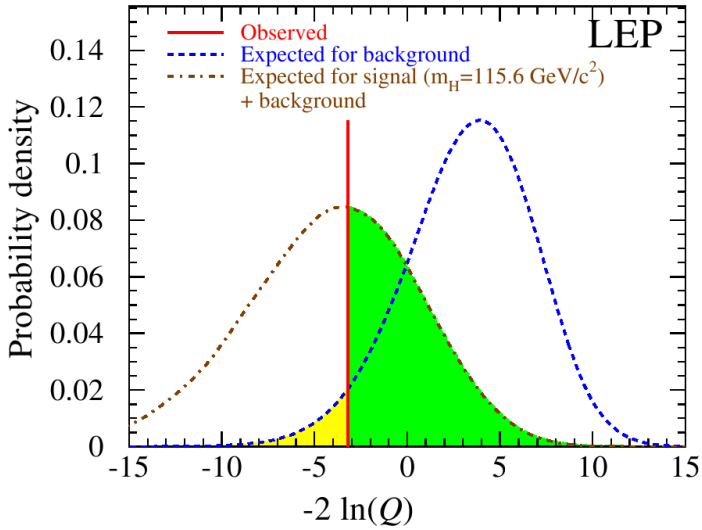

Figure 6.1: Distributions of the test statistic ($-2\ln(Q)$) for b (dashed blue), s+b (dashed-dotted), and the observation (solid red). Taken from [139].

is excluded by a certain confidence level (CL, e.g. CL = 0.95 for a 95% exclusion), if

$$1 - \mathrm{CL_s} \leq \mathrm{CL}. \tag{6.6}$$

In this case, the true value of the parameter of interest, θ, is assumed to be contained within the confidence interval with a 95% chance. The indices "b" and "s" refer to the background only hypothesis ($\mathcal{H}^0$), and the signal hypothesis ($\mathcal{H}^1$), respectively.

$\mathrm{CL_s}$ is called a modified approach, as it is the ratio of two likelihoods. Each of them is defined by ($x = \mathrm{s} + \mathrm{b}, \mathrm{b}$):

$$\mathrm{CL}_x = p_x(Q \leq Q_{\mathrm{obs}}) = \int_{-\infty}^{Q_{\mathrm{obs}}} p(Q|\theta_x)dQ \tag{6.7}$$

Thereby, $p(Q|\theta_x)$ is the probability density of test statistic Q, that is obtained by dicing pseudo-experiments. An example is shown in figure 6.1. There, the probability density is plotted as a function of Q. The dashed blue line thereby corresponds to the background hypothesis, the dashed-dotted line to the signal-plus-background hypothesis, while the actual observation is given by a solid red line. In this example, $\mathrm{CL_b}$ is defined by the blue curve being integrated from infinity to the observation, i.e. its area without the yellow part. Correspondingly, $\mathrm{CL_{s+b}}$ is given by the green area.

The test statistic, Q is a likelihood ratio. There are different possibilities how the Q can be constructed. In the "classic" variant that was used in LEP times, Q is defined as:

$$Q = \frac{\mathcal{L}(x|\mathrm{s}+\mathrm{b})}{\mathcal{L}(x|\mathrm{b})}. \tag{6.8}$$

Nowadays, a "profile likelihood" is used (now including nuisance parameters, ν):

$$Q = \frac{\mathcal{L}(x|\theta, \hat{\nu})}{\mathcal{L}(x|\hat{\theta}, \hat{\nu})}. \tag{6.9}$$

Thereby, $\hat{\theta}$ and $\hat{\nu}$ are those values of θ and ν that maximize the likelihood. Correspondingly, $\hat{\hat{\nu}}$ is the value of ν that maximizes the likelihood under a given θ [142]. The likelihoods themselves are Poisson distributions that are convoluted with the pdf of the nuisance parameters.

The Asymptotic Approximation

Dicing out the pseudo experiments for the test statistic of the CL_s-method can be extremely computing intensive. This can be evaded by parameterizing the likelihood ratio with a known function. Such an ansatz is summarized in [142] being based on work by Wilks [143] and Wald [144].

The basic idea is, as shown in the latter reference, that the likelihood ratio can be approximated by

$$t_\mu = -2\ln(Q) \approx \frac{(\mu - \hat{\mu})^2}{\sigma^2} + \mathcal{O}(1/\sqrt{N}), \tag{6.10}$$

for a signal strength parameter $\mu(\theta)$ that determines the expectation of a measurement

$$E = \mu s + b. \tag{6.11}$$

Thereby, $\hat{\mu} = \mu(\hat{\theta})$ is Gaussian distributed and has the mean μ' and the width σ. If the term $\mathcal{O}(1/\sqrt{N})$ is neglected, t_μ can be described by a non-central chi-square distribution with one degree of freedom. Its non-centrality parameter is then given by

$$\Lambda = \frac{(\mu - \mu')^2}{\sigma^2}. \tag{6.12}$$

The width, σ, can be determined either by the "Asimov" dataset, or the Fischer information matrix [142]. Relying on that, the likelihood ratio can quickly and easily be calculated. However, this approach is an approximation and thus not valid in all cases. Especially for very small numbers of events, the deviation from the full MC-based CL_s-approach becomes increasingly large.

6.1.3 Technical Implementation

Here, limits are computed as single-bin counting experiments, evaluating the complete content of search regions. A multi-bin approach is in principle also possible but not practical for a search in a two-dimensional parameter space, as will be done here. This would lead to a high amount of bins that make the calculation very computing intensive.

The presented final results are calculated using a Bayesian approach. However, due to the amount of necessary calculations, the optimization of search regions, that is presented in the following section, is based on the fast and simple asymptotic CL_s-approximation.

As signal estimator, the expected signal yield at $\Lambda = 10\,\text{TeV}$ and the respective luminosity is used. Expected limits are estimated by dicing pseudo experiments. Their exact number varies, depending on the bin content, but is of $\mathcal{O}(10^4)$. The computation is executed with the help of the HiggsCombine package [145, 146] that makes use of RooStats [147] and is developed and provided from the context of CMS Higgs searches.

6.2 Final Selection: L-Shapes

Properties of a possible excited lepton signal are discussed in section 2.6. There, it is shown that due to the associated production of an excited muon together with an ordinary muon, the excited muon mass, M_{μ^*}, cannot easily be determined from the final state. It is also shown that this can be resolved by calculating the two possible muon-photon invariant masses, sort

them depending on their mass into $M_{min}^{\mu\gamma}$ and $M_{max}^{\mu\gamma}$, and plot both in a two dimensional plane. This results in a typical signal distribution that has the shape of an inverted "L", here simply referred to as "L-shape". An example can be found in figure 6.2. There, the two-dimensional $M_{min}^{\mu\gamma}$-$M_{max}^{\mu\gamma}$ distributions after all cuts, including the Z-veto, are shown for background, data, and two example signal points, for both the Run I and Run II analyses.

Figure 6.2 also illustrates how the Standard Model background behaves in this two dimensional representation. It clusters at values of low $M_{min}^{\mu\gamma}$ and $M_{max}^{\mu\gamma}$ and does not at all follow the signal behavior. Measured data is found to be distributed similarly. This interesting L-shape behavior can be used to further distinguish between signal and background by applying a final set of selections in this particular parameter space. Especially for low μ^*-masses, where the signal's L-shape is overlain by the background, a well-chosen selection in the two-dimensional space promises a good separation between a possible signal and the Standard Model background.

6.2.1 Search Region Optimization

The idea is to model search regions around each considered signal mass point that follow the L-shape behavior. These L-shaped search regions need to balance between a good background rejection, while, at the same time, a good signal selection efficiency needs to be preserved. Thus, it is not feasible to use search regions of one constant width. Instead, the widths of the search regions are variable depending on the excited muon mass, in order to account for individual mass resolutions and intrinsic widths of the signal. Here, the search regions are modeled centrally around each mass point with an individually optimized width.

This approach is outlined in figure 6.3. There, search regions of two exemplary signal masses, M_1 and M_2, are sketched in red and green. Generated masses would thereby be centrally in the regions, as indicated by the dashed white line in the green example. Both L-shapes have an individual width that needs to be determined by an optimization procedure.

In many searches for physics beyond the Standard Model, selections are optimized with respect to the best expected significance. Thus, it is guaranteed that the selection is optimized for a possible discovery. However, in the context of the search for excited leptons, this is not useful. The reason for that is the dependence of the signal cross section on the compositeness scale parameter, Λ, and from this the dependence of the significance on Λ. Thus, the optimization would have to be done either two-dimensional in Λ and M_{μ^*}, or for a certain value of Λ. While the first choice is not applicable due to the computing effort, the latter one has its validity for the given value of Λ, exclusively.

To avoid this, here, the width of the L-shaped search regions is optimized with respect to the best (=lowest) expected cross section limit. The limit setting procedure provides an excluded cross section as result. Thus, it is not sensitive to the chosen value of Λ.

Figure 6.4 shows the outcome of this optimization procedure as done with the signal MC of the Run I analysis. For the five lowest signal points from 200 GeV to 1 TeV, the value of the expected excluded signal cross section times branching ratio is plotted that results from a certain choice of the respective L-shape width. On the x-axis, the ratio M_{cut}/M_{μ^*} is given. Thereby, M_{cut} denotes the mass corresponding to the lower edge of the considered L-shape of mass M_{μ^*} (see also the green example in figure 6.3). E.g., for the signal $M_{\mu^*} = 1\,\text{TeV}$, a ratio of $M_{cut}/M_{\mu^*} = 0.9$ refers to an L-shape with the lower edge at 900 GeV, resulting in a search region from $900 - 1100\,\text{GeV}$, or, correspondingly, in a width of 200 GeV. This representation, as given in figure 6.4 provides a good illustration of all the different masses.

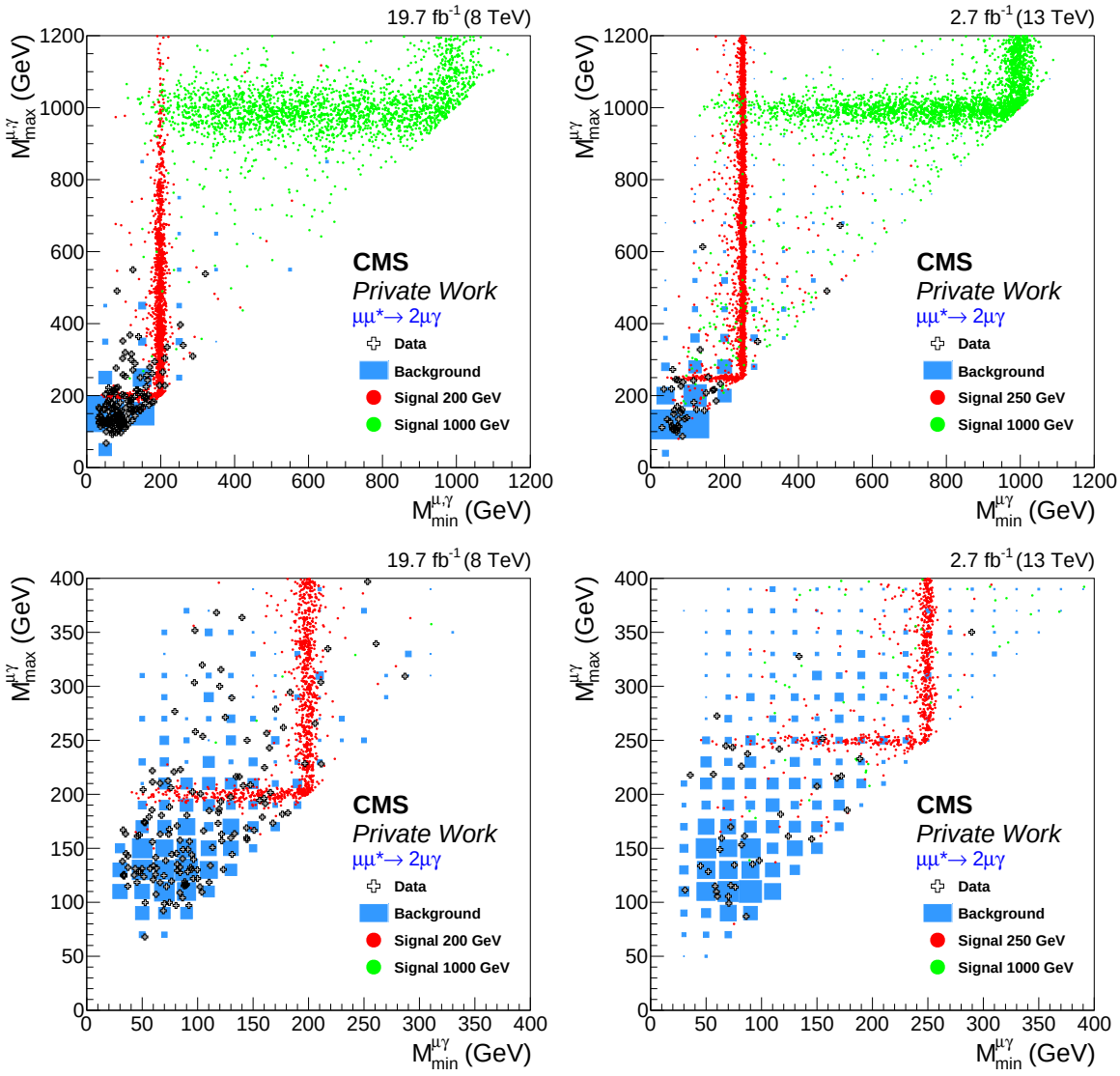

Figure 6.2: Two dimensional $M^{\mu\gamma}_{min}$-$M^{\mu\gamma}_{max}$-distributions after all cuts, including the Z-veto. Backgrounds are added up and shown in blue, various example signals are also presented. Their distributions show the typical "L-shapes". For reasons of presentational style, the signal MC has not been weighted according to cross section or luminosity. The lower plots show a zoom into the low-mass region

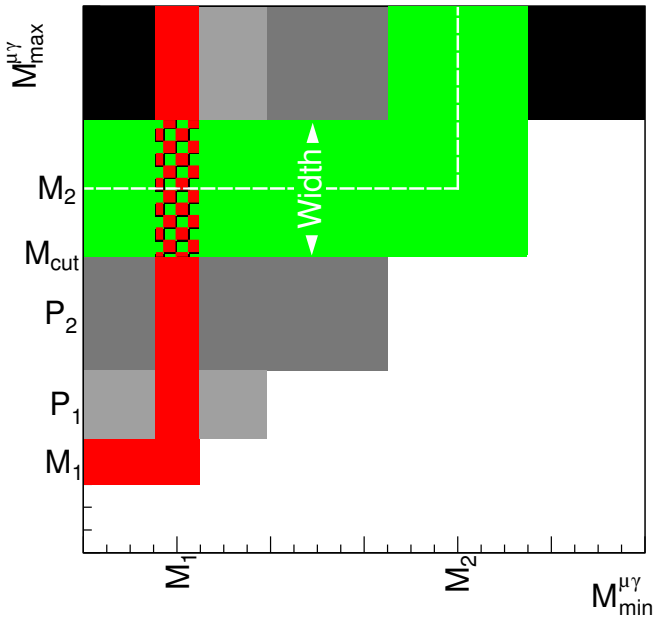

Figure 6.3: Scheme of the L-shape selection. Two windows that are optimized with signal MC at masses M_1 and M_2 are outlined in red and green. Additional interpolated windows at positions P_1 and P_2 are shown in gray.

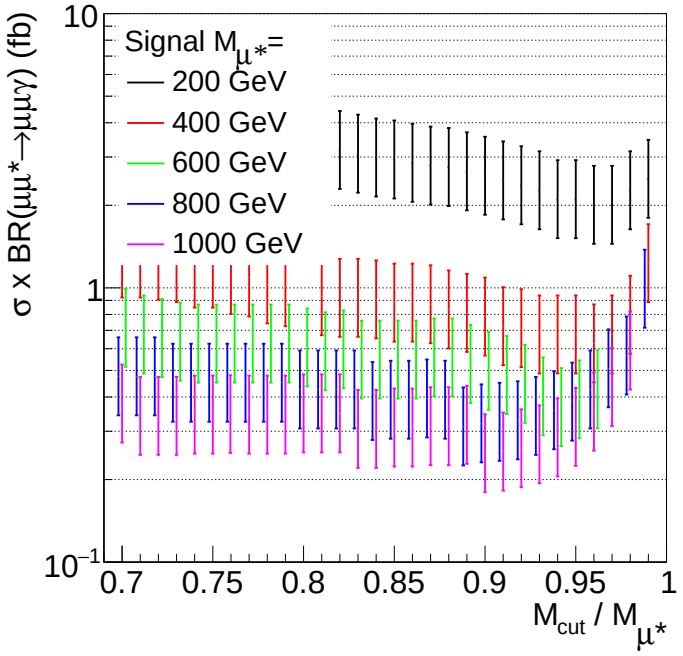

Figure 6.4: L-shape width optimization: Expected excluded signal cross section times branching ratio of different signal masses, as a function of the lower edge of the search region (compare text).

Mass (GeV)	Range (GeV)	Width (GeV)
200	194–206	12
400	384–416	32
600	564–636	72
800	720–880	160
1000	720–1280	560

Table 6.1: Mass range and corresponding width that result from the optimization of the L-shaped search windows.

With narrowing width (increasing M_{cut}), the resulting excluded cross sections tend to go down due to the better background rejection, until, at a certain point, a steep rise can be observed. This rise is caused by cutting away too much of the signal, reducing the signal selection efficiency. As optimal value for M_{cut}, the one is chosen, where the different distributions have their minimum. The outcome is summarized in table 6.1. With rising signal mass, the change from widening the windows becomes more and more irrelevant, as the background contributions become negligible. This is the reason why the optimization procedure is not continued to higher signal masses. In fact, for signal points of $M_{\mu^*} \geq 1\,\text{TeV}$, the search region is simply defined as $M^{\mu\gamma}_{max} > 720\,\text{GeV}$. It will be shown later on that further tightening the requirements from this point on, does not increase the sensitivity.

The width optimization is done with MC that is produced with $\Lambda = 10\,\text{TeV}$, resulting in an intrinsic width of the signal that is narrow in comparison to the mass resolution. The intrinsic width can drastically change for other values of Λ (see figure 2.5 again). A discussion about the interplay of search window width and intrinsic width is given in a later section, when the results of all different search channels are presented.

6.2.2 Interpolation of additional Search Regions

The L-shaped search regions that are found in the previous section leave large gaps in the mass space, in between the single L-shapes. In order to cover this parameter space, and to be sensitive at all signal masses, these gaps are covered by additional search windows that follow the same L-shape behavior. In the scheme of figure 6.3, the gaps are those areas that are not covered by red or green, and the additional search windows are outlined in shades of gray, that are underlain at the positions P_1 and P_2. These additional search regions are obtained by an interpolation procedure that is described in this section.

For any additional search region, the background, data, and signal content has to be determined. Needed input information from Standard Model background and measured data can be obtained by evaluating the two-dimensional $M^{\mu\gamma}_{min}$-$M^{\mu\gamma}_{max}$ distributions. The corresponding information about the excited lepton signal can be obtained by either generating additional signal Monte-Carlo samples, which is unpractical, or by relying on the knowledge from the existing MC. The latter approach is used here and is implemented as described in the following paragraphs.

First, the position (P_1 and P_2 in the example of figure 6.3, i.e. the position of the center in each gray L-shape) and width of the interpolated regions is defined. The interpolation of the

Mass (GeV)	200	209	220	232	245	260	277	296	318	343
Width (GeV)	12	14	14	16	18	18	20	22	24	28
Mass (GeV)	371	403	439	480	527	581	646	729	842	
Width (GeV)	30	34	40	48	58	70	94	130	244	

Table 6.2: Positions of the additional L-shaped search windows, and the width that is obtained from the linear interpolation. The positions are defined by the optimization in the 4e-analysis, while the width is optimized for the Run I $\mu\mu\gamma$-analysis.

width is shown in figure 6.5, which shows the window width depending on the considered signal mass. The windows that are optimized using MC, as introduced in the previous section, are thereby represented by red dots. The widths of new windows are interpolated linearly. This is shown by black crosses.

The windows' positions (x-axis position of the black crosses in figure 6.5) are defined by the optimization procedure in the $ee^* \rightarrow eeZ \rightarrow eeee$-channel. This channel has a good mass resolution, and resulting from that, narrow L-shaped signal distributions. Thus it serves as benchmark channel in order to define a common set of window positions that are used throughout the performed Run I analyses. The goal is that these most narrow search regions fill the gaps in the parameter space of the 4e-analysis consecutively without intersecting. As a result, in all other channels, including the $\mu\mu\gamma$-channels presented here, the broader windows slightly overlap.

In more detail, in the $ee^* \rightarrow eeZ \rightarrow eeee$-channel, a width optimization procedure is performed for the simulated mass samples, similar to that described in the previous section. Then, the interpolated search windows are determined in a way that consecutive windows connect, without leaving uncovered regions, and without intersecting each other. Therefore, the width is again interpolated linearly whereas the position is determined by the requirement of adjoined L-shapes. The positions obtained there, are adopted to all channels of the Run I analyses and to the Run II $\mu\mu\gamma$-analysis. All windows that are found that way, together with their corresponding width from the linear interpolation as described above, are summarized in table 6.2.

Simulated signal samples of Run II do not share all the same mass as those of Run I. In general, the final L-shape selection is adopted to the Run II analysis. Thus, to estimate the Run II width at the generated masses, the same linear interpolation is applied. It is outlined by the green dots in figure 6.5. Detailed numbers are listed in table 6.3.

With the windows defined, it is necessary to estimate the signal content of these windows. This content thereby refers to the signal cross sections and signal selection efficiencies. Signal cross sections and the corresponding k-factors are described in section 2.5, with the corresponding figures 2.7 and 2.8. Their values can thereby estimated by evaluating the fitted function at any mass of interest. The corresponding k-factors are interpolated linearly, if the needed calculation does not exist.

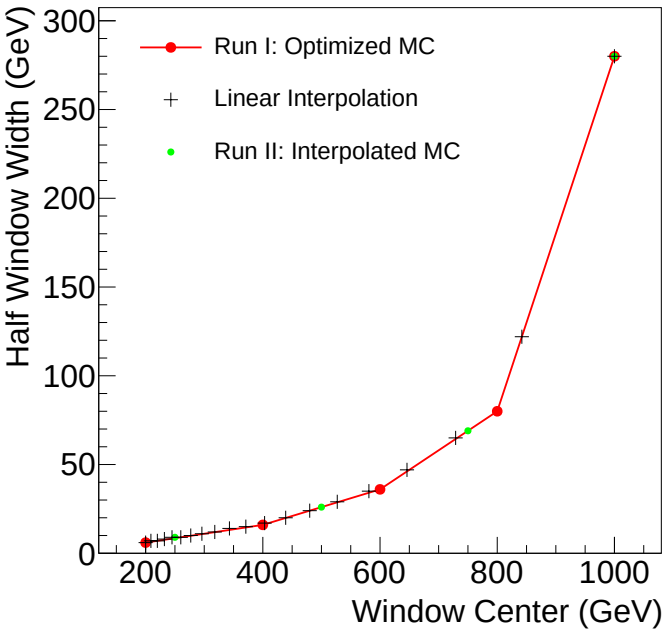

Figure 6.5: Interpolation of L-shaped search windows. Red dots: Widths optimized for the Run I MC samples. Black crosses: Linear interpolation of additional search windows. Green dots: Linear interpolation at the masses of the Run II MC samples.

Mass (GeV)	Range (GeV)	Width (GeV)
250	241–259	18
500	474–526	52
750	681–819	138
$>$ 1000	$>$ 720	–

Table 6.3: Window width at the positions of the Run II MC samples, as obtained from linear interpolation.

Parameter	Run I	Run II
p0	$-2.2 \cdot 10^6 \pm 3.4 \cdot 10^6$	$-2.6 \cdot 10^6 \pm 4.3 \cdot 10^6$
p1	$-7.1 \cdot 10^6 \pm 1.1 \cdot 10^7$	$-8.6 \cdot 10^6 \pm 1.5 \cdot 10^7$
p2	0.475 ± 0.005	0.535 ± 0.003
p3	2.52 ± 0.25	2.60 ± 0.25

Table 6.4: Values for the fit parameters that are obtained from fitting the function 6.13 to the signal efficiencies after all cuts, including the L-shape selection.

Signal efficiencies of the additional search windows are determined by a fit. This is displayed in figure 6.6, left and right for Run I and Run II, respectively. It shows, as blue markers within the considered excited lepton mass range, the signal efficiencies that are obtained after all selections, including the final L-shape windows that are given in table 6.1. The uncertainties are the evaluation of the impact of systematic uncertainties on the signal efficiency. Represented by a red line, a function of the type

$$\mathrm{A} \times \epsilon(\mathrm{M}_{\mu^*}) = \frac{\mathrm{p0}}{(\mathrm{M}_{\mu^*} / \,\mathrm{GeV})^{\mathrm{p3}} - \mathrm{p1}} + \mathrm{p2} \tag{6.13}$$

is fitted to the signal points. The obtained fit parameters are summarized in table 6.4. To perform the fit, the statistical uncertainty, based on the amount of included generated MC events is used. This uncertainty is also outlined by short, thin black lines in figure 6.6. To estimate the impact of the systematic uncertainties on the signal efficiency, the fit is repeated with pseudo-points that are shifted up- and downwards by the systematic uncertainty. Details about the latter are described in the following section. This functional form of the fit is chosen, as it is able to provide a rather steep turn-on at low masses that goes into a flat plateau. Other functions, e.g. such that are able to account for a suppression of the signal efficiency at high masses were also tested[1], but provide considerably worse fit results.

With that parametrization of the signal efficiency, all inputs are available to evaluate the content of all search windows.

6.3 Summary of the Limit-Input

After the final L-shape selection has been defined in the previous section, it is possible to summarize and evaluate the obtained observed and expected final event yields. The overall signal acceptance times efficiency of all selection steps, this time including also the L-shape selection, is shown in figure 6.7. The major impact of the final selection is at low masses, were the windows are rather narrow, in order to reject Standard Model backgrounds. At high masses, the loss of efficiency is very small.

All search windows and their content of measured data, background, and signal are summarized in tables 6.5 and 6.6 for Run I and Run II, respectively. Also, the corresponding systematic uncertainties and, for the background, the uncertainty obtained from the number of simulated events, called statistical uncertainty, is given. The latter is calculated from

[1] E.g. the interpolation used for [148] (more details in [149]) relies on such a function that follows a visible drop in the signal efficiency at high masses.

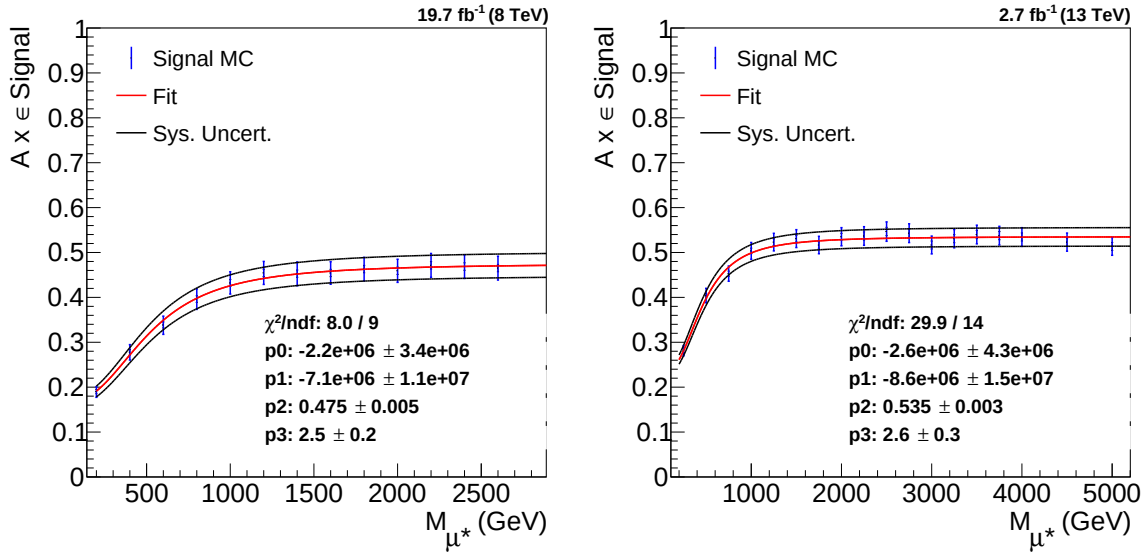

Figure 6.6: Fit to the signal efficiencies for both analyses: Signal efficiency after all cuts, including the final L-shape selection and with systematic uncertainties in blue. Fit to the efficiency as a red line, shifted fit to account for systematic uncertainties in black.

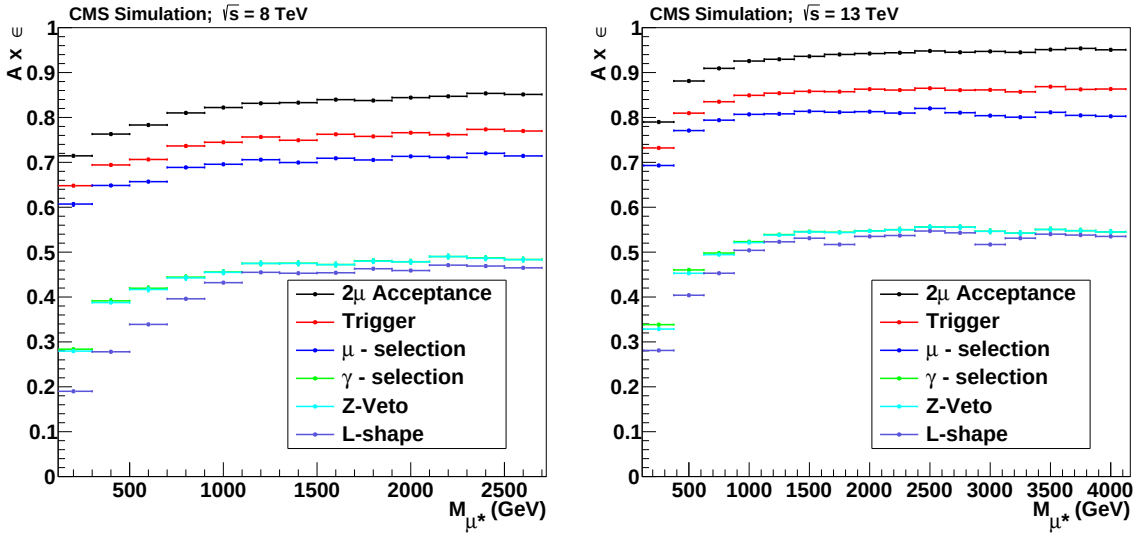

Figure 6.7: Overall signal selection efficiency after various selections for both analyses (analysis level, after reconstruction): After selecting two reconstructed muons within the acceptance, the requirement of the trigger, after applying the quality cuts on both muons, after selecting an additional photon with the respective ID, the negligible impact of the Z-veto, and after the final L-shape selection.

the square-root of the sum over all squared event weights. All contributions from different background samples are added in quadrature. Similar statistical uncertainties on the signal are not considered, as they are very small in comparison.

6.3.1 Systematic Uncertainties

The systematic and statistical uncertainties that are listed in tables 6.5 and 6.6 are another crucial input for the final limits calculation. In this section, the major ingredients, and the composition of the uncertainties as listed in the mentioned tables are summarized.

The statistical uncertainty here refers to the uncertainty that arises from the statistics, i.e. the number of events, in a given sample. The absolute statistical uncertainty is given by

$$\sigma_{\text{Stat}} = \sqrt{\sum_{\text{events}} w^2}, \tag{6.14}$$

where w refers to the weights of all included events, composed from sample-, pileup-, and other individual event weights. This can lead to rather high relative uncertainties that can even be higher than 100%, if a sample is considered that has negative contributions from NLO-calculations. In this case, negative contributions are subtracted when calculating the total event content, but add up for the uncertainty. In principle, such a statistical uncertainty can be also be estimated for the signal samples. However, due to the high selection efficiency, the statistical uncertainties are so small that they are not further considered. Statistical uncertainties are modeled by a gamma distribution as the prior. As being its conjugate prior, the gamma distribution results in a Poisson-distributed likelihood in Bayesian inference [150].

Other systematic uncertainties are summarized in table 6.7. It lists the different contributions and the input values that are used to estimate the impact of the respective uncertainty. References point to the location in this thesis, where the origin of the systematic uncertainty is explained in greater detail. A discussion of the PDF uncertainties is given in the following section.

The input values of the systematic uncertainties represent their $\pm 1\sigma$-variation. To estimate their impact, the variations are inserted into the analysis, i.e. the object momenta are shifted up- and downwards or the event weight is varied, the full selection chain is applied, and the resulting shifted final distributions are evaluated. For the final result, the change of content in the final selected L-shaped search windows is essential. Thus, there are in principle two ways how the systematic change can influence the final selection. On the one hand, by changing the event weights of the contained events. This is the case for uncertainties e.g. on cross sections, ID efficiencies, or pileup weighting. On the other hand, by event fluctuations that can happen when kinematic variables of the objects are modified, as it is the case when considering e.g. energy scales. The outcome of the latter is strongly sensitive to the shape of the distribution, the chosen binning, and event statistics of the considered sample. Thus, it can happen that a single event with a high weight enters or leaves a region with a low contribution. This would result in a high systematic uncertainty. A high statistical uncertainty is a good indicator

M_{μ^*} (GeV)	Window (GeV)	N_{Data} (Events)	$N_{BG} \pm Stat \pm Syst$ (Events)	$A \times \epsilon_{sig} \pm Syst$ (%)
200	$194 - 206$	10	$7.07 \pm 1.40\ ^{+0.81}_{-0.85}$	$19.1\ ^{+0.8}_{-1.0}$
209	$202 - 216$	14	$8.63 \pm 1.62\ ^{+1.03}_{-1.17}$	$19.4\ ^{+0.8}_{-1.0}$
220	$213 - 227$	8	$7.63 \pm 1.52\ ^{+0.92}_{-0.89}$	$19.8\ ^{+0.8}_{-1.0}$
232	$224 - 240$	3	$4.60 \pm 1.04\ ^{+0.71}_{-0.76}$	$20.2\ ^{+0.8}_{-1.0}$
245	$236 - 254$	4	$5.00 \pm 1.16\ ^{+0.48}_{-0.46}$	$20.6\ ^{+0.9}_{-1.0}$
260	$251 - 269$	7	$2.89 \pm 0.91\ ^{+0.51}_{-0.51}$	$21.2\ ^{+0.9}_{-1.1}$
277	$267 - 287$	4	$3.35 \pm 1.01\ ^{+0.75}_{-0.72}$	$21.9\ ^{+0.9}_{-1.1}$
296	$285 - 307$	6	$3.55 \pm 1.08\ ^{+0.47}_{-0.62}$	$22.6\ ^{+0.9}_{-1.1}$
318	$306 - 330$	4	$1.99 \pm 0.73\ ^{+0.20}_{-0.19}$	$23.6\ ^{+1.0}_{-1.1}$
343	$329 - 357$	3	$1.56 \pm 0.64\ ^{+0.15}_{-0.40}$	$24.7\ ^{+1.0}_{-1.2}$
371	$356 - 386$	2	$1.03 \pm 0.56\ ^{+0.33}_{-0.39}$	$25.9\ ^{+1.1}_{-1.2}$
403	$386 - 420$	1	$2.18 \pm 0.79\ ^{+0.63}_{-0.51}$	$27.3\ ^{+1.1}_{-1.3}$
439	$419 - 459$	0	$1.87 \pm 0.75\ ^{+0.19}_{-0.53}$	$28.9\ ^{+1.2}_{-1.3}$
480	$456 - 504$	1	$0.71 \pm 0.41\ ^{+0.12}_{-0.14}$	$30.6\ ^{+1.2}_{-1.4}$
527	$498 - 556$	2	$0.80 \pm 0.54\ ^{+0.48}_{-0.11}$	$32.4\ ^{+1.3}_{-1.4}$
581	$546 - 616$	1	$0.82 \pm 0.58\ ^{+0.30}_{-0.13}$	$34.3\ ^{+1.4}_{-1.4}$
646	$599 - 693$	0	$0.94 \pm 0.53\ ^{+0.10}_{-0.11}$	$36.3\ ^{+1.4}_{-1.5}$
729	$664 - 794$	0	$0.65 \pm 0.46\ ^{+0.13}_{-0.39}$	$38.4\ ^{+1.5}_{-1.5}$
842	$720 - 964$	0	$0.59 \pm 0.40\ ^{+0.06}_{-0.06}$	$40.5\ ^{+1.6}_{-1.6}$
1000	> 720	0	$0.59 \pm 0.40\ ^{+0.06}_{-0.06}$	$42.6\ ^{+1.6}_{-1.6}$
1200	> 720	0	$0.59 \pm 0.40\ ^{+0.06}_{-0.06}$	$44.2\ ^{+1.7}_{-1.7}$
1400	> 720	0	$0.59 \pm 0.40\ ^{+0.06}_{-0.06}$	$45.2\ ^{+1.7}_{-1.7}$
1600	> 720	0	$0.59 \pm 0.40\ ^{+0.06}_{-0.06}$	$45.8\ ^{+1.7}_{-1.7}$
1800	> 720	0	$0.59 \pm 0.40\ ^{+0.06}_{-0.06}$	$46.3\ ^{+1.7}_{-1.7}$
2000	> 720	0	$0.59 \pm 0.40\ ^{+0.06}_{-0.06}$	$46.5\ ^{+1.8}_{-1.8}$
2200	> 720	0	$0.59 \pm 0.40\ ^{+0.06}_{-0.06}$	$46.7\ ^{+1.8}_{-1.8}$
2400	> 720	0	$0.59 \pm 0.40\ ^{+0.06}_{-0.06}$	$46.9\ ^{+1.8}_{-1.8}$
2600	> 720	0	$0.59 \pm 0.40\ ^{+0.06}_{-0.06}$	$47.0\ ^{+1.8}_{-1.8}$

Table 6.5: Summary of the content of all L-shaped search regions that are considered in the Run I analysis.

M_{μ^*} (GeV)	Window (GeV)	N_{Data} (Events)	$N_{BG} \pm Stat \pm Syst$ (Events)	$A \times \epsilon_{sig} \pm Syst$ (%)
200	$194 - 206$	0	$2.02 \pm 0.44\ ^{+0.43}_{-0.42}$	$26.1\ ^{+1.0}_{-1.0}$
209	$202 - 216$	3	$2.36 \pm 0.53\ ^{+0.59}_{-0.54}$	$26.5\ ^{+1.1}_{-1.0}$
220	$213 - 227$	5	$1.89 \pm 0.41\ ^{+0.42}_{-0.42}$	$26.9\ ^{+1.1}_{-1.0}$
232	$224 - 240$	3	$2.22 \pm 0.45\ ^{+0.39}_{-0.37}$	$27.4\ ^{+1.1}_{-1.1}$
245	$236 - 254$	5	$2.54 \pm 0.46\ ^{+0.35}_{-0.32}$	$27.9\ ^{+1.2}_{-1.1}$
260	$251 - 269$	1	$1.31 \pm 0.31\ ^{+0.17}_{-0.19}$	$28.6\ ^{+1.2}_{-1.1}$
277	$267 - 287$	1	$1.39 \pm 0.31\ ^{+0.26}_{-0.30}$	$29.4\ ^{+1.3}_{-1.2}$
296	$285 - 307$	1	$1.23 \pm 0.34\ ^{+0.21}_{-0.20}$	$30.3\ ^{+1.3}_{-1.2}$
318	$306 - 330$	1	$1.29 \pm 0.27\ ^{+0.13}_{-0.14}$	$31.4\ ^{+1.4}_{-1.2}$
343	$329 - 357$	1	$1.05 \pm 0.24\ ^{+0.16}_{-0.20}$	$32.6\ ^{+1.4}_{-1.3}$
371	$356 - 386$	0	$0.95 \pm 0.19\ ^{+0.10}_{-0.12}$	$34.0\ ^{+1.5}_{-1.3}$
403	$386 - 420$	0	$0.80 \pm 0.15\ ^{+0.10}_{-0.10}$	$35.5\ ^{+1.5}_{-1.4}$
439	$419 - 459$	0	$0.65 \pm 0.14\ ^{+0.07}_{-0.08}$	$37.2\ ^{+1.6}_{-1.4}$
480	$456 - 504$	1	$0.62 \pm 0.17\ ^{+0.05}_{-0.05}$	$39.0\ ^{+1.6}_{-1.5}$
527	$498 - 556$	1	$0.56 \pm 0.14\ ^{+0.06}_{-0.17}$	$40.8\ ^{+1.6}_{-1.6}$
581	$546 - 616$	1	$0.41 \pm 0.10\ ^{+0.07}_{-0.04}$	$42.6\ ^{+1.7}_{-1.6}$
646	$599 - 693$	2	$0.27 \pm 0.02\ ^{+0.03}_{-0.03}$	$44.5\ ^{+1.7}_{-1.7}$
729	$664 - 794$	1	$0.23 \pm 0.02\ ^{+0.02}_{-0.03}$	$46.3\ ^{+1.8}_{-1.7}$
842	$720 - 964$	0	$0.20 \pm 0.02\ ^{+0.02}_{-0.02}$	$48.2\ ^{+1.8}_{-1.8}$
1000	> 720	0	$0.30 \pm 0.02\ ^{+0.03}_{-0.03}$	$49.9\ ^{+1.9}_{-1.9}$
1200	> 720	0	$0.30 \pm 0.02\ ^{+0.03}_{-0.03}$	$51.2\ ^{+1.9}_{-1.9}$
1400	> 720	0	$0.30 \pm 0.02\ ^{+0.03}_{-0.03}$	$51.9\ ^{+2.0}_{-2.0}$
1600	> 720	0	$0.30 \pm 0.02\ ^{+0.03}_{-0.03}$	$52.4\ ^{+2.0}_{-2.0}$
1800	> 720	0	$0.30 \pm 0.02\ ^{+0.03}_{-0.03}$	$52.7\ ^{+2.0}_{-2.0}$
2000	> 720	0	$0.30 \pm 0.02\ ^{+0.03}_{-0.03}$	$52.9\ ^{+2.0}_{-2.0}$
2200	> 720	0	$0.30 \pm 0.02\ ^{+0.03}_{-0.03}$	$53.0\ ^{+2.0}_{-2.0}$
2400	> 720	0	$0.30 \pm 0.02\ ^{+0.03}_{-0.03}$	$53.1\ ^{+2.0}_{-2.0}$
2600	> 720	0	$0.30 \pm 0.02\ ^{+0.03}_{-0.03}$	$53.2\ ^{+2.0}_{-2.0}$
2800	> 720	0	$0.30 \pm 0.02\ ^{+0.03}_{-0.03}$	$53.2\ ^{+2.0}_{-2.0}$
3000	> 720	0	$0.30 \pm 0.02\ ^{+0.03}_{-0.03}$	$53.3\ ^{+2.0}_{-2.0}$
3200	> 720	0	$0.30 \pm 0.02\ ^{+0.03}_{-0.03}$	$53.3\ ^{+2.0}_{-2.0}$
3400	> 720	0	$0.30 \pm 0.02\ ^{+0.03}_{-0.03}$	$53.4\ ^{+2.1}_{-2.1}$
3600	> 720	0	$0.30 \pm 0.02\ ^{+0.03}_{-0.03}$	$53.4\ ^{+2.1}_{-2.1}$
3800	> 720	0	$0.30 \pm 0.02\ ^{+0.03}_{-0.03}$	$53.4\ ^{+2.1}_{-2.1}$
4000	> 720	0	$0.30 \pm 0.02\ ^{+0.03}_{-0.03}$	$53.4\ ^{+2.1}_{-2.1}$

Table 6.6: Summary of the content of all L-shaped search regions that are considered in the Run II analysis.

Uncertainty	BG / SG	Input	Reference
μ-scale	BG & SG	5%/ TeV	Sec. 4.2.3
μ-resolution	BG & SG	0.6%	Sec. 4.2.3
γ-scale &-resolution	BG & SG	very small	Sec. 4.3.4
ID & Isolation	BG & SG	$p_{\mathrm{T}}/E_{\mathrm{T}}/\eta$-dependent	App. B
Pileup	BG & SG	5%	Sec. 5.2
Luminosity	BG & SG	2.5% / 2.7%	Sec. 3.2.8
PDF	BG & SG	$2-3\%(/\,\mathrm{TeV})$	Sec. 6.3.2
γ-misID	BG	54% / 50%	Sec. 5.5.1/5.5.2
Zγ-Cross Section	BG	10%	Sec. 5.3.1

Table 6.7: Summary of the theoretical and experimental systematic uncertainties that are considered in both analyses, with the input values that are used to estimate their impact. If different input values are used for Run I and Run II, respectively, both are quoted and separated by "/". References are given to sections, where the origin of the respective uncertainty is explained in greater detail. Uncertainties arising from parton distribution functions are introduced in the following section.

for such effects. On the other hand, a flat distribution can cause very small effects of such systematic uncertainties, as in this case, almost similar numbers of events should enter and leave a region.

The resulting impact of the systematic uncertainties on the background is listed in table 6.8. It shows, for both analyses, the relative change of the event yield of the full selection after the Z-veto, before the L-shape requirement. The dominating impact comes from the Zγ-cross section uncertainty and from background contributions with faked photons. Even though the assumed uncertainty for the latter is similar in Run I and Run II (see table 6.7), the result differs. This is caused by the higher relative contribution of such backgrounds in Run II (compare table 5.8 and table 5.9). Other uncertainties have a smaller impact of some few percent or even lower. In case of the signal, the situation is similar. As the impact of the muon scale uncertainty is determined by the relatively low p_{T}-thresholds, it is low even for the highest mass points. Dominating uncertainties are such from ID-efficiencies that have a impact similar to that on background.

The impact on the yield in the L-shaped search regions is outlined in figure 6.8. It shows the relative change under a certain systematic shift for both, background and signal, and both analyses. For better visibility, systematic uncertainties of a fixed value, e.g. on the luminosity are not plotted. The given reference points are those that have a corresponding simulated signal sample, i.e. those points that are used for the interpolation that is introduced above. To obtain the values given in figure 6.8, the uncertainties are symmetrized for reasons of visualization. That means, the shifts from the up- and downwards variations are averaged. For obtaining the final results, asymmetric uncertainties are used. Also, the distributions of the background uncertainties are not expanded to the full mass range for better visibility at low masses. As the selection and thus the background content does not change at high masses (requirement $\mathrm{M}_{\mu^*} > 1\,\mathrm{TeV}$), the behavior of the systematics can be extrapolated up to the highest masses. The impact of PDF-uncertainties is not yet covered and will be explained in the following section.

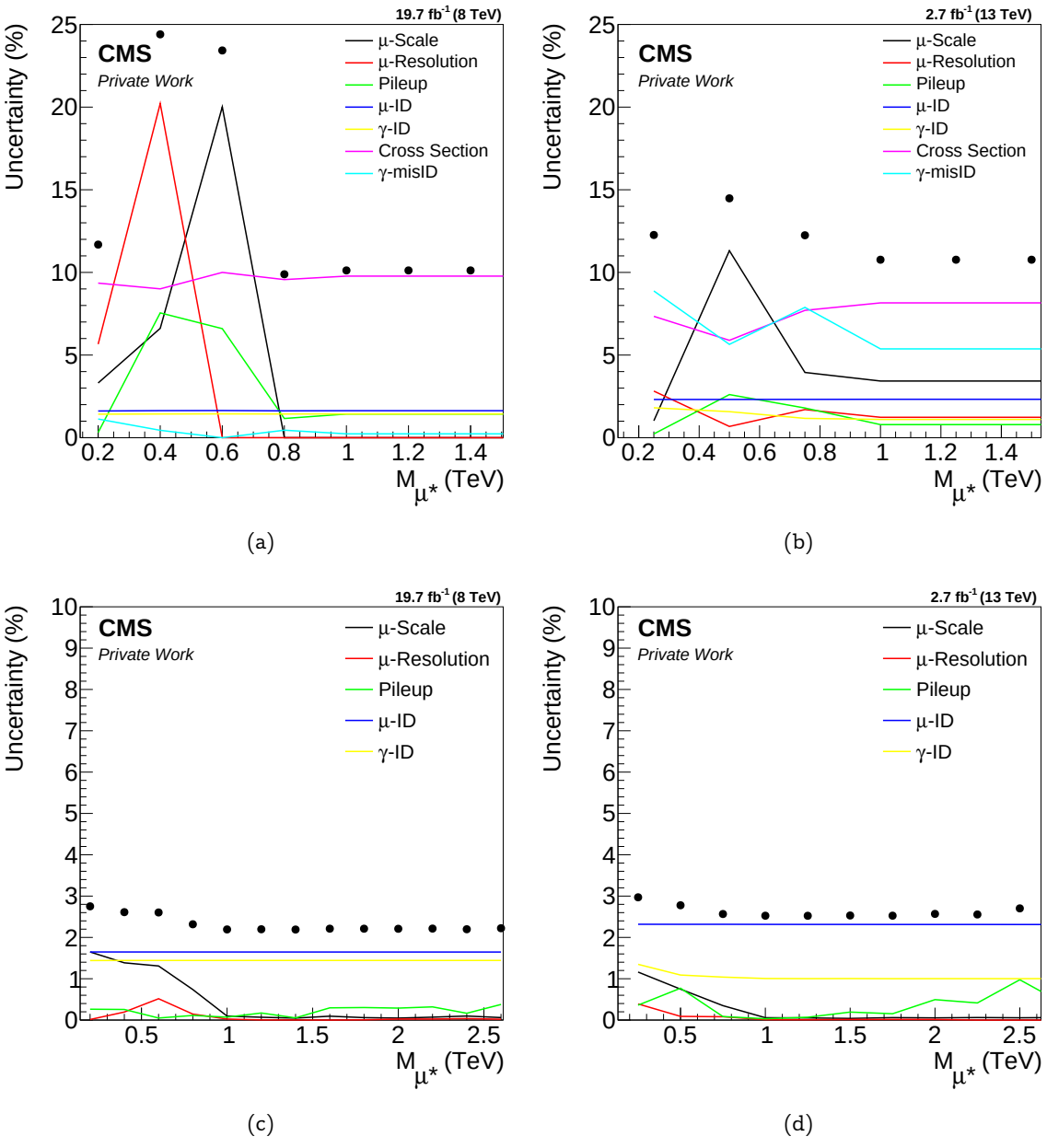

Figure 6.8: Impact of the systematic uncertainties on various search regions as determined for the background (upper two) and various signal samples (lower two) and for the Run I (left two) and Run II (right two) analysis. Black points represent the quadratic sum of all contributions.

Uncertainty	Impact on Ev. yield (%)	
	Run I	Run II
μ-scale	0.8	0.9
μ-resolution	0.6	0.7
μ-ID	1.6	2.3
γ-ID	1.2	1.0
Pileup	0.4	1.3
Luminosity	2.4	2.7
γ-misID	1.8	12.5
Zγ-cross section	8.9	6.9

Table 6.8: Impact on the background event yields of both analyses after all selections, including the Z-veto without the L-shape requirement. All values given in percent.

Overall, the impact of systematic uncertainties is rather small. The systematic uncertainties are dominated by those that have their origin from changes in the event weights. Only the spikes in the Run I background distribution have their origin in fluctuations. There, the L-shaped windows are still rather small, while the background samples tend to become statistically limited. The behavior at search regions of higher masses is on first sight in contradiction to general experiences from other searches[2]. Here, the effect is not comparable due to the inclusive selection at high masses. All systematic uncertainties are modeled by a log-normal prior in the limit calculation. The advantage of the log-normal distribution is its convergence to zero for very small values. Thus, the probability density is prohibited from reaching negative values. A normal distribution would have to be artificially truncated at zero to achieve this property that is wanted for systematic uncertainties.

6.3.2 Parton Distribution Functions and Uncertainties

A *Parton Distribution Function* (PDF), denoted by $f(x, Q^2)$, describes the partonic content of protons, i.e. the probability of a gluon or quark of a certain flavor to carry the energy fraction x at an energy scale Q^2. Thus, to predict cross sections of a certain interaction at high precision, and to produce reliable Monte Carlo, it is mandatory to know the form of PDFs as accurately as possible. The cross section σ for a process in hadronic interactions is given by

$$\sigma = \sum_{i,j} \int_0^1 \int_0^1 \mathrm{d}x_1 \mathrm{d}x_2 \cdot f_i(x_1, Q^2) f_j(x_2, Q^2) \cdot \sigma_{ij}. \tag{6.15}$$

Here, i and j are the possible partons of the initial state with the corresponding cross section σ_{ij}, and 1 and 2 are the interacting partons. A more detailed summary can e.g. be found in [6].

Descriptions for PDFs are obtained by various collaborations relying on data from fixed-target or collider experiments, e.g. using such data from deep-inelastic electron, muon and neutrino scattering, or hadronic Drell-Yan and jet production [151]. Well-known groups are CTEQ, MSTW (MMHT), and NNPDF that provide results being regularly considered in Run I (Run II) analyses. The resulting PDFs, together with their corresponding uncertainties are obtained by either using the *Hessian* approach, where the functions are fitted to data by

[2] For example, the uncertainty on the muon momentum scale becomes very large at high-mass Z′ searches.

minimizing a log-likelihood χ^2-function, or by the *Monte Carlo* approach that is based on the generation of replica of pseudo data [151].

For the generation of MC, a certain PDF parametrization is chosen. In the Run I background and signal samples, this is CTEQ6L1 [152]; in Run II, NNPDF3.0 [153] is used. To estimate the uncertainty on the PDF parametrization in MC, taking into account results from different collaborations, it is not practical to reproduce all samples with different PDF parametrization, but rather to use a remodeling procedure to apply different PDF conditions to the existing simulation. For that, MC events are reweighted one by another based on the underlying hard interaction. Detailed recommendations, including the reweighting procedure and PDF-sets that should be used are provided by the PDF4LHC [151] (PDF4LHC15 [154]) -group. Parametrizations of various PDF sets are provided in the LHAPDF [155] framework.

A major uncertainty on the PDF parametrizations is the choice of the value of α_s, the strong coupling constant [151]. The correlation of α_s and several PDF sets is e.g. investigated in reference [156]. The combined PDF and α_s uncertainty is calculated by adding both contributions in quadrature [151, 154]:

$$\sigma_{\mathrm{PDF},\alpha_s} = \sqrt{\sigma^2_{\mathrm{PDF}} + \sigma^2_{\alpha_s}} \tag{6.16}$$

For the Run II recommendation, the value $\alpha_s(m_Z^2) = 0.1180 \pm 0.0015$ is used [151], where the uncertainty corresponds to the 68% confidence interval.

Here, the results of the PDF reweighting procedure for the Run II analysis are presented, following the recommendations of PDF4LHC15 (summarized in chapter 6 of [154]). There, to estimate the uncertainties, a combination of the PDF sets CT14 [157], MMHT2014 [158] and NNPDF3.0 is proposed. The first two sets are produced with the Hessian approach, the latter one with the MC method. In order to be able to easily combine the different approaches, different procedures were developed in order to convert Hessian sets into the MC representation and vice versa. Here, an all-Hessian description is used, where the sets obtained with the MC-method were converted using the Hessian reduction method "META PDFs" [159, 160]. PDF4LHC15 provides samples of sets that have been reduced in this manner, the one used here, called "PDF4LHC15_nlo_30_pdfas" has 30+2 members representing the variations of the PDF description and α_s, respectively. The corresponding set with NNLO precision is also available. The total uncertainty on the PDF parametrization can then simply be calculated by

$$\sigma_{\mathrm{PDF}} = \sqrt{\sum_{n=1}^{30} (\sigma_n - \sigma_0)^2}, \tag{6.17}$$

where $\sigma_{n,0}$ are the cross sections derived from the n-th PDF-set and the original one that was used for the production. Technically, $\sigma_n - \sigma_0$ is estimated by evaluating the change in the event yield of a given selection.

To understand how the uncertainties behave over wide mass ranges in the analysis, figure 6.9 shows the resulting PDF+α_s-uncertainty as a function of $\mathrm{M}^{\mu\gamma}_{\mathrm{min}}$ ($\mathrm{M}^{\mu\gamma}_{\mathrm{max}}$) in black (red) for NLO and NNLO precision in the left and right plot, respectively. These distributions are obtained using the dominating $Z\gamma$-background, after all selection steps, without the final L-shape requirement. It can be seen that up to masses of 1 TeV, the uncertainties stay below $2-3\%$ and reach values well below 10% far above 2 TeV.

PDFs in the Signal Simulation

For signal MC a study with the same method is performed. Figure 6.10 shows the estimated uncertainty for two signal mass points of lower mass (250 and 750 GeV in black and red,

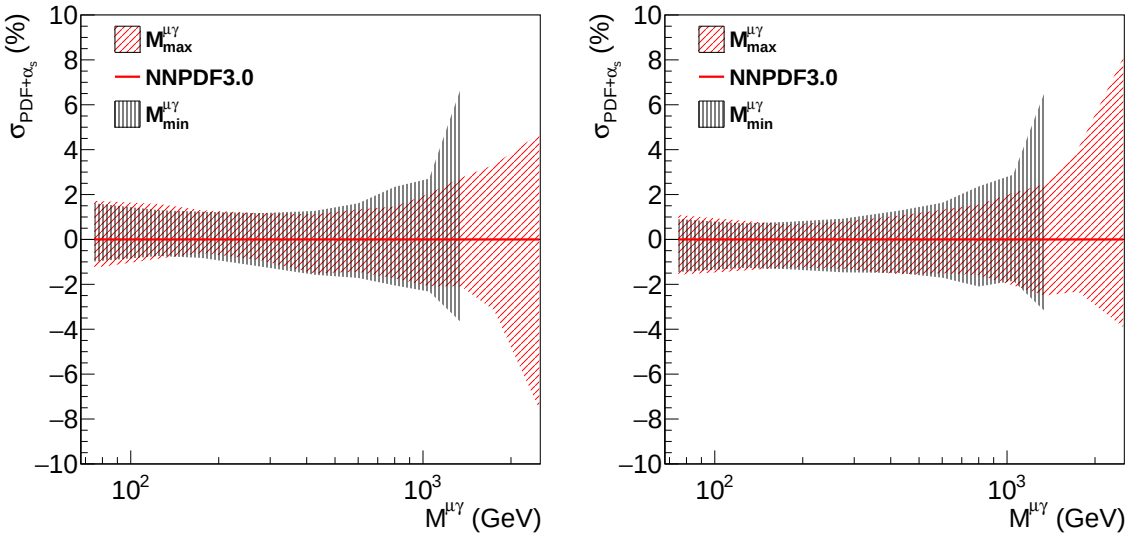

Figure 6.9: PDF+α_s-uncertainties evaluated for the $M^{\mu\gamma}_{min}$ (black) and $M^{\mu\gamma}_{max}$ (red) -distributions of the Zγ-background, after all selection without the final L-shape requirement. The plot on the left belongs to the reweighting of PDF-sets that are NLO in QCD, the right to NNLO.

respectively), depending on $M^{\mu\gamma}_{max}$. Similar to the situation for the background (figure 6.9), the uncertainty is below $2-3\%$ up to masses of approximately 1 TeV. Above that, the uncertainty tends to rise but stays well below 10% up to the highest considered masses. The uncertainty-band of the 750 GeV-point shows a rather unsteady behavior at lower masses. The reason for that is the strongly reduced number of MC-events in regions, where $M^{\mu\gamma}_{max} \ll M_{\mu^*}$.

The plot in figure 6.10, right, demonstrates the PDF+α_s-uncertainties for signal samples with $M_{\mu^*} \geq 1\,\text{TeV}$. It shows the impact of the reweighting, not on a certain mass distribution, but on the complete sample with $M^{\mu\gamma}_{max} \geq 1\,\text{TeV}$. Uncertainties reach from approximately 5% at 1 TeV to $10-20\%$ at the highest masses far beyond 3 TeV.

PDF Uncertainties: Summary

In the previous sections, studies of the magnitude of PDF+α_s-uncertainties in the Run II analysis were presented. For the published results of the Run I analysis [2, 3], an additional flat 10% uncertainty was applied to the Zγ-background in order to account for PDFs and the uncertainty on the cross section. This choice was made based on the experiences of the search for excited leptons with 7 TeV data [43, 161]. For the background of the Run II analysis, the PDF+α_s-uncertainty is applied depending on $M^{\mu\gamma}_{max}$. For $M^{\mu\gamma}_{max} < 1\,\text{TeV}$ an uncertainty of 2% is used. Above that threshold, the uncertainty is described by $2\% \cdot M^{\mu\gamma}_{max}/\,\text{TeV}$. Similarly, for the signal, an uncertainty of 3% is applied up to signal masses of 1 TeV. At higher masses, $3\% \cdot M^{\mu\gamma}_{max}/\,\text{TeV}$ is applied.

The PDF+α_s-uncertainties are estimated in one-dimensional mass distributions only, after applying the full selection without the final L-shape requirement. The latter, two-dimensional cut is not further investigated. For both, signal and background there is reason to assume that this is not necessary. At low masses ($M < 1\,\text{TeV}$), where the influence of the L-shape

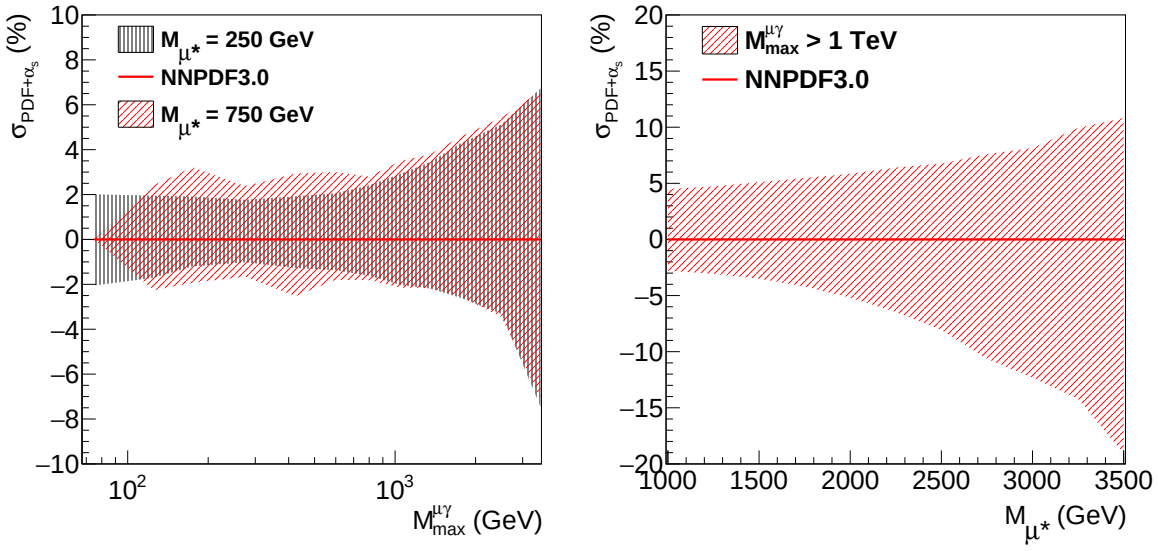

Figure 6.10: Left: PDF+α_s-uncertainties as a function of $M^{\mu\gamma}_{max}$ for two signal samples with masses of 250 GeV and 750 GeV. Right: Evolution of PDF+α_s-uncertainties as a function of M_{μ^*}, evaluated for masses $M^{\mu\gamma}_{max} > 1$ TeV.

requirement is highest (compare figure 6.7), the PDF+α_s-uncertainties are flat. Thus it can be assumed that a further requirement will not change their impact. Above this threshold, the final selection is similar to the requirements in figures 6.9 and 6.10 and the conclusion drawn from there are valid.

The goal of this section was to get an idea of the behavior of the PDF uncertainties in both, signal and background, over wide mass ranges. The presented study is for Run II, only. A corresponding dedicated Run I study is not performed, and the obtained values are adopted for the Run I analysis. The uncertainty of the NNPDF3.0 set is considerably higher than those of CTEQ6L1. Thus, Run I PDF uncertainties tend to be smaller and the approach of using the same parametrization can be seen as a conservative approximation.

6.4 Final Results: Limits

This section provides the final results of the searches for excited leptons. Those are given in form of exclusion limits on the signal cross section and the scale parameter Λ for both analyses. To further increase the sensitivity, a combined limit is presented. Then, results that are obtained from other searches for excited leptons are shown.

6.4.1 Cross Section- and Λ-Limits

The statistical interpretation of the obtained results is done by setting exclusion limits at 95% CL on the signal cross section with the Bayesian approach that was introduced in section 6.1.1. The corresponding plots are shown in figure 6.11.

As a function of M_{μ^*}, they show the median expected excluded cross section as a black dashed line with the one and two sigma uncertainty bands in green and yellow. The observed limit is given by a blue line with black dots at the center of the respective considered L-shaped

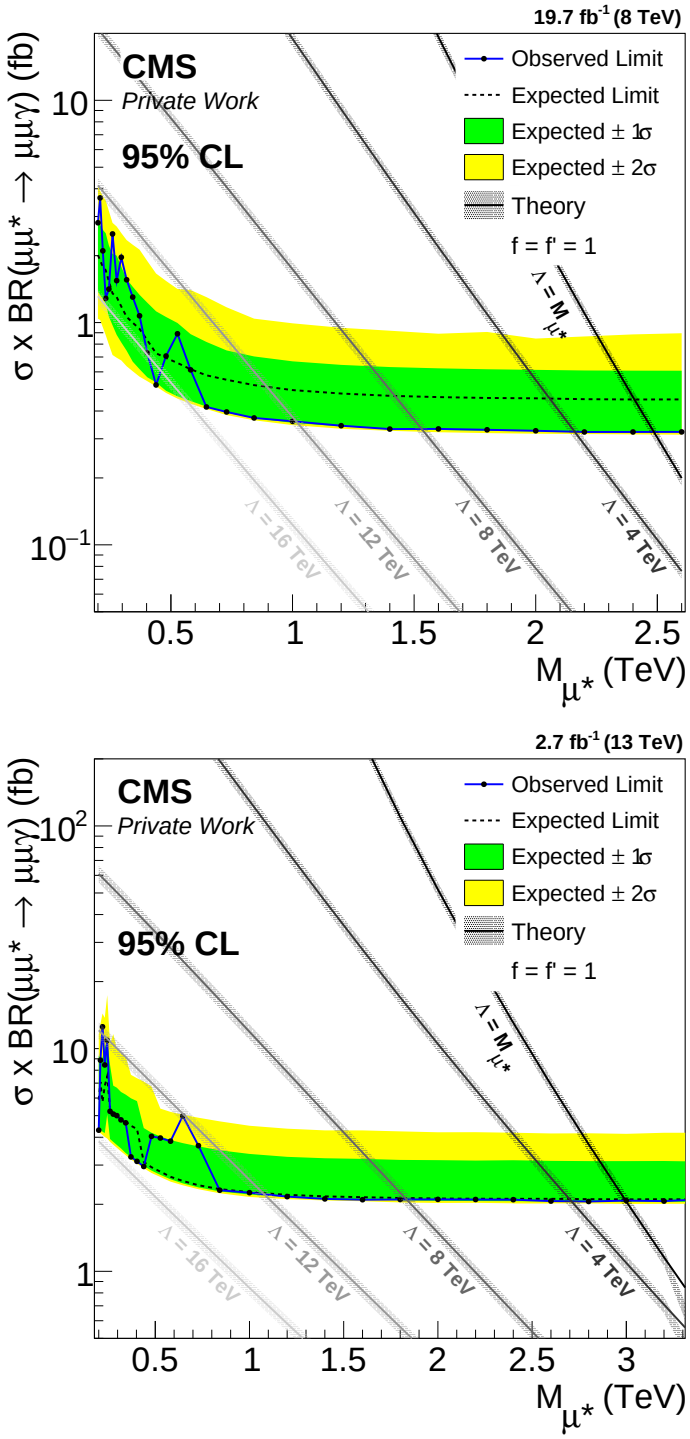

Figure 6.11: Limits on the signal cross section times branching ratio, at 95% CL, as a function of the excited lepton mass, M_{μ^*}, as obtained from the Run I (upper plot) and Run II (lower plot) analyses. Median expected limits are given by a dashed black line, surrounded by the one- and two sigma bands in green and yellow, respectively. Observed limits have a solid blue line with black dots at the considered masses. Theory cross sections are shown for different values of Λ with the assigned 10% cross section uncertainty.

search window. Signal cross sections for different values of Λ, including the case $\Lambda = M_{\mu^*}$, are given by lines in variations of gray. Their shaded areas represent the 10% uncertainty on the signal cross section (refer to section 2.5) that do not enter the limit calculation as an additional prior.

From the Run I results, a cross section of about 0.3 fb at high masses can be excluded. At the lower masses ($M_{\mu^*} \geq 200\,\text{GeV}$), the exclusion is below 4 fb in the worst case. In the Run II analysis, cross sections down to 2 fb can be excluded at high masses, and about 12 fb at the point of weakest exclusion. In both cases, no significant excess over the expected limit can be found.

Instead of comparing cross section lines for different values of Λ to the excluded cross section, the limits can be shown in a representation being two-dimensional in Λ and M_{μ^*}. This is shown in figure 6.12. Giving the excluded value of Λ on the vertical axis, depending on M_{μ^*} on the horizontal axis, the excluded parameter space is here located below the curves. The forbidden area, where $\Lambda < M_{\mu^*}$ is covered by a gray area. Thus, in the Run I analysis, values of Λ up to 17 TeV can be excluded at $M_{\mu^*} \approx 440\,\text{GeV}$. At the edge of the forbidden area, excited muons can be excluded for $\Lambda = M_{\mu^*} = 2.5\,\text{TeV}$. Similarly, for Run II the limit on Λ reaches 15.5 TeV at low masses and excited muons up to 3 TeV can be excluded for the case $\Lambda = M_{\mu^*}$.

When comparing the limits of the two analyses, several differences can be observed. The excluded cross section times branching ratio of the Run I result is considerably lower than that of Run II ($\sim 0.3\,\text{fb}^{-1}$ in Run I compared to $\sim 2\,\text{fb}^{-1}$in Run II). The reason for this is the larger integrated luminosity in Run I (approx. 7.3 times more data), whereas this influence is lowered by the slightly increased acceptance times efficiency in Run II (compare e.g. figure 6.7). At the same time, the exclusion in Λ is comparable at low masses and increases by 0.5 TeV at the edge of the forbidden area of $M_{\mu^*} = \Lambda$ in Run II. This is caused by the rise of the signal cross section that is also discussed in section 2.5 and plotted in figure 2.7, and that can be seen from comparing the theory lines is figure 6.11.

Another striking difference is the behavior of the expected limits and their uncertainty bands in green and yellow at high masses ($M_{\mu^*} \gtrsim 1\,\text{TeV}$). In Run I, the expected limit (dashed black line) lies centrally within the green 1σ-band, while the observed limit is located at the lower edge of the green band. In case of the Run II limit, both, expected and observed limit, share the lower edge of the 1σ-band. The reason for that is the different background expectation, which is 0.6 in Run I compared to 0.3 in Run II. In the first case, the median expected limit coincides with one expected event, while the measurement, the observed limit, is at zero. In the Run II result, both, the measurement and the median expected limit correspond to zero events. As, in this case, the uncertainty cannot reach to negative event counts, the uncertainty bands do not reach to smaller excluded cross sections.

6.4.2 Combination of Run I and Run II

From both μ^*-analyses, wide regions of the theoretical parameter space can be excluded. However, in order to give one common result, it is useful to combine the individual results into one. Thus the sensitivity can be further increased. In order to combine two individual results, it is necessary that both refer to the same choice of theory parameters. The resulting combination can therefore e.g. be presented as the ratio of the excluded cross section to the theoretical cross section. For the individual results, the latter would be the corresponding cross section, for the combination it would be the sum of both cross sections.

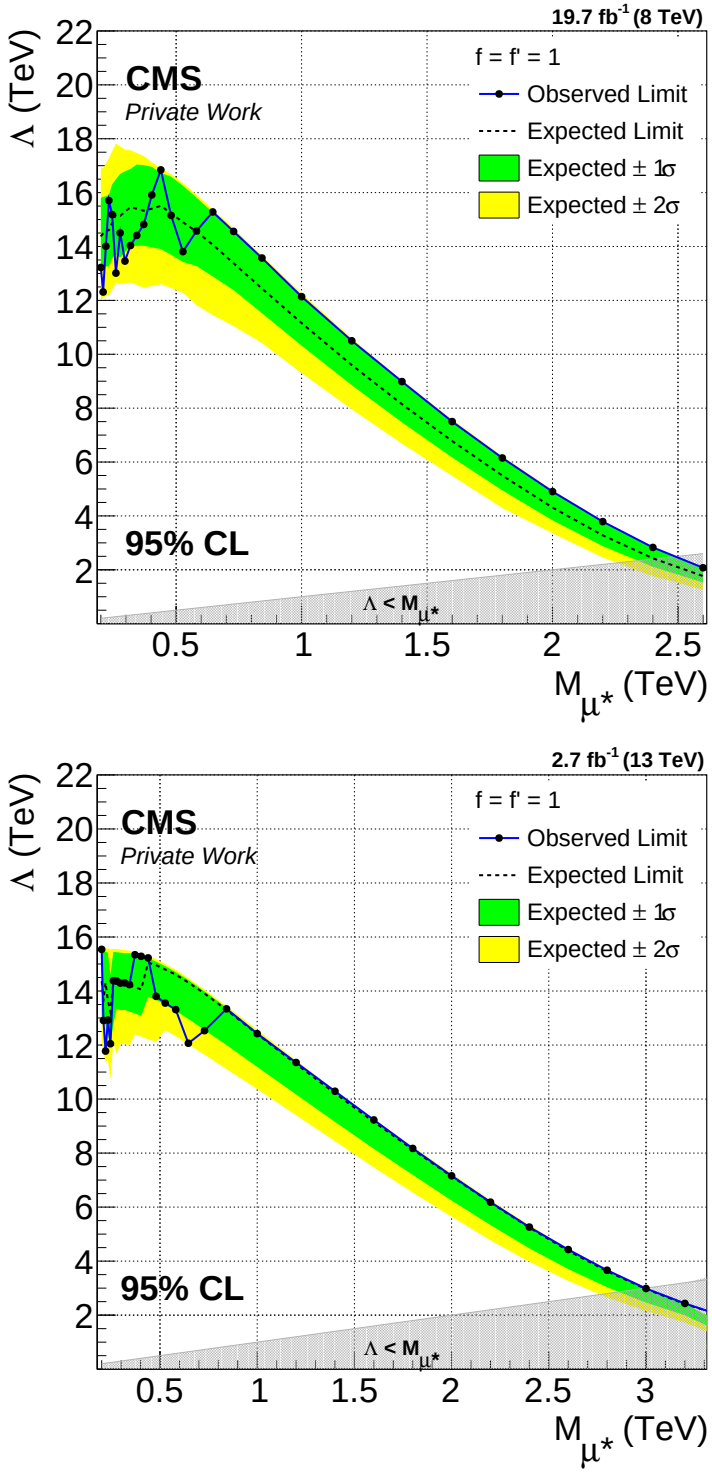

Figure 6.12: Limits on Λ, as a function of the excited lepton mass, M_{μ^*}. Excluded values are below the curves. The gray regime indicates the theoretically forbidden area, where $\Lambda < M_{\mu^*}$.

For cross sections corresponding to $\Lambda = 10\,\text{TeV}$, this is shown in figure 6.13(a). It shows the combined expected and observed limits in the representation that is known from before. The individual observed limits from the Run I and Run II analyses are given by magenta dashed and dashed-dotted lines. Excluded mass-regions are such, where the ratio of excluded to theoretical cross section is smaller than one, i.e. below the red dashed line. In this example, the observed μ^*-limit increases by approximately 200 GeV when comparing the combination to the Run II limit. The step in the combined limit at 2.6 TeV is caused by the fact that the Run I result only extends to 2.6 TeV.

Figure 6.13(b) shows how the combined observed limit changes for various values of Λ in the same representation. By evaluating the value of Λ that can thus be excluded at each mass point, it is possible to determine a combined exclusion in the two-dimensional $\Lambda - M_{\mu^*}$ plane. The outcome is shown in figure 6.13(c). There, again it is possible to compare the combined observed and expected limits to the observed exclusions of the two individual analyses. The gain in excluded parameter space reaches from small impact at the higher masses to up to several TeV in Λ at low and medium excited muon masses (approximately 3 TeV at around $M_{\mu^*} = 800\,\text{GeV}$). At $M_{\mu^*} \approx 440\,\text{GeV}$ the highest excluded value of Λ reaches 19 TeV.

Figure 6.14 shows the combined observed limit in relation to several existing limits on excited muon production that were already discussed in section 2.7. Results from the CMS Collaboration are plotted in blue, while such from ATLAS are represented by green lines. For comparison, the result from the DØ is Collaboration is shown in black. Other experiments, e.g. from LEP or HERA are not shown as they cover lower excited muon masses. Over the complete considered mass range, the result from this thesis surpasses those from the other searches.

Several aspects that were discussed in this thesis can be rediscovered. Comparing the two ATLAS results (green), it can be seen that despite more integrated luminosity, the limit from the decay $\mu^* \to \mu jj$ via CI (dashed-dotted) are considerably weaker that those from $\mu^* \to \mu\gamma$ (dashed) at lower masses, below $M_{\mu^*} \approx 1.2\,\text{TeV}$. Above that, the CI-search is much more sensitive and increases the excluded mass by approximately 700 GeV for the case $M_{\mu^*} = \Lambda$. The reason for that is the behavior of the branching ratio of CI decays for $M_{\ell^*}/\Lambda \to 1$ (compare figure 2.4).

At the low mass region ($M_{\mu^*} < 0.6\,\text{TeV}$), the earlier CMS result from the photon decay (dashed blue) is able to compete with the corresponding ATLAS limit (dashed green), although it was obtained with less integrated luminosity and center of mass energy. This could be achieved by more effectively separating signal from background by a final selection that is comparable to the approach used in this thesis.

6.4.3 Run I Results of other Channels

In this section, searches for excited electrons and muons based on Run I data are presented that are done using channels with different final states. Their final selection follows a similar L-shape approach as the one discussed before, and here, only the final results from this L-shape selection onwards are discussed. Those are obtained by the author of this thesis, using input that is provided by other CMS analysts. Thus, specific analysis features are only briefly summarized here. Details like the individual selections can be found in the given references, and full credit for the analyses goes to the respective authors.

Besides the photon channels ($ee\gamma$ and $\mu\mu\gamma$ final states), the decay via Z-boson radiation is considered, taking into account Z-decays into leptons (electrons and muons) and quarks.

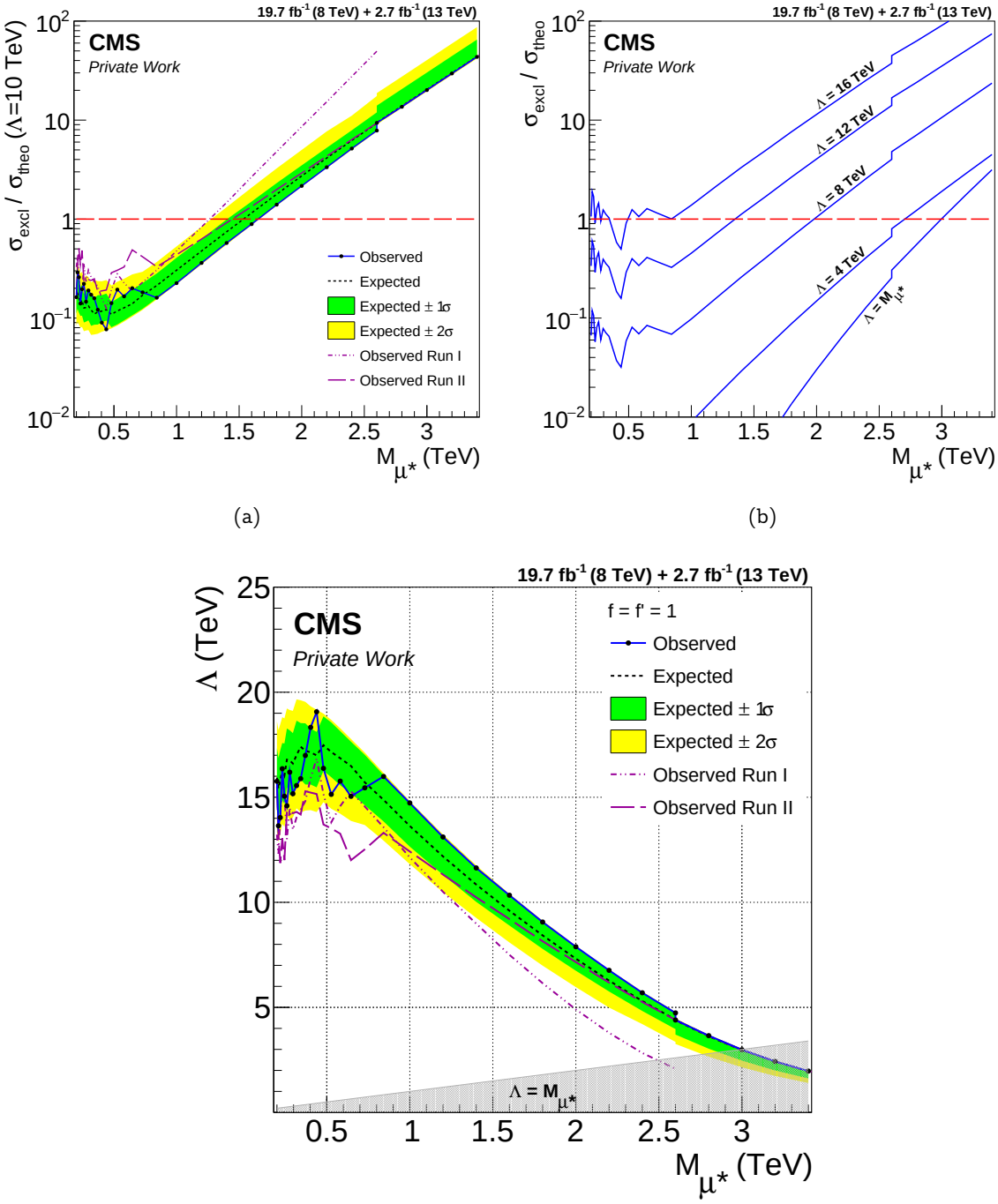

Figure 6.13: Combination of Run I and Run II results: (a) Ratio of the excluded cross section to the theoretical cross section with $\Lambda = 10$ TeV. (b) Ratios of combined observed excluded cross sections to theoretical cross sections of different values of Λ. (c) Combined limit in the $\Lambda - M_{\mu^*}$-plane.

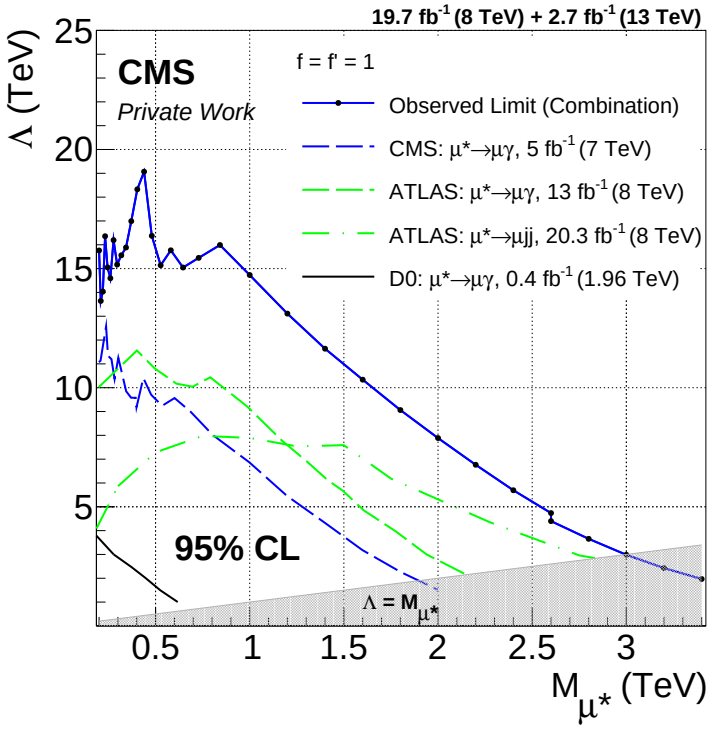

Figure 6.14: Comparison of the combined observed limit as obtained in this thesis (blue with black dots) with a selection of existing results. Blue lines indicate limits from CMS, green from the ATLAS Collaboration. Observed limits obtained from various final states, integrated luminosities, and center of mass energies are compared.

Decay Mode	Channel	Considered Coupling
Radiative Decay $\ell\ell^* \to \ell\ell\gamma$	$ee^* \to ee\gamma$ $\mu\mu^* \to \mu\mu\gamma$	$f = f' = 1$
Neutral Current $\ell\ell^* \to \ell\ell Z$	$ee^* \to eeZ \to eeqq$ $\mu\mu^* \to \mu\mu Z \to \mu\mu qq$ $ee^* \to eeZ \to eeee$ $ee^* \to eeZ \to ee\mu\mu$ $\mu\mu^* \to \mu\mu Z \to \mu\mu ee$ $\mu\mu^* \to \mu\mu Z \to \mu\mu\mu\mu$	$f = f' = 1$ & $f = -f' = 1$

Table 6.9: Summary of all channels that are included into the search for excited leptons [2,3]. Channels with a quark (q) in the final state have signatures with jets.

These open the door for the interpretation in a different parameter space, where the photon channel is not sensitive ($f = -f' = 1$). Thus, overall eight channels are analyzed, selecting the final states that are listed in table 6.9. Summaries about all channels, including the final results and plots that are being presented in this section and that are obtained by the author of this thesis, were published in [2,3].

The analysis of the $ee^* \to ee\gamma$-channel is very similar to the Run I analysis presented in this thesis. The main difference is an additional Z-veto on the two invariant electron-photon masses, $M^{e\gamma}$, and a modeling of backgrounds with mis-reconstructed electrons. More detailed information can be found in [132].

All of the channels with decay via neutral current have in common that the Z-boson is reconstructed from its decay products. Due to the intermediate Z-boson, the decay products of the respective channels obtain a boosted topology that requires special analysis techniques. In case of the two quark channels ($ee^* \to eeZ \to eeqq$ and $\mu\mu^* \to \mu\mu Z \to \mu\mu qq$), this leads to two jets that overlap into one single, broad "fat"-jet. By relying on particle-flow information, the jet's substructure can be resolved, and the two individual sub-jets can be reconstructed. This is described in more detail in [162]. For the four-lepton channels, it is necessary to modify the lepton isolation by subtracting the contribution of the respective other close lepton. Detailed documentation about the latter four channels can be found in [163]. Additionally, a comprehensive description of the analysis of the $\mu\mu^* \to \mu\mu Z \to \mu\mu\mu\mu$-channel can be found in [164].

Each channel goes through a similar L-shape optimization procedure as the one described before. It was also already mentioned that the $ee^* \to eeZ \to eeee$-channel is used to define the positions of the intermediate L-shape windows. The optimized widths of all channels is summarized in figure 6.15, left. In the same figure, on the right side, a comparison of the excited lepton intrinsic width for different values of Λ, with the search window width of two example channels is shown. Selected are the $ee\gamma$- and the 4μ-channels, having rather narrow and wide search windows, respectively. It illustrates that in regions where limits are calculated, the search windows do not interfere with the intrinsic width. More concrete, the width is determined by the resolution of the final state of the respective channel, rather than the intrinsic width. The latter is calculated from the formulas of section 2.4 and particularly large near the forbidden area, where $M_{\ell^*} = \Lambda$. The search windows that are relevant for the limit in this region are sufficiently large. At low masses, where the windows are narrow, the

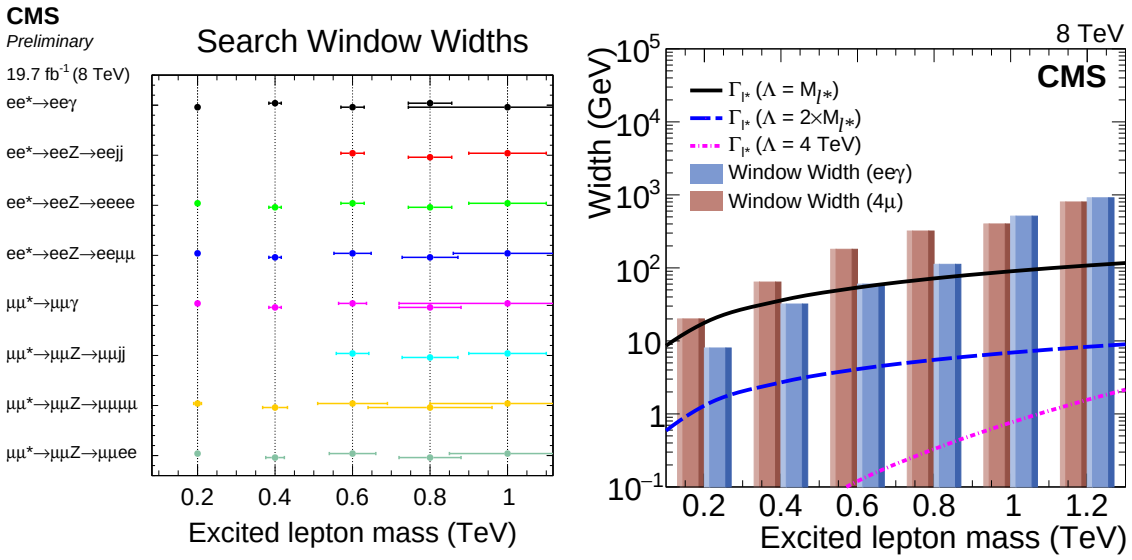

Figure 6.15: Left: Summary of the optimized search window widths of all considered channels. Previously published in [2]. Right: Comparison of the intrinsic excited lepton width at different values of Λ with the search window widths of two different channels. Previously published in [3].

analyses are sensitive for Λ-values of several TeV. Thus, also here, a conflict with the intrinsic width is avoided.

Figure 6.16 shows the signal efficiencies, after all selections, including the final optimized L-shape. Thereby, the left plot summarizes the outcome of the photon- and the jet channels. The right one corresponds to the four-lepton channels. Differences in efficiency that can be observed when comparing similar channels can be explained by different object selection efficiencies. In general, muons have a better selection efficiency than electrons. The efficiency to select a fat-jet is considerably lower. In the best case, the efficiencies reach approximately 30% in the jet channels, and almost 70% in the four muon channel.

In the following figures 6.17-6.19, the resulting limits are shown. That of the respective electron channel is always on the left, while the one of the corresponding muon channel is on the right. All figures show the excluded observed and expected cross section times branching ratio as a function of the excited lepton mass. Cross sections for various values of Λ are given by black lines.

The procedure how the limits were obtained have some few differences compared to the one described before. For one, as can be seen, the uncertainty on the signal cross section is not outlined on the black lines. Second, the systematic uncertainties have been symmetrized before entering the prior functions. Third, a mixture of interpolated mass points and such with MC was used. I.e. at high masses, the following limits rely on the simulated mass points, which leads to slightly unsteady limit curves. The last difference is the calculation of the cross sections. For the limits of this section, the Pythia version that is able to simulate the decay via contact interaction (Pythia8.205, refer to section 2.5) was not yet available. For that reason, the existing cross sections were corrected for the CI-branching fraction by relying on the formulas in chapter 2. However, despite the differences, when comparing the $\mu\mu\gamma$-results obtained with the newer approach described in the sections before with those from the publications, an excellent agreement between figures 6.11, upper, and figure 6.17, right, is found.

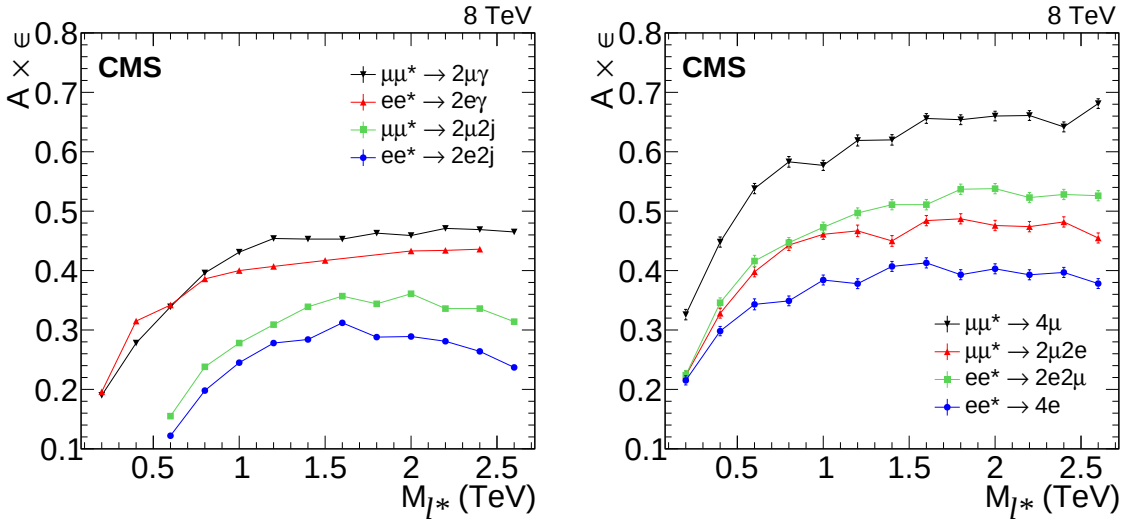

Figure 6.16: Signal acceptance times efficiency after all analysis requirements, including the final L-shape selection as a function of M_{ℓ^*} for the different $\ell\ell\gamma$- and $\ell\ell$jj-channel on the left, and the 4ℓ-channels on the right. Previously published in [3].

The first pair of limits in figure 6.17 is from the photon channels. Due to a slightly lower background expectation, the uncertainty bands in the electron channel are not as distinct as those of the muon channel. Overall both results are quite comparable with a slightly more stringent exclusion in the muon channel, as one would expect from comparing the signal efficiencies in figure 6.16, left.

Limits from the jet channels are shown in figure 6.18. They have additional cross section lines for the case $f = -f' = 1$, shown in dashed black. As in this case the photon channel does not contribute, the corresponding cross sections are larger. The excluded cross section times branching ratio is higher (less stringent) than that of the photon channels and rises at higher masses.

Limits of the four-lepton channels, belonging to the same excited lepton flavor, are combined, as can be seen in figure 6.19. Common systematic uncertainties therefore are treated as fully correlated, all others as uncorrelated. Again, the cross sections for the case $f = -f' = 1$ are shown by dashed black lines, to gain from that increased sensitivity.

Limits of all channels are also provided as the exclusion of the compositeness scale parameter Λ, as already done in figure 6.12. This is shown in figure 6.20. On the left, it shows all observed limits that are obtained for the case $f = f' = 1$. The photon channels thereby reach excluded values of $\Lambda < 17\,\text{TeV}$ at low masses, and cross the line of the forbidden parameter space at $M_{\ell^*} = \Lambda \approx 2.5\,\text{TeV}$. The remaining channels are considerably lower. As before, lepton channels of the same excited lepton flavor are combined. On the right, the corresponding results for $f = -f' = 1$ are shown. The photon channels do not contribute and instead the jet channels have the highest sensitivity, reaching excluded values of $\Lambda = 10 - 11\,\text{TeV}$. For $M_{\ell^*} = \Lambda$, the limits reach almost 2.4 TeV.

All values of observed limits at the point, where $M_{\ell^*} = \Lambda$ are summarized in figure 6.21. Again it is distinguished between $f = f' = 1$ and $f = -f' = 1$. Values of all lepton channels, including the combinations of 4ℓ channels from same excited lepton flavors, are incorporated, too.

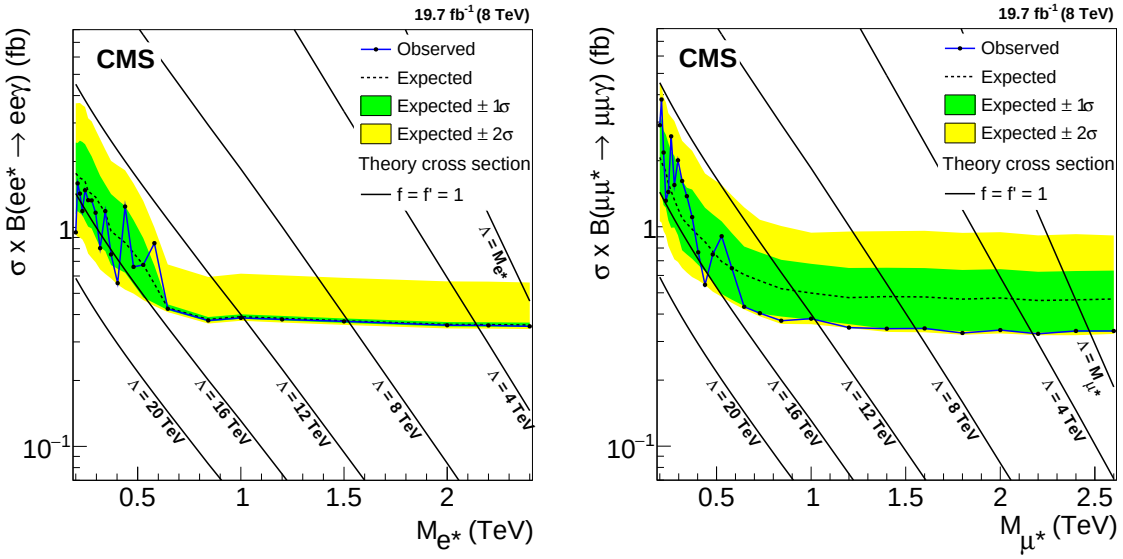

Figure 6.17: Cross section limit of the eeγ- (left) and $\mu\mu\gamma$- (right) channel. Previously published in [3].

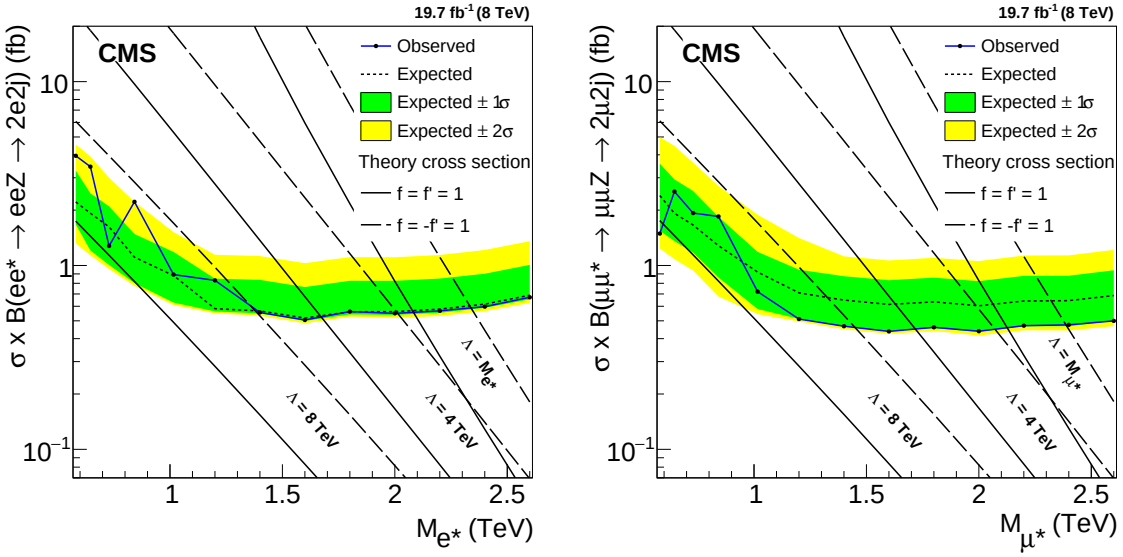

Figure 6.18: Cross section limit of the 2e2j- (left) and 2μ2j- (right) channel. Previously published in [3].

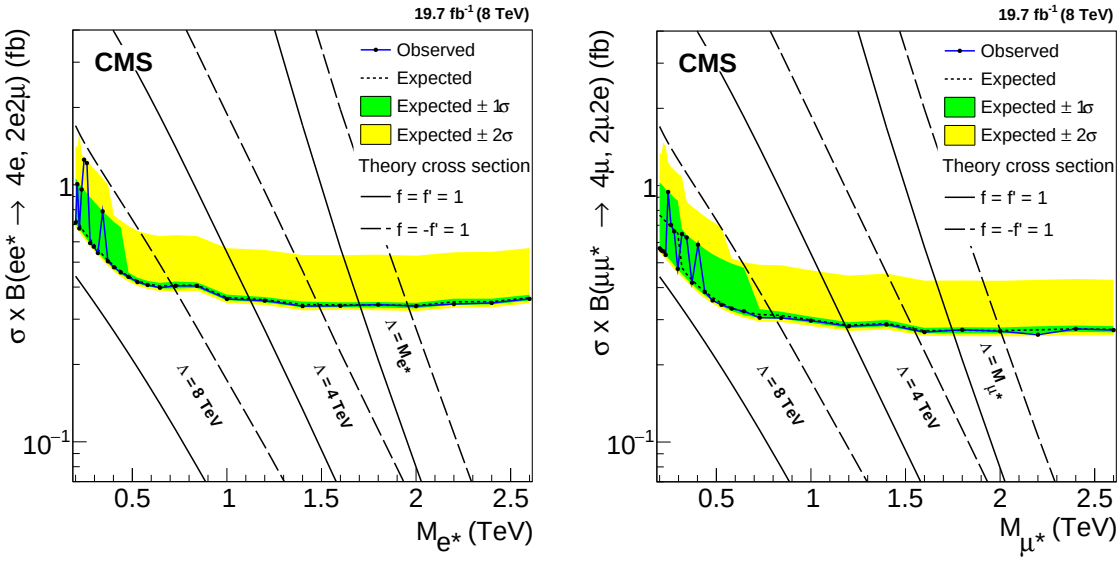

Figure 6.19: Cross section limit of the 2e2ℓ- (left) and 2μ2ℓ- (right) channel. Previously published in [3].

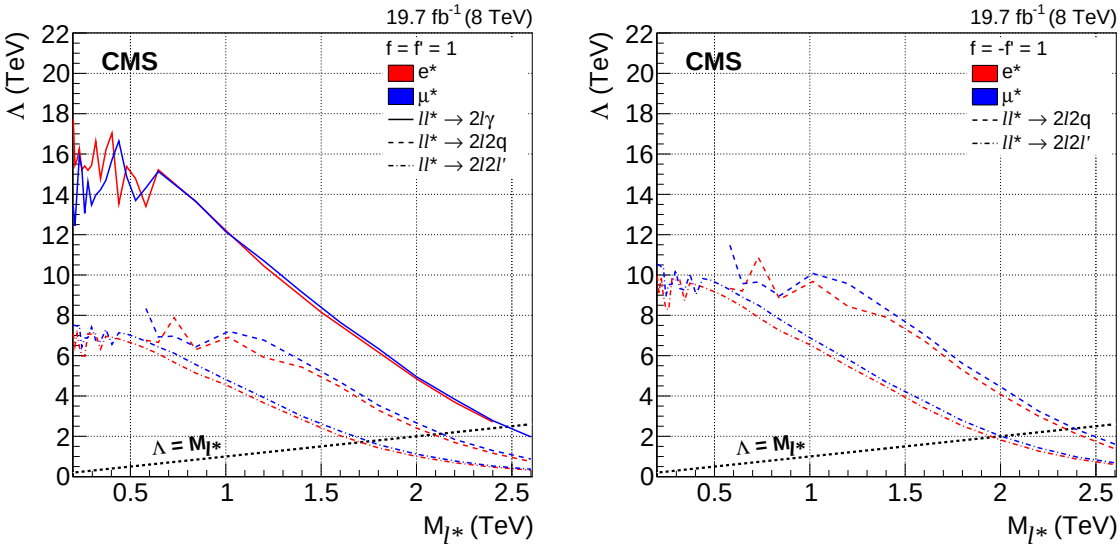

Figure 6.20: Limits on the compositeness scale Λ of all considered channels for the case $f = f' = 1$ (left) and $f = -f' = 1$ (right). In the latter case, the photon channels are suppressed. Limits of 4ℓ-channels belonging to the same excited lepton flavor are combined. Previously published in [3].

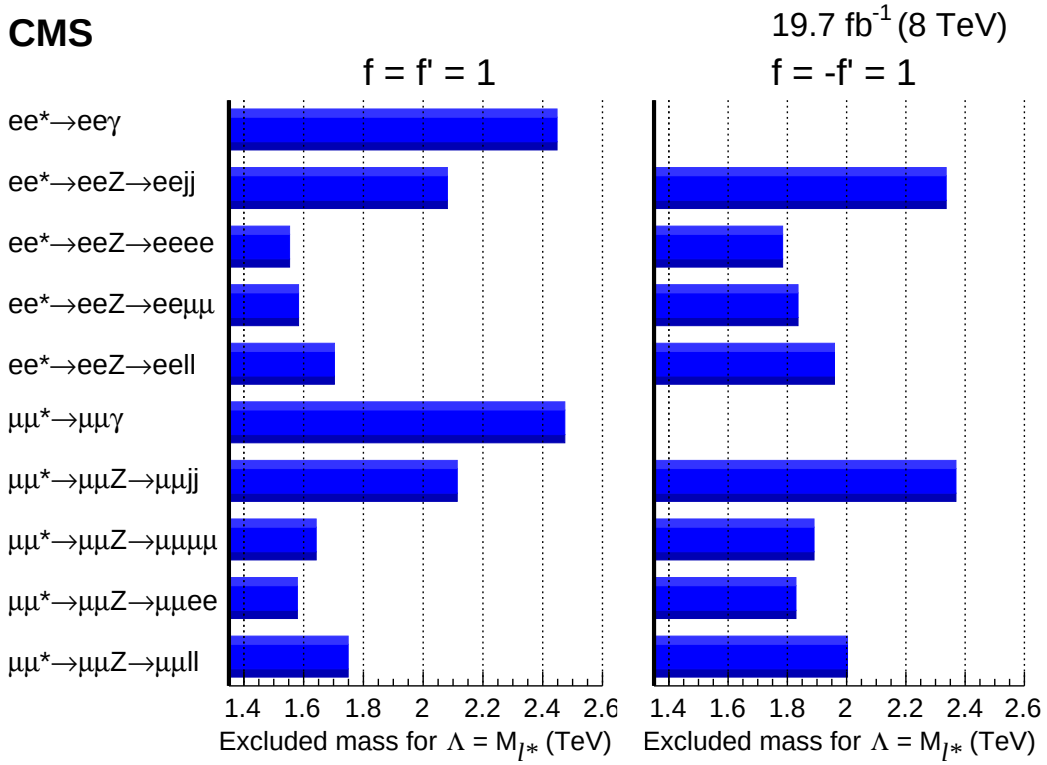

Figure 6.21: Summary of all limits on the compositeness scale Λ in the case $\Lambda = M_{\ell^*}$ for $f = f' = 1$ and $f = -f' = 1$. In the latter case, the photon channels are suppressed. Previously published in [3].

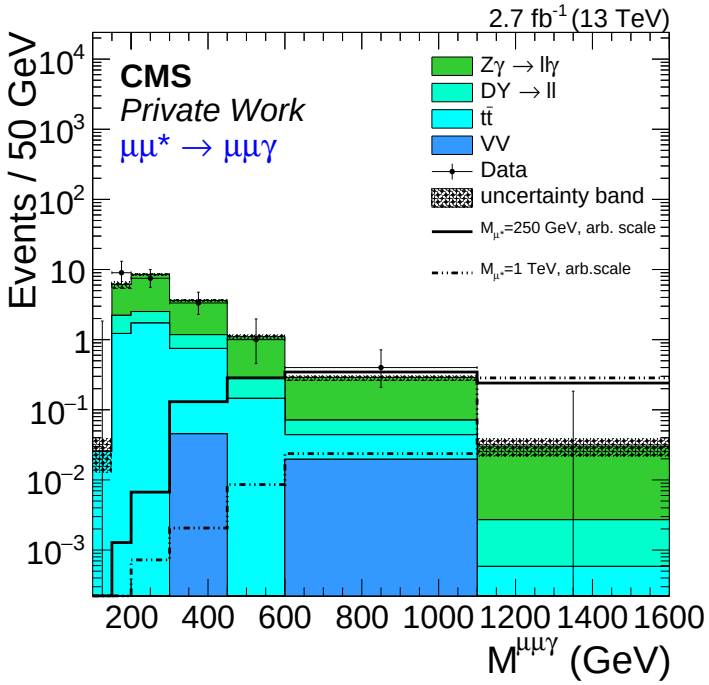

Figure 6.22: Distribution of the three-body invariant mass, $M^{\mu\mu\gamma}$, after all selections, including the Z-veto.

6.4.4 Limits from the Three Body Invariant Mass $M^{\mu\mu\gamma}$

In this section, an alternative approach to the final selection is tested. Here, limits are derived in the three-body invariant mass, $M^{\mu\mu\gamma}$. There are several reasons to present these alternative results.

On the one hand, they serve as a cross check. Thus, it is possible to compare the gain that can be achieved with the rather complicated L-shape approach. Also, the search in $M^{\mu\mu\gamma}$ is the approach that was until now chosen for $\ell\ell\gamma$-excited lepton searches by ATLAS [44]. On the other hand, a more general selection is suited better for a possible re-interpretation. As the cuts of the L-shape approach are very model-specific, they leave tiny room for different interpretations.

In this thesis, the comparison is done with Run II results, exclusively. The corresponding distribution of background expectation, signal, and measured data in $M^{\mu\mu\gamma}$ is shown in figure 6.22. As one would expect from the experiences in section 2.6.2, signal events are above the respective excited lepton mass, almost exclusively. Thus, as final selection criterion, here an invariant mass cut of $M^{\mu\mu\gamma} > M_{\mu^*}$ is applied, depending on the signal mass under investigation. The content of all search regions is summarized in table 6.10.

Throughout the whole mass spectrum, an excellent agreement between the Standard Model expectation and the measurement can be observed. The corresponding limits are shown in figure 6.23, the excluded cross section being given on the left, while the right plot shows the excluded values of the compositeness scale parameter Λ in the known representation. The latter also shows the expected limit that is obtained from the optimization and interpolation

M_{μ^*} (GeV)	N_{Data} (Events)	$N_{BG} \pm$ Stat $\pm$ Syst (Events)	$\epsilon_{sig} \pm$ Syst (%)
250	25	$24.13 \pm 1.42\ ^{+4.45}_{-4.44}$	$32.3\ ^{+1.2}_{-1.2}$
500	6	$5.29 \pm 0.56\ ^{+0.77}_{-0.77}$	$44.8\ ^{+1.7}_{-1.7}$
750	2	$1.42 \pm 0.23\ ^{+0.20}_{-0.21}$	$48.5\ ^{+1.8}_{-1.8}$
1000	0	$0.52 \pm 0.15\ ^{+0.08}_{-0.09}$	$50.7\ ^{+1.9}_{-1.9}$
1250	0	$0.19 \pm 0.11\ ^{+0.03}_{-0.04}$	$52.4\ ^{+2.3}_{-2.3}$
1500	0	$0.05 \pm 0.05\ ^{+0.04}_{-0.08}$	$52.8\ ^{+2.7}_{-2.7}$
1750	0	$0.03 \pm 0.03\ ^{+0.02}_{-0.02}$	$51.4\ ^{+3.0}_{-2.9}$
2000	0	$0.01 \pm < 0.01\ ^{+0.01}_{-0.02}$	$53.0\ ^{+3.4}_{-3.4}$
2250	0	$< 0.01 \pm < 0.01\ <^{+0.01}_{-0.01}$	$53.0\ ^{+3.8}_{-3.8}$

Table 6.10: Event content in regions with $M^{\mu\mu\gamma} > M_{\mu^*}$. Higher masses are not listed as the corresponding event yields become extremely small (< 0.01).

procedure of the L-shape approach as a solid black line. This direct comparison reveals that the L-shape approach provides a gain of up to more than three TeV in the limit on Λ. Excited muons can be excluded up to $M_{\mu^*} < 3\,\text{TeV}$ which is the same value as the one from the L-shape approach. Also, it becomes obvious that from a signal mass of about 1 TeV onwards, it does not make a difference in terms of the exclusion strength, if the search window threshold further increases or stays at a fixed value (720 GeV in the L-shape approach).

6.5 Excited Lepton Candidate Events

Graphical representations of the events with the highest $M^{\mu\gamma}_{max}$ after all cuts including the Z-veto are shown in figure 6.24 and 6.25 for the Run I and Run II analysis, respectively. A full list of all events that survive this selection, including more details about the reconstructed masses, is given in Appendix C.

In both events, the three objects (two muons, one photon) are well separated and have average transverse momenta, being $p_T < 300\,\text{GeV}$. In the transverse plane (upper figures), both events seem well balanced, which is confirmed by the small amount of missing transverse energy. Corroborating the discussion of the pileup-occurrence in section 5.2, the Run I event shows a much higher amount of pileup, represented by additional yellow tracks and deposits in the calorimeters. When considering the $\eta - r$-plane, none of the events shows a considerable boost into the direction of a beam and particularly the Run II event is very central. Noticeable about the latter event are two tracks that point to the calorimeter deposit of the photon having transverse momenta of $p_T = 86\,\text{GeV}$ and 58 GeV (see figure 6.26 for details). Assuming that tracks and deposit have the same origin, this indicates a converted photon rather than electrons passing the conversion safe electron veto (CSEV, see section 4.3.2). Overall, both events look as expected and no obvious sign of any mis-reconstruction can be seen.

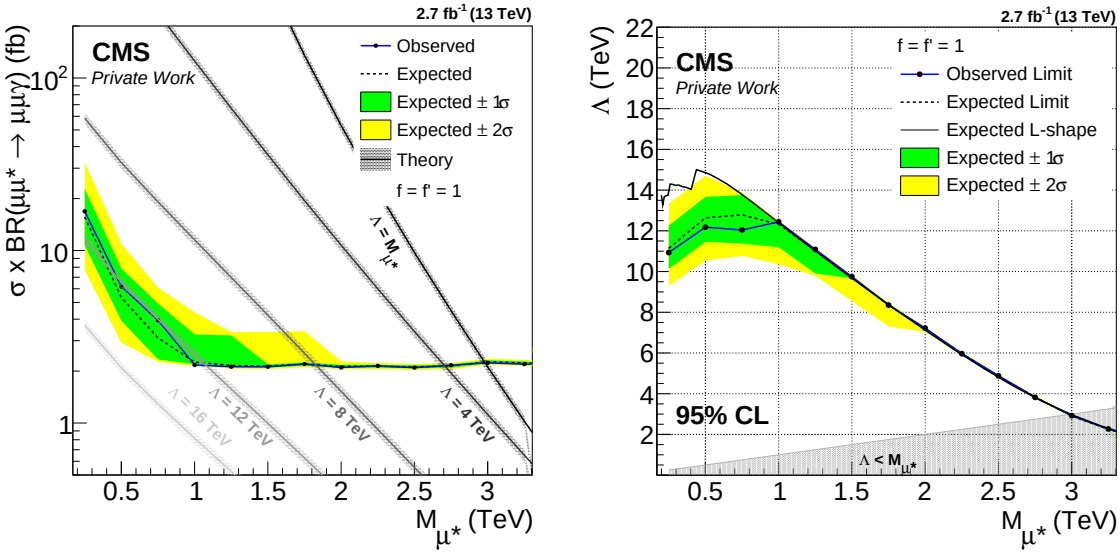

Figure 6.23: Cross section- and Λ-limits as derived from the three-body invariant mass, $M^{\mu\mu\gamma}$.

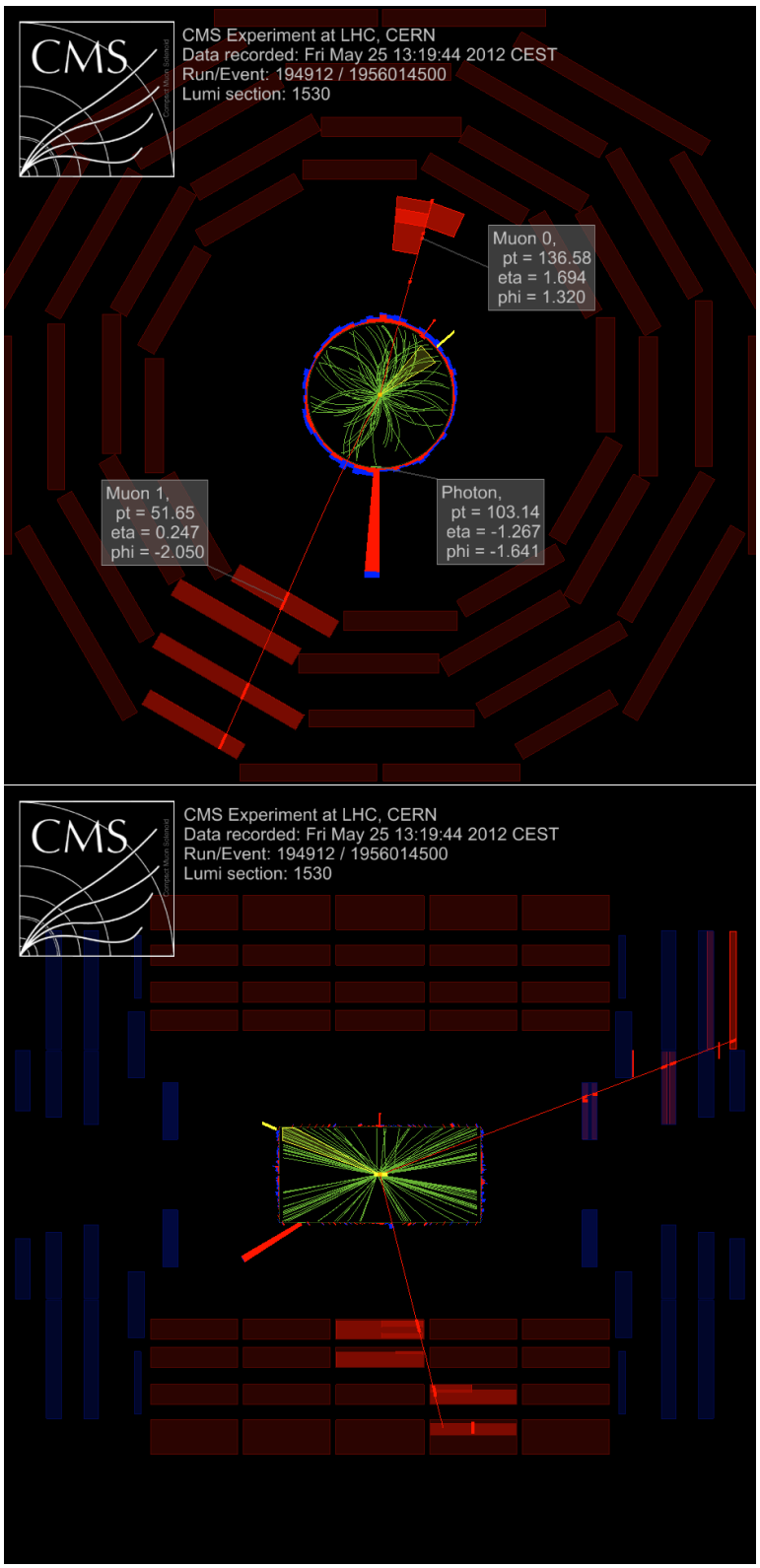

Figure 6.24: Event display of the $\mu\mu\gamma$-event with the highest maximum invariant mass ($M^{\mu\gamma}_{max} = 548.3\,GeV$) as found in the Run I analysis, after applying all selections, including the Z-veto.

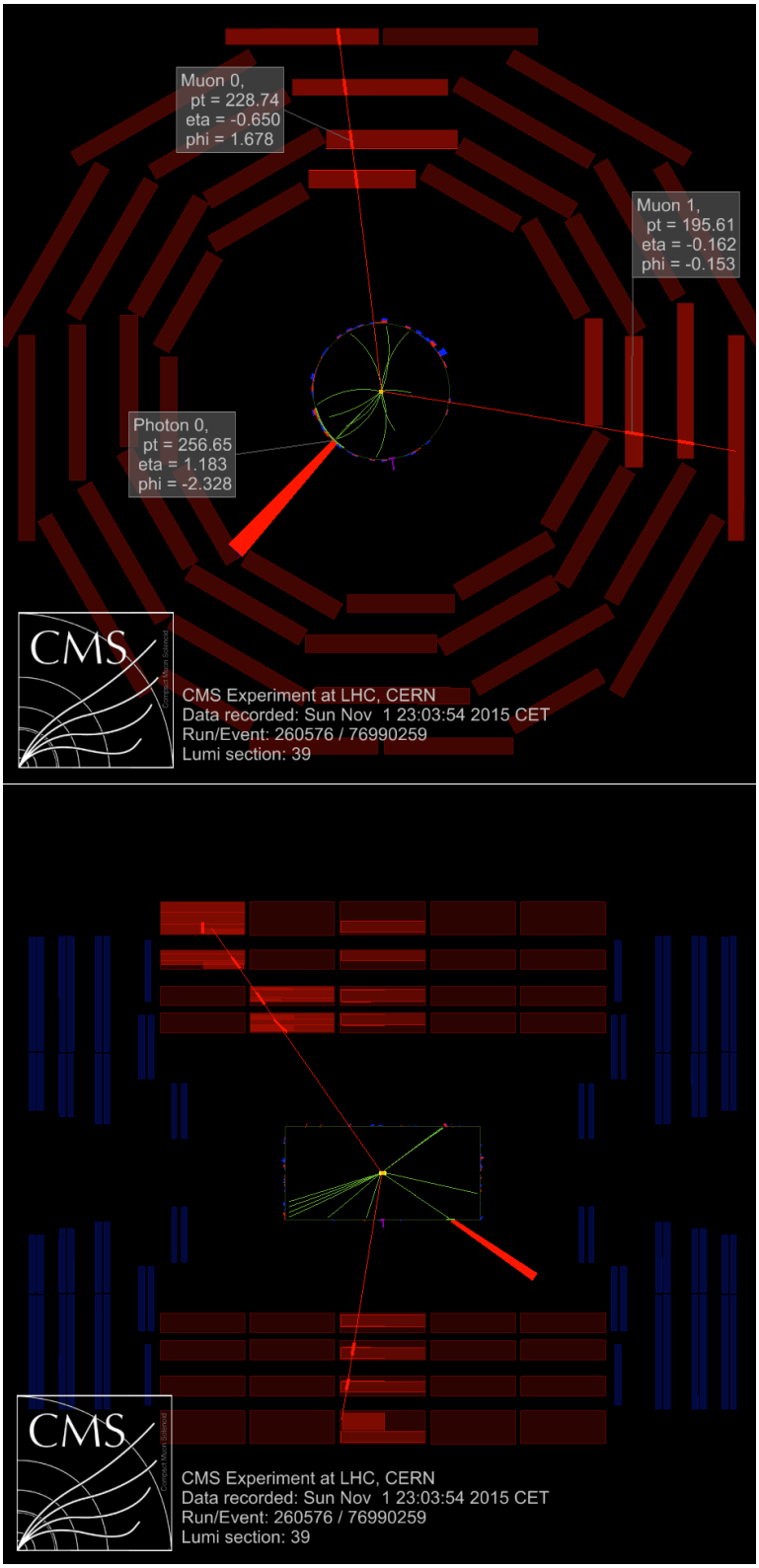

Figure 6.25: Event display of the $\mu\mu\gamma$-event with the highest maximum invariant mass ($M^{\mu\gamma}_{max} = 672.8\,GeV$) as found in the Run II analysis, after applying all selections, including the Z-veto.

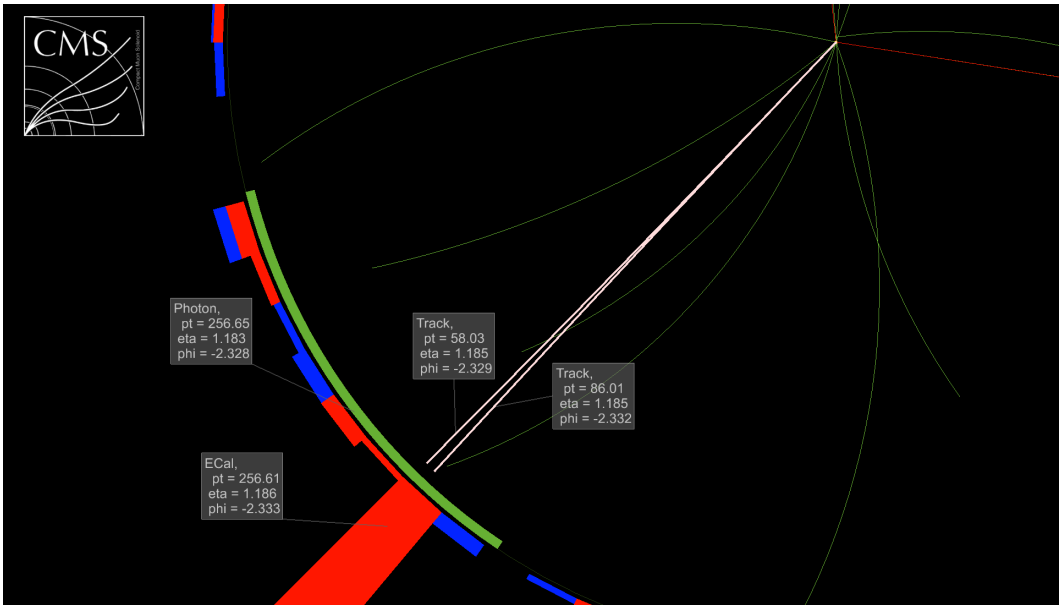

Figure 6.26: Detailed view into the transverse plane of the event from figure 6.25 with focus on the photon, its main ECal deposit, and the tracks pointing into the same direction.

7 | Conclusions

In this thesis, the search for excited muons in the channel $q\bar{q} \to \mu\mu^* \to \mu\mu\gamma$ using CMS data was presented. Two similar analyses were described, both relying on CMS data; i.e. $19.7\,\text{fb}^{-1}$ of data, taken at $\sqrt{s} = 8\,\text{TeV}$, and $2.7\,\text{fb}^{-1}$ at $\sqrt{s} = 13\,\text{TeV}$, respectively. In the considered signal model, excited muons are produced in association with an ordinary muon in a four-fermion contact interaction (CI), and decay under gauge-mediated emission of a photon. Investigating the signal properties, it was found that due to the associated production, the potential signal mass can be reconstructed and identified in a two-dimensional mass plane. The resulting characteristic mass distribution has the shape of an inverted "L" and can thus be used to efficiently distinguish between a possible signal and the standard model background that is dominated by $Z\gamma$-contributions. By optimizing individual search regions, it is possible to scan a wide parameter space for a possible excited muon signal.

No significant deviation from the Standard Model background could be found. Thus, limits on the excited muon cross section could be set. Masses from 200 GeV up to 2.5 (3.0) TeV could be excluded for the case $M_{\mu^*} = \Lambda$ for the Run I (Run II) analysis. By generalizing the results into the $M_{\mu^*} - \Lambda$ plane, values of Λ could be excluded up to 17 (15) TeV at low signal masses. By combining both results, this exclusion could be extended up to 19 TeV. These results are summarized in figure 7.1(a).

These results were determined for the case $f = f' = 1$. Limits were determined from the results of other searches for excited leptons, including excited electrons that decay under the emission of a Z-boson. Thus, excited electrons and muons could be excluded for masses up to 2.4 TeV for the case $M_{\mu^*} = \Lambda$ and $f = -f' = 1$. The latter analyses were performed with Run I data, exclusively, and are summarized in figure 7.1(b).

With the efficient selection it was possible to obtain the most stringent limits on excited muons (and electrons with Run I data) decaying via photon radiation. However, in the future of searches for lepton substructure, it might become beneficial to consider decays via contact interaction to push the boundaries of the case $M_{\mu^*} = \Lambda$. Still, such a search will hardly be able to challenge the high reach in Λ at low masses that is given by the approach that is described in this thesis.

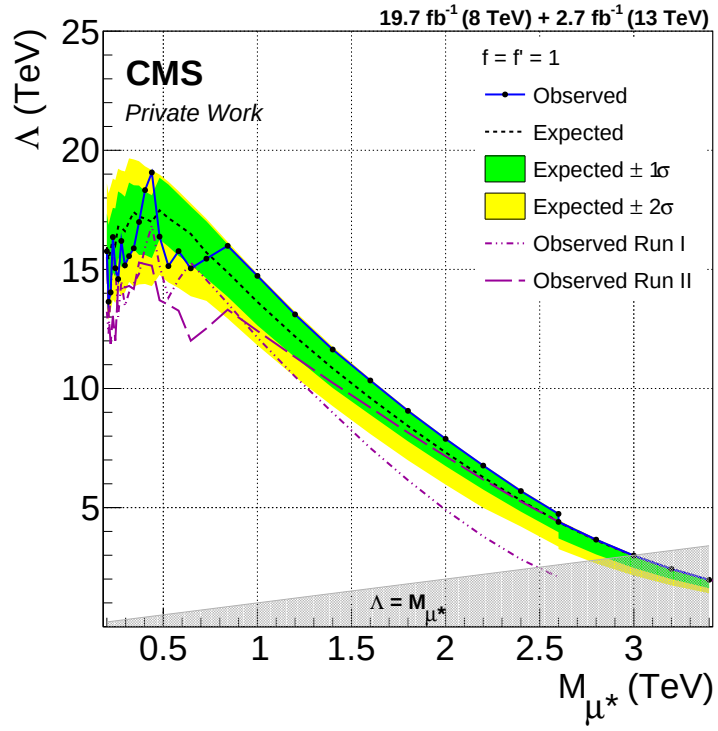

(a)

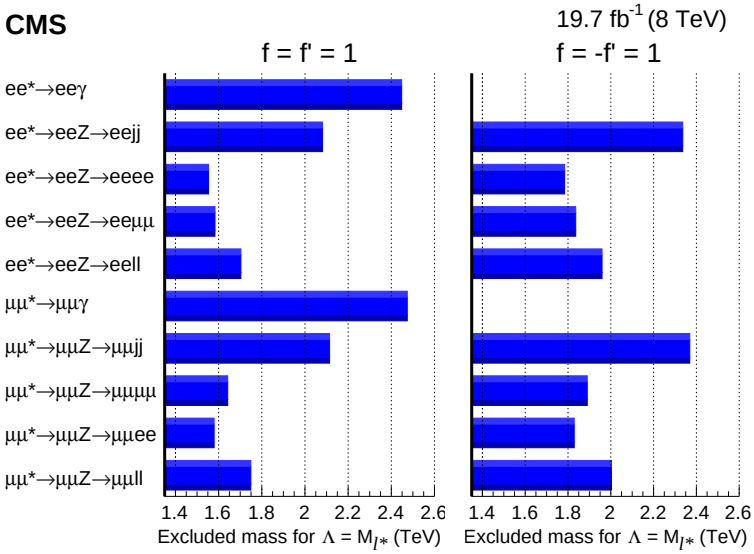

(b)

Figure 7.1: Final results: (a) Excluded parameter space obtained from the Run I and Run II searches for excited muons in the $\mu\mu\gamma$-final state, assuming $f = f' = 1$. (b) Summary of the excluded excited electron and -muon masses for the special case, where $M_{\ell^*} = \Lambda$, as obtained from various searches with Run I data. Here, the cases $f = f' = 1$ and $f = -f' = 1$ are taken into account.

A | Monte Carlo Samples

Here, the signal- and background samples are listed, that are used in both analyses. The signal samples are named

- /pythia_mustar_L10000_m*_GEN_SIM_pythia8175_v1/cmkuo-pythia_mustar_L10000_m*_RECO_v3-3664d28163503ca8171ba37083c39fc9/USER
- /Mustar_MuG_L10000_m*_13TeV-pythia8/RunIIFall15MiniAODv2-PU25nsData2015v1_76X_mcRun2_asymptotic_v12-v1/MINIAODSIM

for Run I and Run II, respectively. Thereby, m* is the mass of the considered sample, being in the range of 200-2600 GeV with a 200 GeV spacing for Run I, and between 250 GeV and 4 TeV with a spacing of 250 GeV for Run II.

For reasons of space, the table with the background samples can be found on the following page. Besides the process, the full sample names and the corresponding cross sections are given.

Run I		
Process	Sample	σ (pb)
$Z\gamma \to \mu\mu\gamma$	/8TeV_MuMuG_ISR_GPt10_Sherpa_SIM/hindrich-MuMuG_ISR_GPt10_8TeV_Sherpa	
	_AOD53_v1-7d29be866a1280479bdc4dddc0d18345/USER	14.9
$t\bar{t}\gamma \to$ incl. $+\gamma$	/TTGJets_8TeV-madgraph/Summer12_DR53X-PU_S10_START53_V7A-v1/AODSIM	1.44
WW $\to$ incl.	/WW_TuneZ2star_8TeV_pythia6_tauola/Summer12_DR53X-PU_S10_START53_V7A-v1/AODSIM	56.0
WZ $\to$ incl.	/WZ_TuneZ2star_8TeV_pythia6_tauola/Summer12_DR53X-PU_S10_START53_V7A-v1/AODSIM	23.7
ZZ $\to$ incl.	/ZZ_TuneZ2star_8TeV_pythia6_tauola/Summer12_DR53X-PU_S10_START53_V7A-v1/AODSIM	17.0
DY+Jets$\to \ell\ell$	/DYJetsToLL_M-50_TuneZ2Star_8TeV-madgraph-tarball/Summer12_DR53X-PU_S10_START53_V7A-v1/AODSIM	3531.9
Run II		
Process	Sample	σ (pb)
$Z\gamma \to \ell\ell\gamma$	/ZGTo2LG_TuneCUETP8M1_13TeV-amcatnloFXFX-pythia8/RunIIFall15MiniAODv1-PU25nsData2015v1_76X_mcRun2_asymptotic_v12-v1/MINIAODSIM	117.9
$Z\gamma \to \ell\ell\gamma$	/ZLLGJets_MonoPhoton_PtG-130_TuneCUETP8M1_13TeV-madgraph/RunIIFall15MiniAODv2-PU25nsData2015v1_76X_mcRun2_asymptotic_v12-v1/MINIAODSIM	0.143
$Z \to \mu\mu$	/ZToMuMu_NNPDF30_13TeV-powheg_M_50_120/RunIIFall15MiniAODv2-PU25nsData2015v1_76X_mcRun2_asymptotic_v12-v1/MINIAODSIM	1975.
$Z \to \mu\mu$	/ZToMuMu_NNPDF30_13TeV-powheg_M_120_200/RunIIFall15MiniAODv2-PU25nsData2015v1_76X_mcRun2_asymptotic_v12-v1/MINIAODSIM	19.32
$Z \to \mu\mu$	/ZToMuMu_NNPDF30_13TeV-powheg_M_200_400/RunIIFall15MiniAODv2-PU25nsData2015v1_76X_mcRun2_asymptotic_v12-v1/MINIAODSIM	2.731
$Z \to \mu\mu$	/ZToMuMu_NNPDF30_13TeV-powheg_M_400_800/RunIIFall15MiniAODv2-PU25nsData2015v1_76X_mcRun2_asymptotic_v12-v1/MINIAODSIM	0.241
$Z \to \mu\mu$	/ZToMuMu_NNPDF30_13TeV-powheg_M_800_1400/RunIIFall15MiniAODv2-PU25nsData2015v1_76X_mcRun2_asymptotic_v12-v1/MINIAODSIM	0.01678
$Z \to \mu\mu$	/ZToMuMu_NNPDF30_13TeV-powheg_M_1400_2300/RunIIFall15MiniAODv2-PU25nsData2015v1_76X_mcRun2_asymptotic_v12-v1/MINIAODSIM	0.00139
$Z \to \mu\mu$	/ZToMuMu_NNPDF30_13TeV-powheg_M_2300_3500/RunIIFall15MiniAODv2-PU25nsData2015v1_76X_mcRun2_asymptotic_v12-v1/MINIAODSIM	8.948e-05
$Z \to \mu\mu$	/ZToMuMu_NNPDF30_13TeV-powheg_M_3500_4500/RunIIFall15MiniAODv2-PU25nsData2015v1_76X_mcRun2_asymptotic_v12-v1/MINIAODSIM	4.135e-06
$Z \to \mu\mu$	/ZToMuMu_NNPDF30_13TeV-powheg_M_4500_6000/RunIIFall15MiniAODv2-PU25nsData2015v1_76X_mcRun2_asymptotic_v12-v1/MINIAODSIM	4.135e-07
$Z \to \mu\mu$	/ZToMuMu_NNPDF30_13TeV-powheg_M_6000_Inf/RunIIFall15MiniAODv2-PU25nsData2015v1_76X_mcRun2_asymptotic_v12-v1/MINIAODSIM	2.066e-08
$t\bar{t} \to 2\ell 2\nu$	/TTTo2L2Nu_13TeV-powheg/RunIIFall15MiniAODv2-PU25nsData2015v1_76X_mcRun2_asymptotic_v12-v1/MINIAODSIM	87.31
$t\bar{t}\gamma \to$ incl. $+\gamma$	/TTGJets_TuneCUETP8M1_13TeV-amcatnloFXFX-madspin-pythia8/RunIIFall15MiniAODv2-PU25nsData2015v1_76X_mcRun2_asymptotic_v12-v1/MINIAODSIM	3.697
WW $\to$ incl.	/WW_TuneCUETP8M1_13TeV-pythia8/RunIIFall15MiniAODv2-PU25nsData2015v1_76X_mcRun2_asymptotic_v12-v1/MINIAODSIM	63.21
WZ $\to$ incl.	/WZ_TuneCUETP8M1_13TeV-pythia8/RunIIFall15MiniAODv2-PU25nsData2015v1_76X_mcRun2_asymptotic_v12-v1/MINIAODSIM	47.13
ZZ $\to$ incl.	/ZZ_TuneCUETP8M1_13TeV-pythia8/RunIIFall15MiniAODv2-PU25nsData2015v1_76X_mcRun2_asymptotic_v12-v1/MINIAODSIM	16.523
Cosmics		
p_T-bin (GeV)	Sample	
$10 - 100$	/TKCosmics_p10/Summer12-CosmicSuperPointing-COSMC_53_PEAC_cosmics-v1/GEN-SIM-RAW-RECO	
$100 - 500$	/TKCosmics_p100/Summer12-CosmicSuperPointing-COSMC_53_PEAC_cosmics-v1/GEN-SIM-RAW-RECO	
$500 - \infty$	/TKCosmics_p500/Summer12-CosmicSuperPointing-COSMC_53_PEAC_cosmics-v1/GEN-SIM-RAW-RECO	

Table A.1: Background samples as used in the Run I (Run II) analysis in the upper (middle) part of the table. Below: Cosmic MC samples.

B | Data-MC Scalefactors

In this chapter, the scalefactors that were used in the two analyses are presented. Scalefactors are used to account for differences between the simulation and measured data. The numbers shown here were not obtained by the author but determined by groups within the CMS-Collaboration and then provided to the analysts. In most cases they are evaluated depending on particle properties like transverse momentum or pseudorapidity. To apply those factors, MC is weighted event-by-event, applying the factors depending on the particle kinematics. The impact of the uncertainties is estimated by additionally wheighting up- and downwards by the value. Scalefactors are usually close to one, and, within their uncertainties, often compatible with one. As in most cases the range of the provided numbers is restricted (usually some few hundred GeV in p_{T}), events are weighted with the highest available bin, if the particle properties exceed such thresholds. The corresponding references are given in the caption of the respective figure.

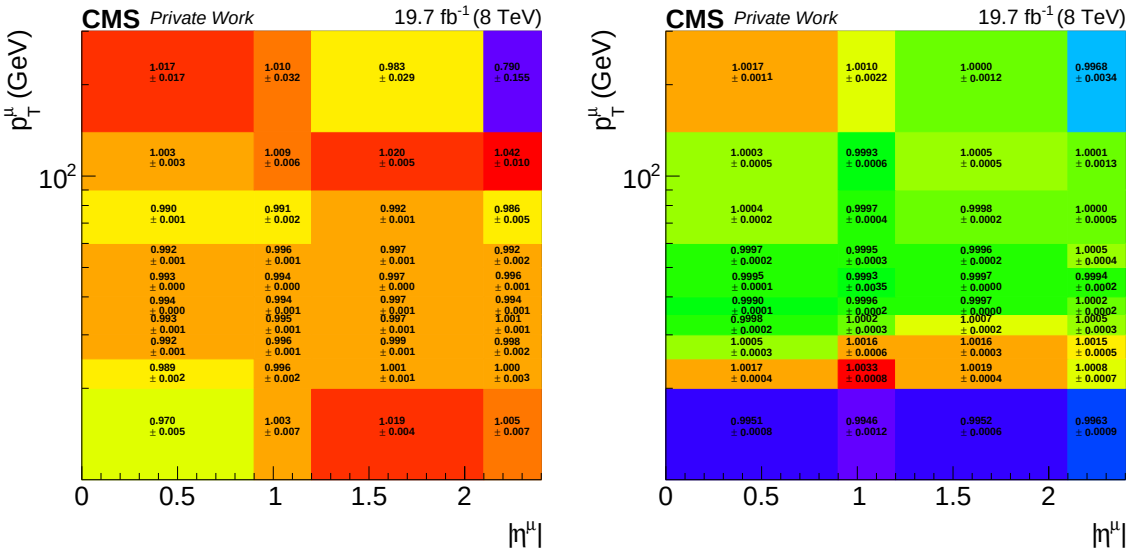

Figure B.1: Scalefactors for the High-p_{T} muon ID (left) and the relative tracker isolation for muons (right) as they are applied in **Run I** analyses [88].

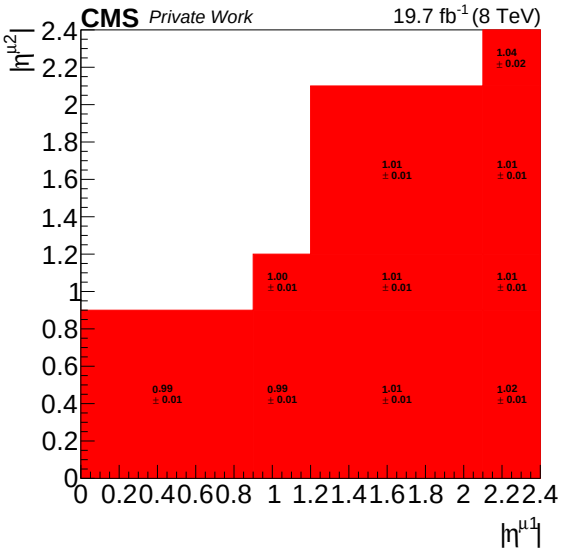

Figure B.2: Scalefactors for the di-muon trigger of the **Run I** analysis. An additional systematic uncertainty of 0.8% is applied [88].

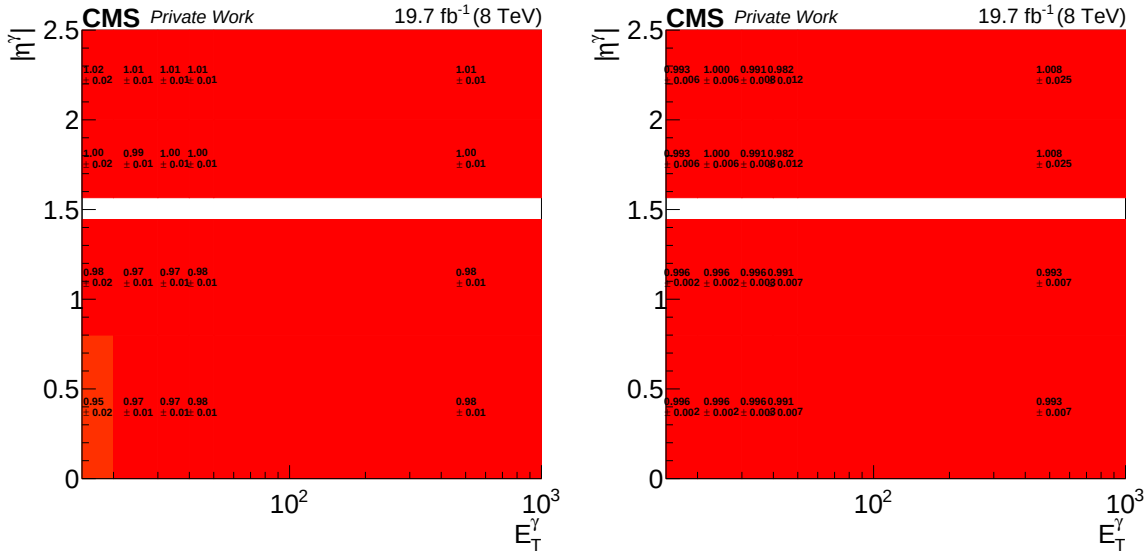

Figure B.3: For **Run I**, scalefactors are provided separately for the simple cut based photon ID, tight working point (left) and the conversion safe electron veto (right) [102].

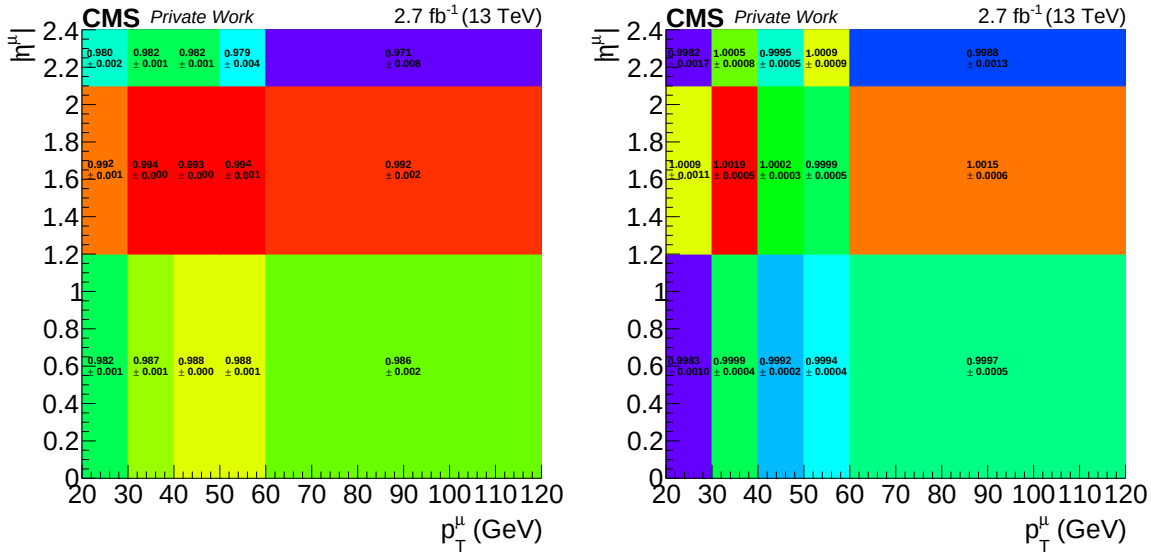

Figure B.4: Scalefactors for the High-$p_T$muon ID (left) and the relative tracker isolation for muons (right) as they are applied in **Run II** analyses. Additional systematic uncertainties of 1% for the ID and 0.5% for the isolation are applied [89].

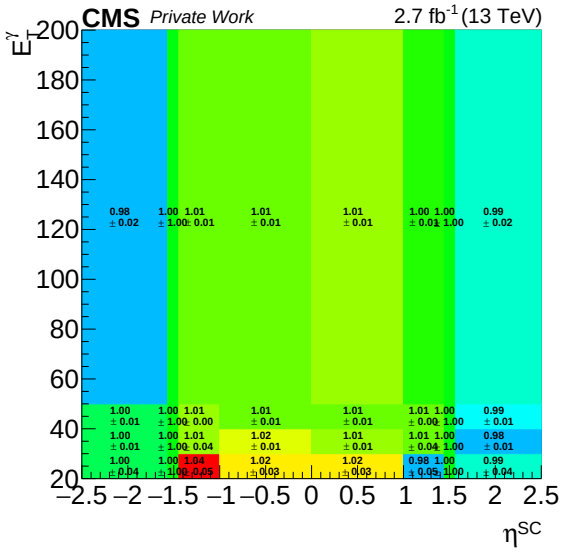

Figure B.5: Scalefactors for the MVA photon ID of **Run II** analyses [165].

C | Excited Lepton Candidate Events

In this chapter, all events are listed that pass all selections, including the Z-veto but before the final L-shape requirement. The exact identification in terms of Run-, Lumi Section- (LS), and Run number are given, as well as the maximum and minimum invariant muon-photon masses, and the three-body invariant mass. Events from the Run I analysis can be found in table C.1, those from Run II are listed in C.2.

Run	LS	Event	$M^{\mu\gamma}_{min}$ (GeV)	$M^{\mu\gamma}_{max}$ (GeV)	$M^{\mu\mu\gamma}$ (GeV)
191834	344	402307809	147.851	208.214	317.906
193621	66	24928734	104.889	318.418	519.674
193575	512	392764493	116.825	368.245	526.729
194120	323	239165852	145.957	249.956	407.821
194050	456	441649550	320.869	539.926	639.164
194050	270	262330893	43.7117	131.334	213.739
195937	228	185824039	32.1274	137.608	206.686
195950	951	870019227	34.1178	163.144	206.555
195552	1097	1322776900	69.5907	92.3521	193.642
195775	93	87082286	89.4244	119.807	191.197
194479	544	600794012	123.629	130.918	313.822
195304	906	1023521558	253.35	396.442	507.617
196239	692	631686723	70.7259	139.16	200.31
194789	547	664535209	161.576	224.039	394.27
195113	180	233975889	133.933	162.18	395.527
194912	1530	1956014500	125	548.342	601.403
194691	131	156700596	36.4191	143.656	197.066
194912	1180	1643467189	144.594	158.054	291.949
196453	331	305544847	110.936	134.792	212.404
195916	173	166107546	91.6639	128.89	326
196203	4	2692447	161.544	191.662	318.059
196218	536	789930803	216.292	334.501	505.14
195540	83	47518833	45.2723	160.915	256.202
196438	2	1267032	78.4015	221.95	379.359
195304	912	1027876064	92.8705	157.741	229.012
196453	327	302606561	97.4221	121.115	228.221
194699	4	3904544	46.8868	128.61	191.475
195016	365	406776068	128.268	197.743	296.195
199752	256	313187177	48.2398	130.164	185.165
201196	774	591520074	81.8184	490.814	567.029
201168	244	270085658	86.8031	149.843	301.757
201278	276	381516891	211.95	302.636	450.517
199436	189	135819324	74.9456	189.092	276.579
200991	481	623450338	85.4831	157.462	330.052
198955	837	935110671	90.4126	181.03	241.001
198955	29	36304047	66.0153	162.489	258.688
199703	63	58026472	53.9687	172.239	214.912
201602	297	400036442	158.638	197.879	284.73
200491	106	83376207	88.837	116.434	272.716
202087	1004	1143131833	102.677	109.4	193.534
199572	140	122807135	87.6013	141.352	272.068
201191	221	322573197	63.9179	125.817	334.214
201729	189	284811280	121.106	163.397	368.351
201625	777	1006267478	128.522	159.455	240.761
200525	834	1030974629	47.4326	127.721	223.499
202013	10	16762459	59.4261	155.01	210.306
199608	289	345563496	59.681	221.426	274.472
199833	1100	1175743218	118.773	300.664	345.813
200042	421	342360676	80.7377	135.813	220.673
199754	115	131184725	113.493	150.387	231.662
202272	283	330019909	87.4389	115.455	259.901
202087	983	1123178801	125.386	270.996	396.323
202060	523	659809393	94.127	203.03	271.635
199428	511	615901669	170.047	278.518	553.815
200991	225	322945108	130.401	288.527	544.739
202504	167	193418803	32.7631	166.087	232.969
202060	494	625974666	96.7845	256.495	304.352
199571	412	437877504	97.9896	351.477	431.726
201168	589	645049964	35.0416	145.577	200.166
202237	997	1320939561	69.0209	125.718	236.866
199804	411	478022152	140.636	362.787	457.308
201159	82	40472593	176.328	181.433	399.572
200369	492	525956378	197.004	229.321	326.961
198487	876	968162088	164.987	243.122	439.708
202272	811	928485421	87.4614	105.236	186.793
199608	170	184876520	74.4369	167.056	241.561
199021	870	1018569477	56.9551	179.07	285.097
201097	291	383536695	118.042	172.802	247.812
199428	95	93863988	165.704	200.187	292.666
200525	125	113982155	144.467	158.168	276.597
202478	917	948218632	47.8851	162.878	212.859
201278	326	455016870	50.388	204.692	268.946
198969	330	436641666	81.9768	144.543	286.541

199319	30	48952177	81.5499	171.685	280.376
202093	192	133732312	58.0635	210.469	341.782
199698	102	92193674	44.5857	118.16	181.06
202237	89	111457086	76.255	119.893	211.165
201706	33	53549234	59.2591	184.953	240.002
199319	466	643350422	162.195	257.824	410.207
202237	845	1162578804	62.0143	130.45	223.468
202305	317	287865807	84.196	222.713	298.786
199429	96	107852979	89.5272	114.065	272.292
205344	49	59551504	96.9037	303.799	368.502
202972	375	496023322	110.174	185.042	258.511
204564	543	597369540	140.858	208.49	332.728
198487	1349	1378544001	73.7279	213.234	317.578
199973	74	29816453	98.0462	131.89	228.476
205921	324	496041560	85.0607	132.232	247.757
206448	408	397575599	286.176	309.531	464.185
201678	69	62536881	42.89	125.277	193.704
204576	205	311716181	118.511	182.048	329.502
205694	390	408290517	66.9083	118.462	244.928
208429	192	216147671	159.35	179.391	294.694
206512	657	849593372	137.718	216.361	297.563
206210	312	287575476	261.415	338.493	476.275
205683	302	392618903	67.529	211.945	506.28
206512	101	64630152	131.114	145.628	236.502
207099	799	1084616700	95.9441	131.531	208.569
204250	279	365997484	53.4007	66.1735	157.462
207491	310	318069632	121.457	193.872	543.786
206866	129	137607062	180.75	183.642	310.693
207492	193	159655736	78.4494	277.965	355.627
204114	229	247759118	71.3587	99.8137	232.616
206745	583	640337666	121.749	156.923	234.255
206246	1263	1032844741	36.2405	114.592	198.467
204113	476	716519387	118.041	186.287	531.62
205666	219	339319334	62.2296	141.943	198.363
206745	1756	1590756660	36.851	133.844	183.554
206066	138	131688278	104.678	252.729	354.48
205781	143	234932733	98.9832	121.987	210.729
204250	718	912533868	205.996	264.542	404.797
208427	306	488063569	97.8478	139.793	219.936
208551	456	731107834	145.005	169.732	267.102
206446	203	262887548	167.307	173.418	282.625
205774	13	20931830	32.6827	124.168	181.048
205667	537	574443088	70.248	114.282	184.578
206302	160	255479991	95.4673	144.491	250.838
207477	305	481898432	89.1464	116.175	254.297
207099	569	814021560	93.1596	133.73	213.866
206595	92	136304839	211.498	229.013	516.833
205666	256	401648017	91.3187	148.074	211.837
207231	1451	1818332843	155.462	195.47	279.251
206243	169	238712574	32.43	125.971	186.435
205111	360	506089066	32.4606	125.797	231.383
206869	512	489507290	58.3107	121.929	187.446
207905	176	218309434	81.3848	97.6275	183.33
207920	131	149676350	67.4293	180.878	292.278
206859	660	967864303	102.324	201.533	298.445
207454	869	1203693222	56.1133	131.124	202.488
207920	146	180419261	80.4685	128.961	388.091
208551	521	819832853	105.23	167.79	349.171
206859	371	562811942	84.4958	126.731	229.305
207477	418	663471552	73.7763	163.058	251.879
207515	685	1039835320	151.8	166.719	264.121
206208	437	474685895	102.73	114.572	209.656
206513	88	85992875	120.429	315.192	402.636
205921	257	402402077	75.3043	206.77	424.949
206303	254	301376642	63.3655	107.62	172.121
207515	958	1357343794	182.414	294.035	418.777
206476	185	237762374	77.5522	145.68	213.82
207320	57	48330169	51.7573	122.14	207.587
206484	120	116805749	61.7928	132.386	260.84
194533	347	486522618	177.27	260.701	401.253
194711	595	500097331	134.04	216.465	293.798
195397	359	533707589	83.2171	108.697	192.925
208353	78	99159598	52.2916	99.8416	164.33
196452	715	980523025	51.8706	175.134	301.409
194076	236	255457212	110.977	118.295	222.612
194050	1797	1556881038	74.2058	99.7711	173.981
201278	337	470817419	93.9355	97.1604	237.106

Table C.1: Properties of all Run I events that remain after all selections, including the Z-veto, but no L-shapes. (LS = Lumi Section)

Run	LS	Event	$M^{\mu\gamma}_{min}$ (GeV)	$M^{\mu\gamma}_{max}$ (GeV)	$M^{\mu\mu\gamma}$ (GeV)
258706	98	173721983	31.5	111.7	175.2
258749	145	227550579	63.2	159.4	242.1
256843	1196	1637575297	149.3	207.5	412.4
258440	100	152202498	171.1	216.7	551.0
260425	110	190094140	116.3	241.5	547.6
258694	111	201720160	188.2	232.2	400.9
258705	91	164408165	59.9	110.0	190.4
260577	19	36903056	117.7	181.6	248.9
260424	569	1056124055	124.6	161.7	283.1
259809	61	52880591	56.5	218.4	411.5
258177	1605	2220195304	140.2	613.1	848.4
257487	662	1153717639	75.7	134.5	289.3
258425	100	180251608	91.0	135.5	205.6
259811	78	145856657	86.6	86.8	185.1
257822	168	250705330	155.8	251.5	427.9
257969	177	271428031	82.8	153.9	351.1
257751	387	579097066	70.8	105.5	194.6
258177	1169	1663268948	58.1	115.0	176.4
259686	68	127316468	476.7	490.8	697.3
258158	1138	1736298526	177.9	185.3	283.3
258177	1008	1449424801	73.4	243.7	470.0
258742	97	179860218	59.7	272.5	361.7
256729	1255	1764024879	145.1	158.1	270.2
260575	15	18996898	87.6	237.3	361.2
257751	27	40248521	133.3	327.5	388.9
258745	63	103650456	76.3	113.6	179.8
257487	356	618203373	81.3	226.0	288.0
258742	150	278343155	44.5	133.7	260.5
259862	124	208222269	70.7	99.4	176.1
258749	156	244710990	168.8	214.1	347.5
257613	384	606871497	98.0	138.3	267.9
258177	543	803454670	84.8	162.0	233.6
258712	189	301465371	51.7	128.5	222.2
258702	284	461419137	72.8	169.5	234.8
258742	621	1113645097	72.4	115.2	181.7
258440	93	141925512	290.0	350.2	702.2
260576	39	76990259	512.6	672.8	915.9
259637	28	43715074	62.9	148.3	235.4
257822	881	1226649473	35.5	217.1	332.3
257613	326	515162417	67.8	244.5	294.3
256729	1704	2349692056	60.2	105.8	173.6

Table C.2: Properties of all Run II events that remain after all selections, including the Z-veto, but no L-shapes. (LS = Lumi Section)

Bibliography

[1] I. Kant, "Kritik der reinen Vernunft". Number 978-3-86647-408-6. Anaconda, Köln, 2009. Vollst. Ausg. nach der zweiten, hin und wieder verb. Aufl. 1787, vermehrt um die Vorr. zur ersten Aufl. 1781.

[2] CMS Collaboration, "Search for excited leptons in proton proton collisions at $\sqrt{s} = 8$ TeV", CMS Physics Analysis Summary CMS-PAS-EXO-14-015, CERN, Geneva, 2015.

[3] CMS Collaboration, "Search for excited leptons in proton-proton collisions at $\sqrt{s} = 8$ TeV", *JHEP* 03 (2016) 125, arXiv:1511.01407. doi:10.1007/JHEP03(2016)125.

[4] CMS Collaboration, "Search for excited leptons in the $\ell\ell\gamma$ final state at $\sqrt{s} = 13$ TeV", CMS Physics Analysis Summary CMS-PAS-EXO-16-009, CERN, Geneva, 2016.

[5] D. Griffiths, "Introduction to Elementary Particles", *Weinheim, Germany: Wiley-VCH 454 p* (2008). ISBN-9783527406012.

[6] Particle Data Group Collaboration, "Review of Particle Physics", *Chin. Phys. C* 38 (2014) 090001. doi:10.1088/1674-1137/38/9/090001.

[7] V. N. Aseev, A. I. Belesev, A. I. Berlev et al., "Upper limit on the electron antineutrino mass from the Troitsk experiment", *Phys. Rev. D* 84 (Dec, 2011) 112003. doi:10.1103/PhysRevD.84.112003.

[8] E. Fermi, "Versuch einer Theorie der β-Strahlen. I", *Zeitschrift für Physik* 88 (1934), no. 3, 161–177. doi:10.1007/BF01351864.

[9] E. J. Eichten, K. D. Lane, and M. E. Peskin, "New Tests for Quark and Lepton Substructure", *Phys. Rev. Lett.* 50 (Mar, 1983) 811–814. doi:10.1103/PhysRevLett.50.811.

[10] F. E. Low, "Heavy Electrons and Muons", *Phys. Rev. Lett.* 14 (Feb, 1965) 238–239. doi:10.1103/PhysRevLett.14.238.

[11] F. Renard, "Limits on masses and couplings of excited electrons and muons", *Physics Letters B* 116 (1982), no. 4, 264 – 268. doi:http://dx.doi.org/10.1016/0370-2693(82)90339-2.

[12] S. J. Brodsky and S. D. Drell, "Anomalous magnetic moment and limits on fermion substructure", *Phys. Rev. D* 22 (Nov, 1980) 2236–2243. doi:10.1103/PhysRevD.22.2236.

[13] N. Cabibbo, L. Maiani, and Y. Srivastava, "Anomalous Z decays: excited leptons?", *Physics Letters B* 139 (1984), no. 5, 459 – 463. doi:http://dx.doi.org/10.1016/0370-2693(84)91850-1.

[14] A. de Rujula, L. Maiani, and R. Petronzio, "Search for excited quarks", *Physics Letters B* 140 (1984), no. 3, 253 – 258. doi:http://dx.doi.org/10.1016/0370-2693(84)90930-4.

[15] J. Kühn and P. Zerwas, "Excited quarks and leptons", *Physics Letters B* 147 (1984), no. 1, 189 – 196. doi:http://dx.doi.org/10.1016/0370-2693(84)90618-X.

[16] J. Kühn, H. Tholl, and P. Zerwas, "Signals of excited quarks and leptons", *Physics Letters B* 158 (1985), no. 3, 270 – 275. doi:http://dx.doi.org/10.1016/0370-2693(85)90969-4.

[17] K. Hagiwara, D. Zeppenfeld, and S. Komamiya, "Excited Lepton Production at LEP and HERA", *Z. Phys.* C29 (1985) 115. doi:10.1007/BF01571391.

[18] F. Boudjema, A. Djouadi, and J. L. Kneur, "Excited fermions at e^+e^- and eP colliders", *Zeitschrift für Physik C Particles and Fields* 57 (1993), no. 3, 425–449. doi:10.1007/BF01474339.

[19] O. Cakir, C. Leroy, R. R. Mehdiyev et al., "Production and decay of excited electrons at the LHC", *Eur. Phys. J.direct* C30 (2003) 005, arXiv:hep-ph/0212006. [Eur. Phys. J.C32,no.S2,1(2004)]. doi:10.1140/epjcd/s2003-01-005-5.

[20] O. J. P. Eboli, S. M. Lietti, and P. Mathews, "Excited leptons at the CERN large hadron collider", *Phys. Rev.* D65 (2002) 075003, arXiv:hep-ph/0111001. doi:10.1103/PhysRevD.65.075003.

[21] U. Baur, M. Spira, and P. M. Zerwas, "Excited-quark and -lepton production at hadron colliders", *Phys. Rev. D* 42 (Aug, 1990) 815–824. doi:10.1103/PhysRevD.42.815.

[22] UA1 Collaboration, "Experimental observation of lepton pairs of invariant mass around $95\,\mathrm{GeV}/c^2$ at the CERN SPS collider", *Physics Letters B* 126 (1983), no. 5, 398 – 410. doi:http://dx.doi.org/10.1016/0370-2693(83)90188-0.

[23] UA2 Collaboration, "Evidence for $Z^0 \to e^+e^-$ at the CERN pp collider", *Physics Letters B* 129 (1983), no. 1, 130 – 140. doi:http://dx.doi.org/10.1016/0370-2693(83)90744-X.

[24] R. H. Kleiss and P. M. Zerwas, "Excited quarks and leptons at e^+e^- and pp colliders", in *Workshop on Physics at Future Accelerators, La Thuile, Italy*, number PITHA-87-29, p. 10 p. Jan, 1987.

[25] I. Bars and I. Hinchliffe, "Effects of quark compositeness at the Superconducting Super Collider", *Phys. Rev. D* 33 (Feb, 1986) 704–710. doi:10.1103/PhysRevD.33.704.

[26] HERA Collaboration, "Study on the proton electron storage ring project HERA". DESY, Hamburg, 1980. https://cds.cern.ch/record/101470.

[27] LEP Collaboration, "LEP Design Report: Vol.2. The LEP Main Ring". https://cds.cern.ch/record/102083, 1984.

[28] LEP Collaboration, C. Wyss, "LEP design report, v.3: LEP2". https://cds.cern.ch/record/314187, 1996. Vol. 1-2 publ. in 1983-84.

[29] "Design report Tevatron 1 Project", Technical Report FERMILAB-DESIGN-1984-01, Fermilab, 1984. https://cds.cern.ch/record/1478620.

[30] T. Sjöstrand, S. Mrenna, and P. Skands, "PYTHIA 6.4 physics and manual", *JHEP* 2006 (2006), no. 05, 026, arXiv:hep-ph/0603175. doi:10.1088/1126-6708/2006/05/026.

[31] T. Sjostrand, S. Mrenna, and P. Z. Skands, "A Brief Introduction to PYTHIA 8.1", *Comput. Phys. Commun.* 178 (2008) 852–867, arXiv:0710.3820. doi:10.1016/j.cpc.2008.01.036.

[32] S. Majhi, "QCD corrections to excited lepton (pair) production at the LHC", *Phys. Rev. D* 88 (Oct, 2013) 074028, arXiv:1210.8307. doi:10.1103/PhysRevD.88.074028.

[33] W. J. Stirling, "PARTON LUMINOSITY AND CROSS SECTION PLOTS". http://www.hep.ph.ic.ac.uk/~wstirlin/plots/plots.html. Private Communication.

[34] Mark J Collaboration, "Experimental Limits on the Production of Excited Leptons and Stable Heavy Leptons", *Phys. Rev. Lett.* 48 (Apr, 1982) 967–970. doi:10.1103/PhysRevLett.48.967.

[35] ALEPH Collaboration, "Search for excited leptons at $130 - 140\,\text{GeV}$", *Physics Letters B* 385 (1996), no. 1, 445 – 453. doi:10.1016/0370-2693(96)00961-6.

[36] DELPHI Collaboration, "Search for excited leptons in e^+e^- collisions at $\sqrt{s} = 189 - 209\,\text{GeV}$", *The European Physical Journal C - Particles and Fields* 46 (2006), no. 2, 277–293. doi:10.1140/epjc/s2006-02501-3.

[37] L3 Collaboration, "Search for excited leptons at LEP", *Physics Letters B* 568 (2003), no. 1-2, 23 – 34. doi:10.1016/j.physletb.2003.05.004.

[38] OPAL Collaboration, "Search for unstable heavy and excited leptons at LEP2", *The European Physical Journal C - Particles and Fields* 14 (2000), no. 1, 73–84. doi:10.1007/s100520000345.

[39] ZEUS Collaboration, "Searches for excited fermions in ep collisions at HERA", *Physics Letters B* 549 (2002), no. 1-2, 32 – 47. doi:10.1016/S0370-2693(02)02863-0.

[40] H1 Collaboration, "Search for excited electrons in ep collisions at HERA", *Physics Letters B* 666 (2008), no. 2, 131 – 139. doi:10.1016/j.physletb.2008.07.014.

[41] CDF Collaboration, "Search for Excited and Exotic Muons in the $\mu\gamma$ Decay Channel in $p\bar{p}$ Collisions at $\sqrt{s} = 1.96\,\text{TeV}$", *Phys. Rev. Lett.* 97 (Nov, 2006) 191802. doi:10.1103/PhysRevLett.97.191802.

[42] DØ Collaboration, "Search for excited muons in $p\bar{p}$ collisions at $\sqrt{s} = 1.96\,\text{TeV}$", *Phys. Rev. D* 73 (Jun, 2006) 111102. doi:10.1103/PhysRevD.73.111102.

[43] CMS Collaboration, "Search for excited leptons in pp collisions at $\sqrt{s} = 7$ TeV", *Physics Letters B* 720 (2013), no. 4–5, 309 – 329, arXiv:1210.2422. doi:http://dx.doi.org/10.1016/j.physletb.2013.02.031.

[44] ATLAS Collaboration, "Search for excited electrons and muons in $\sqrt{s} = 8\,\text{TeV}$ proton-proton collisions with the ATLAS detector", *New J. Phys.* 15 (2013) 093011, arXiv:1308.1364. doi:10.1088/1367-2630/15/9/093011.

[45] ATLAS Collaboration, "A search for an excited muon decaying to a muon and two jets in pp collisions at $\sqrt{s} = 8\,\text{TeV}$ with the ATLAS detector", *New Journal of Physics* 18 (2016), no. 7, 073021, arXiv:1601.05627. doi:10.1088/1367-2630/18/7/073021.

[46] CMS Collaboration, "Search for excited quarks in the photon + jet final state in proton proton collisions at 13 TeV", CMS Physics Analysis Summary CMS-PAS-EXO-16-015, CERN, Geneva, 2016.

[47] ATLAS Collaboration, "Search for new phenomena with photon+jet events in proton-proton collisions at $\sqrt{s} = 13\,\text{TeV}$ with the ATLAS detector", *JHEP* 2016 (2016), no. 3, 41, arXiv:1512.05910. doi:10.1007/JHEP03(2016)041.

[48] CMS Collaboration, "Search for excited quarks in the γ + jet final state in proton–proton collisions at $\sqrt{s} = 8\,\text{TeV}$", *Physics Letters B* 738 (2014) 274 – 293, arXiv:1406.5171. doi:10.1016/j.physletb.2014.09.048.

[49] L. Evans and P. Bryant, "LHC Machine", *JINST* 3 (2008), no. 08, S08001. doi:10.1088/1748-0221/3/08/S08001.

[50] M. Benedikt, P. Collier, V. Mertens et al., "LHC Design Report". https://cds.cern.ch/record/823808, 2004.

[51] ATLAS Collaboration, "The ATLAS Experiment at the CERN Large Hadron Collider", *JINST* 3 (2008) S08003. doi:10.1088/1748-0221/3/08/S08003.

[52] CMS Collaboration, "The CMS experiment at the CERN LHC", *JINST* 3 (2008) S08004. doi:10.1088/1748-0221/3/08/S08004.

[53] ALICE Collaboration, "The ALICE experiment at the CERN LHC", *JINST* 3 (2008) S08002. doi:10.1088/1748-0221/3/08/S08002.

[54] LHCb Collaboration, "The LHCb Detector at the LHC", *JINST* 3 (2008) S08005. doi:10.1088/1748-0221/3/08/S08005.

[55] TOTEM Collaboration, V. Berardi et al., "TOTEM: Technical design report. Total cross section, elastic scattering and diffraction dissociation at the Large Hadron Collider at CERN", technical report, 2004.

[56] TOTEM Collaboration, "The TOTEM experiment at the CERN Large Hadron Collider", *JINST* 3 (2008) S08007. doi:10.1088/1748-0221/3/08/S08007.

[57] LHCf Collaboration, "The LHCf detector at the CERN Large Hadron Collider", *JINST* 3 (2008) S08006. doi:10.1088/1748-0221/3/08/S08006.

[58] CERN, "The CERN accelerator complex". http://cdsweb.cern.ch/record/1260465, Accessed 2016/04/12.

[59] CMS Collaboration, "CMS-PHO-GEN-2012-002-5". http://cdsweb.cern.ch/record/1433717, Accessed 2016/04/14.

[60] CMS Collaboration, "The CMS tracker system project: Technical Design Report". https://cds.cern.ch/record/368412, 1997.

[61] CMS Collaboration, "The CMS electromagnetic calorimeter project: Technical Design Report". https://cds.cern.ch/record/349375, 1997.

[62] CMS Collaboration, "Performance of Photon Reconstruction and Identification with the CMS Detector in Proton-Proton Collisions at $\sqrt{s} = 8$ TeV", *JINST* 10 (2015), no. 08, P08010, arXiv:1502.02702. doi:10.1088/1748-0221/10/08/P08010.

[63] CMS Collaboration, "The CMS hadron calorimeter project: Technical Design Report". https://cds.cern.ch/record/357153, 1997.

[64] CMS Collaboration, "The CMS magnet project: Technical Design Report". https://cds.cern.ch/record/331056, 1997.

[65] CMS Collaboration, "The CMS muon project: Technical Design Report". https://cds.cern.ch/record/343814, 1997.

[66] CMS Collaboration, "Performance of CMS muon reconstruction in pp collision events at $\sqrt{s} = 7$ TeV", *JINST* 7 (2012), no. 10, P10002. doi:10.1088/1748-0221/7/10/P10002.

[67] I. Bird, K. Bos, N. Brook et al., "LHC computing Grid. Technical design report", technical report, Geneva, 2005.

[68] CMS Collaboration, "CMS Luminosity Based on Pixel Cluster Counting - Summer 2013 Update", CMS Physics Analysis Summary CMS-PAS-LUM-13-001, CERN, Geneva, 2013.

[69] S. van der Meer, "Calibration of the Effective Beam Height in the ISR", Technical Report CERN-ISR-PO-68-31. ISR-PO-68-31, CERN, Geneva, 1968.

[70] C. Barschel, M. Ferro-Luzzi, J.-J. Gras et al., "Results of the LHC DCCT Calibration Studies". https://cds.cern.ch/record/1425904, Feb, 2012.

[71] G. Anders, N. Bacchetta, V. Balagura et al., "STUDY OF THE RELATIVE LHC BUNCH POPULATIONS FOR LUMINOSITY CALIBRATION". https://cds.cern.ch/record/1427726, Feb, 2012.

[72] CMS Collaboration, "CMS Luminosity Measurement for the 2015 Data Taking Period", CMS Physics Analysis Summary CMS-PAS-LUM-15-001, CERN, Geneva, 2016.

[73] CMS Collaboration, "CMS DQM: Certification Run-I". /afs/cern.ch/cms/CAF/CMSCOMM/COMM_DQM/certification/Collisions12/8TeV/Reprocessing, Accessed 2016/06/12.

[74] CMS Collaboration, "CMS DQM: Certification Run-II". /afs/cern.ch/cms/CAF/CMSCOMM/COMM_DQM/certification/Collisions15/13TeV/Reprocessing, Accessed 2016/06/12.

[75] CMS Collaboration, "CMSSW: CMS Offline Software at github". https://github.com/cms-sw/cmssw.

[76] R. Brun and F. Rademakers, "ROOT: An object oriented data analysis framework", *Nucl. Instrum. Meth.* A389 (1997) 81–86. doi:10.1016/S0168-9002(97)00048-X.

[77] D. Binosi and L. Theußl, "JaxoDraw: A graphical user interface for drawing Feynman diagrams", *Computer Physics Communications* 161 (2004), no. 1–2, 76 – 86. doi:10.1016/j.cpc.2004.05.001.

[78] CMS Collaboration, "Particle-Flow Event Reconstruction in CMS and Performance for Jets, Taus, and MET", CMS Physics Analysis Summary CMS-PAS-PFT-09-001, CERN, Apr, 2009.

[79] CMS Collaboration, "Commissioning of the particle-flow event reconstruction with the first LHC collisions recorded in the CMS detector", CMS Physics Analysis Summary CMS-PAS-PFT-10-001, CERN, 2010.

[80] CMS Collaboration, "WorkBook: 7.8 Muon Analysis". https://twiki.cern.ch/twiki/bin/view/CMSPublic/WorkBookMuonAnalysis, Accessed 2016/04/15.

[81] R. Frühwirth, "Application of Kalman filtering to track and vertex fitting", *Nuclear Instruments and Methods in Physics Research Section A: Accelerators, Spectrometers, Detectors and Associated Equipment* 262 (Dec, 1987) 444–450. doi:10.1016/0168-9002(87)90887-4.

[82] CMS Collaboration, "Muon Reconstruction in the CMS Detector", CMS Analysis Note CMS-AN-2008/097, CERN, Geneva, 2008.

[83] CMS Collaboration, "Search for a Narrow Resonance Produced in 13 TeV pp Collisions Decaying to Electron Pair or Muon Pair Final States", CMS Physics Analysis Summary CMS-PAS-EXO-15-005, CERN, Geneva, 2015.

[84] CMS Collaboration, "Muon Reconstruction and Identification Improvements for Run-2 and First Results with 2015 Run Data". https://cds.cern.ch/record/2037372, 07, 2015.

[85] CMS Collaboration, "Search for physics beyond the standard model in dilepton mass spectra in proton-proton collisions at $\sqrt{s} = 8$ TeV", *JHEP* 04 (2015) 025, arXiv:1412.6302. doi:10.1007/JHEP04(2015)025.

[86] CMS Collaboration, "Baseline muon selections for Run-I". https://twiki.cern.ch/twiki/bin/view/CMSPublic/SWGuideMuonId, Accessed 2016/04/15.

[87] CMS Collaboration, "Baseline muon selections for Run-II". https://twiki.cern.ch/twiki/bin/view/CMS/SWGuideMuonIdRun2, Accessed 2016/04/15.

[88] CMS Collaboration, "Reference muon id and isolation efficiencies". https://twiki.cern.ch/twiki/bin/viewauth/CMS/MuonReferenceEffs, Accessed 2016/04/16.

[89] CMS Collaboration, "Reference muon id, isolation and trigger efficiencies for Run-II". https://twiki.cern.ch/twiki/bin/viewauth/CMS/MuonReferenceEffsRun2, Accessed 2016/04/16.

[90] CMS Collaboration, "Measurement of Momentum Scale and Resolution of the CMS Detector using Low-mass Resonances and Cosmic Ray Muons", CMS Physics Analysis Summary CMS-PAS-TRK-10-004, CERN, 2010. Geneva, 2010.

[91] N. Kypreos, "cosmic and generalized endpoint results on 2012 data". https://indico.cern.ch/getFile.py/access?contribId=4&resId=0&materialId=slides&confId=188598, 07, 2012. Talk in "Muon POG Meeting", Jul. 23rd 2012.

[92] S. Zaleski and J. Sturdy, "Constraining Muon pT Scale using Cosmic Endpoint Method using 2015 data and MC". https://indico.cern.ch/event/543050/contributions/2205538/attachments/1292158/1925076/CosmicEndpointUpdate_Jun6.pdf, 06, 2016. Talk in Meeting: "Discussion on high-pT muon performance studies", Jun 15th 2016.

[93] CMS Collaboration, "Reference muon momentum scale and resolution". https://twiki.cern.ch/twiki/bin/view/CMS/MuonReferenceResolution, Accessed 2016/07/06.

[94] CMS Collaboration, "Performance of CMS Muon Reconstruction in Cosmic-Ray Events", *JINST* 5 (2010), no. 03, T03022, arXiv:0911.4994. doi:10.1088/1748-0221/5/03/T03022.

[95] J. M. Tucker, "High transverse momentum muon reconstruction, a search for narrow dimuon resonances, and statistical techniques for LHC analyses". PhD thesis, Cornell University, 2011.

[96] CMS Collaboration, "2012 cosmic JSON file for MUONS". https://twiki.cern.ch/twiki/bin/view/CMS/Cosmic12JSON, Accessed 2017/01/24.

[97] P. Biallass and T. Hebbeker, "Parametrization of the Cosmic Muon Flux for the Generator CMSCGEN", arXiv:0907.5514.

[98] L. Sonnenschein, "CMS: Cosmic muons in simulation and measured data", arXiv:1107.0427.

[99] CMS Collaboration, "The CMS Offline SW Guide: 7.3 ECAL Clustering". https://twiki.cern.ch/twiki/bin/view/CMSPublic/SWGuideEcalRecoClustering, Accessed 2016/04/21.

[100] CMS Collaboration, "Performance of electron reconstruction and selection with the CMS detector in proton-proton collisions at $\sqrt{s} = 8$ TeV", *JINST* 10 (2015), no. 06, P06005, arXiv:1502.02701. doi:10.1088/1748-0221/10/06/P06005.

[101] CMS Collaboration, "Photon reconstruction and identification at sqrt(s) = 7 TeV", CMS Physics Analysis Summary CMS-PAS-EGM-10-005, CERN, Geneva, 2010.

[102] CMS Collaboration, "Simple Cut Based Photon ID 2012". https://twiki.cern.ch/twiki/bin/viewauth/CMS/CutBasedPhotonID2012, Accessed 2016/04/27.

[103] A. Hocker et al., "TMVA - Toolkit for Multivariate Data Analysis", *PoS* ACAT (2007) 040, arXiv:physics/0703039.

[104] R.-S. Lu, "Update Photon ID with Spring 15 Samples and Studies on 50ns Data". https://indico.cern.ch/event/369241/contribution/1/attachments/1140148/1632879/egamma-Aug14-2015.pdf, August, 2015. Presentation in Identification e/g meeting.

[105] CMS Collaboration, "General Purpose MVA-based Photon Identification". https://twiki.cern.ch/twiki/bin/view/CMS/MultivariatePhotonIdentificationRun2, Accessed 2016/05/12.

[106] CMS Collaboration, "Efficiencies and scale factors". https://twiki.cern.ch/twiki/bin/view/CMS/EgammaIDRecipesRun2, Accessed 2016/05/12.

[107] J. Campbell, K. Ellis, and C. Williams, "MCFM - Monte Carlo for FeMtobarn processes". http://mcfm.fnal.gov/.

[108] CMS Collaboration, "PREP Admin Control Panel". http://cms.cern.ch/iCMS/jsp/mcprod/admin/campaignmanagement.jsp.

[109] J. Alwall, M. Herquet, F. Maltoni et al., "MadGraph 5: Going Beyond", *JHEP* 06 (2011) 128, arXiv:1106.0522. doi:10.1007/JHEP06(2011)128.

[110] CMS Collaboration, "Standard Model Cross Sections for CMS at 8 TeV". https://twiki.cern.ch/twiki/bin/view/CMS/StandardModelCrossSectionsat8TeVInclusive, Accessed 2016/05/15.

[111] R. Gavin, Y. Li, F. Petriello et al., "FEWZ – Fully Exclusive W, Z Production through NNLO in pQCD". http://gate.hep.anl.gov/fpetriello/FEWZ.html.

[112] CMS Collaboration, "Summary table of samples produced for the 1 Billion campaign, with 25ns bunch-crossing". https://twiki.cern.ch/twiki/bin/view/CMS/SummaryTable1G25ns, Accessed 2016/05/16.

[113] J. Alwall, R. Frederix, S. Frixione et al., "The automated computation of tree-level and next-to-leading order differential cross sections, and their matching to parton shower simulations", *JHEP* 07 (2014) 079, arXiv:1405.0301. doi:10.1007/JHEP07(2014)079.

[114] CMS Collaboration, "Campaigns page McM". https://cms-pdmv.cern.ch/mcm/campaigns?page=0&shown=63, Accessed 2016/05/16.

[115] M. Czakon and A. Mitov, "Top++: A Program for the Calculation of the Top-Pair Cross-Section at Hadron Colliders", *Comput. Phys. Commun.* 185 (2014) 2930, arXiv:1112.5675. doi:10.1016/j.cpc.2014.06.021.

[116] S. Alioli, P. Nason, C. Oleari et al., "A general framework for implementing NLO calculations in shower Monte Carlo programs: the POWHEG BOX", *JHEP* 06 (2010) 043, arXiv:1002.2581. doi:10.1007/JHEP06(2010)043.

[117] T. Gleisberg, S. Höche, F. Krauss et al., "Event generation with SHERPA 1.1", *JHEP* 2009 (2009), no. 02, 007, arXiv:0811.4622. doi:10.1088/1126-6708/2009/02/007.

[118] P. Nason, "A New method for combining NLO QCD with shower Monte Carlo algorithms", *JHEP* 11 (2004) 040, arXiv:hep-ph/0409146. doi:10.1088/1126-6708/2004/11/040.

[119] S. Frixione, P. Nason, and C. Oleari, "Matching NLO QCD computations with Parton Shower simulations: the POWHEG method", *JHEP* 11 (2007) 070, arXiv:0709.2092. doi:10.1088/1126-6708/2007/11/070.

[120] S. Agostinelli, J. Allison, K. Amako et al., "Geant4—a simulation toolkit", *Nuclear Instruments and Methods in Physics Research Section A: Accelerators, Spectrometers, Detectors and Associated Equipment* 506 (2003), no. 3, 250 – 303. doi:10.1016/S0168-9002(03)01368-8.

[121] J. Allison, K. Amako, J. Apostolakis et al., "Geant4 developments and applications", *IEEE Transactions on Nuclear Science* 53 (Feb, 2006) 270–278. doi:10.1109/TNS.2006.869826.

[122] CMS Collaboration, "Estimating Systematic Errors Due to Pileup Modeling". https://twiki.cern.ch/twiki/bin/view/CMS/PileupSystematicErrors, Accessed 2016/06/15.

[123] M. Grazzini, S. Kallweit, and D. Rathlev, "Wγ and Zγ production at the LHC in NNLO QCD", *JHEP* 07 (2015) 085, arXiv:1504.01330. doi:10.1007/JHEP07(2015)085.

[124] J. M. Campbell and R. K. Ellis, "An Update on vector boson pair production at hadron colliders", *Phys. Rev.* D60 (1999) 113006, arXiv:hep-ph/9905386. doi:10.1103/PhysRevD.60.113006.

[125] J. M. Campbell, R. K. Ellis, and C. Williams, "Vector boson pair production at the LHC", *JHEP* 07 (2011) 018, arXiv:1105.0020. doi:10.1007/JHEP07(2011)018.

[126] J. M. Campbell, R. K. Ellis, and W. T. Giele, "A Multi-Threaded Version of MCFM", *Eur. Phys. J.* C75 (2015), no. 6, 246, arXiv:1503.06182. doi:10.1140/epjc/s10052-015-3461-2.

[127] CMS Collaboration, "Measurement of the Zγ production cross section in pp collisions at 8 TeV and search for anomalous triple gauge boson couplings", *JHEP* 2015 (2015), no. 4, 1–40, arXiv:1502.05664. doi:10.1007/JHEP04(2015)164.

[128] O. Hindrichs, "Analysis of the production of Z plus gamma in proton-proton collisions at $\sqrt{s} = 7$ TeV and $\sqrt{s} = 8$ TeV with the CMS experiment at the LHC". PhD thesis, Aachen, 2014. Zsfassung in dt. und engl. Sprache; Aachen, Techn. Hochsch., Diss., 2014.

[129] S. Frixione and B. R. Webber, "Matching NLO QCD computations and parton shower simulations", *JHEP* 06 (2002) 029, arXiv:hep-ph/0204244. doi:10.1088/1126-6708/2002/06/029.

[130] S. Jain, M. Endres, K. Hoepfner et al., "Search for excited leptons in $\ell\ell\gamma$ final state at $\sqrt{s} = 13$ TeV", CMS Analysis Note CMS-AN-2016/017, 2016.

[131] Y. Yang, S. Jain, M. Soares et al., "Photon Fake Rate Studies for Exotica Analyses", CMS Analysis Note CMS-AN-2010/356, 2010.

[132] S. Jain, M. Endres, K. Hoepfner et al., "Search for Excited Electrons and Mouns in pp Collisions at $\sqrt{s} = 8$ TeV with the CMS Experiment", CMS Analysis Note CMS-AN-2012/418, 2014.

[133] S. Jain, "Approval of Search for excited leptons in $\ell\ell\gamma$ final state at $\sqrt{s} = 8$ TeV". https://indico.cern.ch/event/368957/, 01, 2015.

[134] S. Jain, C.-M. Kuo, and R.-S. Lu, "Measurement of the differential cross section of prompt photon and photon + jet production in proton-proton collision at $\sqrt{s} = 13$ TeV", CMS Analysis Note CMS-AN2015/224, 2016.

[135] R. D. Cousins, "Why isn't every physicist a Bayesian?", *Am. J. Phys.* 63 (1995) 398. doi:10.1119/1.17901.

[136] G. Cowan, "STATISTICAL DATA ANALYSIS". Oxford University Press Inc., 1998.

[137] R. Bayes, "An essay toward solving a problem in the doctrine of chances", *Phil. Trans. Roy. Soc. Lond.* 53 (1764) 370–418. doi:10.1098/rstl.1763.0053.

[138] R. E. Kass and L. Wasserman, "The Selection of Prior Distributions by Formal Rules", *Journal of the American Statistical Association* 91 (1996), no. 435, 1343–1370. doi:10.1080/01621459.1996.10477003.

[139] A. L. Read, "Presentation of search results: the CL_stechnique", *J. Phys.* G28 (2002), no. 10, 2693–2704. doi:10.1088/0954-3899/28/10/313.

[140] A. L. Read, "Modified frequentist analysis of search results (the CL_s method)". https://cds.cern.ch/record/451614, 2000.

[141] T. Junk, "Confidence level computation for combining searches with small statistics", *Nucl. Instrum. Meth.* A434 (1999), no. 2, 435 – 443, arXiv:hep-ex/9902006. doi:10.1016/S0168-9002(99)00498-2.

[142] G. Cowan, K. Cranmer, E. Gross et al., "Asymptotic formulae for likelihood-based tests of new physics", *Eur. Phys. J.* C71 (2011) 1554, arXiv:1007.1727. [Erratum: Eur. Phys. J.C73,2501(2013)]. doi:10.1140/epjc/s10052-011-1554-0, 10.1140/epjc/s10052-013-2501-z.

[143] S. S. Wilks, "The Large-Sample Distribution of the Likelihood Ratio for Testing Composite Hypotheses", *Annals Math. Statist.* 9 (1938), no. 1, 60–62. doi:10.1214/aoms/1177732360.

[144] A. Wald, "Tests of Statistical Hypotheses Concerning Several Parameters When the Number of Observations is Large", *Transactions of the American Mathematical Society* 54 (1943), no. 3, 426–482. doi:10.2307/1990256.

[145] CMS, ATLAS Collaboration, The LHC Higgs Combination Group, "Procedure for the LHC Higgs boson search combination in Summer 2011", CMS Note CMS-NOTE2011/005, 2011.

[146] CMS Collaboration, "Documentation of the RooStats -based statistics tools for Higgs PAG". https://twiki.cern.ch/twiki/bin/viewauth/CMS/SWGuideHiggsAnalysisCombinedLimit, Accessed 2016/12/10.

[147] L. Moneta, K. Belasco, K. S. Cranmer et al., "The RooStats Project", *PoS* ACAT2010 (2010) 057, arXiv:1009.1003.

[148] CMS Collaboration, "Search for high-mass resonances and quantum black holes in the eμ final state in proton-proton collisions at $\sqrt{s} = 13\,\text{TeV}$", CMS Physics Analysis Summary CMS-PAS-EXO-16-001, CERN, Geneva, 2016.

[149] CMS Collaboration, S. Erdweg, H. Keller, S. Mukherjee et al., "Search for lepton flavour violating decays of heavy resonances to eμ pairs in pp collisions at $\sqrt{s} = 13\,\text{TeV}$", CMS Analysis Note CMS-AN-2015/191, CERN, Geneva, 2016.

[150] S. I. Bityukov, "Signal significance in the presence of systematic and statistical uncertainties", *JHEP* 09 (2002) 060, arXiv:hep-ph/0207130. [Nucl. Instrum. Meth.A502,795(2003)]. doi:10.1088/1126-6708/2002/09/060, 10.1016/S0168-9002(03)00586-2.

[151] S. Alekhin et al., "The PDF4LHC Working Group Interim Report", arXiv:1101.0536.

[152] J. Pumplin, D. R. Stump, J. Huston et al., "New generation of parton distributions with uncertainties from global QCD analysis", *JHEP* 07 (2002) 012, arXiv:hep-ph/0201195. doi:10.1088/1126-6708/2002/07/012.

[153] NNPDF Collaboration, "Parton distributions for the LHC Run II", *JHEP* 04 (2015) 040, arXiv:1410.8849. doi:10.1007/JHEP04(2015)040.

[154] J. Butterworth et al., "PDF4LHC recommendations for LHC Run II", *J. Phys.* G43 (2016) 023001, arXiv:1510.03865. doi:10.1088/0954-3899/43/2/023001.

[155] A. Buckley, J. Ferrando, S. Lloyd et al., "LHAPDF6: parton density access in the LHC precision era", *Eur. Phys. J.* C75 (2015) 132, arXiv:1412.7420. doi:10.1140/epjc/s10052-015-3318-8.

[156] F. Demartin, S. Forte, E. Mariani et al., "The impact of PDF and alphas uncertainties on Higgs Production in gluon fusion at hadron colliders", *Phys. Rev.* D82 (2010) 014002, arXiv:1004.0962. doi:10.1103/PhysRevD.82.014002.

[157] S. Dulat, T.-J. Hou, J. Gao et al., "New parton distribution functions from a global analysis of quantum chromodynamics", *Phys. Rev.* D93 (2016), no. 3, 033006, arXiv:1506.07443. doi:10.1103/PhysRevD.93.033006.

[158] L. A. Harland-Lang, A. D. Martin, P. Motylinski et al., "Parton distributions in the LHC era: MMHT 2014 PDFs", *Eur. Phys. J.* C75 (2015), no. 5, 204, arXiv:1412.3989. doi:10.1140/epjc/s10052-015-3397-6.

[159] J. Gao and P. Nadolsky, "A meta-analysis of parton distribution functions", *JHEP* 07 (2014) 035, arXiv:1401.0013. doi:10.1007/JHEP07(2014)035.

[160] G. Watt and R. S. Thorne, "Study of Monte Carlo approach to experimental uncertainty propagation with MSTW 2008 PDFs", *JHEP* 08 (2012) 052, arXiv:1205.4024. doi:10.1007/JHEP08(2012)052.

[161] S. Jain, S. Banerjee, and S. Bhattacharya, "Search for Excited Electron in pp Collisions at $\sqrt{s} = 7\,\text{TeV}$ in the CMS Experiment with $4.7\,\text{fb}^{-1}$ of data", CMS Analysis Note CMS-AN-2011/452, 2011.

[162] L. Kaur Saini, Y. Maravin, M. Endres et al., "Search for excited leptons in $\text{pp} \to \ell\ell^* \to \ell\ell\text{qq}$ production using CMS data at $\sqrt{s} = 8\,\text{TeV}$", CMS Analysis Note CMS-AN-2014/148, 2015.

[163] T. Esch, M. Endres, K. Hoepfner et al., "Search for excited leptons in the channel $\ell\ell^* \to \ell\ell\text{Z}$ with four leptons in the final state", CMS Analysis Note CMS-AN-2013/263, 2014.

[164] T. Esch, "Search for excited muons in the process $\text{pp} \to \mu\mu^* \to \mu\mu\text{Z} \to 4\mu$ with CMS data". https://web.physik.rwth-aachen.de/~hebbeker/theses/esch_master.pdf, 01, 2014. Masterthesis.

[165] CMS Collaboration, "Instructions for applying electron and photon ID". https://twiki.cern.ch/twiki/bin/view/CMS/EgammaIDRecipesRun2, Accessed 2016/09/01.

Acknowledgements

I want to express my gratitude to my advisor, Prof. Dr. Thomas Hebbeker, for his support and the opportunity to work on an interesting topic at a fascinating experiment and during exciting times. Also, a multitude of travels and the six month stay at CERN were a great experience.
Also, I want to thank Dr. Oliver Pooth for agreeing to be the second referee of this thesis.

I thank Dr. Kerstin Höpfner for all her advise, support, and encouragement. Thanks to her coordination it was possible to combine so many analyses to one comprehensive Run I result, and to successfully publish the analyses from the two different run-periods.

Aside from Kerstin, the other members of the CMS ℓ^*-group made great contributions to this thesis. Thus, my thanks goes to: Thomas Esch, with whom I had countless fruitful discussions about excited lepton specific problems. He also contributed with his 4μ-analysis. Shilpi Jain, who did the eeγ-analysis and photon-fake estimation for Run I. The latter results directly went into the analysis presented in this thesis. Satyaki Bhattacharya, for loads of expertise in e/γ-related topics. Chia-Ming Kuo, especially for taking care of the signal production. Shu-Hao Mai, for his contributions from the "mixed" 4ℓ-channels. Yurii Maravin and Lovedeep Kaur Saini for contributing with the 4eand jet-channels. In the Run II period with its corresponding PAS, Pen-Hsuan Wang took care about the electron channel and Rong-Shyang Lu investigated the photon fake contributions.
Additionally, I want to thank the various PAG-conveners and ARC-members who helped during the publication processes by giving feedback and reviewing the analyses and documentation.
Also, many thanks to Julien Caudron, who was responsible for the predecessor μ^*-analysis with 7 TeV data, and Otto Hindrichs who provided input from his Zγ cross section measurement.

The analyses, and by that this thesis, could not have been performed successfully without a good working environment. Thus, I thank the (Aachen) computing groups and the CMS and LHC Collaborations for their work to make such an amazing experiment possible.

I also want to thank the institute members (and some associates) who created a constructive and agreeable working climate. Especially I want to mention those I shared a longer time with at the institute, who were always reliable colleagues, nice companions during the many trips we made, but also pleasant people to have great times with off-work. They are, office-wise: Andreas Güth, Sören Erdweg, Thomas Esch, Kerstin Hoepfner, Arnd Meyer, Markus Merschmeyer, Adriana Del Piero, Deborah Duchardt, Simon Knutzen, Paul Papacz, Tobias Pook, Jonas Römer, Michael Brodski, Andreas Albert, Swagata Mukherjee, Klaas Padeken, Mark Olschewski, Sebastian Thüer, Markus Radziej, Leila Ali Cavasonza, Ilya Bekman, Daniel Teyssier and the "Hallenbewohner".

Finally, I would like to thank my parents for giving me the opportunity to study physics, which is the very basis for this thesis.